



University
of Glasgow

<https://theses.gla.ac.uk/>

Theses Digitisation:

<https://www.gla.ac.uk/myglasgow/research/enlighten/theses/digitisation/>

This is a digitised version of the original print thesis.

Copyright and moral rights for this work are retained by the author

A copy can be downloaded for personal non-commercial research or study,
without prior permission or charge

This work cannot be reproduced or quoted extensively from without first
obtaining permission in writing from the author

The content must not be changed in any way or sold commercially in any
format or medium without the formal permission of the author

When referring to this work, full bibliographic details including the author,
title, awarding institution and date of the thesis must be given

Enlighten: Theses

<https://theses.gla.ac.uk/>
research-enlighten@glasgow.ac.uk

THE ALEPH ELECTROMAGNETIC CALORIMETER FOR LEP

by

BUTRUS YOUKHANA ALTOON

**Submitted for the Degree of Master of Science
to the Faculty of Science at the University of Glasgow**

September 1988

ProQuest Number: 10998191

All rights reserved

INFORMATION TO ALL USERS

The quality of this reproduction is dependent upon the quality of the copy submitted.

In the unlikely event that the author did not send a complete manuscript and there are missing pages, these will be noted. Also, if material had to be removed, a note will indicate the deletion.



ProQuest 10998191

Published by ProQuest LLC (2018). Copyright of the Dissertation is held by the Author.

All rights reserved.

This work is protected against unauthorized copying under Title 17, United States Code
Microform Edition © ProQuest LLC.

ProQuest LLC.
789 East Eisenhower Parkway
P.O. Box 1346
Ann Arbor, MI 48106 – 1346

ACKNOWLEDGEMENTS

I would like to thank Professor I. O. Skillicorn, the Head of Glasgow University High Energy Physics group, for his interest and support.

I am most grateful to my supervisor, Dr. K. M. Smith, for his teaching and supervision during the period of this work.

The financial support of the Iraqi Republic Government is gratefully acknowledged.

I would like to thank the other members of the High Energy Physics group, for their help and support, especially Dr. A.S. Thompson for his computing assistance and advice.

I thank the Department of Physics and Astronomy under the direction of Professor I. S. Hughes, and the staff of Rutherford Appleton Laboratory, and CERN for their assistance in carrying out this research.

I would like to thank Dr. C. Raine and my colleague, John Hearns, for their cooperation and assistance.

I would like to thank A. Seath for his technical assistance in preparing the stack layer for anode wire pulsing, and Mrs M. Waterson, Miss C. Macintyre for their assistance in the preparation of this thesis.

Finally I thank my wife and children for their patient support. To them I dedicate this work.

SUMMARY

This thesis is an account of work carried out at the Physics Department, University of Glasgow in cooperation with Rutherford Appleton Laboratory, Didcot, and CERN, Geneva, between October 1986 and October 1988.

The object of the work was to study the uniformity of the ALEPH electromagnetic calorimeter petals, eight of which have been built in the Department.

This work deals mainly with the analysis of the anode wire pulsing tests of the modules which were built in this department, and also the analysis of the test beam data taken on the X7b beam in the west area at CERN during the summer of 1987.

The results of wire pulsing, cosmic ray tests and test beam running are compatible with the designed response uniformity of 1%. Wire pulsing has proved to be an important tool for the discovery of faults during the construction stage, due to e.g. missing pads, missing towers, broken wires etc. Results from the test beam proved that the calorimeter modules show good linearity and an energy resolution consistent with the design value for the calorimeter. A uniformity of better than 2% has been achieved so far from the cosmic ray and the beam tests. A detailed description of the systems used in these tests is given in chapters 4 and 5.

Chapter 1 reviews physics related to e^+e^- colliders and in particular the LEP collider. The chapter includes a brief description of the LEP experiments and a discussion of some detailed aspects of the physics to be studied at LEP, e.g. e^+e^- interactions, physics at the Z° pole, toponium physics, neutrino counting and Higgs particles.

The second chapter reviews the published work related to electromagnetic and hadron calorimeters and their performance.

Chapter 3 describes the construction and performance of the ALEPH detector. Some results of tests on the ALEPH components carried out by different groups within the ALEPH collaboration are presented.

Chapter 4 deals with the construction of the Electromagnetic Calorimeter (ECAL), in particular with the operations carried out in the department and with the test procedures adopted during construction.

The results of the analysis of the module uniformity carried out during the period of this work are presented and discussed in chapter 5.

Chapter 6 gives a summary of the tests and conclusions.

CONTENTS

	Page No.
CHAPTER 1 - INTRODUCTION	11
1.1 Colliders	11
1.2 Electron - Positron Interactions	11
1.3 The LEP Electron Positron Collider	13
1.4 Physics at LEP	13
1.4.1 Physics at the Z⁰ Pole	13
1.4.2 Neutrino Counting	15
1.4.3 Toponium Physics at LEP	16
1.4.4 Higgs Particles	17
1.4.5 Physics with the Highest Energies Available at LEP	18
1.5 The LEP Detectors	18
1.6 The LEP Machine	19
1.6.1 Energy	20
1.6.2 Luminosity	20
1.6.3 Energy Spread	22
1.7 Measurement of Luminosity at LEP	22
1.8 Experimental Background Problems	24
CHAPTER 2 - CALORIMETRY	26
2.1 Electromagnetic Calorimeters	27
2.1.1 Energy Resolution	29
2.1.2 Homogeneous Electromagnetic Calorimeters (EMC)	31
2.1.3 Sampling Calorimeters	32

2.2	Hadron Calorimeters	33
2.3	Read Out Systems	35
2.4	Spatial Resolution	37
CHAPTER 3 - THE ALEPH DETECTOR		38
3.1	The Superconducting Coil	38
3.2	The Minivertex Detector	39
3.3	The Luminosity Monitor	40
3.3.1	The Tracking Device (SATR)	41
3.3.2	The Luminosity Calorimeter (LCAL)	41
3.4	The Inner Tracking Chamber (ITC)	42
3.5	The Time Projection Chamber (TPC)	43
3.5.1	Electronics	44
3.5.2	The Laser Calibration System	45
3.5.3	Gating	46
3.5.4	The Field Cage for the ALEPH TPC	47
3.5.5	Gas System	47
3.5.6	Performance	48
3.6	The Electromagnetic Calorimeter (ECAL)	51
3.7	The Hadron Calorimeter (HCAL)	51
3.8	The Muon Detector	52
3.9	The Trigger	53

CHAPTER 4 THE ALEPH ELECTROMAGNETIC CALORIMETER (ECAL)	55
4.1 General Description of the Calorimeter	55
4.2 Electronics	57
4.3 ECAL Petal Construction	59
4.3.1 Wire Plane	59
4.3.2 Lead Pad Board Layer	60
4.3.3 Stacking the Layers	61
CHAPTER 5 - TESTS OF COMPLETE ECAL MODULES	62
5.1 Effect of Mechanical Tolerances on Uniformity	62
5.2 Calibration Procedure	64
5.2.1 Calibration of the Electronics	64
5.2.2 Tests of Complete Modules	64
CHAPTER 6 - SUMMARY AND CONCLUSIONS	71
APPENDIX 1 The LEP Accelerator Sub-Systems	73
APPENDIX 2 Polarisation in LEP	77
REFERENCES	79

FIGURE CAPTIONS - CHAPTER 1

- 1.1 Differential Cross-sections for Principal e^+e^- QED Interactions at 1 GeV
- 1.2 Energy Dependence of R , the Ratio of Hadron Production to Muon Pair Production in e^+e^- Interactions
- 1.3 Qualitative Features of σ total variation with energy
- 1.4 Layout of the LEP Accelerator
- 1.5 Contribution to $Z^0 \rightarrow \gamma + (\text{Nothing})$ from Neutrino - Antineutrino Pairs
- 1.6 Photon Energy Spectra from $Z^0 \rightarrow \gamma\nu\bar{\nu}$
- 1.7 Photon Energy Spectra from $Z^0 \rightarrow \gamma\nu\bar{\nu}$ at different values of \sqrt{s}
- 1.8 Decay of Charged Higgs into (a) $H t \bar{b}$ and (b) $H^0 \gamma$ via Toponium
- 1.9 The DELPHI Detector
- 1.10 The OPAL Detector
- 1.11 The L3 Detector
- 1.12 Typical Variation of Luminosity with Circulating Beam Energy
- 1.13 Synchrotron Radiation Intensity per Metre, for an Electron Beam of 100 mA and Bending Radius 12 m, as a Function of Photon Cut-off Energy

FIGURE CAPTIONS - CHAPTER 2

- 2.1 Model of the Development of an Electromagnetic Shower
- 2.2 Longitudinal Distribution of E.M. Shower Energy Deposition in Different Materials
- 2.3 Radial Distribution of E.M. Shower Energy Deposition

- 2.4 Effects of Leakage on E.M. Shower Energy Deposition
- 2.5 Influence of Sampling Layer Thickness on Energy Resolution in a Liquid Argon Calorimeter
- 2.6 Effects of Sampling, Path-Length and Landau Fluctuations on Energy Resolution in
 - (a) Wire Proportional and (b) Tube Chambers
- 2.7(a,b) Longitudinal and Transverse Energy Distribution in a Hadronic Shower
- 2.8 'Visible' Shower Energy vs. Primary Hadron Energy Interacting with a Hadron Calorimeter
- 2.9 Ratio of visible energies of π mesons and electrons at the same energy ('response ratio') in iron-scintillator calorimeter.
- 2.10 Results from a Uranium Calorimeter, Showing Effects of 'Compensation'
- 2.11 Relative Energy Resolution $\sigma(E)/E$ for Different Calorimeters
- 2.12 Pulse Height Distribution from Iron-Scintillator Hadron Calorimeter for Monoenergetic π mesons Using the 'Weighting' Technique
- 2.13 Reduced Energy Resolution $\sigma(E)/\sqrt{E(\text{GeV})}$ in units of (% $\sqrt{\text{GeV}}$) for π mesons in a lead-scintillator Calorimeter
- 2.14 Energy Resolution Dependence on Thickness of Sampling Layer in a Hadron Calorimeter
- 2.15 Illustration of Different Calorimeter Read-out Systems
- 2.16 The radial shower profile of 1 GeV electrons in aluminium

FIGURE CAPTIONS - CHAPTER 3

- 3.1 Overall layout of ALEPH
- 3.2(a,b) Facility for Inserting/Withdrawing MVD Outer Layer Sections
- 3.2(c) The Minivertex Detector (MVD)
- 3.2(d) Mechanical Support Structure of MVD Inner Layer
- 3.2(e) Mechanical Support of the two halves of the Inner Layer
- 3.3 Al_2O_3 support for Pre-amplifiers
- 3.4 Voltage vs. (a) current, (b) capacity, (c) interresistance of a silicon detector
- 3.5 Results of Tests of Silicon Detectors with a Beta Source
- 3.6 Illustration of z - Strip Detector with Front-end Electronics
- 3.7 Block Diagram of MVD Read - out Electronics
- 3.8 Noise vs. Input Capacity for One Multiplexer Channel
- 3.9 Luminosity Monitor Components
- 3.10(a) SATR Viewed from Interaction Point
- 3.10(b) SATR Tube Orientation
- 3.10(c) Detail of End - Structure of SATR Tubes
- 3.11 The LCAL Structure
- 3.12 Location of ITC Relative to Other Parts of ALEPH
- 3.13 $r - \phi$ Resolution of ITC: (a) Layer 1; (b) Other Layers

- 3.14 TPC End - Plate Geometry
- 3.15 TPC Pad Layout
- 3.16 Functional Block Diagram of TPC Pad and Wire Signal Read-out
- 3.17 Laser Calibration System for TPC
- 3.18(a) Gating Grids in the TPC
- 3.18(b) Gating Voltage Waveforms
- 3.19 Structure of the TPC Field Cage
- 3.20(a) Momentum Resolution vs. Azimuthal Angle in the TPC
- 3.20(b) Momentum Resolution After Angular Correction
- 3.21 Percentage of Unambiguous Points vs. Two - Track Separation Capability from M.C. jets in the TPC
- 3.22 e - π and π - K Separation vs. Momentum in dE/dx Resolution Units in the TPC
- 3.23(a) Structure of an HCAL Layer
- 3.23(b) Mixing of 7 - and 8 - Tube Boxes in HCAL
- 3.23(c) HCAL End - Cap Module Structure
- 3.23(d,e) Dead Regions in which HCAL is Insensitive
- 3.24(a) HCAL Tower Geometry
- 3.24(b) HCAL End - CAP Module Pad Arrangement
- 3.25(a) Muon Detector Read - Out Strips

3.25(b) Muon Chamber Coverage of Barrel Notches

FIGURE CAPTIONS - CHAPTER 4

- 4.1 Illustration of ECAL construction
- 4.2 Structure of a petal layer
- 4.3 Isometric view of pad towers in a petal
- 4.4 ECAL electronics schematic
- 4.5(a) ECAL electronics
- 4.5(b) Multiplexing organisation in petal read-out
- 4.6 Wire termination detail
- 4.7 Terminating electronics on a wire plane
- 4.8 Flare test photographs of (a) a faulty plane and (b) a good plane
- 4.9 PCB arrangement in a cathode plane

FIGURE CAPTIONS - CHAPTER 5

- 5.1 ECAL petal signal (from 20 GeV electrons) as a function of E.H.T.
- 5.2 ECAL petal signal versus pressure in module
- 5.3 Response of one petal layer to wire pulsing, showing effects of a missing wire and of missing pads.
- 5.4 Uniformity map of petal surface area from wire pulsing test
- 5.5 Distribution of normalised pad signals, from pad (25-12), in each layer of petals 4

and 6

- 5.6 Block diagram of electronics used to test wire pulsing of a single wire plane
- 5.7 Cathode PC board layout
- 5.8 Pad signal vs. pulsing voltage on anode wires
- 5.9 Pad signal vs. capacitance for fixed pulsing voltage
- 5.10 Diagram to illustrate approximate calculation of wire-pad capacitance
- 5.11 Diagram of R.A.L. cosmic ray test rig
- 5.12 Calibration regions of petal surface
- 5.13 Pedestal variations for a typical tower and typical wire plane
- 5.14 Layout of the X7b test beam area at CERN
- 5.15 Signal in ECAL due to 10 GeV π^-
- 5.16 Linearity of ECAL Measured in Test Beam
- 5.17 Energy Resolution of ECAL with Electrons
- 5.18 Energy Resolution of ECAL with Pions
- 5.19 e / h Ratio for ECAL vs. Energy
- 5.20 Pad signal from muons vs. $\sec \theta$
- 5.21 Wire signal from muons vs. $\sec \theta$
- 5.22 Pad signal from muons vs. ϕ
- 5.23 Wire signal from muons vs. ϕ

5.24 Longitudinal energy deposition by muons in a petal, measured on the anode wire planes

5.25 Test beam muon signal uniformity plot

FIGURE CAPTIONS CHAPTER 6

6.1 The Uniformity map for petal 9

FIGURE CAPTIONS APPENDIX 1

1.B1 The Phase Space Trajectory

FIGURE CAPTIONS APPENDIX 2

1.B2 The build up time of polarisation as a function of energy

1.B3 Degree of polarisation at LEP in the presence of the linear spin resonance

Chapter 1 - Introduction

In this chapter, a review is given of typical interactions which have been studied previously with e^+e^- colliders and of the reaction channels which will be the main focus of attention at LEP. Details of experimental problems which must be overcome in the extraction of physics results are discussed at some length, together with the accelerator properties which help to define experimental limitations.

1.1 Colliders

In colliding beam accelerators, ('colliders'), two beams of high energy charged particles circulating in opposite directions collide head-on at various points (interaction regions). If the two beams have opposite charge, (e.g. proton-antiproton, electron-positron), the same ring of confining magnets may be used for both; otherwise two different rings must be used. Table 1 summarizes the existing and planned e^+e^- colliders, the latest of which, LEP, is expected to come into operation in the second half of 1989. The high C.M. energy obtained from the colliders has great advantages in particle physics research, in particular enabling two main goals to be achieved :

1. For the creation of a new particle of mass (m) we need a minimum amount of energy (E) such that $E=m c^2$: the heavier the particle, the higher energy required.
2. To investigate the structure of a particle down to the particle radius (R), we need to transfer a momentum (ΔP) such that $R(\Delta P) = \hbar$, so to go to small (R) the momentum transfer must be large, and the available energy must be high. For circulating beam energies E_1 and E_2 , the energy available at the interaction point is given by

$$E_{c.m.} = E_1 + E_2 = \sqrt{s}$$

The number of interactions of a given type produced in a collider experiment is given by the product of the interaction cross-section and the so-called "luminosity" of the accelerator, which is discussed further below. The true number is only obtained only after allowance for backgrounds due to synchrotron radiation, scattering of beam particles off residual gas in the vacuum chamber and cosmic radiation, all of which are also considered below.

1.2 Electron-Positron Interactions

At low energies the main channels of e^+e^- interactions are $e^+e^- \rightarrow e^+e^-, \mu^+\mu^-$, $e^+e^- \gamma, \gamma\gamma$. The cross-section for the above channels is (s) dependent, with $\sigma \propto s^{-1}$. The

differential cross-section for the most important channels is shown in Fig.1.1 for a beam energy of 1GeV. The largest cross-section is for Bhabha scattering at small angles. The QED predictions and measured cross-sections for e^+e^- , $\mu^+\mu^-$, and two photon annihilation are in good agreement. Evidence from deep inelastic e-nucleon scattering has led to the hypothesis that the photon-nucleon interaction is basically a photon-quark interaction. As a consequence, assuming the quarks are point-like spin-1/2 particles, we expect $e^+e^- \rightarrow$ hadrons to proceed via the formation of quark-antiquark pairs, on a similar basis to pair production. The quarks are presumed to fragment to hadrons with unit probability. The lowest bound states of the $q\bar{q}$ system are $\rho^0(u\bar{u})$ and $\omega(d\bar{d})$, with higher states $\phi(s\bar{s})$, $\psi(c\bar{c})$ and $T(b\bar{b})$. The first three are non-strange vector mesons which have the same quantum numbers as the photon.(1) The study of the $e^+e^- \rightarrow$ hadrons channel is often referred to in terms of the ratio R, where

$$\begin{aligned} R &= \sigma(e^+e^- \rightarrow \gamma^* \rightarrow h) / \sigma(e^+e^- \rightarrow \gamma^* \rightarrow \mu^+ \mu^-) \\ &= \sigma(e^+e^- \rightarrow \gamma^* \rightarrow q\bar{q}) / \sigma(e^+e^- \rightarrow \gamma^* \rightarrow \mu^+ \mu^-) \\ &= N_c \sum_q e^2_q \end{aligned}$$

The sum is over quarks with $m_q < \sqrt{s}/2$, where e_q is the quark charge in units of the electron charge, and N_c is the number of types (colours) of each quark flavour. The measured value of R is limited in accuracy by systematic errors, mostly from the incomplete coverage of the 4π solid angle. The R dependence on the the centre-of-mass energy up to 40 GeV is shown in Fig.1.2. The value of R varies from (2 - 2.5) near charm threshold at 4 GeV, rising sharply to reach a new level of (4 - 4.5) above this threshold. It is expected to rise to 5 due to the existence of a sixth quark with a charge of 2/3. The values of R corresponding to different quark flavours are listed below

R	q
2	d,u,s
10/3	d,u,s,c
11/3	d,u,s,c,b
15/3	d,u,s,c,b,t

The steps in the data are consistent with the quark interpretation provided that each quark flavour has three colours. The qualitative features of the cross-section variation with energy are shown in Fig.1.3. Apart from the two peaks at the ψ and T resonance regions, the cross-section falls steadily up to $\sqrt{s} \approx 90$ GeV, where the Z^0 peak occurs with a cross-section of 40 nb, 1000 times the QED cross-section there. The energy region $\sqrt{s} = (10-40)$ GeV is covered by PEP, PETRA and TRISTAN. Higher energies will be provided by the new LEP

accelerator, which will now be described.(4)

1.3 The LEP Electron Positron Collider

The LEP collider is being constructed at CERN, the European High Energy Physics laboratory situated just outside Geneva. It consists of a tunnel 27 kilometers in length, containing an evacuated circular beam pipe. Electrons and positrons are accelerated round this ring in opposite directions to produce collisions at eight interaction points with centre of mass energy of approximately 100 GeV. (Later the energy should be increased up to about 200 GeV.) Typical events are expected to be complex, with many particles each, distributed in jets over the entire sphere. The machine layout is shown in Fig.1.4.

1.4 Physics at LEP

LEP will be used as a Z^0 "factory". In each of the four intersection regions, 47 GeV (LEP1) electrons and positrons will collide and annihilate, producing stationary Z^0 bosons at mass 94 GeV. Each Z^0 boson will decay (within 10^{-2} s) but the decay products can be observed in the experimental apparatus surrounding the interaction region and the Z^0 reconstructed. Each of the four LEP experiments should record several million Z^0 decays during the first three years of operation. Studying Z^0 decay will become the principle method of probing deeper into the structure of matter.

The areas of physics to be studied in the first phase of operation of LEP are discussed in some detail below, and a review is given of other aspects of physics to be studied in phase 2.

1.4.1 Physics at the Z^0 Pole

At the luminosities of the SLC and LEP 1 colliders, $10^{30} - 10^{31} \text{ cm}^{-2} \text{ s}^{-1}$, the interaction cross-section corresponds to about $10^4 Z^0$ events per day. Such high event rates allow precision tests of the 'Standard Model' (4) and sensitive searches for possible new particles produced in Z^0 decays. To start with, measurements will be made of the Z^0 mass and width. It is proposed to carry out the measurements by collecting data in 2 GeV steps, during intervals of two days, (assuming 100% efficiency), at each of 13 energy intervals spanning the resonance. In addition, a number of days will be dedicated to data taking on the Z^0 pole; (> 100 days is desirable). Through the above procedure of data collection, the Z^0 mass and width may be determined by reconstructing the line shape of the Z^0 resonance in the channel $e^+e^- \rightarrow \mu^+\mu^-X$, subject to uncertainties which may be summarised as follows.(8)

1. Statistical errors

The statistical errors obtained from $e^+e^- \rightarrow \mu^+\mu^-X$ in about 10 days would be given by

$$(\delta m_z)_{\text{stat.}} \leq \pm 10 \text{ MeV}$$

$$(\delta \Gamma_z)_{\text{stat.}} \leq \pm 15 \text{ MeV}$$

There is very little dependence of these numbers on additional running time.

2. Systematic Errors

The systematic errors can be put in the following categories:

i) The machine energy spread, as planned for LEP beams, will be given by $\Delta E/E = 0.78 \times 10^{-3} (E/50 \text{ GeV})$ at the Z° pole. This corresponds to $\Delta W = 70 \text{ MeV}$ where $W = m_z = E_{\text{c.m.}}$. The spread of energy is well known and can be taken into account rather precisely, so it is not a problem at LEP.

ii) For the measurement of the Z° mass and width at LEP from an energy scan around the Z° pole, the absolute normalization of the luminosity drops out, and only the relative luminosity is important. Systematic errors which are energy dependent, (e.g. electro-weak corrections), and contributions which stem from changes in running conditions, (e.g. changes of the beam size and position), must be considered, however.

iii) The absolute energy scale (which must be stable, reproducible, and known)

iv) The main limitation on the accuracy of the measured value of m_z appears to arise from the absolute determination of the beam energy. The energy determination is made by measuring the line integral of the magnetic field over the magnetic length:

$$E \approx \int B(I) dL \approx B(I) L_{\text{mag.}}$$

A variation of $(\Delta E/E) \approx \pm 3 \times 10^{-4}$ leads to an uncertainty δm_z of $\pm 28 \text{ MeV}$. The energy determination can be improved by spin-resonance calibration, (transverse polarization is adequate for this purpose); then $\{\delta E/E\}_{\text{abs.}} \approx \pm 1 \times 10^{-5}$ leading to $\delta m_z \approx \pm 1 \text{ MeV}$. The reproducibility of the beam energy is dominated by magnetic field stability. A relative stability of $\{\delta E/E\}_{\text{rel.}} \approx \pm 1 \times 10^{-4}$ leads to $\delta m_z \approx \delta \Gamma_z \approx \pm 10 \text{ MeV}$.

3. Radiative Corrections

The Z° resonance, in lowest order, has a Breit-Wigner line shape which is characterized by experimentally measurable quantities: the peak position or mass, the width, and cross-section. The mass is related to $\sin^2 \theta_W$, the width depends on the number of particles of

mass less than half the mass of the Z^0 which couple to Z^0 , and the peak cross-section is related to the vector and axial vector couplings, and hence $\sin^2 \theta_W$. Since the mass and the width of the Z^0 will be measured using the beam energy, it is of importance to know the absolute value and the energy spread to a high degree of accuracy. The Z^0 resonance is profoundly altered from its zeroth order Breit-Wigner shape by radiative corrections. In particular, bremsstrahlung from the annihilating e^+ and e^- alters the effective centre-of-mass energy and significantly changes any quantity related to s . This results in shifts of hundreds of MeV in the mass and width of the resonance, and lowers the peak cross-section by tens of percent. Radiative corrections to the Z^0 are dominated by initial state QED effects. Recent work extending the calculations to second order has given confidence that QED radiative corrections are well understood and that the precision achievable in these corrections is significantly better than the 45 MeV limit currently expected from experimental measurements. For precision measurements of the mass and width of Z^0 at SLC and LEP, calculations include exponentiation of the soft and virtual photons. Corrections to at least first order are found to be adequate.(6)

1.4.2 Neutrino Counting

The experimental accuracy achieved at LEP 1 will be more than adequate to test the predictions of the Standard Model for Γ_{total} (7,8)

$$\Gamma_{\text{total}} = (2645 \pm 20 \pm 30 \pm 10 \pm 4) \text{ MeV}$$

where the errors estimated are for the uncertainties in a_s , the strong coupling constant, m_t , the top quark mass, $\sin^2 \theta_W$ and M_Z . Thus LEP1 should be able to determine whether there are additional neutrinos, or other light neutral excitations which couple to the Z^0 , beyond those of the three known generations. The above method is rather an indirect one. The alternative and more direct way to do this neutrino counting uses the process $Z^0 \rightarrow \gamma + (\text{Nothing})$. Here 'Nothing' stands for any kind of neutral penetrating excitation and includes, in particular, neutrino pairs. Near the Z^0 resonance this process has dominant contributions from neutral excitations produced by virtual Z^0 's. This is illustrated, for the particular case of neutrinos, by Fig.1.5. The size of cross-section depends directly on the partial width of the Z^0 into neutral unseen excitations and so a measurement of $e^+e^- \rightarrow \gamma + \text{Nothing}$ in the vicinity of $\sqrt{s} = M_Z$ serves as a measure of this width. The photon energy spectrum is shown in Fig.1.6. The height of the peak is proportional to N_ν , which for this figure is taken as 3. Counting the number of neutrinos this way at LEP depends mostly on how successful one is in suppressing the normal QED background from the process $e^+e^- \rightarrow e^+e^-\gamma$, in which both final charged particles are lost in the beam pipe. At LEP an electron is lost if $\theta_e \leq 6^\circ$ or $\theta_e \geq$

174° . Since photons produced at large angle with respect to the beam axis do not arise, in general, from configurations with forward going electrons or positrons, the cut $20^\circ < \theta_\gamma < 160^\circ$ should substantially reduce the QED background. Gaffo, Gatto and Remiddi predict much more QED background, however, and suggest that the neutrino counting experiment be carried out at energies only slightly above the Z^0 mass, where the cross-section shown in Fig.1.7 is rather large and, if an accurate background subtraction can be performed, one may in the end be better off. This same point was made some time ago by Bartels, Fridman, Wu and Schwarz. An alternative possibility, however, is to run at energies much above the Z^0 mass where, even though the cross-section is smaller, the background is really rather negligible. This is also illustrated in Fig.1.7.

1.4.3 Toponium Physics at LEP

(Searches for toponium and studies of its properties)

Since the discovery of the J/ψ more than a decade ago heavy quarkonia have played a central role in particle physics. The ψ and T families of the ($c\bar{c}$) and ($b\bar{b}$) bound states become the "Hydrogen atom" of strong interactions. Their decay patterns support the quark-gluon picture of perturbative quantum chromodynamics (QCD), and from some of their properties one can obtain a quantitative determination of the QCD scale parameter Λ .

The standard gauge theory of strong and electroweak interactions predicts the existence of the top-quark (t), a sixth heavy quark which should complete the third quark-lepton family. So far the search for ($t\bar{t}$) spectroscopy at PETRA and PEP has not been successful. The present lower bound on the mass of the ($t\bar{t}$) ground state has reached 46 GeV. Present UA1 results indicate a mass range of $(100 \rightarrow 200)$ GeV for ($t\bar{t}$) states which will be accessible at SLC and LEP. In contrast to the ψ and T spectroscopies, in the ($t\bar{t}$) system the weak interactions will play a major role. Production and annihilation of decays of toponium states are strongly affected by the Z^0 boson, and furthermore the β -decay of the t -quark becomes increasingly important for a t -quark mass above 30GeV. On the experimental side, compared with quarkonium physics at SPEAR, DORIS and CERN, the main challenge is the large spread of energy which decreases the height of the resonance peak. The search for the toponium S-states is performed in two steps:

- i) The scanning region is reduced to a region of about 2GeV through a rough measurement of the t -quark mass.
- ii) This region is then scanned in steps of $2\delta W$... (δW denotes the spread in the centre-of-mass energy), looking for a signal in the total hadronic cross-section, and eventually applying additional topological cuts. The strategy for limiting the scanning region to 2

GeV is very different for toponium above or below Z^0 mass. If the t-quark is light enough, a large number of T-mesons can be produced at the Z^0 resonance in the e^+e^- reactions, and the t-quark mass can be determined. If it is above the Z^0 , it will be more efficient to search for the top threshold.(9)

1.4.4 Higgs Particles

Higgs particles are an essential ingredient of present gauge theories of the weak interactions. They are the agents of symmetry breaking and are responsible for mass generation of the known particles. Their experimental investigation is, then, of the highest importance. In the minimal GSW model, one neutral Higgs particle H^0 is needed. In extensions of the standard model, (e.g. SUSY, technicolour, ... etc.), many charged and neutral Higgs-like scalars are expected - $H^0_1, H^0_2, \dots, H^+_1, H^-_2, \dots$. In both cases the masses of these particles are almost completely undetermined. On the other hand the fermion-Higgs couplings g_{fH} are usually assumed to be proportional to the fermion (quark or lepton) masses. This immediately suggests that toponium is an interesting source of the Higgs particles with masses $m_H < m_{tt}$.

1. Charged Higgs Particles

The detection of charged Higgs particles with masses less than the t-quark mass, m_t , will be easy since, in this case, the heavy quark (antiquark) of the bound state will predominantly decay into H^+ (H^-) and b (\bar{b}), Fig.1.8(a). The amplitude for this decay is proportional to $\xi_{Htb}(m_t/v)$, where ξ_{Htb} represents an unknown (t,b) mixing angle and v is the Higgs vacuum expectation value.

2. Neutral Higgs Scalars

The importance of heavy vector-meson decay into $H^0 + \gamma$ Fig.1.8(b) was first recognized by Wilczek. This reaction has a clear signature characterized by a monochromatic photon, the Higgs mass being identified by the missing-mass technique. The number of events obtained for 1000 hours of running time under normal conditions in LEP is quite high, even for large Higgs masses, as shown in Table 2.

1.4.5 Physics with the highest energies available at LEP

In addition to more detailed tests of QCD, and investigations of gamma gamma interactions and heavy quark physics, the higher energy at LEPII will enable an extension of the search for new particles. Experiments at the highest LEP energies up to and beyond the W^+W^- pair production threshold will provide possibilities for pursuing physics beyond the Standard Model.

The above goals will be achieved by the detectors of the four experiments of LEP, which are briefly reviewed below.

1.5 THE LEP DETECTORS

ALEPH

The details of construction and performance are given in chapter 3. Chapters 4 and 5 deal with the electromagnetic calorimeter which is one of the most important parts of the detector.

DELPHI

The DELPHI detector has some similar features to ALEPH, but DELPHI is more complicated, mainly because of the additional instrumentation for particle identification, particularly the RICH detectors. The identification of fast charged hadrons (π , K, p) with efficient tagging of charm and (especially) beauty decays by a very precise silicon microstrip detector, and high spatial resolving power in the barrel electromagnetic calorimeter, is intended to provide the best possible tools for fully reconstructing and understanding the hadronic Z^0 decays. The RICH detectors are large and complicated. To make room for them, the solenoid is slightly larger than that in ALEPH, (though with slightly lower field, 1.2 T), and the TPC is smaller (2.4 m in diameter and 2.7 m long). The muon identifier is partly inside and partly outside the iron yoke. The smallest detector in DELPHI is the microvertex detector which uses silicon strips to obtain 5 μm precision on track positions at two radii near the beam pipe to help identify charm, top and beauty decays. A layout of the detector is shown in Fig.1.9.

OPAL

The OPAL design is relatively conservative compared to the other LEP detectors. A rapid and problem-free start is expected due to the implementing of a design which is already tested.

The 0.5 T solenoidal magnetic field is produced by a conventional coil. The large central tracking detector, 3.7 m in diameter and 4.0 m long, is based on the much smaller but very successful jet chamber of the JADE experiment at PETRA. Similarly, the electromagnetic calorimeter uses lead glass blocks which, in the barrel region, lie outside the magnetic field. The OPAL vertex detector is mounted inside the central tracking detector. It will be a very precisely constructed drift chamber which aims to measure tracks with a point precision of 30 μm , to tag decaying particles with lifetimes down to 10^{-13} s and also to produce a fast track trigger. A layout of the detector is shown in Fig.1.10.

L3

L3 is the largest of the detectors and it aims for great accuracy in many of its measurements on the particles emerging from collisions. It is distinguished from other detectors by having its magnet outside of the detector volume. The magnet, which is of conventional type rather than superconducting, is very big, incorporating 8500 tonnes of iron. The detector L3, in contrast to the other detectors, is not mobile, due to its very large size. The concentric inner detectors include a central tracking chamber, lepton calorimeter, hadron calorimeter and high precision muon tracking chambers. The detector hopes to achieve a mass determination to better than 1% for leptons. The lepton calorimeter of the L3 detector is built of 10000 crystals of bismuth germanium oxide (BGO), i.e. it is a homogeneous calorimeter, while the lepton calorimeters in the other LEP experiments are sampling calorimeters. A layout of the detector is shown in Fig.1.11.

1.6 The LEP Machine

The Beams

The electron and positron beams will be injected into LEP each in four bunches equally spaced around the ring. The C.M. energy will be 100 GeV in the first phase of LEP and will be increased to 200 GeV in the second phase. Bunch size and shape is due to an equilibrium between the oscillations around the ideal orbit and the radiation damping due to synchrotron radiation. Nevertheless there remain instabilities due to large oscillations, scattering on the residual gas in the pipes and collective effects inside the bunches, all of them leading to a limited lifetime for a stored beam. Rejection is necessary after a time generally measured in hours - for LEP it is about two hours. Details of other characteristics of the $e^- e^+$ beams in LEP are discussed below. (See also Appendix 1).

1.6.1 Energy

The maximum energy of the beam depends on the power needed in the RF cavities in order to compensate the energy loss by the synchrotron radiation. Beam energy can be measured during the operation of the collider either directly from the magnet set up which fixes the orbits, (measurement of the field in the magnets), or indirectly from the kinematics of particles in a well-known e^+e^- reaction. The e^+, e^- energy resolution is of the order 10^{-3} .

1.6.2 Luminosity

The luminosity L is defined by the following relation

$$L = (n_1 n_2 / F) f B$$

where n_1 and n_2 are the numbers of particles per bunch, F = beam cross section, B = number of bunches per beam and f = rotation frequency.

$$F = 4\pi \sigma_x \sigma_y$$

where σ_x, σ_y are the rms radii.

Luminosity can be measured in two ways :

- a. Directly by measuring the beam currents during operation.

$$L = I_1 I_2 / (4\pi e^2 \sigma_x \sigma_y f B)$$

where, I_1, I_2 are the beam currents, and $I = n e f B$

- b. Indirectly during running, through monitoring the event rate for a known cross-section, where N (the number of events) = $L \sigma$. Usually, the rate of a well-known (QED) reaction, Bhabha scattering, $e^+e^- \rightarrow e^+e^-$ at small angles is chosen because it has the largest cross-section, the interference between γ and Z^0 is negligible, and because QED is known to work at small momentum transfers. The maximum luminosity depends strongly on energy. The main limiting factors are :

Synchrotron Radiation

The radiated energy depends on the beam energy E and the bending radius ρ ,

$$U_{\text{syn.}} = 88E^4 (\text{GeV}) / \rho (\text{m})$$

The energy loss per turn in DORIS is 1 MeV per electron, while in LEP at 55 GeV it is 260 Mev per turn. The photon emission leads to an increase of the beam cross section, $\sigma_{x,y}$, which is proportional to beam energy E .

Beam-Beam Interaction

To maximize the luminosity and the event rate the current should be stored in a few bunches, usually equal to half the number of beam intersection points, (four for LEP), and the beam focussed to small transverse dimensions (σ_x, σ_y small) at the interaction point. Typical beam dimensions at the crossing points are $\sigma_x = 0.1\text{cm}$ in the bend plane and $\sigma_y = 0.01\text{cm}$ normal to the bend plane. The stored current is limited by beam-beam interactions at low energies and few bunches. If the betatron oscillation frequencies of the beam particles around the ideal orbit in the vertical and horizontal directions are an integral multiple (or submultiple) of the revolution frequency, then the particles traverse the magnets in the same orbit. Any imperfection in the magnetic field will be encountered each revolution and its effect on the beam amplified. In practice this will lead to a very rapid loss of the beam, so that the working point should be selected away from resonance. However when bunches cross, each bunch acts as an electromagnetic lens to the other and the crossing will lead to smearing by an amount :

$$\Delta Q_x^- = r_e n_+ \beta_x^- / \gamma 2\pi(\sigma_x + \sigma_y) \sigma_x$$

(with an equivalent expression for ΔQ_y^-).

Here $\gamma = E/m_e c^2$, r_e = the classical electron radius = $2.282 \times 10^{-13} \text{ cm}$, and $\beta_{x,y}$ = the betatron amplitude functions at the interaction point $\approx (10-100) \text{ cm}$.

If the smearing is so large that any part of the bunch will have a betatron frequency close to an integer (or submultiple) of the revolution frequency, the bunch will be lost. In practice stable operation can be achieved for $\Delta Q_{x,y} \approx 0.06$. This limits the number of particles per bunch $\propto E^3$ and the luminosity (with fixed B)

$$L = (n_+ n_-) E^4 / \sigma_x \sigma_y$$

Power Limitation

The total power radiated as synchrotron radiation is given by:

$$W = U_{\text{syn}} (n_+ + n_-) e f B$$

It increases for a fixed B as $W \propto E^7$. Once the maximum power available is reached, the number of particle in the ring has to decrease as

$$n \propto E^{-4} (E > E_0)$$

which causes the luminosity to drop as $L \propto E^{-10}$ ($E > E_0$).

A typical luminosity curve is shown in Fig.1.12. At energies below E_0 the luminosity can be increased beyond the $B = 1$ beam-beam limit by increasing the number of bunches. The

maximum luminosity is obtained when at each energy, B is chosen such that the power limit is being reached. In this case $B \propto E^{-7}$ and $L \propto E^{-3}$. Many-bunch operation requires a double ring structure, since in a single ring the number of bunches is limited to half the number of interaction points in order to avoid bunch crossing outside these points.

1.6.3 Energy spread

The energy spread σ_E of the beam is determined by synchrotron radiation. It depends on E and the ring radius ρ .

$$\sigma_E \propto E^2/\sqrt{\rho}$$

For DORIS and SPEAR $\sigma_E \approx 0.9 (E/2\text{GeV})^2$. For LEP it is planned that the energy spread will be given by

$$\Delta E/E \approx 0.78 \times 10^{-3} (E/50\text{GeV})$$

at the Z° pole.

1.7 Measurement of Luminosity at LEP

The luminosity at LEP is measured by observing small-angle Bhabha events using the luminosity monitor (LCAL and SATR) calorimeters, in addition to a tracking device. Details of their construction and performance are given in Ch.3. The absolute luminosity is needed for the determination of the cross-section. Since it is a steep function of the scattering angle, an energy measurement is essential to reject background both in the trigger and in the off-line analysis.

$$\sigma = N/L$$

where N = Number of observed events, which should be high to reduce the statistical errors, and σ = the cross-section for the process $e^- e^+ \rightarrow X$. The integrated luminosity is determined by the following formula:

$$\begin{aligned} L &= N_{\text{Bhabha}}/\sigma_{\text{Bhabha}} \\ &= N_{\text{Bhabha}}/\{\int (d\sigma/d\Omega) d\Omega\} \end{aligned}$$

where N_{Bhabha} is the corrected number of events and $d\sigma/d\Omega$ is the differential cross-section given by the electro-weak theory to $O(a^3)$. From the above formula there are three main sources of errors in the luminosity measurements:

- the differential cross-section (given by theory)
- the acceptance (determined by construction, survey, beam size and position), and

- the number of events (corrected for background and efficiencies)

The absolute luminosity drops out when measuring m_Z and Γ_Z . In this case, only the variations of the luminosity with the beam energy are needed (the relative luminosity). The effects of linear and quadratic variations of the errors in the luminosity have been estimated as follows :

- A linear variation of the error in the luminosity of 2%, within an interval of the beam energy of $\pm 5\text{GeV}$, will lead to an error in the determination of m_Z of about 10 MeV, but will not influence the determination of Γ_Z .
- A quadratic variation of the error in the luminosity of 1%, at 5GeV away from the Z^0 -pole, will lead to an error in the determination of Γ_Z of about 10 MeV, but will not influence the determination of m_Z .

Error contributions fall into the following categories:

Statistics

Through an energy scan with equal integrated luminosity per energy setting. To first approximation we may neglect electro-weak effects at small angles, so that

$\sigma_{\text{Bhabha}} \propto E^{-2}\text{beam}$ and hence $N_{\text{Bhabha}} \propto E^{-2}\text{beam}$. The statistical error is given by $1/\sqrt{N} \propto E_{\text{beam}}$. Quantitatively, a luminosity of $10^{31}\text{cm}^{-2}\text{s}^{-1}$ and two days of running per energy setting will result in a statistical error of about $0.01 E_{\text{beam}}/\text{GeV} \%$. The influence of this error on the determination of the mass and the width of the Z^0 must still be calculated.

Physics

Missing higher order radiative corrections, hadron vacuum polarization, weak interaction contributions, transverse beam polarization and beam energy uncertainties all affect the physics results.

Geometry

For beam energy measurements there are two types of error: errors in average quantities and errors in the spread. To evaluate the above errors the following parameters should be known:

- the size and position of the acceptance area
- the shift of average vertex position in the beam direction
- the shift perpendicular to the beam direction
- rotation around an axis perpendicular to the beam
- rotation around beam axis
- the angular spread of the beam
- the spread of the vertex position
- the angular resolution and
- the magnetic field

Errors in the counting rates

The counting rate must be corrected for two effects:

- i) Background contributions due to processes like $e^+ e^- \rightarrow \gamma\gamma, \tau^+\tau^-, \gamma\gamma X$, and other annihilation reactions. It has already been reported that the contribution of these e^+e^- interactions is negligible. Background from LEP (due to off-momentum particles, beam-gas interactions and synchrotron radiation) will hardly fake Bhabha events if the energy threshold of the Bhabha trigger is set above about 35GeV.
- ii) Inefficiencies in the trigger or in event reconstruction. The uncertainties in the corrections contribute to the errors in the luminosity measurement.

A summary of all contributions to systematic error in the luminosity measurements is detailed in Table 3. From the results above, there is a possibility of measuring the luminosity with systematic uncertainties of below 2%.

1.8 Experimental Background Problems

Beam gas scattering

The gas pressure in the beam pipe is typically about 10^{-9} Torr (which is a factor of 10^3 higher than in a $p\bar{p}$ ring due to synchrotron radiation). The $e^+ e^-$ beams interact with the gas nuclei mainly by quasi-real γ -N scattering and produce background at a rate

$$N \text{ (events/s)}_{\text{beam-gas}} = (I_+ + I_-) \rho L r \int \sigma_{\gamma N}^{(k)} dk/k$$

where ρ = nucleon density, L = length of beam seen by the detector and $\sigma_{\gamma N}$ = total cross section for γ -N scattering. The factor r measures the relative flux of quasi real photons.

For typical machine parameters one finds

$$r dk/k = (a/\pi) \ln(0.1 \text{ GeV}^2 / Q_{\min}^2) dk/k = 7\% dk/k$$

which is roughly four or five orders of magnitude larger than the signal, for a typical machine:-

$$N_{\text{beam-gas}} \approx 10^3 \text{ Hz}$$

Cosmic Rays

The flux of cosmic ray particles incident on a horizontal surface is $2 \times 10^{-2} \text{ cm}^{-2} \text{ s}^{-1}$, or $2 \times 10^3 \text{ /s}$ for a detector covering 10 m^2 in area. These particles can in general trigger the detector and will produce unwanted background. Both beam-gas background and cosmic ray events increase the event rate accepted by the data taking system by a factor of 10^2 - 10^3 . At the analysis stage they are, in general, easily recognised and may be discarded.

Synchrotron Radiation

The number of photons per second with $k > k_\gamma$ produced by synchrotron radiation per mA of beam current and metre of path length is given roughly by

$$N(k > k_\gamma) \approx 10^{1.6} \exp(-0.5k_\gamma \rho/E^3)$$

where ρ = radius of bending magnet. In Fig.1.13, $N(k > k_\gamma)$ is plotted for a current of 100 mA, an electron path length 1 m, and bending radii of 12 m, (corresponding to the DORIS bending radius in the ring), and 60 m (DORIS vertical bending radius before interaction point). The number of photons is seen to rise extremely rapidly from below 100 to $10^{1.8}$ photons /second. Photons above a certain minimum energy (1 keV) will produce knock-on electrons in proportional chambers. Some shielding is provided by the beam pipe. For the DASP experiment at DORIS, which used an aluminium pipe of wall thickness 2 mm, the critical energy and flux were found to be $k_\gamma \geq 30 \text{ keV}$, $N_\gamma \approx 10^6/\text{s}$. Therefore, synchrotron radiation produces a sharp limit for the maximum useful beam energy. This can be overcome by adding radiation shielding in or around the beam pipe, but on the other hand this may be undesirable, e.g. for clean photon detection.

Table 1.1

Existing and Planed Colliders

Name	Place	Beams and Energies	E_{cm}	\mathcal{L}	
DCI	Orsay	$e^+ e^-$	1.7×1.7	3.4	$2 \cdot 10^{30}$
BEPC	Beijing (1988)	"	2.8×2.8	5.6	10^{31}
SPEAR	Stanford	"	3.9×3.9	7.8	$3 \cdot 10^{31}$
VEPP 4	Novosibirsk	"	5×5	10	—
DORIS	Hamburg	"	7×7	14	10^{31}
CESR	Cornell	"	8×8	16	10^{31}
PEP	Stanford	"	15×15	30	$4 \cdot 10^{31}$
PETRA	Hamburg	"	23×23	46	10^{31}
TRISTAN	Tsukuba	"	30×30	60	10^{31}
SLC	Stanford	"	50×50	100	10^{30}
LEP I	CERN (1989)	"	60×60	120	10^{31}
LEP II	CERN (1995)	"	100×100	200	10^{31}
CLIC	CERN (?)	"	1000×1000	2000	10^{33}
HERA	Hamburg (1990)	ep	30×820	315	$2 \cdot 10^{31}$
LHC	CERN (?)	"	50×8000	1300	$2 \cdot 10^{32}$
SPS	CERN	$p\bar{p}$	315×315	630	$2 \cdot 10^{30}$
TEVATRON	FNAL	$p\bar{p}$	1000×1000	2000	10^{31}
ISR	CERN	pp	32×32	63	10^{31}
UNK	Serpukhov (1995?)	pp	600×3000	2700	—
LHC	CERN (?)	pp	8500×8500	$1.7 \cdot 10^4$	10^{33}
SSC	USA (1995?)	pp	$2 \cdot 10^4 \times 2 \cdot 10^4$	$4 \cdot 10^4$	10^{33}

Table 1.2

**Number of $\theta \rightarrow H^0 + \gamma$ events per 1000 hours
for different choices of m_{H^0}**

m_{H^0} (GeV)	10	30	50	60	70	80	85	90	100
m_θ (GeV) [$\int L dt$ (pb^{-1})]									
70 [32]	202	160	102	52					
90 [49]	107	95	75	60	43	22	12		
110 [65]	39	36	31	28	25	19	16	13	7

Table 1.3

source of error	contribution in %
neglected higher orders in QED	0.12
hadronic vacuum polarisation	0.25
electro-weak effects	0.2
transverse beam polarisation*	10^{-4}
natural energy spread*	0.12
absolute energy scale*	0.06
<i>differential cross section</i>	0.4
inner radius of SATR acceptance	0.5
outer radius of SATR acceptance	0.1
<i>z</i> -position of one detector	0.04
<i>z</i> -position of both detectors	0.1
<i>z</i> -position of one detector	0.1
radial vertex position	0.1
longitudinal vertex position	0.1
width of the interaction region in <i>x</i>	0.1
width of the interaction region in <i>y</i>	< 0.01
width of the interaction region in <i>z</i>	0.1
beam divergence	0.02
<i>geometrical acceptance</i>	0.6
trigger efficiency*	< 0.5
reconstruction efficiency*	< 0.5
background from off-momentum electrons*	< 0.1
background from $e^+e^- \rightarrow \gamma\gamma^*$	< 0.05
background from $e^+e^- \rightarrow \tau\tau^*$	< 10^{-4}
background from $\gamma\gamma$ reactions*	< 0.2
<i>Bhabha rate</i>	< 0.8

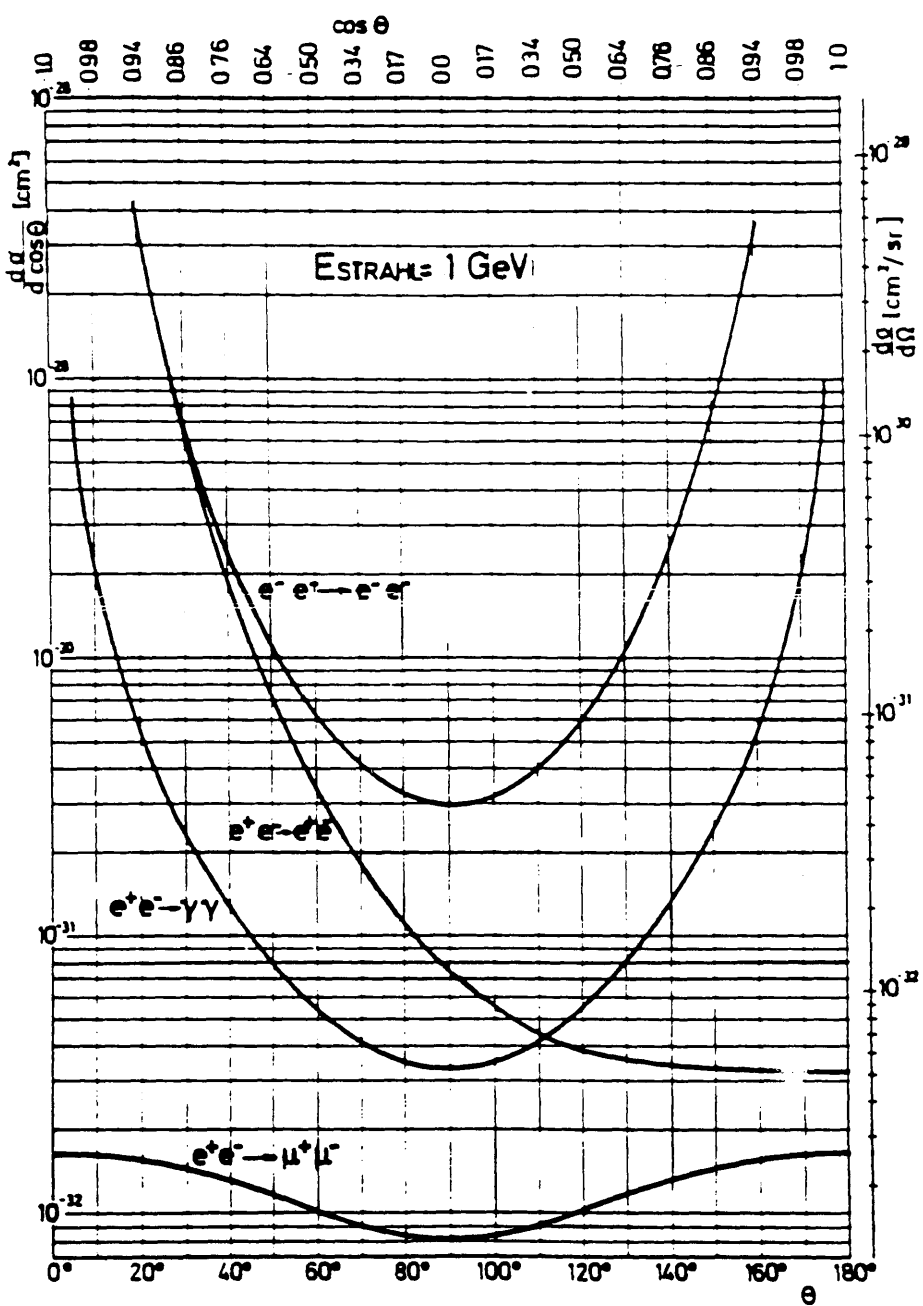


Fig.1.1

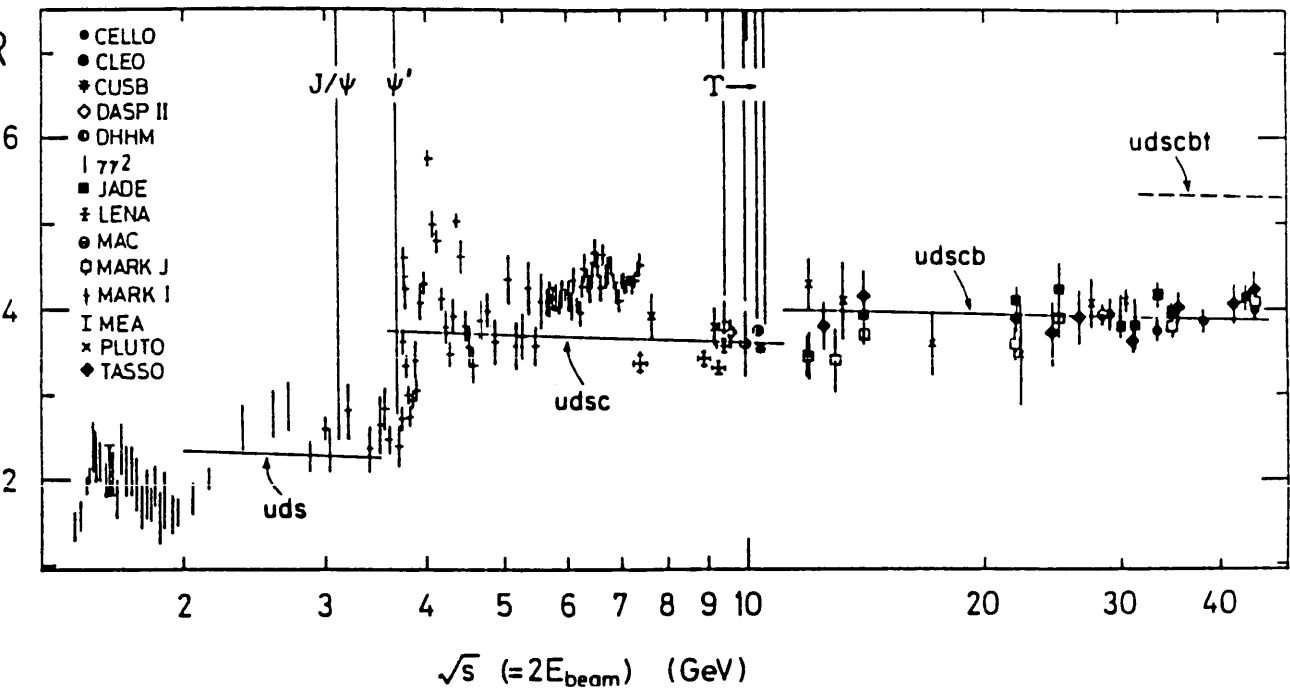


Fig.1.2

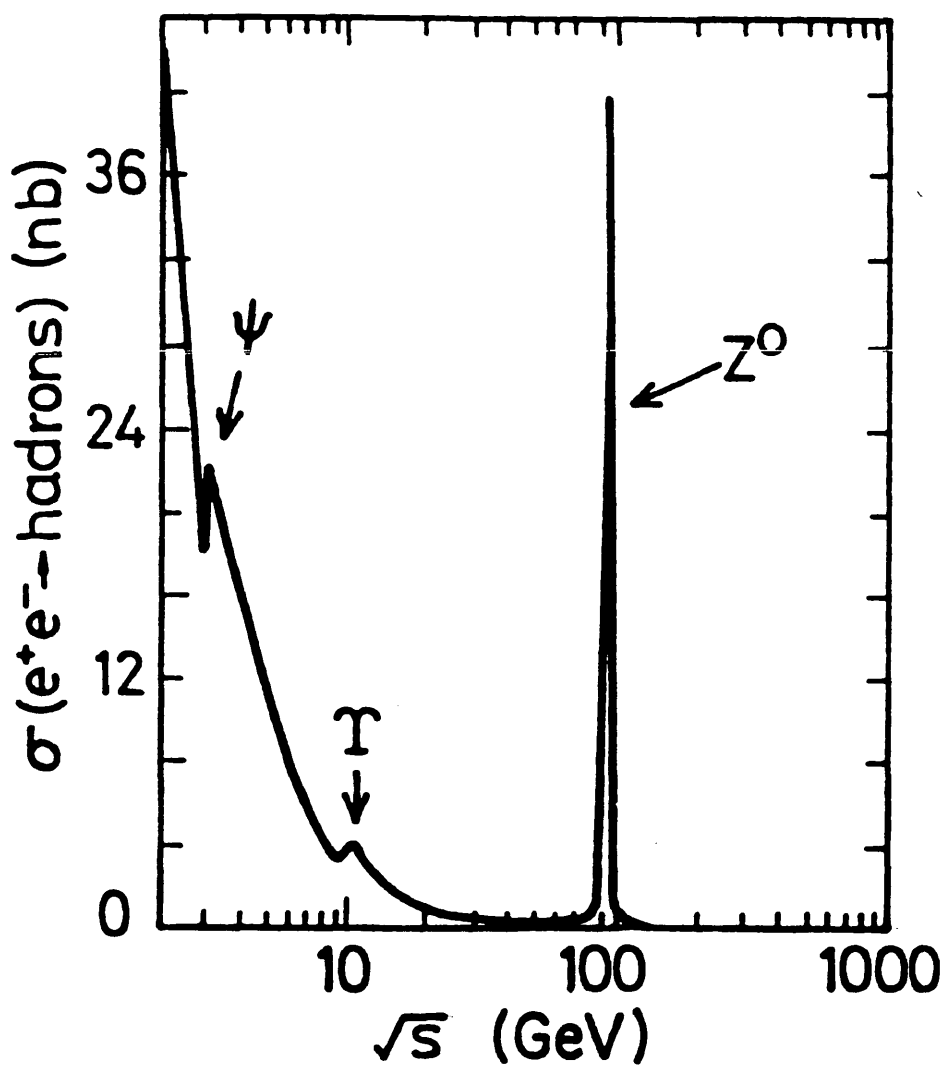
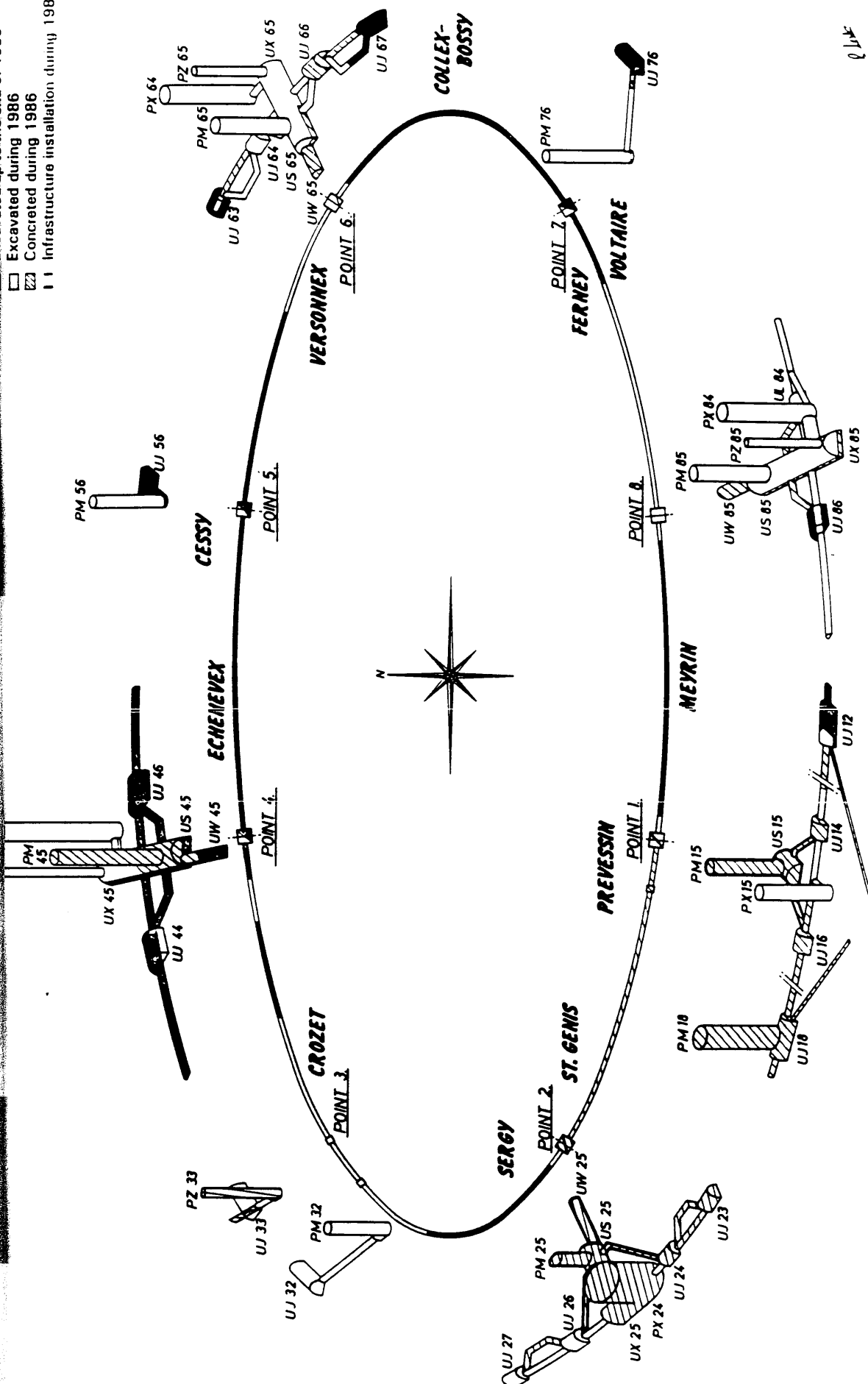


Fig.1.3

- Excavated during 1986
- Concreted during 1986
- Infrastructure installation during 1986



The progress of LEP excavation and installation in 1986. The diagram illustrates the 27 kilometre ring with its eight access points. Alongside each access point, the configuration of the shafts down to tunnel level and of the underground halls is drawn.

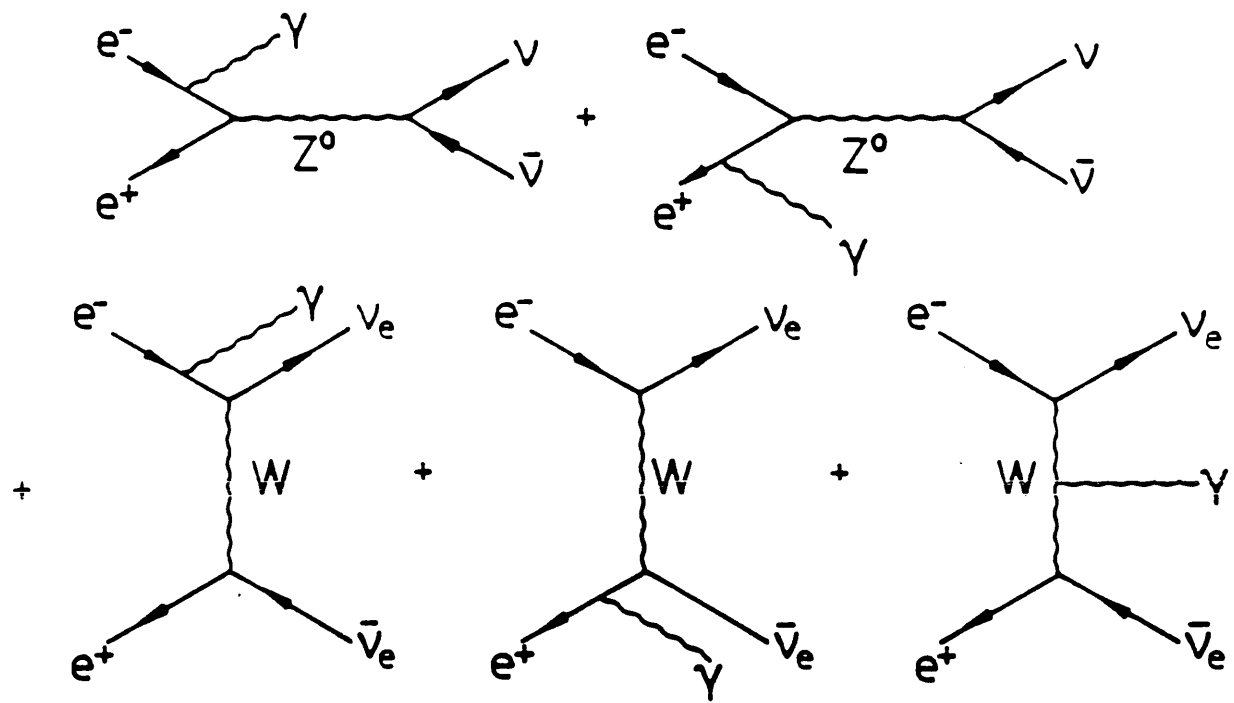
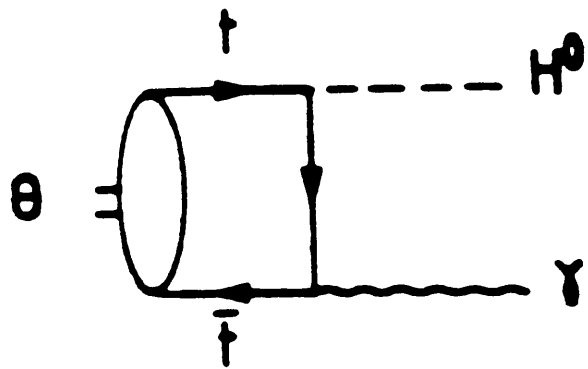
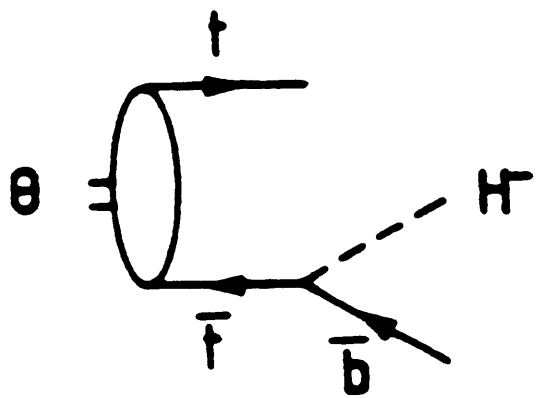


Fig.1.5



b)



a)

Fig.1.8

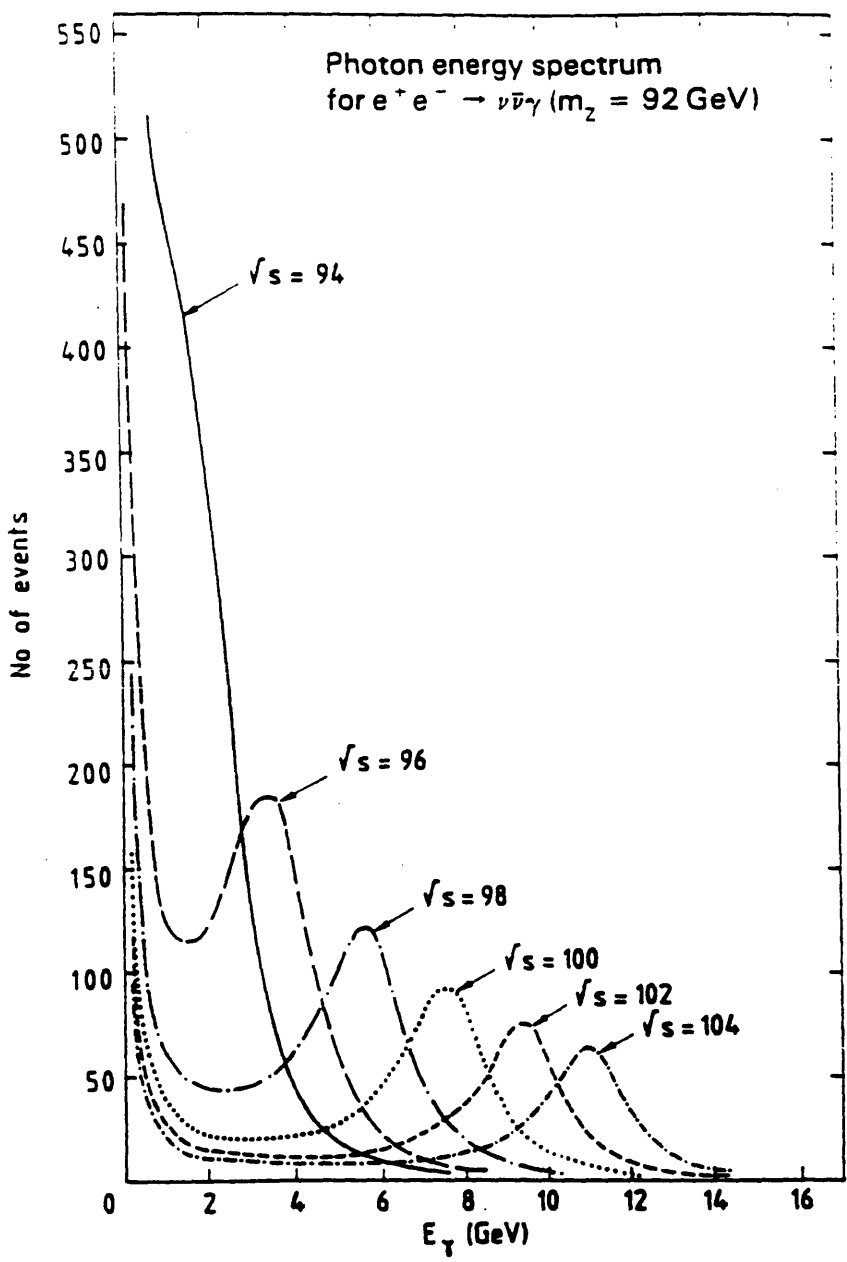


Fig.1.6

DELPHI

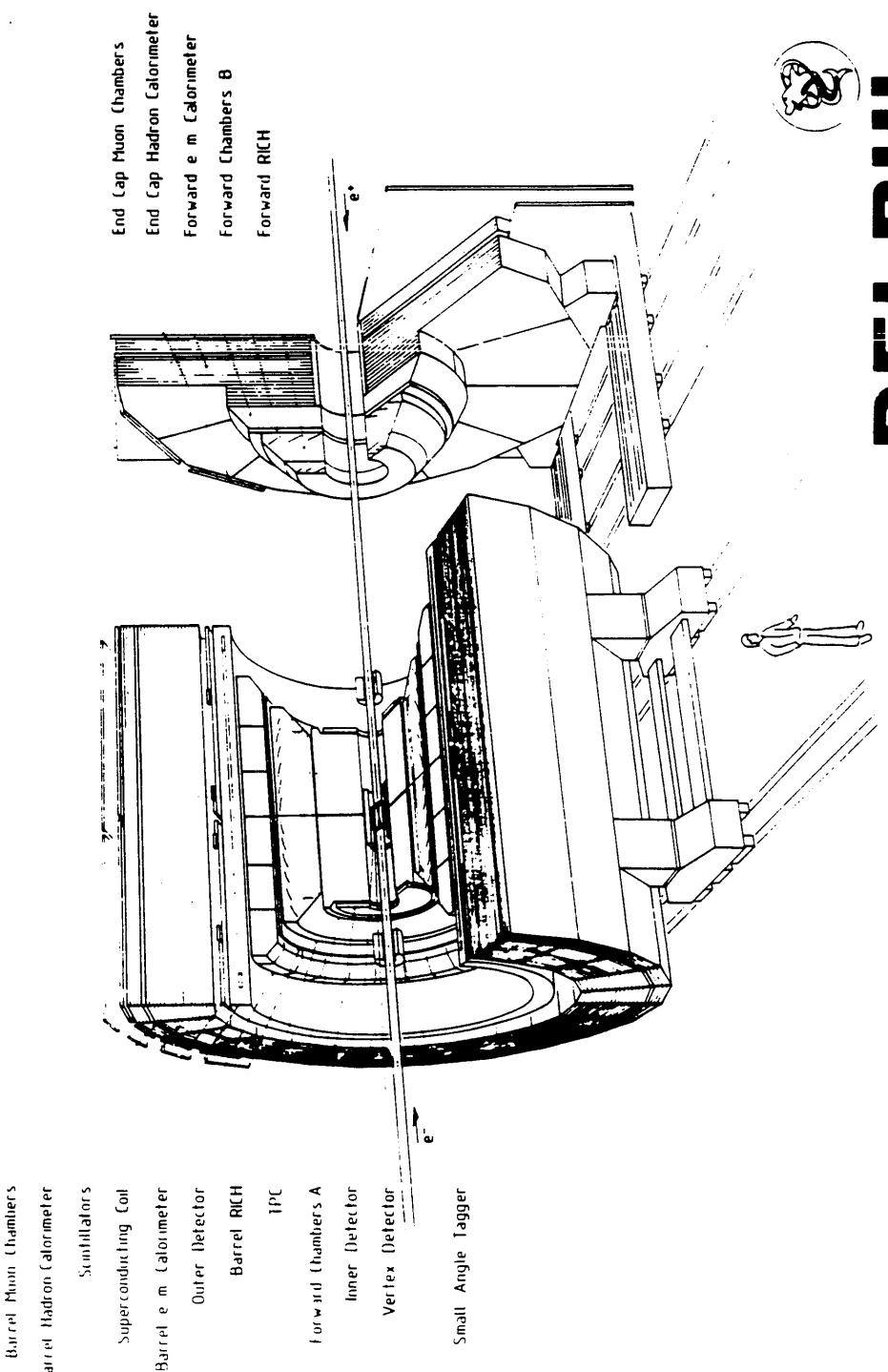


Fig.1.9

O P A L

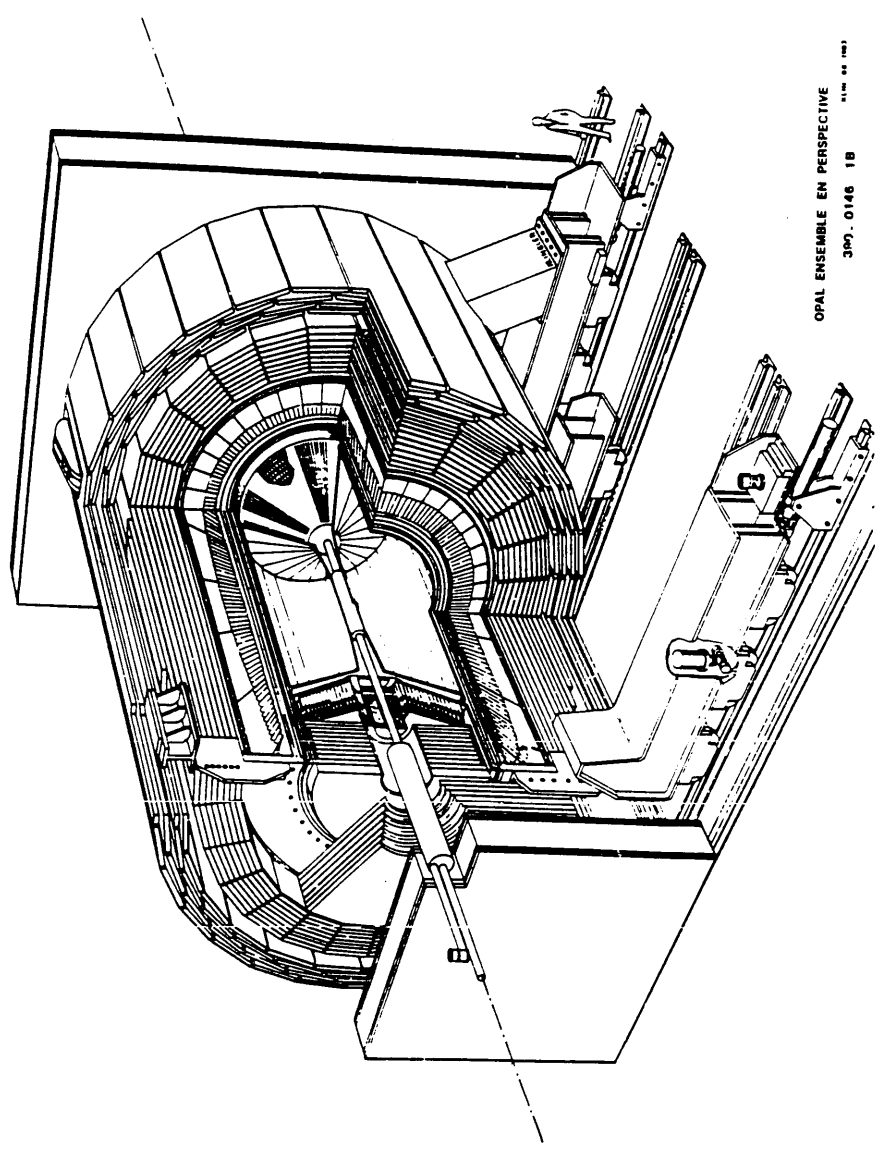


Fig.1.10

L 3

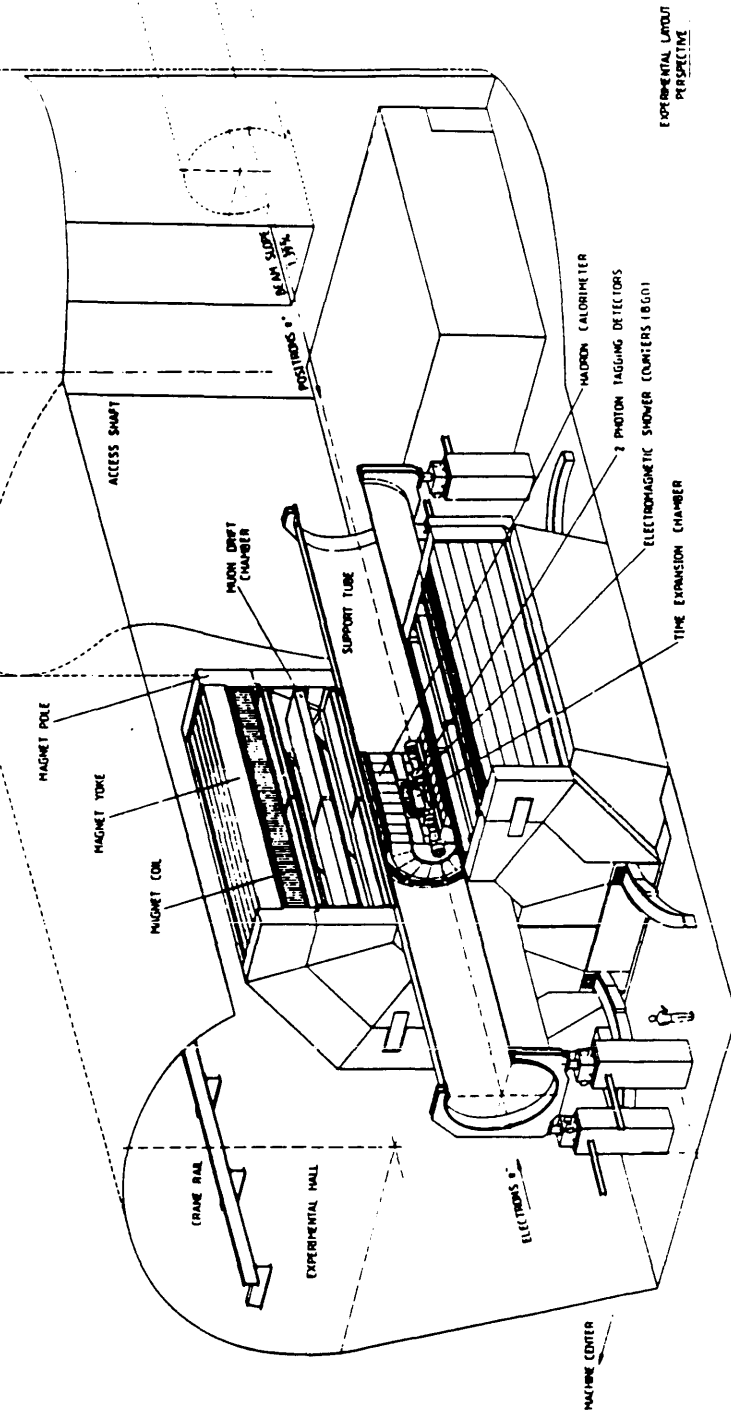
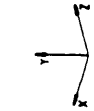


Fig.1.11

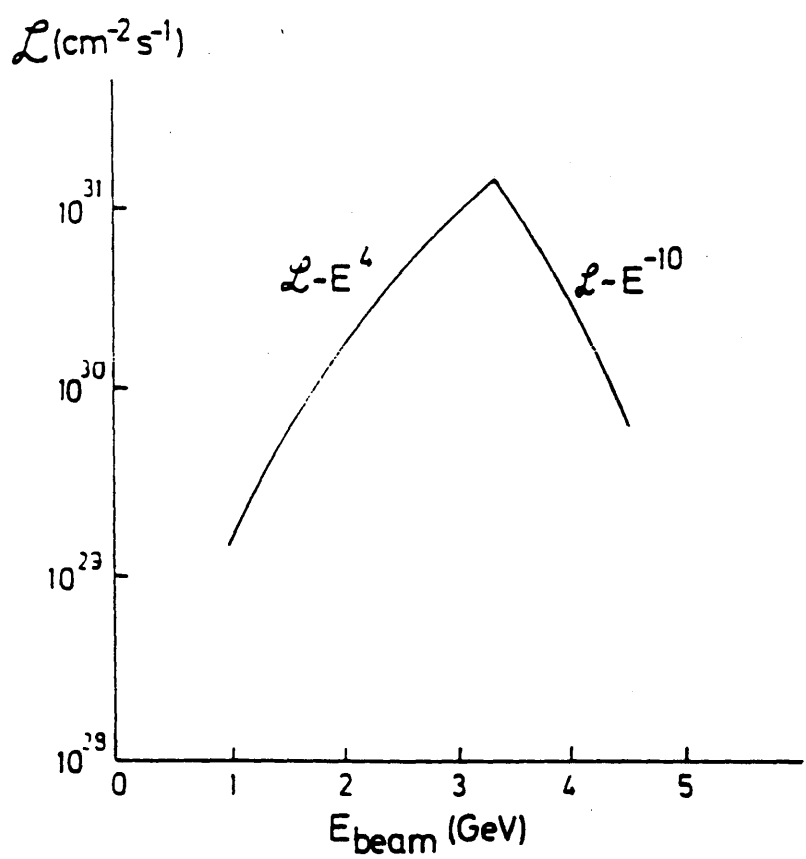


Fig.1.12

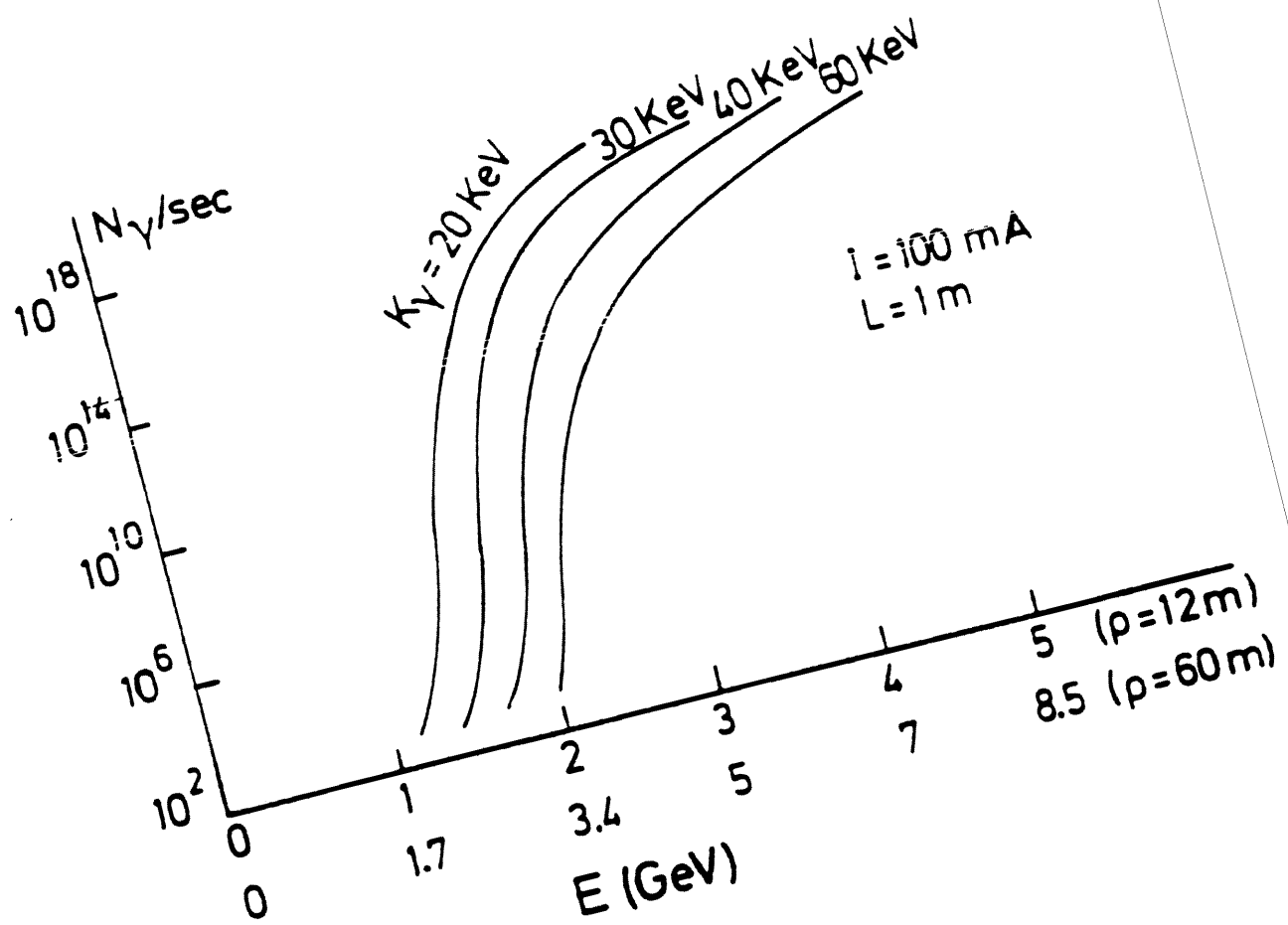


Fig.1.13

Chapter 2 CALORIMETRY

Among the most recently developed devices used in high energy physics experiments in the area of particle and shower detection is the "CALORIMETER" or " TOTAL ABSORPTION DETECTOR". Calorimeters are used to measure the energy, spatial position, direction and the nature of primary particles (22,24).

In a calorimeter the primary particle intercepts a block of matter in which the particle loses all its energy by ionization and excitation processes. The energy eventually appears as heat, hence the name calorimeter. Some fraction of the energy deposited through the calorimeter material is detectable in the form of a more practical signal, (such as scintillation light in NaI(Tl), BGO, BaF₂,....detectors, Cerenkov light in glass scintillator or lead-glass and ionization charge in liquid argon or gas proportional chambers), which is proportional to the initial energy.

Calorimeters were first used in cosmic ray studies (Morzin 1967), but they developed rapidly in the late 1970's when large accelerators were built, {e.g the CERN-ISR, Fermilab (FNAL), CERN-SPS}. In the new environment magnetic spectrometers become unable to analyse the very high energy particle momenta in a large solid angle, whereas '4π' calorimeters have been successfully installed in the interacting region of storage rings. In addition they can often work with high efficiency inside high magnetic fields (22,23,24).

The use of calorimeters is growing and continuing growth seems probable with the continuing development in read out systems. Calorimeters offer many advantages relative to magnetic spectrometers. For example

- a) They are sensitive to both charged and neutral particles.
- b) The "energy degradation" through the development of the particle cascade is a statistical process, and the average number (N) of secondary particles is proportional to the energy of the incident particle. In principle the uncertainty in the energy measurement is governed by statistical fluctuations of N, and hence the relative energy resolution σ/E improves as $1/\sqrt{N} \propto E^{-1/2}$.
- c) The length of the detector scales logarithmically with particle energy E, whereas for magnetic spectrometers the size scales with momentum p as $p^{1/2}$, for a given momentum resolution $\sigma(p)/p$.
- d) With segmented detectors, information on the shower development allows precise

measurements of the position and angle of the incident particle.

- e) Their different response to electrons, muons, and hadrons can be exploited for particle identification.
- f) Their fast response allows operation at high particle rates, and the pattern of energy deposition can be used for rapid on-line event selection.

There are two main types of calorimeter. The first deals with electromagnetic showers from electron or gamma interactions and the second with hadronic showers. Research in high energy physics now continues towards the development of a new generation of calorimeters having equal response to both electromagnetic and hadronic showers. Different groups have already made significant progress in this area (32,38).

The following paragraphs discuss the general characteristics of each type and the differences in their performance. The need for a calorimeter which responds equally well to electrons, gammas and hadrons is discussed and a review is given of recent developments leading towards a "universal" calorimeter.

2.1 Electromagnetic Calorimeters

When an electron or photon of energy above 10 MeV passes through a material, an electromagnetic shower develops in it, through bremsstrahlung and pair production processes, which is distributed through the material laterally and longitudinally. A simple model for the development of an electromagnetic shower is shown in Fig.2.1. The above processes in the material will continue in a cascade process and will stop only when the energy of electrons and positrons approaches the critical energy E_c when the energy losses through bremsstrahlung equal the losses through ionization:

$$(dE/dX)_{\text{ion.}} = (dE/dX)_{\text{brem.}}$$

The mean rate of energy loss of a charged particle due to ionization at " E_c " is given by the Bethe-Bloch formula :

$$\frac{dE}{dx} = \frac{4\pi N_0 Z^2 e^4}{mv^2} \frac{Z}{A} \left[\ln \left(\frac{2mv^2}{I(1 - \beta^2)} \right) - \beta^2 \right]$$

where m is the electron mass, z and v are the charge (in units of e) and the velocity of

the particle, $\beta = v/c$, N_0 is Avogadro's number, Z and A the atomic and mass number of the atoms of the medium, and x is the path length in the medium measured in $g \text{ cm}^{-2}$ or kg m^{-2} . The quantity I is the effective ionization potential, averaged over all electrons, with approximate magnitude $I = 10 Z$ (eV).

The longitudinal distribution is set by the "radiation length", X_0 , where

$$X_0 = 180x A/Z^2 \quad \text{gm/cm}^2$$

The depth required for containment of the shower depends logarithmically on the energy, so the length needed for containment of the shower depends upon the energy of the incident particle and the nature of the material in which the shower develops. E.g. it is about $20 X_0$ for lead at $E = 100 \text{ GeV}$.

The longitudinal distribution of energy deposition for different materials in an electromagnetic shower is shown in Fig.2.2. The minimum kinetic energy required for detection is called the "cut-off energy", E_k for electrons and positrons.

The spatial resolution of the shower is determined by the "track length" (T) which depends on the cut-off energy. The total track length of electrons and positrons is proportional to the total energy, as is the number of particles at shower maximum, N_{\max} . The depth at which the maximum occurs, T_{\max} , increases logarithmically with the energy:

$$T_{\max}/X_0 = \ln(E_0/E_k) - t$$

where $t = 1.1$ for electrons and $t = 0.3$ for photons.

The depth for 95% longitudinal containment, $L_{0.95}$ is:

$$L_{0.95}(X_0) = t_{\max} + 0.08Z + 9.6$$

The lateral distribution of the shower is dominated by multiple scattering of low energy electrons and scales in units of the "Moliere radius" R_m , where,

$$R_m = 7 A/Z \quad \text{gm/cm}^2$$

The distribution of shower energy deposition around the shower axis is independent of material used, as shown in Fig.2.3, and 99% of the energy is contained inside a radius of $3R_m$.

2.1.1 Energy Resolution

The Energy resolution of a zero energy leakage homogeneous calorimeter of finite dimensions is limited only by statistical fluctuations, and depends on the cut-off energy. The ultimate energy resolution is given by

$$\sigma(E)/E = \sigma(T)/T = 0.7\% / \sqrt{E(\text{GeV})}$$

This ultimate limitation applies to both homogeneous and sampling calorimeters. As shown above the resolution of the energy measurement is limited by the fluctuation of detectable track length. One important instrumental contribution to the energy resolution comes from incomplete containment of the showers - "energy leakage", both longitudinally and laterally. The contribution of both kinds is shown in Fig.2.4. The contribution of longitudinal leakage to the energy resolution is normally more than that of lateral leakage.

Another contribution to the resolution comes from fluctuations in the number of photoelectrons detected in the detector. In addition to the above contributions one can add

- i) Noise in the active layers
- ii) Electronic noise
- iii) Statistical fluctuations and gain variations in photomultiplier tubes
- iv) More than one event within the time resolution (pileup)

For sampling calorimeters additional contributions are due to : (21,22)

Sampling fluctuations

Fluctuations in the number of particles (N) crossing the active layers spaced by thickness (X) of material:

$$\{\sigma(E)/E\}_{\text{samp.}} = 3.2\% (550 d/X_0)/Z F(z) E_0(\text{GeV})$$

where d =layer thickness, X_0 = radiation length, Z = atomic number of material

$$F(z) = e^Z \{1 + \ln(z/1.526)\},$$

where $z = 4.58 Z E_{\text{cut-off}}/A E_c$ and A = atomic number. Further variations to the relation above need to be made if multiple scattering is taken into account. This will reduce the energy resolution. A Monte-Carlo calculation gives a resolution due to sampling fluctuations:

$$\sigma(E)/E = 4.6\% / \sqrt{E(\text{GeV})}$$

Landau fluctuations

Fluctuations of the energy deposited in the active signal planes, which can be estimated to contribute :

$$\{\sigma(E)/E\}_{\text{Landau}} = 3 / \sqrt{N_x X \ln 1.3 \times 10^4 \delta}$$

$\{\delta(\text{MeV})\}$ is the energy loss per active detector plane, N_x = number of particles crossing the active planes,

X = thickness of the active layer. δ is of the order of a few MeV for a few mm's of scintillator but it becomes comparable to sampling fluctuations for gaseous detectors.

Path-length fluctuations

Because of the high Z of materials used in calorimeters, low-energy electrons may be multiply scattered into the active plane of the detector and then travel distances much larger than, for example, the gap thickness in the gaseous medium, depositing considerably more energy than in a perpendicular traversal. Path length fluctuations are more important in gaseous detectors for the following reasons :

- a) The energy loss of scattered electrons can be much larger than that of electrons parallel to the shower axis.
- b) In gaseous detectors the electrons leaving the absorber at large angles can travel undisturbed over a long range while in solid detectors they are diffused back into the absorbing matter before crossing a long sensitive layer. Hence if we decrease the thickness of the active layer we expect a smaller contribution to the energy resolution due to path-length fluctuations. The energy resolution for various thicknesses of an active liquid-argon layer is shown in Fig.2.5.

Contributions of fluctuations due to sampling, path-length fluctuations and Landau fluctuations to the relative energy resolution in sampling calorimeters using (a) wire chambers (b) wire tubes are shown in Figs.2.6a and 2.6b. Both path-length fluctuations and Landau fluctuations give small contributions in calorimeters with proportional layers.

2.1.2 Homogeneous Electromagnetic Calorimeters (EMC)

This group of calorimeters splits into two main types depending on the material used :

a) Homogeneous EMC using inorganic crystals

Crystals of NaI (Tl), BaF₂, CsI and BGO are used in many calorimeters. Some properties of scintillating inorganic crystals are listed in Table 1. Among the above crystals the best resolution is achieved with NaI crystals. Crystals of NaI with diameter $3R_m = 13$ cm and $24X_0 = 62.16$ cm length yield an energy resolution of

$$(\sigma E/E) = 0.9\% \{E(\text{GeV})\}^{1/4}$$

With the new crystals of BGO ($B_4Ge_3O_{12}$) a resolution of

$$(\sigma E/E) = 2.5\% \{E(\text{GeV})\}^{1/2}$$

is achieved. The L3 collaboration recently reported that an energy resolution of 1% is achieved at energies from (2-50) GeV. The main advantages of BGO over NaI are the shorter radiation length, superior handling and inertness against humidity in addition to the reduced sensitivity of BGO towards radiation compared to NaI. Its main disadvantages are the high price and the small size of the crystals. A resolution of $0.98/E^{1/4}$ from crystals of BaF₂ has been achieved and a better resolution is expected. With its intermediate radiation length between that of NaI and BGO and its low price for the raw materials w.r.t. BGO, emphasis on improvement in the radiation damage caused by impurities may put it on the level of BGO and NaI.

b) Homogeneous EMC with lead glass, using Cerenkov light detection

The resolution in this type of EMC is limited by photo-electron statistics. This has little effect on the resolution of NaI and BGO because of the high rate of photo-electrons from NaI and BGO, in which typically (10^6 - 10^7) photo-electrons are produced per GeV. The energy resolution for a fully contained shower takes the form:

$$(\sigma E/E) = 0.006 + 0.03/\xi^{1/2} E^{1/2}$$

where ξ =the ratio of the photocathode area to that of the radiation exit aperture, (typically $\xi= 0.5$). Scintillating glass is also used in homogeneous E.M.C. and different types have been used, for example SCG1-C scintillating glass which is suitable for high energy shower measurements. This type differs from the other types of lead glass, F8 and SF5, which have been used in high energy shower measurement in two ways:

- i) This glass has barium oxide rather than lead oxide as a high Z material.
- ii) It contains Ce_2O_3 which acts both as a scintillator and a wavelength shifter for Cerenkov radiation. Tests were carried out at SLAC using high energy positrons and a resolution of

$$(\sigma E/E) = 1.64\% + 1.13\%/E^{1/2}$$

with a good linearity was achieved.

2.1.3 Sampling Calorimeters

The most common types of electromagnetic sampling calorimeter consist of alternate layers of heavy metal radiator to enhance photon conversion and some active substances to sample the energy loss. The metal radiator is usually made of lead. The calorimeter cells are typically arranged in either strip or tower arrangement. Examples of sampling calorimeters are

Metal-Scintillator sandwich

Metal-Liquid Argon ionization chamber

Metal-Gaseous PWC sandwich

Recently streamer tubes have been used as active layers in sampling calorimeters with some advantages:

- a) The resolution improves in principle due to the absence of Landau fluctuations.
- b) The saturated mode permits simple monitoring and less strict tolerance in mechanical uniformity.

- c) The large signals generated in the streamer process improve the signal to noise ratio.

In these calorimeters the total signal produced is proportional to the total energy deposited in the calorimeter. The gaseous PWC detectors are cheaper than the other types of detector and can operate satisfactorily in a magnetic field. With three dimensional readout they can also give the correlation between the projections of the shower. This is important for resolving ambiguities in multishower events. Disadvantages of PWC detectors include worse energy resolution, slow response, and lower density than other calorimeters. The high density is important for achieving the reduction in the size of the calorimeters which is demanded by the limited area available for experiments. In addition, small calorimeter size will reduce the overall cost of the surrounding of iron ... etc. in 4π detectors. In Table 2 different types of sampling calorimeters are listed with their properties.

2.2 Hadron Calorimeters

Hadron calorimeters are similar in construction to electromagnetic calorimeters. Table 3 lists some properties of different types of hadronic calorimeter. When a high energy hadron penetrates a block of matter, it will at some point interact with one of the nuclei in the block. Mesons like pions, kaons... etc. are produced as a result of this interaction and a fraction of the primary particle energy is transferred to the nucleus. The excited nucleus will release this energy by emitting a certain number of nucleons, and in a later stage gammas, and lose its kinetic energy (recoil energy) by ionization. The particles produced in these reactions, (pions, kaons, nucleons and gammas), may either lose their energy by ionisation or induce new reactions in turn, and so a shower develops. So far the hadronic showers consist of two parts, the hadronic and the electromagnetic components. The calorimeter signal is due to the charged particles produced in the hadronic shower which ionize the active layers. Due to the large variations in the interaction processes, there are much larger fluctuations in hadronic shower development than in electromagnetic showers. The spatial development of the hadronic shower is given by the absorption length λ , derived from the inelastic cross-section σ_x ,

$$\lambda = A/\sigma_x N_0 \rho$$

where A = mass number of one mole of the material, σ_x the cross-section for inelastic scattering, N_0 Avogadro's number and ρ the density. Values of λ are given for different materials in Table 4.

For a small hadron calorimeter a material with short absorption length is clearly needed. Hadron calorimeters are more normally large, however. Typical values for iron are 2 m in depth and 0.6 m transverse size. The longitudinal and transverse distribution of energy deposited in a H.C. is demonstrated in Fig.2.7(a,b). If the hadron shower is completely contained in the calorimeter, the "visible" (detected) energy registered in the calorimeter is proportional to the energy of the primary hadron. Such a linear relation is demonstrated in Fig.2.8. The visible energy for incident hadrons is less than that for incident electrons of the same energy, for various reasons. (see Fig.2.9) For example, there are particles escaping from the calorimeter and carrying away energy, like muons and neutrinos from pion decay (1% at 140 GeV primary energy). Some fraction of the energy is completely lost via nuclear binding energy. Energy leakage due to gaps and dead materials is \approx (20-30)% of the total energy at 10 GeV for an iron calorimeter, and is in addition to leakage effects due to the finite size of the calorimeter. This will lead to fluctuations in the visible energy for the hadron shower, mainly due to the fluctuations of the π^0 which contribute to the visible energy more than π^+ and π^- . In addition to fluctuations in the visible energy, sampling fluctuations play a large role and give rise to poorer energy resolution as well. A typical value for the energy resolution of a hadron calorimeter is :

$$\sigma(E)/E = 45\%/\sqrt{E(\text{GeV})}$$

The fluctuations in energy leakage and in the electromagnetic component of the hadron shower lead to an energy resolution of about

$$\sigma(E)/E \approx (0.9 - 0.1)/\sqrt{E(\text{GeV})}$$

if the thickness of material between sampling devices is less than 5 cm of iron. The energy resolution of a hadron calorimeter can be improved, for example by the following methods:

- i) The loss of visible energy through nuclear excitation and break-up mechanisms can be nearly completely compensated by the energy release in nuclear fission of ^{235}U , as shown in a first attempt made at CERN by Fabjan et al. Energetic neutrons from fission contribute to the observed signal such that the pulse height for hadron showers becomes nearly equal to that for electromagnetic showers, as shown in Fig.2.10. This means the calorimeter will have equal response to both hadronic and electromagnetic showers, i.e. $e/h = 1$. The corresponding fluctuations disappear and the energy resolution improves by about a factor of two. Experimental results for a uranium calorimeter are shown in Fig.2.11. They correspond to

$$\sigma(E)/E = 0.3/\sqrt{E(\text{GeV})}$$

ii) The fluctuations due to the electromagnetic component may be reduced by weighting the response in individual counters. Electromagnetic parts of the shower are localised, therefore producing very large depositions in individual counters. If the measured response in one counter (E_k) is corrected downwards for large response, $E'_k = E_k(1-CE_k)$, then the resulting resolution in the sum ($\sum E'_k$) improves markedly over ($\sum E_k$), as shown in Fig.2.12 for a 2.5 cm Fe sampling calorimeter exposed to π^- mesons of 100, 200 and 300 GeV. The resolution can be approximately

$$\sigma(E)/E = 0.58 / \sqrt{E(\text{GeV})}$$

The measured values for $\sigma(E)/E$ as a function of E are given in Fig.2.13.

The energy resolution of a hadron calorimeter depends on the sampling thickness "d" of the absorber layers. Since the number of particles registered in the counters between plates is inversely proportional to "d", one can expect the relative resolution to vary with (\sqrt{d}) . If the contribution of sampling fluctuations is dominant, as in the case of EMC, the actual dependence is more complicated. The energy resolution dependence on the thickness of the sampling layers is shown in Fig.2.14. Indications from energy resolution measurements indicate that one cannot achieve considerable improvement in energy resolution by reducing the plate thickness below "d = 2 cm" and that the limit for $d \rightarrow 0$ is

$$\sigma(E)/\sqrt{E(\text{GeV})} \approx 0.5$$

2.3 Read out Systems

The method used for the calorimeter read-out system is imposed by the requirements on the calorimeter performance with respect to :

- energy resolution
- signal linearity as a function of energy
- signal uniformity: ideally, the signal should not depend on the spatial position of the detected particle.

- position resolution, intimately linked to the read-out granularity.
- hermeticity: the fraction of the solid angle which is occupied by support structure and other "dead" elements, rather than by the sensitive detector volume should be small.
- rate capability, crucial at hadron colliders
- radiation resistivity of the active materials
- electronic stability, and possibilities of calibrating the detector
- capability of operating in a magnetic field and
- compensation

The active layers used in sampling calorimeters are either materials in which scintillation light can be detected or any active material in which an electric charge can be collected from a shower induced in the the material. The advantages of using scintillators are their good rate capability, very small dead space and a time resolution of typically a few ns. Their disadvantages are their poor granularity, signal uniformity and, for at least some, their radiation sensitivity. For detectors based on measurement of electric charge, the charge may be collected from solids, liquids or gases. Semiconductors like silicon have been successfully used in small sampling electromagnetic calorimeters. The advantages of using semiconductors are their compactness, good granularity, signal uniformity and stability and rate capability. Silicon is as fast as scintillator. The disadvantages are their high cost and vulnerability to neutrons which cause lattice dislocations. The best known liquid used in sampling calorimeters is liquid argon. The charge is collected without any internal signal amplification in an ionisation chamber mode. The major practical problem is keeping the electron-absorbing impurities at a sufficiently low level, (less than 1ppm). The advantages of this method of read out are its long term operating stability, owing to the absence of radiation damage, the possibility of fine segmentation and a response which is uniform to better than 1%. The main disadvantages are, poor hermeticity, as a consequence of the fact that the detector has to be cryogenically operated, and poor rate capability. The rate limitation is a common problem with all techniques based on electrons drifting over macroscopic distances. The charge collection time is larger than 100 ns, and more often 1 μ s in such devices.

Electric charge may also be measured by gas filled wire chambers which can be operated in proportional, Geiger, streamer or flash tube mode. The charge in such devices is internally amplified through avalanche development in gases. The advantages of such devices are their good spatial resolution in three dimensions, good efficiency for electrons and photons and in addition low cost. Different arrangements for read out systems are shown in Fig.2.15.

2.4 Spatial Resolution

The main limitation to spatial resolution comes from the lateral spread of the shower, which is caused mainly by multiple scattering of electrons that do not radiate but travel away from the axis. The shower exponential fall-off in the transverse direction is shown in Fig.2.16, obtained from a wire tube calorimeter. In order to distinguish between two adjacent showers and to measure their energy separately, they have to be at least one Moliere radius apart. 95% of the shower energy is contained in a cylinder of $2 R_m$. R_m is large for high Z materials because of the small critical energy, therefore the showers are wider transversely in low Z materials. In order to keep the Moliere radius small the calorimeter has to be as compact as possible to avoid too much overlap of contiguous showers. In reality, the limitation to spatial resolution is due to the longitudinal and transverse granularity of the calorimeter and because of the segmentation of wire chamber calorimeters they are superior to most other competing techniques, since a large number of cells can be read out without major complications. The simplest way of finding the shower position is to measure the centre of gravity of the lateral energy released. A resolution of 13 mm is reported from the CLEO calorimeter, and a 2 mm resolution is achieved with a strip width of 10 mm. In the ALEPH electromagnetic calorimeter a resolution of about 1 mm is expected.

Table 2.1

Scintillator	NaI(Tl)	LiI(Tl)	CsI(Tl)	Bi ₄ Ge ₃ O ₁₂	BaF ₂
Density (g/cm ³)	3.67	4.06	4.51	7.13	4.9
Melting point (°C)	650	450	620		
Decay time (μs)	0.23	1.3	1.0	0.35	0.62
λ_{max} (emission) (nm)	410	470	550	480	310
Light yield (photons/MeV)	4×10^4	1.4×10^4	1.1×10^4	2.8×10^3	6.5×10^3
Radiation length X_0 (cm)	2.59			1.12	2.1
Refractive index n	1.85			2.15	1.56
$(dE/dx)_{\text{min}}$ (MeV/cm)	4.8			8	6
Temperature coefficient of light output (%/°C)	0.22–0.9			1.7	
Radiation damage	yes			yes	
Hygroscopic	yes			no	

Table 2.2

Device passive/active (mm)	Al/scint. 89/30	Fe/LAr 1.5/2.0	Cu/scint. 5/2.5	W/Si detector 7.0/0.2	Pb/Ar/CO ₂ at NTP 2.0/10.0	U/scint. 1.6/2.5
Energy resolution						
measured at 1 GeV(%)	20	7.5	13.0	25.0	≤ 20.0	11.0
η (MeV)	3.0	0.7 (?)	0.7 (?)	0.7 (?)	≤ 0.6 (?)	0.7 (?)
F(ξ) ^{-1/2}	1.16	1.10	1.10	1.18	1.18	1.20
(cos θ) ^{-1/2}	1.00	1.03	1.03	1.27	1.36	1.51
σ ^{sample}	23	4.8	9.2	19.1	8.2	10.6
σ _{Landau}	3.8	1.0	1.0	4.5	8.70	1
σ _{path length}		5.7	6	17.5	13.0	6 (?)
σ _{estimated}	23	7.5	10.0	25.9	17.7	12.2

Table 2.3

Examples of hadronic calorimeters

Detector	Absorber thickness (mm)	Sensitive thickness ^a (mm)	σ/E (%/ \sqrt{E})
AFS	6 U + 5 Cu	2.5 Sc	35
CDHS	25 Fe	5 Sc	58
CHARM	80 marble	PDT, 30 Sc	45
FNAL ν	16 Fe/sand	flashtubes	80
MAC	27 Fe	PWC	75
Tagged γ	25 Fe	Sc	70
UA-1	50 Fe	10 Sc	80
UA-2	15 Fe	5 Sc	60

^a Sc, plastic scintillator.

Table 2.4

Material	Z	A	ρ^a (g/cm ³)	σ_T (barns)	X_{coll} (g/cm ²)	σ_{abs} (barns)	λ (g/cm ²)
H ₂	1	1.008	0.0708	0.0387	43.3	0.033	50.8
D ₂	1	2.01	0.162	0.073	45.7	0.061	53.7
He	2	4.00	0.125	0.133	49.9	0.102	65.1
Li	3	6.94	0.534	0.211	54.6	0.157	73.4
Be	4	9.01	1.848	0.268	55.8	0.199	75.2
C	6	12.01	2.265	0.331	60.2	0.231	86.3
N ₂	7	14.01	0.808	0.379	61.4	0.265	87.8
O ₂	8	16.00	1.14	0.420	63.2	0.292	91.0
Ne	10	20.18	1.207	0.507	66.1	0.347	96.6
Al	13	26.98	2.70	0.634	70.6	0.421	106.4
Ar	18	39.95	1.40	0.868	76.4	0.566	117.2
Fe	26	55.85	7.87	1.120	82.8	0.703	131.9
Cu	29	63.54	8.96	1.232	85.6	0.782	134.9
Sn	50	118.69	7.31	1.967	100.2	1.21	163
W	74	183.85	19.3	2.767	110.3	1.65	185
Pb	82	207.19	11.35	2.960	116.2	1.77	194
U	92	238.03	~18.95	3.378	117.0	1.98	199

^a Density for solids or liquids at boiling point.

Source: Particle Data Group, Rev. Mod. Phys. 56: S1, 1984.

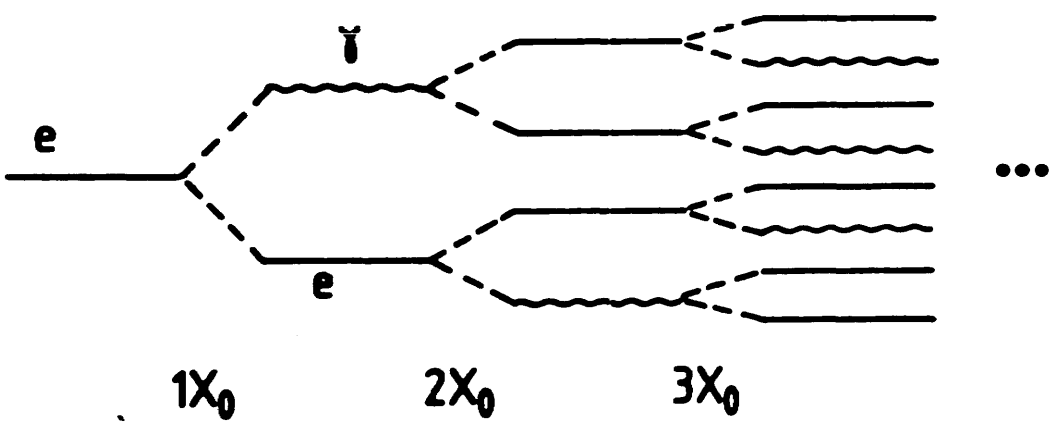


Fig.2.1

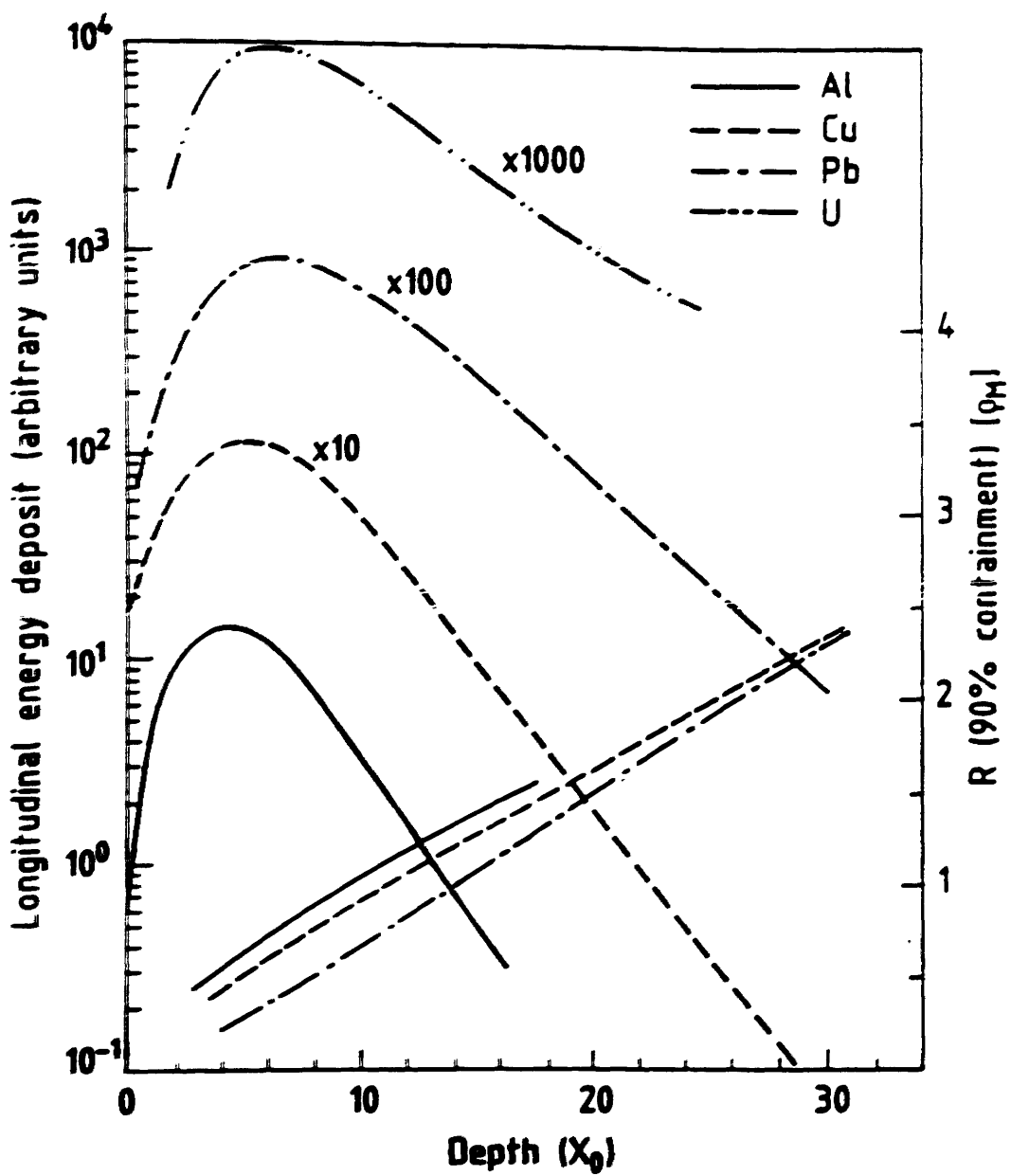


Fig.2.2

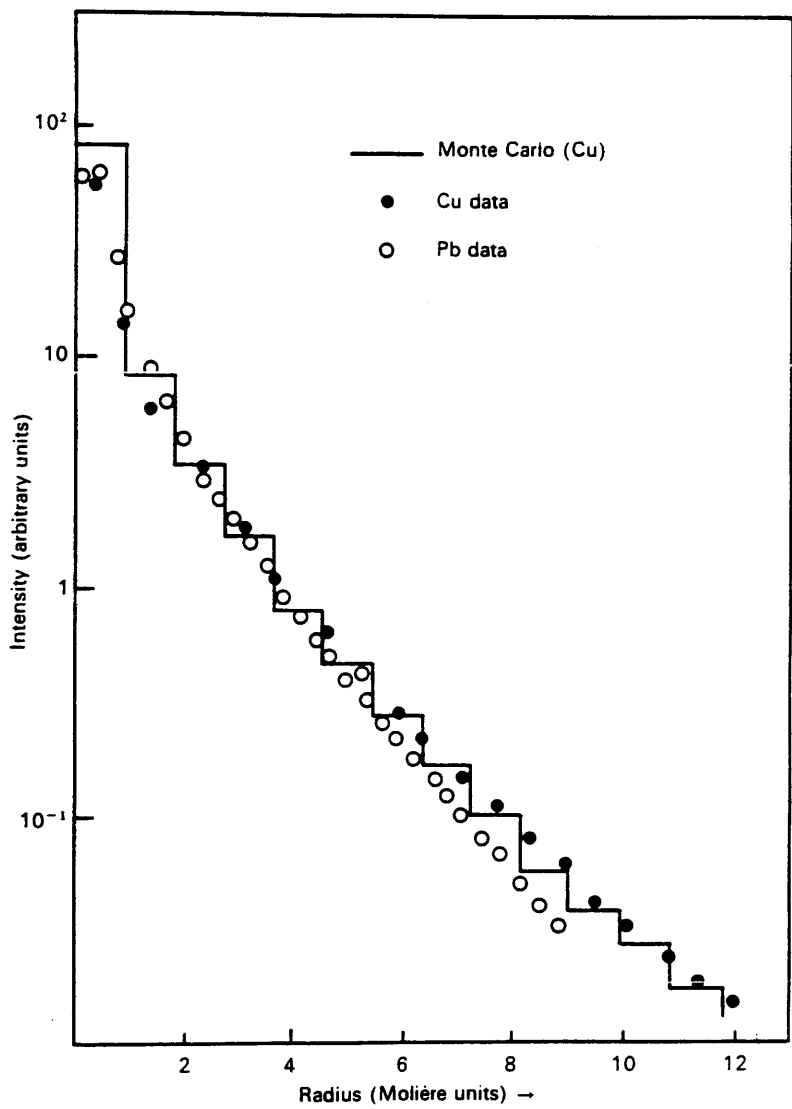


Fig.2.3

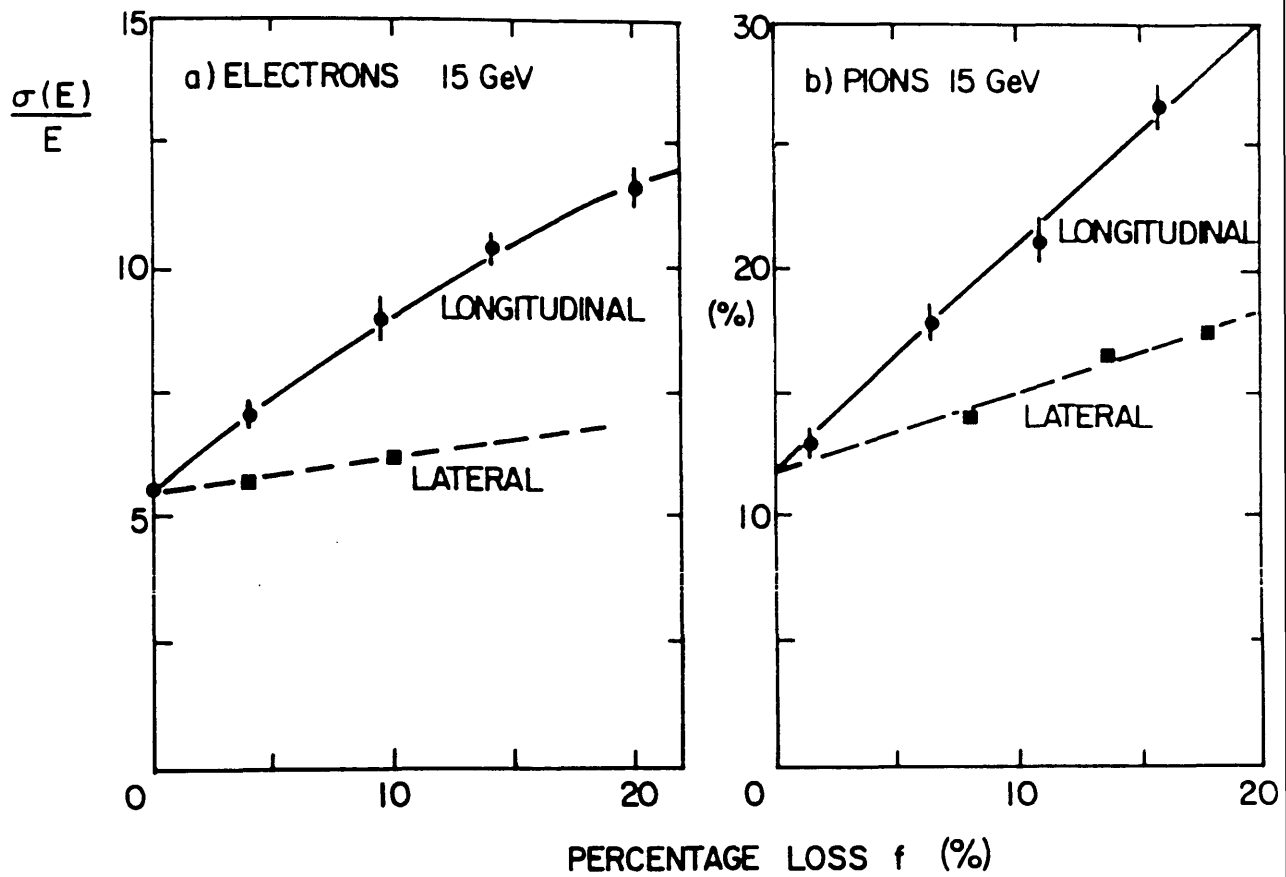


Fig.2.4

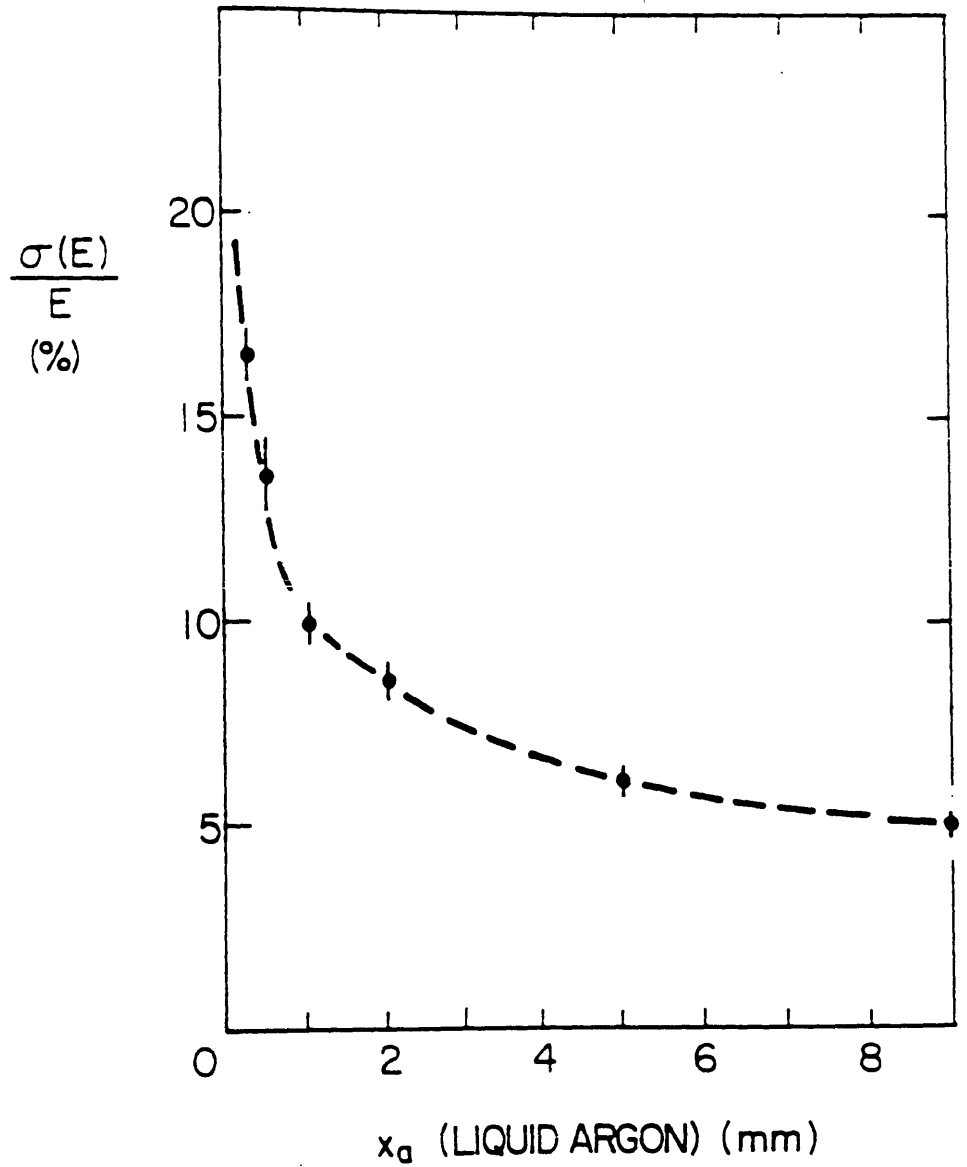
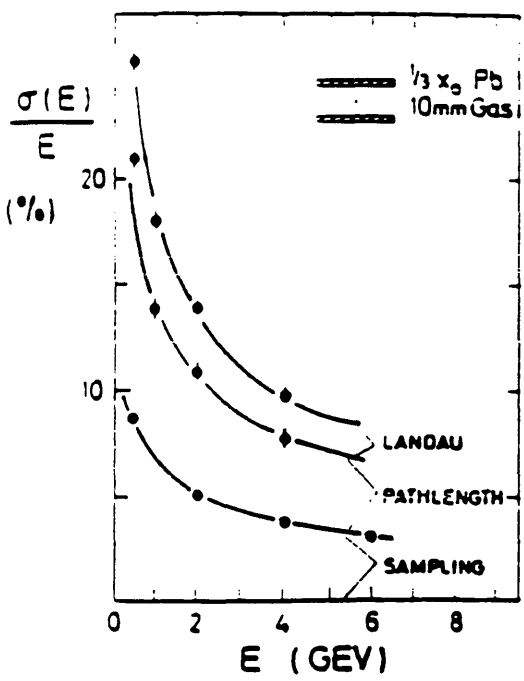
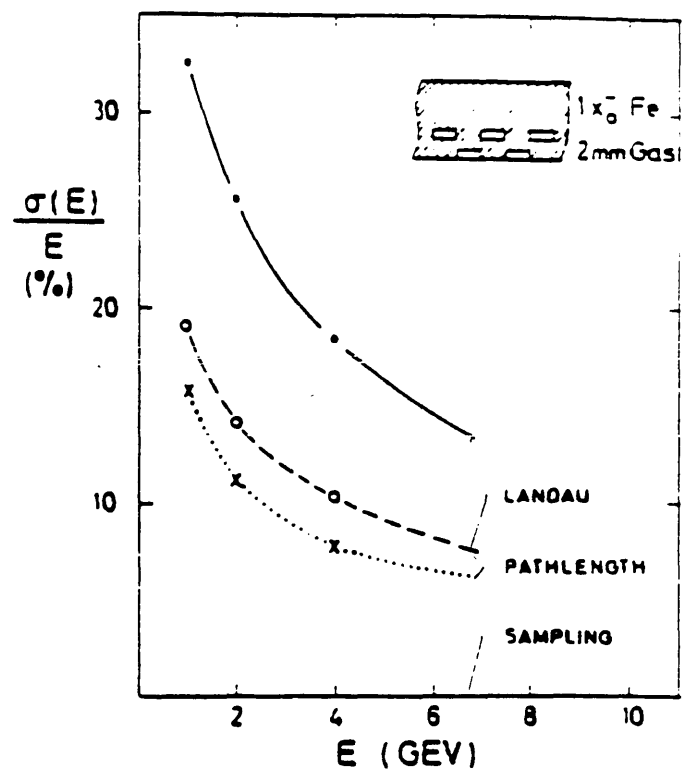


Fig.2.5



(a) Wire Proportional



(b) Tube Chambers

Fig.2.6

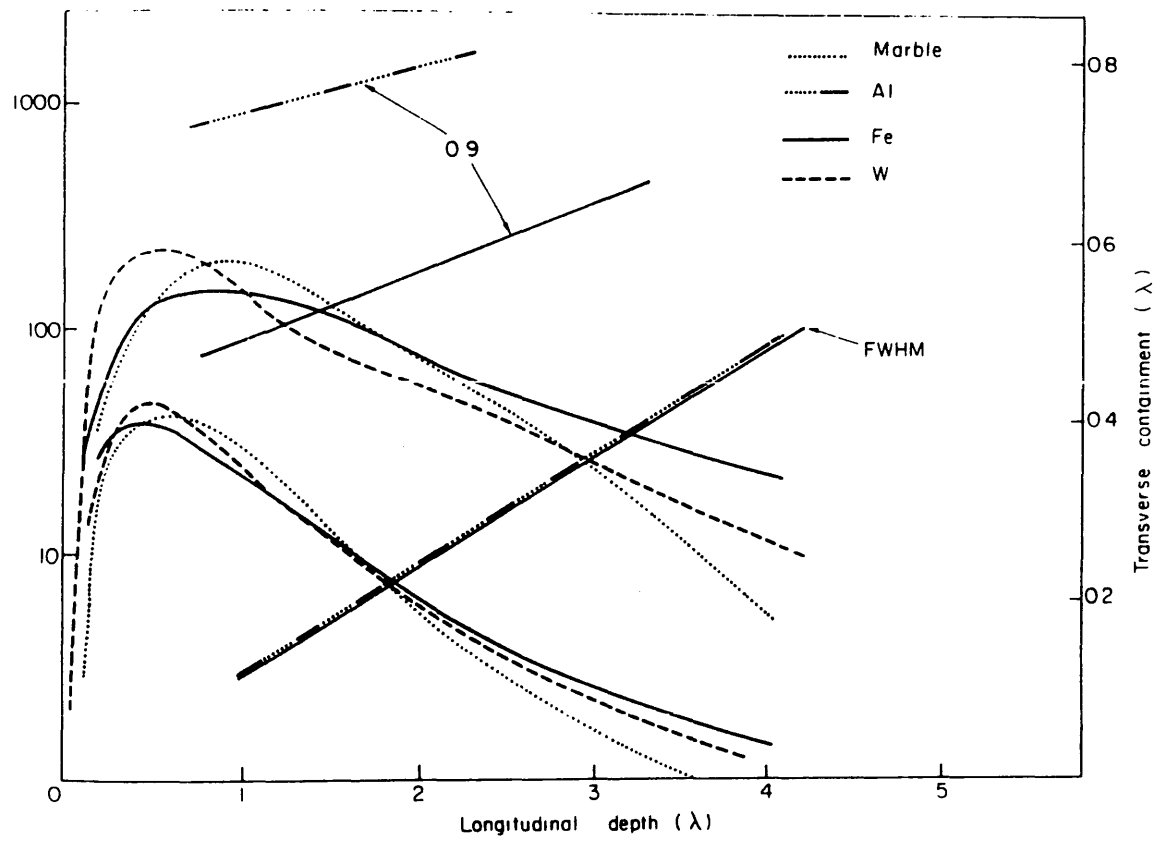


Fig.2.7 (a)

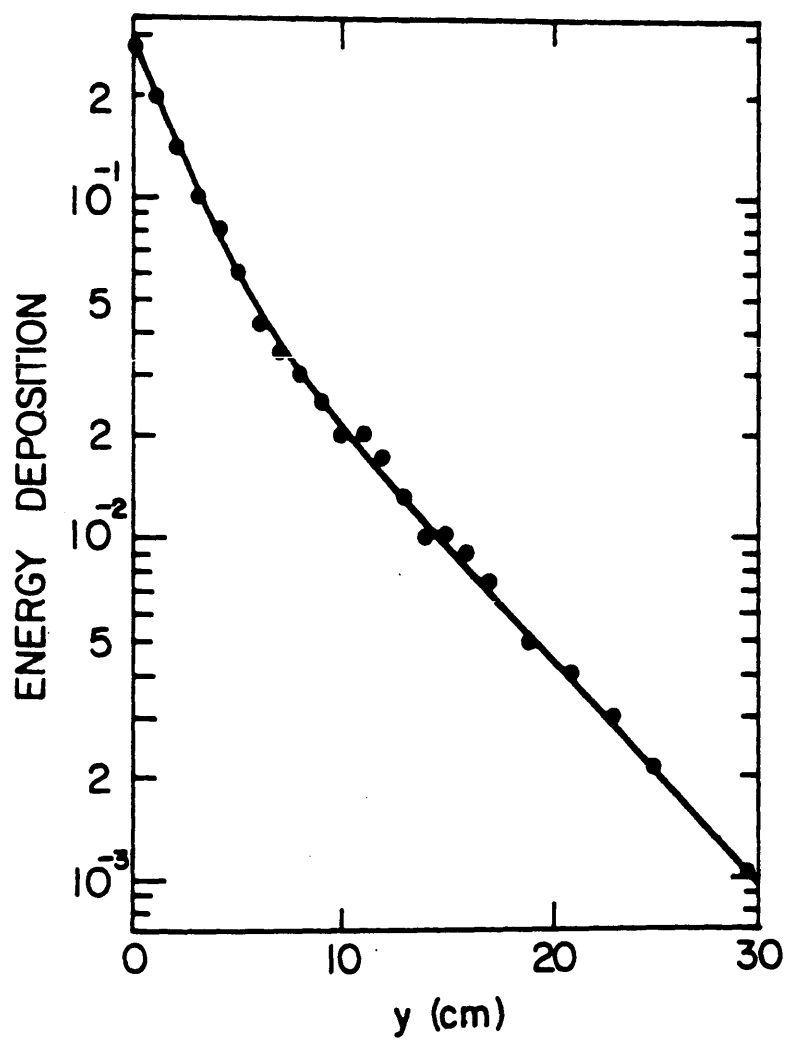


Fig.2.7 (b)

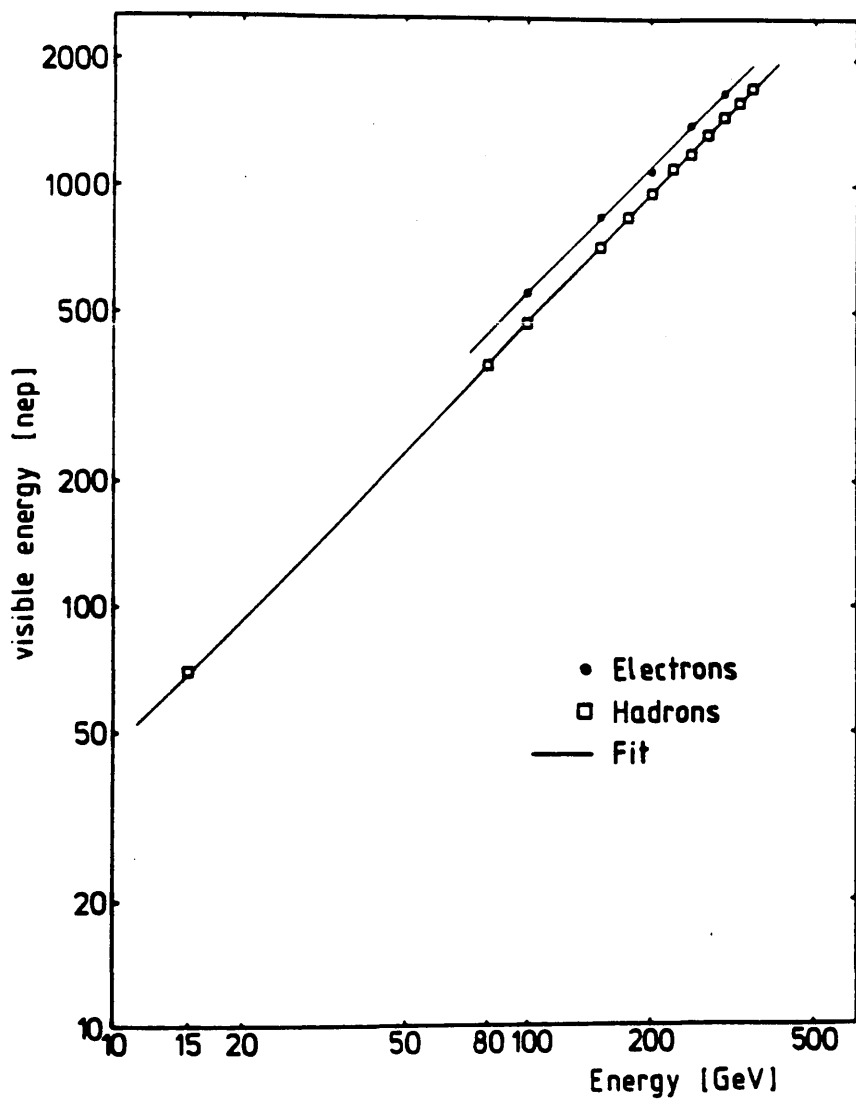


Fig.2.8

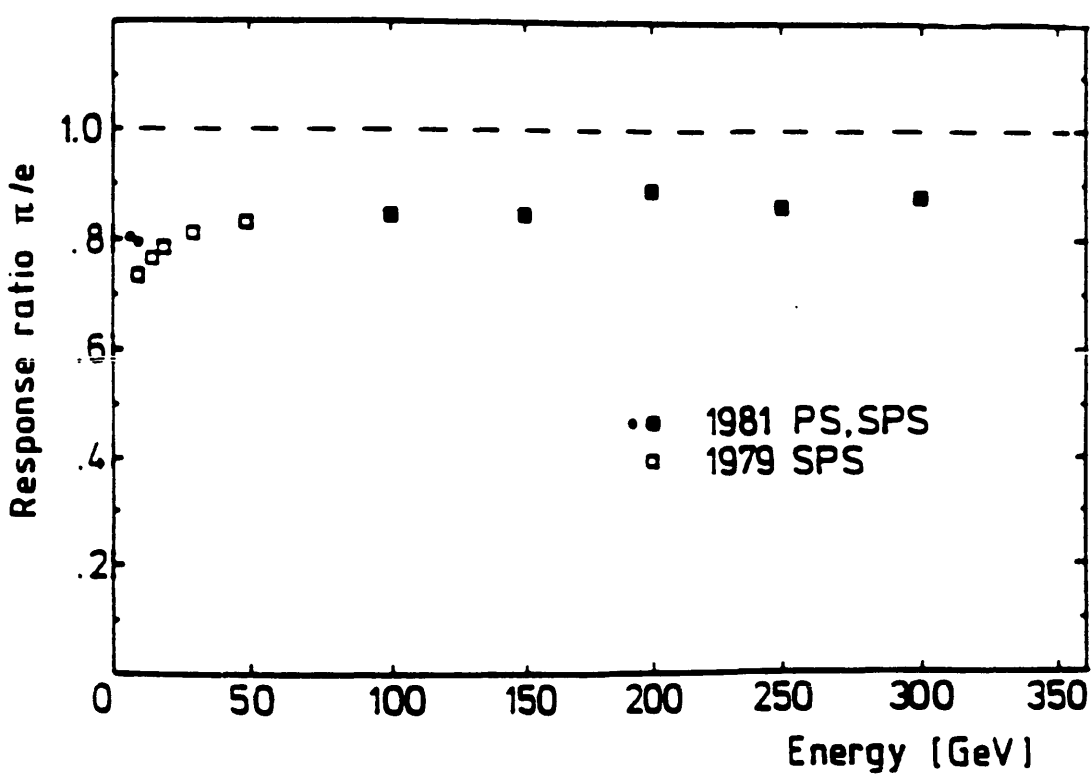


Fig.2.9

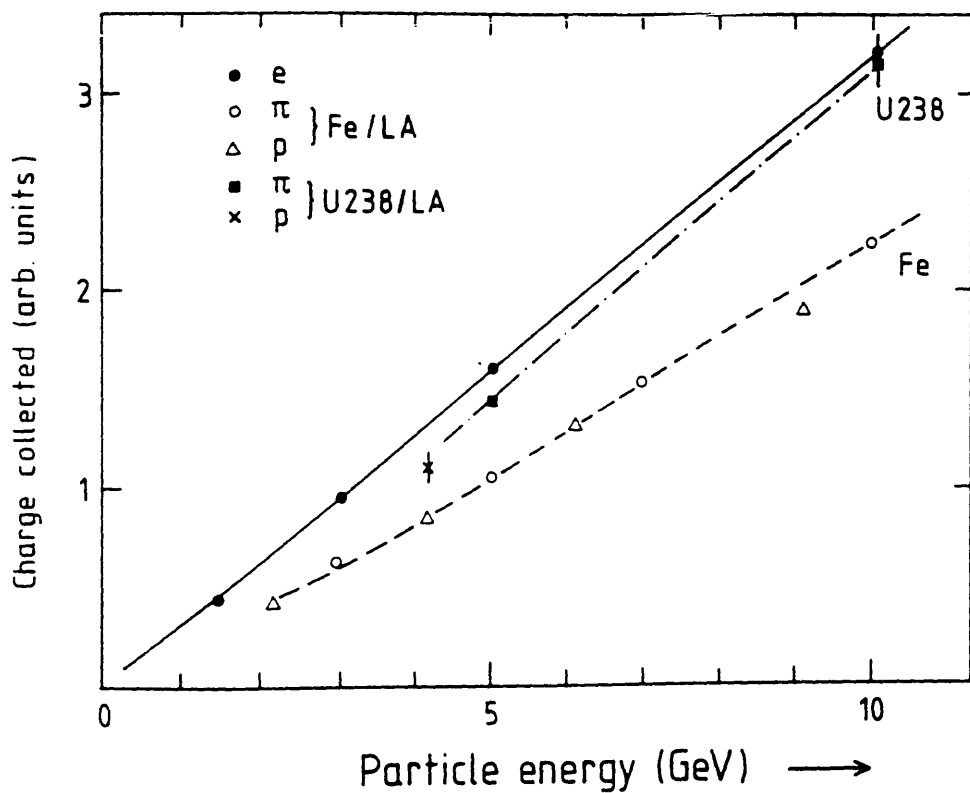
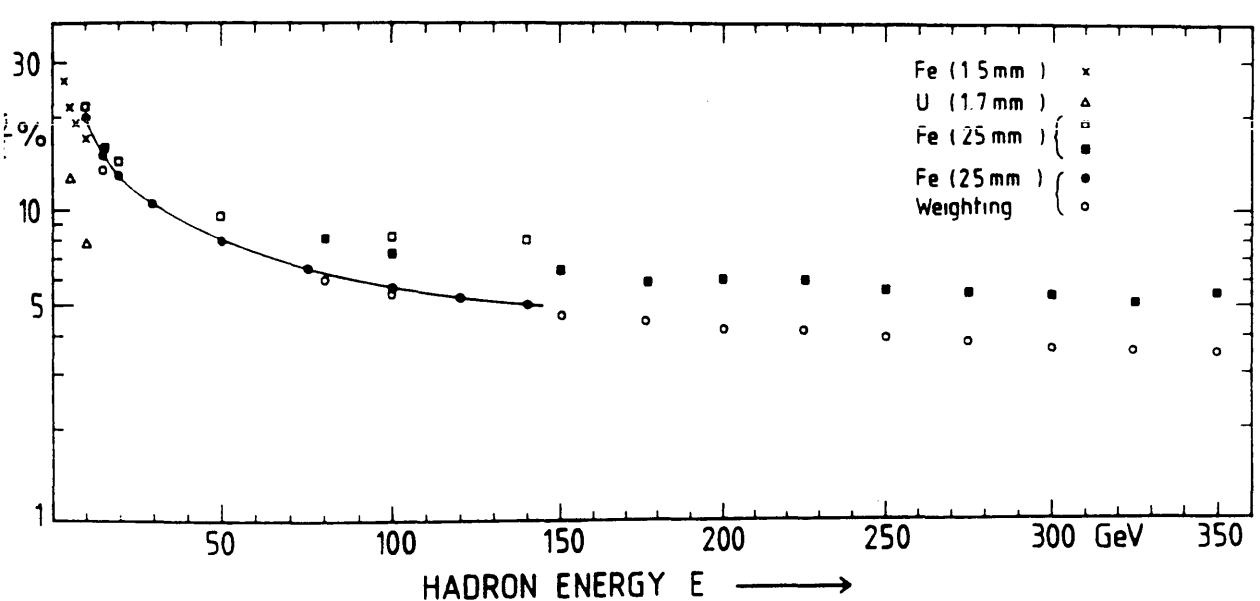


Fig.2.10



-- Fig.2.11

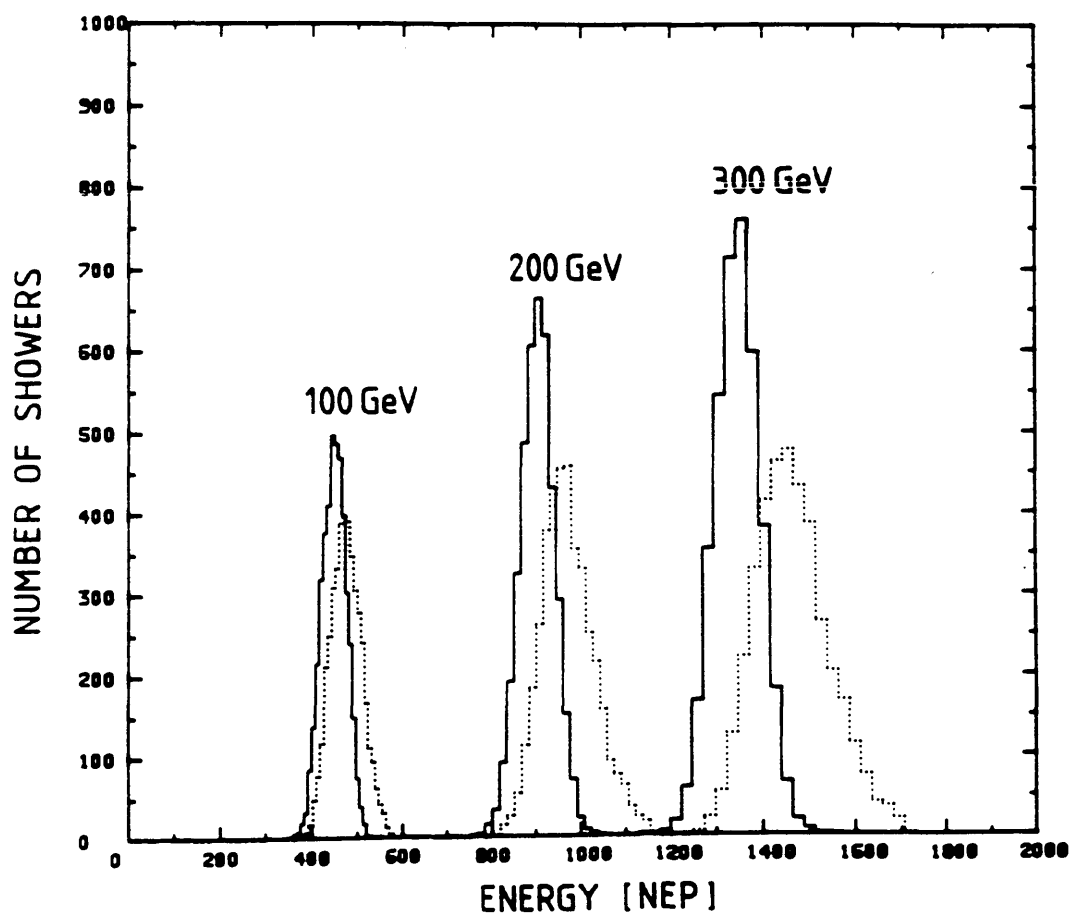


Fig.2.12

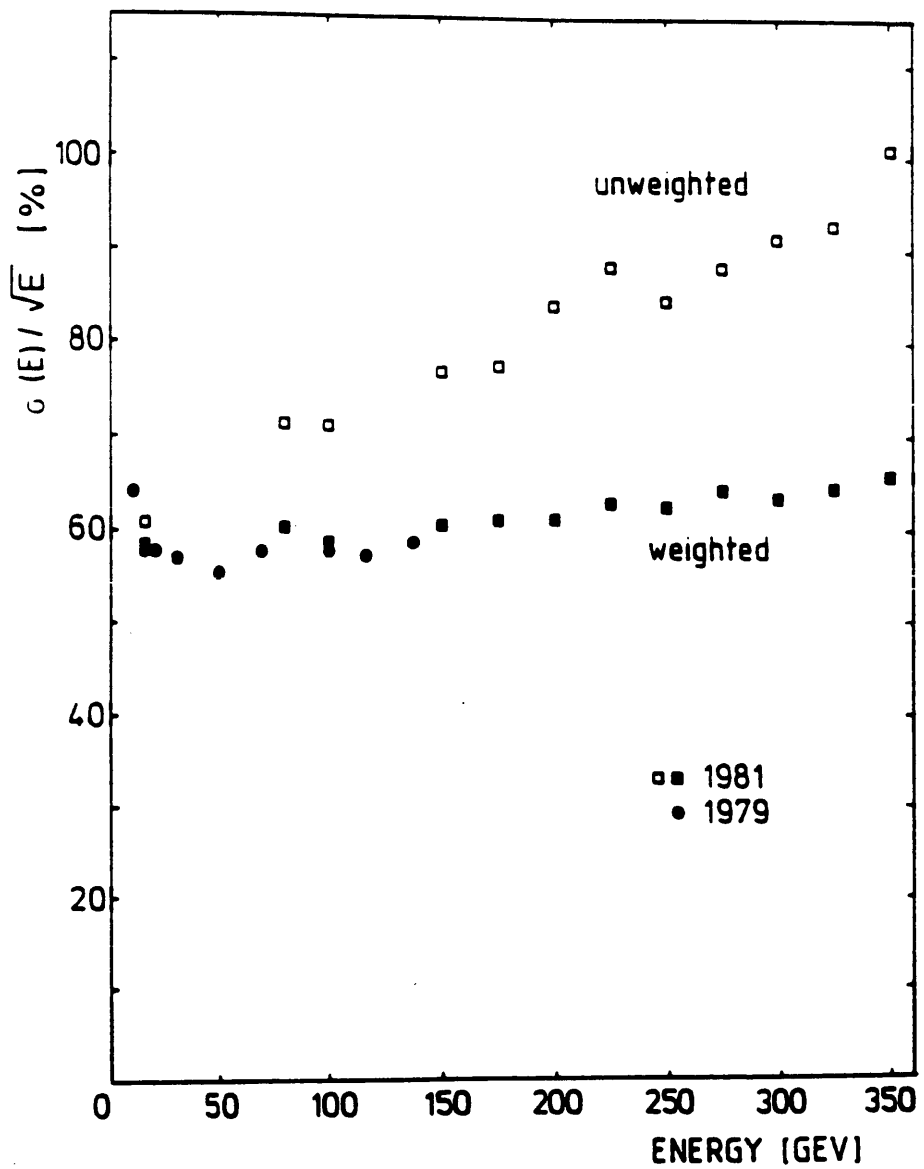


Fig.2.13

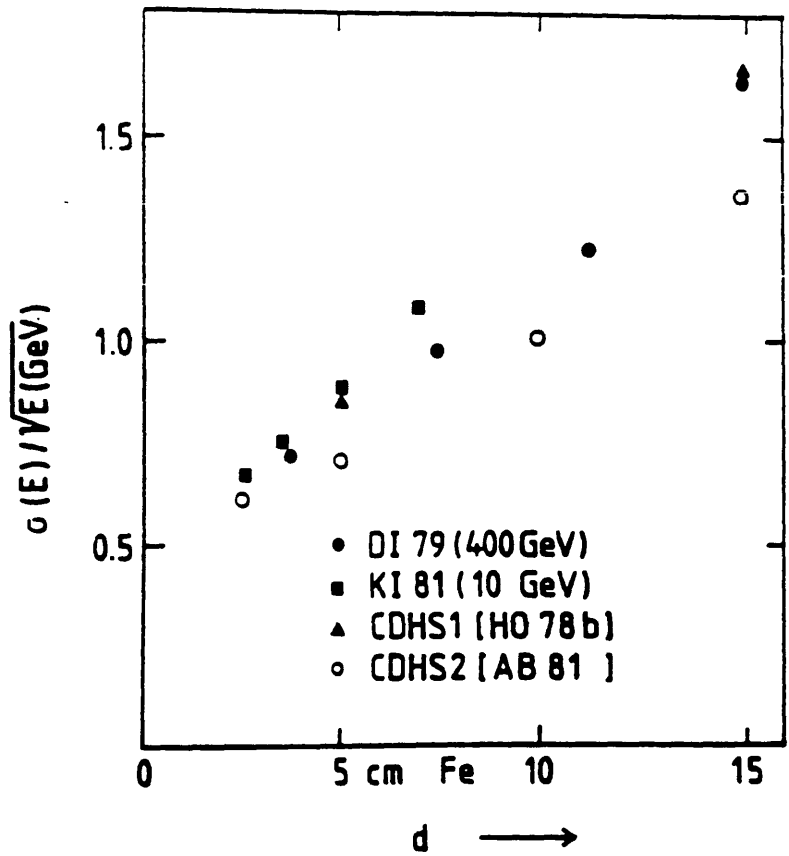
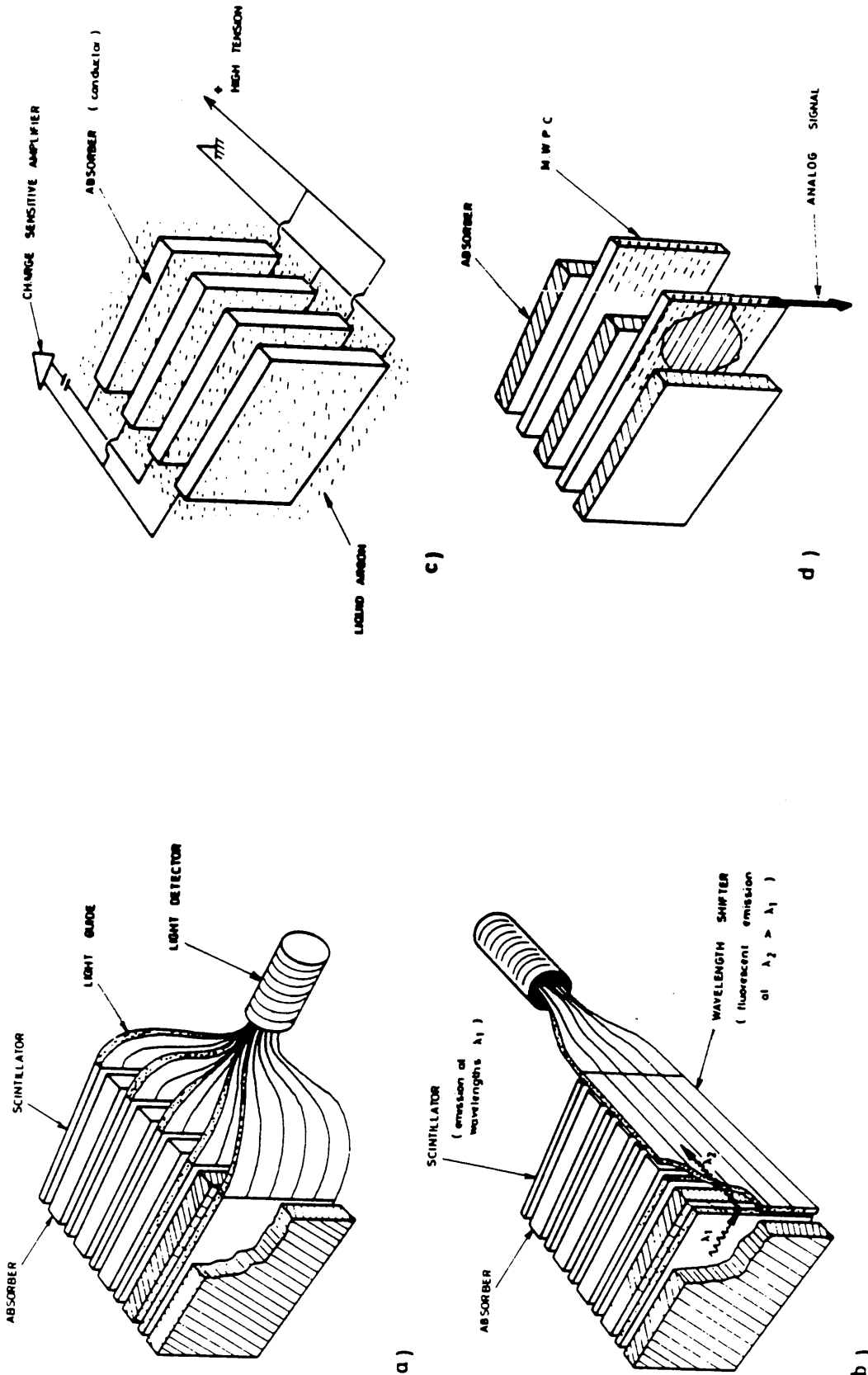


Fig.2.14

Fig.2.15



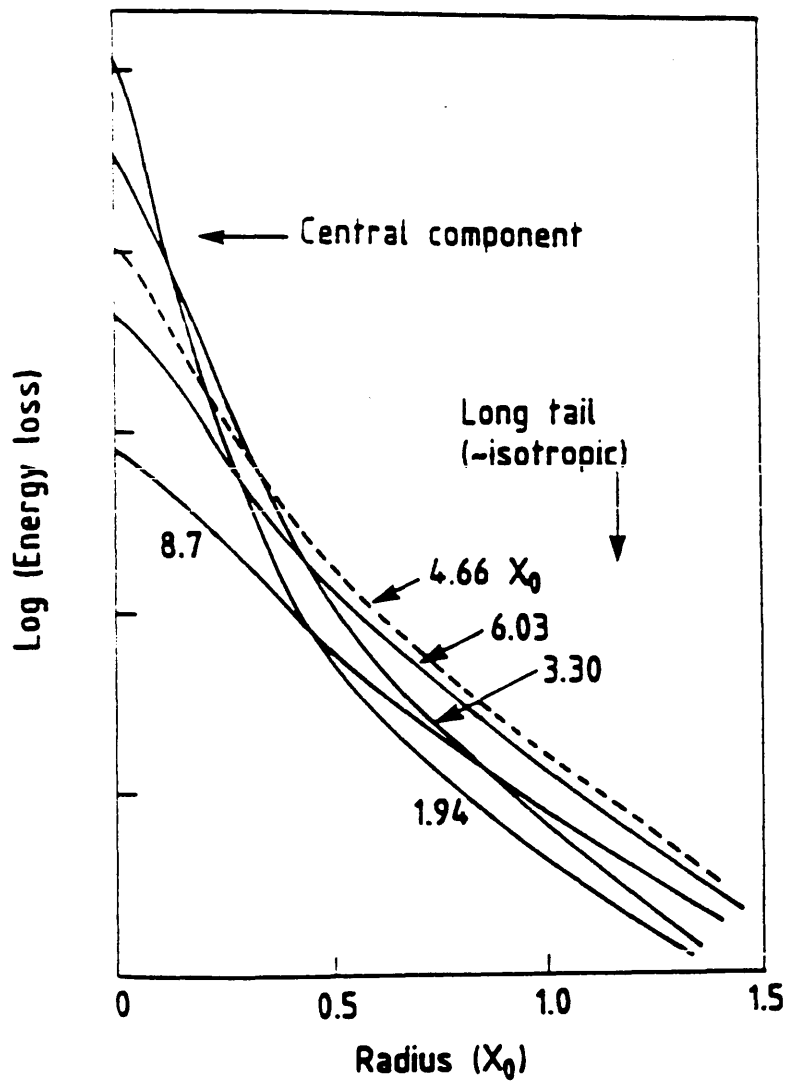


Fig.2.16

Chapter 3 - THE ALEPH DETECTOR

The ALEPH detector will be installed in pit 4 of LEP in late 1988, ready for first collisions expected early in 1989. It is designed to accumulate for each event as much information over as much of the solid angle as is practical. Of central importance in the detector are the magnetic track detector, designed to permit precise momentum determination of charged secondaries up to the highest energies. Detection is accomplished in consecutive layers. The over-all detector layout is shown in Fig.3.1. In the following paragraphs the construction of and performance of the important parts of the detector are discussed.

3.1 The Superconducting Coil

The solenoid is required to supply the ampere turns with an adequate current distribution for producing, in combination with the laminated iron-yoke structure, a magnetic field of 1.5 T in the central detector with the appropriate field uniformity. A current of 5000 A is needed to provide such a field, and it takes 1h to build up the current. The total energy stored in the magnet is 130 M Joule. Due to the large number of ampere turns ($\approx 8 \times 10^6$) and the size of the coil, a superconducting winding has been chosen. The conductor used in the coil is made of aluminium around NbTi/Cu. The solenoid with its cryostat weighs 55 tons, and they are located between the electromagnetic and the hadron calorimeters. The solenoid is 7 m long with outer radius 2.92 m and inner radius 2.48 m. The effective thickness of the material used, (coil + cryostat), is $1.6 X_0$ and $0.3 \lambda_{abs}$. Another constraint for the mechanical design of the solenoid is the requirement of supporting the central detector and the electromagnetic calorimeter on the inner vacuum tank of the cryostat, (weight ≈ 130 tons).

The condition for field homogeneity is expressed as a tolerance on the integral of the radial field component along a line parallel to the beam axis in either half of the TPC, which is 2.2 m long and 3.6 m in diameter. The required condition is

$$\int_0^{220} \frac{B_r}{B_z} dz < 2 \text{ mm}$$

The field homogeneity $\Delta B/B = \pm 2 \times 10^{-4}$.

The solenoid is cooled in a closed-loop refrigerator and takes 10 days to cool down from 300K to 4.2K. The refrigeration power required is 100W at 4.2K and 2400W at 60K (30 l/h of liquid He). The solenoid is cooled indirectly via cooling pipes thermally coupled to the support cylinder of the winding. This cooling mode relies on the thermal conductivity of the materials used in the coil. On the other hand, the stability of the superconductor, or its reliable behaviour against the small disturbances likely to occur in a solenoid of this type, is governed by the two related properties of high thermal conductivity and low resistivity of the

substrate in which is embedded.

3.2 The Minivertex Detector

This kind of detector is used for the location of decay vertices of short-lived particles. The detector is dodecagonal in shape, made out of two layers of thin multi-electrode silicon detectors (MESD's) surrounding the pipe at a distance from the beam line of 85 and 105 mm, respectively. The angular coverage is $44^\circ \leq \theta \leq 136^\circ$ and $0^\circ \leq \phi \leq 360^\circ$. The whole structure of the assembled detector looks like two concentric barrels, and is shown in Fig.3.2(c). The inner layer is 20 cm long and 8.65 cm in radius and the outer layer has the same length with a radius of 12.30 cm. For the inner barrel (θ layer), the readout strips of the MESD's run round about the beam line, whilst the outer (ϕ layer) has strips parallel to the beams. The ϕ -strips have the following dimensions, 2x50 mm, 25 μm pitch, and 100 μm readout. The total length of the barrels along the pipe is 230 mm. Each detection layer is a mosaic of MESD's, 300 μ thick, with readout strips 20 μm wide and 250 μm apart. To satisfy the requirement that charged particles and photons should not pass through high-density and high-Z mechanical supports, the material employed for the assembly of the detector is Rohacell 71, a material of relatively good hardness, machinable, and with very low density (0.07g/cm³). The " θ layer" z-strips of dimensions 50 mm, 50 μm pitch, and 200 μm readout, is assembled on a Rohacell support made with eight independent "Roman arches", as shown in Fig.3.2(d). Four assembled adjacent "Roman arches" make up one half of the inner barrel. The two halves are mounted around the pipe and are held by a swallowtail-shaped plastic rod (see Fig.3.2(e)) which fits into suitable notches machined in the Rohacell. Six silicon crystals forming a z-layer element are glued with an amine-free epoxy on each arch, as shown in Fig.3.2(d). The two arches of the outer barrel, (ϕ -layer), can be mounted after the θ -layer assembly and are supported by the two end-caps shown in Fig.3.2(c). Twelve independent slides, each one carrying four MESD's, are mounted on the supporting outer structure. Each ϕ -layer element can be independently slid in and out of each side of the outer barrel on rails machined on a Rohacell surface, as shown in Fig.3.2(a,b). The readout ϕ strips of each crystal are microbonded to the corresponding strips of the adjacent crystal with 20 μm pure gold wire. The resulting element of four crystals is therefore equivalent to a single detector 23 cm long. Similarly, the readout strips of the six ϕ crystals glued onto a "Roman arch" of the inner barrel are microbonded to the corresponding strips of adjacent MESD's to make a detection element acting as a single polygon-shaped crystal. At the extreme borders of each side for the ϕ layer and of each "Roman arch" for the θ layer are fixed two thin ($\text{Al}_2\text{-O}_3$) sheets, 0.6 mm thick, 4.2 mm wide, glued together for housing the required preamplifiers as shown in Fig.3.3. The characteristics of the silicon detectors have been studied, on a structure

of $(0.12 \times 4.9 \text{ cm}^2)$. The relation between the applied voltage and some related factors e.g. the current, the capacity, and the interresistance of the detector are shown in Fig.3.4(a,b,c). It was found that the silicon detectors were fully depleted at ≈ 155 V. The p^+ -strips and the n^- -strips were tested using a β -source. The results are shown in Fig.3.5.

Minivertex Electronics

Summing 27500 $r\phi$ and 27500 θ strips with a local multiplexing of 1:256, will give 4400 readout channels. Specially developed amplifiers for the MESD's will be used in the first stage of the electronic system, which can be densely packed on a ceramic sheet with a density of one channel every 400-500 μm , satisfying the construction requirements of the MINIVERTEX. Fig.3.6 shows the front-end electronics combined with the z-strips. A block diagram for the readout electronics is shown in Fig.3.7. In Fig.3.8, the noise vs. the input capacity for different sampling times for a single channel of analog multiplexer is demonstrated. The radiation damage of the CMOS electronics has been studied by exposing 1 AMX chip under power to 660 keV γ 's from ^{137}Cs at CERN. It was found that up to 6.5 krad no change in the performance was seen but the electronics become non-functional for radiation levels more than 13 krad. The rest of the chips have still to be tested.

3.3 The Luminosity Monitor

As mentioned in Chapter 1, the luminosity at LEP will be measured from the rate of Bhabha events at small angles. There the interference between the γ and Z° is negligible and the cross-section is well known from pure QED. A systematic uncertainty below 2% is expected at LEP, so that the error in the annihilation cross-section will not be dominated by the uncertainty of the luminosity. To achieve such a precision, measurement of the energy is essential to reject background both in the trigger and in the off-line analysis. In addition a precise measurement of the angles is necessary since the Bhabha cross-section is a steep function of the scattering angle.

The basic element of the detector is the luminosity calorimeter, LCAL. Its spatial resolution is not adequate for defining the acceptance with the required precision. A tracking device is needed for measuring the polar angle of the Bhabha electrons with better precision than can be reached with a calorimeter alone. (A single plane device to measure the impact points of Bhabha electrons is not sufficient because of the back-scattering from the calorimeter, which generates false hits.) The space reserved for the luminosity measurements consists of two zones symmetrically situated on each side of the interaction point in the z region between 2445 and 3086 mm. In these zones a pair of counting devices is installed, each being a

combination of a tracking device and a shower counter as shown in Fig.3.9. The shower counter extends the angular coverage of the ECAL.

3.3.1 The Tracking Device (SATR)

The tracking device consist of nine layers of chambers, separated in depth into three groups of three layers each. Each group has the same mechanical structure. A structure of separated tubes is used, because they are known to behave better than MWC's in a high background. The tubes are of brass, with cross-section $9.95 \times 9.95 \text{ mm}^2$ and 0.3 mm wall thickness. The wire lengths vary from place to place from 76.8 mm to 192.7 mm due to the construction geometry. Each layer consists of eight 45° sectors of identical design. There are three types of sector, called A, B, and C, with different tube alignment as shown in Fig.3.10(b). The first of each group is made of sectors of type A, the second of type B, and the third of type C. The relative orientation of the tube chambers within one group, as seen from the collision point, is shown in Fig.3.10(a).

To avoid dead zones, the second group is rotated by 15° in azimuthal angle with respect to the first group, and the third by 30° . Each sector consist of 14 tubes covering the acceptance up to the opening angle of the beam-pipe funnel (80 mrad). To minimize dead zones between two adjacent sectors, the wires are fixed to a "pertinax comb" at the end of the tubes as shown in Fig.3.10(c). In this way the dead space between the sectors due to the mechanics is reduced to 6 mm. There is, however, a wider dead space due to the fact that the tubes are not cut perpendicular to the wires, giving a loss of sensitivity close to the end.

So as to make the mounting around the beam tube possible, the groups have been split vertically into two halves. Each half is contained in a gas box divided into three packages, each containing a group of three layers. The total amount of material in the tracking device corresponds to $0.5 X_0$.

3.3.2 The Luminosity Calorimeter (LCAL)

The LCAL consists of two symmetrical parts on each side of the interaction point. Each part is split into two half cylinders with outer radius 52 cm and inner radius 10 cm. The design of the (LCAL) is similar to that of ECAL. It consists of 38 layers of wire tubes ($4.5 \times 3.5 \text{ mm}^2$), operated in a saturated mode, interspersed between Pb converter sheets of 2.8 mm, (stack 1 and 2), and 5.6 mm thickness (stack 3). The readout is by segmented pads which are arranged in a projective tower geometry ($\approx 0.2 \text{ msr}$) as seen from the interaction region. LCAL is segmented in depth into three sections, stack 1 (10 layers), stack 2 (19 layers), and stack 3 (9 layers). Inside the tower signals are added separately to improve the

π/e rejection. The LCAL structure is shown in Fig.3.11. Only the four innermost rings of the towers are used for luminosity measurement and triggering.

The first stage electronics used in LCAL are similar to those used in the ECAL. The total number of channels per shower counter is ≈ 900 , of which ≈ 360 are part of the luminosity trigger and counter.

The resolution of LCAL is given by

$$\sigma/E = \sqrt{45/38} \times \sigma_{\text{ECAL}}/E (= 20\%/\sqrt{E})$$

3.4 The Inner Tracking Chamber (ITC)

The Inner Tracking Chamber (ITC) has two functions. One is to provide an essential part of the level 1 trigger, the second is to enhance the over-all charged particle tracking of ALEPH, particularly in the critical area close to the beam pipe. The position of the ITC relative to adjacent parts of the detector is shown in Fig.3.12. The chamber is a conventional, small cell drift chamber. It has eight layers of sense wires (W/Au 30 μm in diameter), 96 cells on the inner four layers, 144 on the outer four. These are separated into four sub-chambers, using polystyrene shells which support hooped cathode strips on the inner and outer walls to provide the z readout. Each pair of layers are separated by a wire mesh of Al/Au 256 guard wires 14 μm in diameter. The azimuthal position of the sense wires is offset by half a cell from layer to layer in order to resolve left-right ambiguities and achieve good two-track resolution. The wires are held in aluminium end-pieces in feedthroughs, the position of which is known after optical alignment to better than 20 μm . A mixture of argon/CO₂ is used for all sub-chambers. An addition of a small amount of hydrocarbon may become necessary in order to achieve a reasonable drift velocity and the required precision.

To reduce the material in the detector to a minimum, the walls of each sub-chamber are constructed by bonding together 1 mm thick polystyrene sheets. Since the ITC provides an essential part of the Level 1 trigger, it must be highly reliable and must not be made inoperative by a broken wire. The shells also perform this function, as a broken wire will affect at most two layers. Additionally, the high-voltage supply is highly segmented so that small groups of cells will be able to be switched off independently. The z-measurements are done using the time difference for the pulse to reach the ends of the wire, providing correlated r- ϕ -z information for a fast 3-dimensional track trigger. The construction of the detector is now finished and all the necessary checks have been done. It has been tested at CERN in a test beam, with the aim of evaluating the chamber performance, front end electronics, and the r- ϕ resolution. This was done using a new DAQ FASTBUS readout.

When tested in a high energy beam it operates normally up to 2.4 kV with no problems.

The $r\phi$ resolution

The $r\phi$ resolution was studied assuming a linear drift-time relation through the following procedure:

- fit track to hits
- remove hits greater than $600 \mu\text{m}$ away and
- refit and then plot the residuals.

The $r\phi$ resolution for layer 1 of the detector is shown in 3.13(a) and for the other layers of the detector in Fig.3.13(b). A $r\phi$ resolution of $\approx 120\text{-}123 \mu\text{m}$ is expected.

z-measurement

The basic principle in the z-measurement is that an electric charge proportional to the time difference of the pulse arrival at the two ends of the wire is stored in a capacitor. This is then discharged slowly and the discharge time measured. The "time expansion" is proportional to the discharge rate. For the space-point processor each layer is discharged at a rate proportional to $1/\text{radius}$, so for constant θ all layers discharge at the same time. With timing accuracy Δt , $\Delta z \approx (c/z) \Delta t$. Hence $300 \text{ mm} \approx 200 \text{ ps}$.

The expansion factor ranges from 100 for the outer layer to 160 for the inner, so that the z-measurements have a resolution of $\approx 2.5 \text{ cm}$.

3.5 Time Projection Chamber (TPC)

The TPC is designed to provide good momentum and angular resolution, as well as ease in pattern recognition and additional resolving power in $e\pi$ separation. It is built on the basis of previous work at Berkeley, with a cylindrical active volume of $2 \times 2.2 \text{ m}$ length and circular end-plates of 1.77 m outer radius and 0.33 m inner radius, as measured inside the cylindrical field cages. The total gas volume of 42 m^3 is filled with an argon-methane (80-20)% mixture at atmospheric pressure and the drift field is 20 kV/m . Electrons drift to the end-plates of the TPC, where they are recorded by a system of proportional wires and capacitively coupled cathode readout pads. Points along the tracks of charged particles are thus measured in three dimensions (z, r, ϕ) through the drift time (z) and the pad coordinates (r, ϕ). The pulse heights on the proportional wires are a measure of the ionization density dE/dx along the track. The design of wires and pads is such that up to 21 space points and 320 ionization samples are measured per track. The active area of the end-plate is $\approx 9 \text{ m}^2$, as

shown in Fig.3.14. An end-plate is subdivided into 18 "sectors" of three different types, 6 inner sectors (type K) and 12 outer sectors (type M + W). A striking property of this layout is the radial zig-zag boundary between sectors so that straight tracks never fall completely on the radial boundary, i.e. they are always visible. The most important feature of the end-plate is, however, the arrangement of the pads in 21 concentric circles as shown in Fig.3.15 for 3 dimensional coordinate measurement ($r\phi$ from pad position, and z through drift time). The pads have a radial length of 30 mm and a width of 6.7 mm. The reason behind the choice of long radial pads is the improvement it provides in the $r\phi$ spatial resolution. Each sector is equipped with special trigger pad rows. There are 20500 pads and 3240 wires with a spacing of 4 mm on an end-plate. The total number of electronic channels is 47400. Corrections to the sagitta distortion caused by the electric and magnetic inhomogeneities in the TPC are achieved with the help of the laser calibration system. Distortion due to the space charge effects of the slowly drifting positive ions will be avoided by gas amplifying the drifting electrons only when there is a valid "level 1" trigger. In the following sub-sections, different aspects of the construction and performance of the TPC are discussed.

3.5.1 Electronics

The TPC electronics determine the time of arrival of the wire chamber signals as well as their amplitude. This is done by a recurrent sampling of the pulse height of the signals from wires and pads during the entire drift time, $\approx 35 \mu s$. A functional block diagram of the pad and wire signal readout system is shown in Fig.3.16.

The first element in the chain which processes pad or wire signals is a low-noise preamplifier-cable driver, constructed in thick-film hybrid form, and mounted in groups of 16 on motherboards, directly on the end plate of the TPC.

The preamplifier signals are transmitted to the digitizing system via ≈ 30 m high quality shielded twisted-pair cables. The digitizing system is designed according to the FASTBUS specification. It basically consists of three modules, the Time Projection Digitizer (TPD), the Time Projection Processor (TPP), and a Clock Fan-out Trigger Time Interpolator (CFTTI). The Segment Interconnect is a standard FASTBUS device. The total number of the electronic channels for the pad readout is 41000 and for the wires 6400. The number of the TPD's for the pads is 660 and for the wires 108, whereas the number of the TPP's is 36 for the pads and 36 for the wires.

3.5.2 The laser calibration system

Due to non-axial components of both the electric and magnetic fields and a possible tilt angle between the fields, a particle track undergoes distortions leading to unwanted sagitta errors. The laser calibration system is designed for the TPC to monitor the drift velocity and to measure the systematic displacements of particle trajectories, where no direct access to the TPC is possible. It is built up from two identical subsystems, one for the calibration of the left half and the other for the right half. Fig.3.17 shows the setup of the calibration system of the left half of the TPC which is identical to the other half.

Two Q-switched Nd-Yag-lasers with two frequency-doubler crystals are fixed on the top of the ALEPH-detector, one for each subsystem mentioned above. The laser beam first passes through the "beam switch", which allows the beam to be guided either into the left subsystem or the right subsystem if there is a breakdown in one laser. The beam is then deflected by an "actuator", which is the main steering unit of the laser beam and which deflects the beam down into the first "mirror knee". After passing the second mirror knee the beam reaches the "splitter ring". The splitter ring has two functions, first to split the beam into three beams of equal intensity at azimuthal angles $\phi = 96, 216$, and 336 degrees and then to send them into the TPC along the inner field cage and parallel to the beam axis. In the TPC there are sets of five partly transparent mirrors, which split each of the three beams into a further five beams with polar angles $18, 30, 39, 67$, and 90 degrees, so that finally 15 tracks are created by one initial laser beam. The reflection ratios are chosen in such a way that all of the 15 beams have nearly the same intensity.

Initially, the laser beams will be adjusted by hand, so that the beams strike the mirrors in the TPC. As there is no reason to believe that the beams will remain in this position, some corrections may have to be made to allow for deviations from the correct path, so the mirrors in the actuator can be moved by four stepping motors, which are computer-controlled. The path of the laser beam is detected by five diodes. One lateral diode is fixed in the actuator, the second is placed in the so-called "pipe bowl" at the splitter ring. There are three further diodes in the splitter ring on the opposite end-cap of the TPC. The system is in the correct state if the diode in the pipe bowl and the three diodes in the opposite splitter ring are struck centrally; then each of the three beams passes correctly through its five mirrors in the TPC. The diodes are position-sensitive lateral or quadrant diodes. Each diode provides four pulses, if it is hit, from which one can estimate the position of the laser beam on the diode. With this information the mirror in the actuator can be moved in such a way that the laser beam is moved to the middle of the diodes. The laser calibration system has already been used to measure the drift velocity and electric field in the ALEPH-TPC, proving that the above goals can be achieved by the system. Results also show that the influence of the

magnetic field on the transverse electron diffusion is different below and above a characteristic B-field given by the equality of the electron cyclotron frequency with the mean collision frequency.

3.5.3 Gating

The gating system of the TPC serves three purposes:

- to prevent the build up of positive ions in the fiducial TPC volume by trapping them at the gating grid.
- to increase the chamber lifetime by reducing the electron flux into the proportional region.
- to provide for compensation of the ExB effect at the sense wires by exploiting the ExB effect at the gating grid.

To achieve the above goals the TPC must therefore be operated in a shutter-like or gated mode. In analogy to optical devices, the TPC would remain insensitive as long as no suitable event candidate is present (to be determined by an external trigger). Only in the case of such a pre-trigger signal would an electronic shutter be "opened" and the TPC end-plate "exposed" to the particle tracks. One way of achieving this goal is to use a gating grid, which can be appropriately operated in order to be either totally opaque or transparent to drifting electrons approaching the detection plane of the TPC. The arrangements of grids in a gated TPC are shown in Fig.3.18(a). Since the gating grid is located inside the drift space of the chamber, a suitable common bias must be applied to all gating wires so as not to absorb any field lines coming from the central drift field, which would result in loss of primary charge. This bias is denoted V_G . To close the gating grid, opposing voltages $\pm \Delta V_G$ are provided symmetrically on neighbouring wires, such that none of the drift field lines can pass through the grid, as shown in Fig.3.18(a). The gating grid is to be operated with potentials:

$$\begin{aligned} V_+ &= V_G + \Delta V_G(t), \\ V_- &= V_G - \Delta V_G(t). \end{aligned}$$

according to Fig.3.18(b).

Good values for V_G , i.e. "gate open" voltage, were established using a small test chamber.

3.5.4 The field cage for the ALEPH TPC

The active volume of the ALEPH TPC consists of an outer cylinder of length 4.4 m and 3.6 m diameter and an inner cylinder of about 60 cm diameter. This volume is divided into two halves by a plane central partition which serves as the negative electrode. The working field is $\approx 200\text{V/cm}$ (corresponding to 45 kV over-all between the central plane and the end). This field is maintained by a system of electrodes on the cylindrical walls. Particles produced in e^+e^- interactions traverse the walls of the TPC, making it essential that the field cage should present as little matter as possible, compatible with safe working of the TPC. This is particularly true of the inner field cage.

The field cage of the TPC is constructed as shown in Fig.3.19. A layer of 75 μm thick kapton supports copper field-defining electrodes (35 μm thick for the outer field cage and 17 μm thick for the inner one). As can be seen, the electrodes are staggered; this is to prevent the high field in the insulator from penetrating into the volume of the TPC and thus causing distortions. In the manufacture of the copper-kapton-copper laminate the metallic foils are glued to the substrate using an epoxy adhesive. Etching the foils to remove unwanted copper does not attack the epoxy layer so that all the kapton is covered with a thin ($\approx 10 \mu\text{m}$) layer of epoxy. Since the epoxy has a resistivity which is several orders of magnitude less than the kapton, it might be thought to have the effect of screening the volume of the TPC from voltage variations on the back electrodes and, if the conductivity is sufficiently high, to help dissipate any charge which might accumulate on the inter-electrode gaps.

Tests done on the epoxy layer show that it is effective both in rapidly diffusing deposited charge and in screening against variations in the potential of the back electrode. One unexplained result of the above test is that the behaviour is different depending on whether the particles under consideration are electrons or ions. The tests show different decay times for electrons and ions, possibly due to the different nature of the charge carriers. For example the mobility of the hole in a material might be greater than that of the electrons.

3.5.5 Gas system

The gas used in the TPC should have the following properties:

- the drifting electrons should undergo small diffusion transverse to the magnetic field.
- the drift velocity should be high and
- the electron attachment probability should be small.

A mixture of argon and methane (80-20%) is used to fill the TPC ($\approx 42 \text{ m}^3$), since this mixture suits best these requirements. To get the best purification of the gas used with minimum impurities the following procedures are to be followed:

Flushing with argon, about five times the volume of the TPC, will reduce the amount of air to about 5×10^{-3} .

This will be followed by flushing the volume about five times with the proper mixture, leading to an oxygen content of $\approx 10 \text{ ppm}$.

For normal operation a flow recirculation with purification will maintain the level of purity needed. The recycling flow rate depends on the TPC construction, i.e. leak and outgassing rates. A level of O_2 contamination of $\leq 10 \text{ ppm}$ could be achieved by OXISORB purifiers. A small fraction of the gas flow will be vented and replaced by fresh gas to compensate for the removed quenching agent and for N_2 contamination.

The operating pressure has to be 3-5 mb above atmospheric pressure, in order to accomodate pressure transients caused by the zone ventilation. Special arrangements have been made to keep the pressure at the above level.

The gas mixture, pressure, purity, and temperature will be monitored and fully or partially servo-controlled. This will be done by measurements at $\approx 1/2$ hour intervals of the drift velocity, the resolution, and the signal attenuation by attachment.

3.5.6 Performance

In the following paragraphs some aspects of the TPC performance are discussed.

r ϕ Spatial Resolution

The r ϕ -spatial resolution is governed by the following factors:

- electronic noise
- diffusion of the electron swarm drifting towards the anode
- spread of the ionization collection along the wire due to E_BB effect and to the crossing angle of the track with respect to the anode wire and
- fluctuation in the size of the avalanche on each wire contributing to the pad signal.

Momentum Resolution

The momentum resolution $\Delta p_T/p^2 T$ can be calculated using the Gluckstern formula

assuming 21 equally spaced measurements inside the TPC. The expected momentum resolution as a function of the azimuthal angle without angular correction and assuming a blind region of ± 2.5 cm near the boundary of the sector is shown in Fig.3.20(a). The momentum resolution after corrections is shown in Fig.3.20(b). From both figures it appears that the dependence of the resolution on the azimuthal angle is very small. A mean value for the momentum resolution is

$$\Delta p_T/p^2 T \approx 1 \times 10^{-3} (\text{GeV}/c)^{-1}$$

This corresponds to a statistical error on the sagitta measurement of about 150 μm . It is very hard to estimate the systematic error on this measurement. The laser calibration system allows correction for the field distortion, and the systematic error is the uncertainty on this correction. Since the correction is at the most 1 mm, one can assume a systematic error of 100 μm . If a systematic error of 100 μm is added in quadrature to the above, a value of $\Delta p_T/p^2 T \approx 1.2 \times 10^{-3} (\text{GeV}/c)^{-1}$ for the momentum resolution is reached.

z and polar angle resolution

The z resolution is limited by the longitudinal diffusion and the error on the drift time due to the readout system. The longitudinal diffusion is not reduced by the magnetic field and the precision attainable on the measurement of the centroid of the electron cloud is $\sigma = 720 \mu\text{m}$ for 1 m drift length.

The PEP-4 Group at the SPEAR accelerator quotes an average z resolution of 857 μm at 1.5 atm. Their estimated average contribution of the diffusion is $\approx 300 \mu\text{m}$. It follows that in their case the readout system error is $\approx 800 \mu\text{m}$. In the case of the ALEPH TPC, if the readout system has the same performance as that of the PEP-4 group, a value of 1.1 mm will be obtained for the z resolution. Assuming an average of 300 z measurements a polar angle resolution of 0.1 mrad is obtained.

Two-track separation capability

The two space points of different tracks cannot be separated if, at the same radius, their $r\phi$ distance is less than $\Delta r\phi$ and their z distance is less than Δz . The definition of double track capability depends on the definition of Δz and $\Delta r\phi$.

a) $r\phi$ separation

The pad response function in the TPC geometry has a width of about 3.2 mm and the actual pad width is 6 mm. In this case, the induced signal is always limited to two or three pads. An optimistic value for $r\phi$ separation is two pad widths, (12 mm); a

pessimistic one is three pad widths (18 mm).

b) z separation

The physical limit on the z separation capability is the longitudinal diffusion, but this limit is never reached because of the stretching in time of the signals due to the integration time of the shaping amplifier. This long integration time is needed in order to have a good signal-to-noise ratio in the pulse height measurement, important for both dE/dx and $r\phi$ resolutions. The pulse width of the shaping amplifier is about 400 ns, and with this value a Δz between 20 mm and 30 mm is expected.

c) Two-track separation

Since the quantities $\Delta r\phi$ and Δz are independent of radius, the two-track separation capability increases with the radius owing to the increasing mean distance between the tracks. The two-track separation has been studied with a Monte Carlo simulation of jet events at 80 GeV centre-of-mass energies. The percentage of unambiguous points as a function of the radius for both optimistic and pessimistic figures for $\Delta r\phi$ and Δz are shown in Fig.3.21.

Particle identification

A sum of ≈ 300 samples of primary ionization, each of projective 4 mm, corresponding to the wire spacing, can be achieved through the measurement of pulse height on the TPC proportional wires from all sectors traversed by a charged particle. With a gas mixture of 90% argon + 10% methane at 1 atm., such a measurement is expected to achieve particle separations for $e-\pi$ and $\pi-K$ in units of ionization resolution (R) which are shown by the dashed curves in Fig.3.22 plotted as a function of momentum (p). Here it is assumed that R varies with the number (n) of the ionization samplings as $n^{0.43}$, and that the relativistic rise can be obtained from a parametrization which includes a dependence on the sampling length.

However, it has been argued that there may be saturation of R such that no improvement comes from increasing n , and also some experimental results show that the relativistic rise appears to be independent of the sampling length. In this case, the particle separation would be degraded as shown in Fig.3.22, so that dE/dx measurements would only be useful at the level of ≥ 1 st. dev. for $e-\pi$ below 10 GeV/c. These estimates take no account of the systematic errors in wire pulse-height calibration, or of angular effect. For the dE/dx to be more useful, a great deal of attention has to be paid to monitoring and correcting for fluctuations in temperature, pressure, and gas composition.

3.6 The Electromagnetic Calorimeter (ECAL)

Details of this component are discussed in detail in Chapters 4 and 5.

3.7 Hadron Calorimeter (HCAL)

The hadron calorimeter is used to measure the flux of hadronic energy. It consists of consecutive layers of iron and streamer tubes. The iron structure of the Hadron Calorimeter constitutes the main support of ALEPH and the return yoke for the magnetic field. The iron yoke consists of two parts, the central (barrel) part which is constructed from 24 modules and the two end parts, (end-caps), each constructed from 6 modules. Each of these three parts can be moved individually along the experiment axis. The purpose of the yoke is to shape the longitudinal field, which must be uniform at least in the central region occupied by the TPC. It also accomplishes the function of hadron calorimeter and muon filter. For this the yoke is segmented into 23 slabs of 5 cm thickness except for the outside slab, which is 10 cm thick for mechanical reasons. Being the heaviest and strongest part of the apparatus, it is used as a support for all other elements of the ALEPH detector. The total thickness of the iron used in both the barrel and the end-caps is 120 cm ($6.1 \lambda_{\text{abs}}$).

The rolled steel plates are interleaved with gaps of 2.2 cm which accommodate the active part of the detector, consisting of planes of streamer tubes with an outer cross-section of $\phi_{\text{tube}} = 1 \times 1 \text{ cm}^2$, and an active cross-section of $0.9 \times 0.9 \text{ cm}^2$. A $100 \mu\text{m}$ wire runs at 4 mm from the lower wall and is kept in place every half metre by plastic supports. The gas used is one part of argon, two parts of CO_2 , and one part of n-pentane. The inner walls of the tube have a graphite coating characterized by a resistivity in the range $0.1 \text{ m}\Omega$ to $1 \text{ M}\Omega$ per square. Each tube layer is equipped with pad readout on one side for integrated energy flux measurements, and with strips parallel to each tube on the other side, for digital reconstruction of the pattern of individual events. Each strip is 0.4 cm wide, with a pitch of 1 cm. This digital information, which is read also on two double layers positioned outside the magnet, is the basic tool for muon identification. Pads and strips are made from a PVC support, 1 mm thick, covered by aluminium foils $40 \mu\text{m}$ thick. The structure of the active layer is demonstrated in Fig.3.23(a).

The streamer tubes are differently arranged in the barrel and the endcaps due to the geometrical shape of the iron. The 7m long tubes are grouped in 24 modules of 23 layers in the barrel. The first layer of each module contains 71 tubes and the last one 110 tubes. For mechanical reasons and for simplicity of gas flow, several tubes are grouped into larger boxes. The mixing of boxes with 7 tubes and with 8 tubes allows the intermediate layers to be filled completely, with an accuracy always better than 1 cm, as shown in Fig.3.23(b). Each

module contains 2324 tubes for a total of 55776 tubes in the barrel.

In the end-caps, tubes of decreasing length are arranged into sextants of the iron structure, as shown in Fig.3.23(c). The 2 cm spacers which couple successive iron sheets every 92 cm define the lateral dimension of the boxes. A total of 82200 tubes, ranging from 0.5 m to 3.85 m in length, constitute the active volume of the end-caps. Due to the geometry of the magnet, tubes can not be installed in several regions, leading to dead regions. In the barrel, 8% of the average surface is lost because of bars connecting successive iron layers and notches for cables and pipes. Moreover, at the ends of the tubes, 2.5% of the surface is insensitive (6 cm on each side), to which the insensitive ends of the tubes (3 cm) add another 1.5%. The location of the dead regions is shown in Fig.3.23(d,e).

The pulse height is read from pads of consecutive layers which are connected in a projective geometry pointing to the vertex. The barrel module is subdivided into 144 towers. A single tower covers the angular range $\Delta\phi = 3.75^\circ$ and $\Delta\theta \approx 2.7^\circ$, as shown in Fig.3.24(a). A total of 2688 towers are fully contained in the barrel itself ($\theta > 50^\circ$), while 384 towers on each side of the barrel module continue smoothly into similar towers, with crossed geometry, in the external part of the end-caps ($40^\circ < \theta < 50^\circ$). These also define, therefore, the tower dimensions in the end-caps, except for the innermost four rings, where the angular granularity becomes larger to avoid towers of too small dimensions ($\Delta\phi = 7.5^\circ$ for $18^\circ < \theta < 34^\circ$, and $\Delta\phi = 15^\circ$ for $6^\circ < \theta < 18^\circ$). A description of the pad arrangement in the end-caps is shown in Fig.3.24(b). Pads which are interrupted by the reinforcement spacers are reconstructed at the electronic level, by summing the signals of the two parts. A total of 1320 are fully contained in the end-caps, in addition to the 768 towers shared with the barrel.

3.8 The Muon Detector

The digital information on individual strips in the HCAL is already an essential part of the muon detector. In addition to it, external to the magnet, both the barrel and the end-caps, two double layers (50 cm apart) of streamer tubes are installed to identify tracks crossing the full thickness of iron and to measure their angle. The readout strips are arranged in two projections each with an effective pitch of 5 mm, as shown in Fig.3.25(a). In the barrel the projections are orthogonal; in the end-caps the strips cross at 60° . The muon layer around the barrel is structured in 12 parts, corresponding to the decagonal shape of the magnets. Two out of the twelve modules are specially segmented to allow the passage of the magnet legs, causing 3.5% dead space in the coverage of both muon layers. In addition, the bottom module of the second layer has reduced length to avoid interference with chariots and rails. In the end-caps the muon chambers are structured in quadrants, instead of sextants as in the HCAL. In this way the number of tubes is reduced, together with the dead zones at the tube ends.

Moreover, whilst the two upper quadrants are shaped as 90° circular sectors, the lower two have rectangular shape, running down to the floor. This allows the reduction of the dead space caused in the coverage by the end-cap legs in the so called "middle-angle-muon detector" around $\theta = 45^\circ$. Since layers backing the barrel and the end-caps reproduce the structure of the hadron calorimeter, additional tubes are needed to cover the gaps left open in the boundary region. This solution has been chosen, in contrast to lengthening the barrel tubes, to leave the space facing the barrel notches free for all outgoing cables. (See Fig.3.25(b)). The total fraction of solid angle not covered by at least one double layer of muon chambers is approximately 5%.

3.9 The Trigger

The trigger is used to reduce the rate of background events to a level acceptable for the TPC, (a few hundred Hertz), while accepting all good events under the Z^0 peak. Assuming the design luminosity, this rate is of the order of 1 Hz. The first trigger signal should come within $\approx 1.5 \mu\text{s}$, and open the gate of the TPC. Subsequent trigger signals will then reduce the rate to a level tolerable for tape writing. The detectors start their digitization upon arrival of a bunch crossing signal. The readout is then inhibited if the trigger condition fails. A high level of flexibility has to be built into the triggers since the nature of backgrounds and their rates are not well known. The main sources of background events which should be rejected by the trigger are beam-wall interactions of off-momentum particles and beam-gas interactions. The end-cap calorimeters and the inner chambers are likely to be most affected by this background. Synchrotron radiation, on the other hand, will probably not be seen by calorimeters but will produce hits in the chambers.

The trigger system is organized in three levels:

Level 1 trigger

The detector elements used in the Level 1 trigger are the Inner Tracking Chamber, Hadron Calorimeter, Electromagnetic Calorimeter, Muon Chamber and the Luminosity Calorimeter. This trigger should be sensitive to tracks and/ or energy deposits, and is inspired by the experience of PETRA and PEP experiments. It will be fast, to achieve a total rate from beam crossing up to the input of the TPC gating system of the order of one hundred Hz. The trigger serves to open the TPC gate and to initialize the level 2 trigger. It will not introduce any dead-time, since beam crossings occur only every 23 microseconds.

Level 2 trigger

This is based mainly on the TPC information, and decides whether to continue processing the data or to clear the data acquisition system in case of failure.

Level 3 trigger

To reduce the level 2 trigger rate to a rate acceptable for tape writing, (1-2 Hz), a post-read-out selection process will be used, based on sophisticated event builders acting on the whole data.

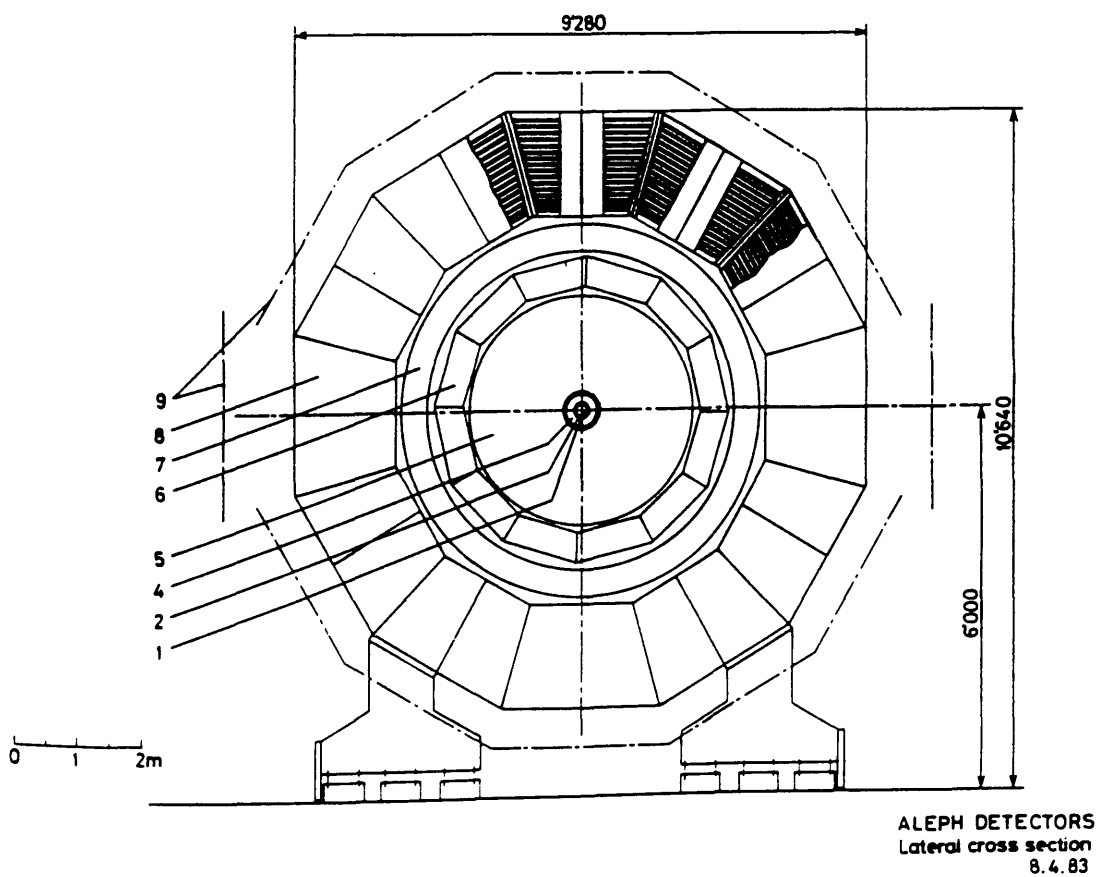
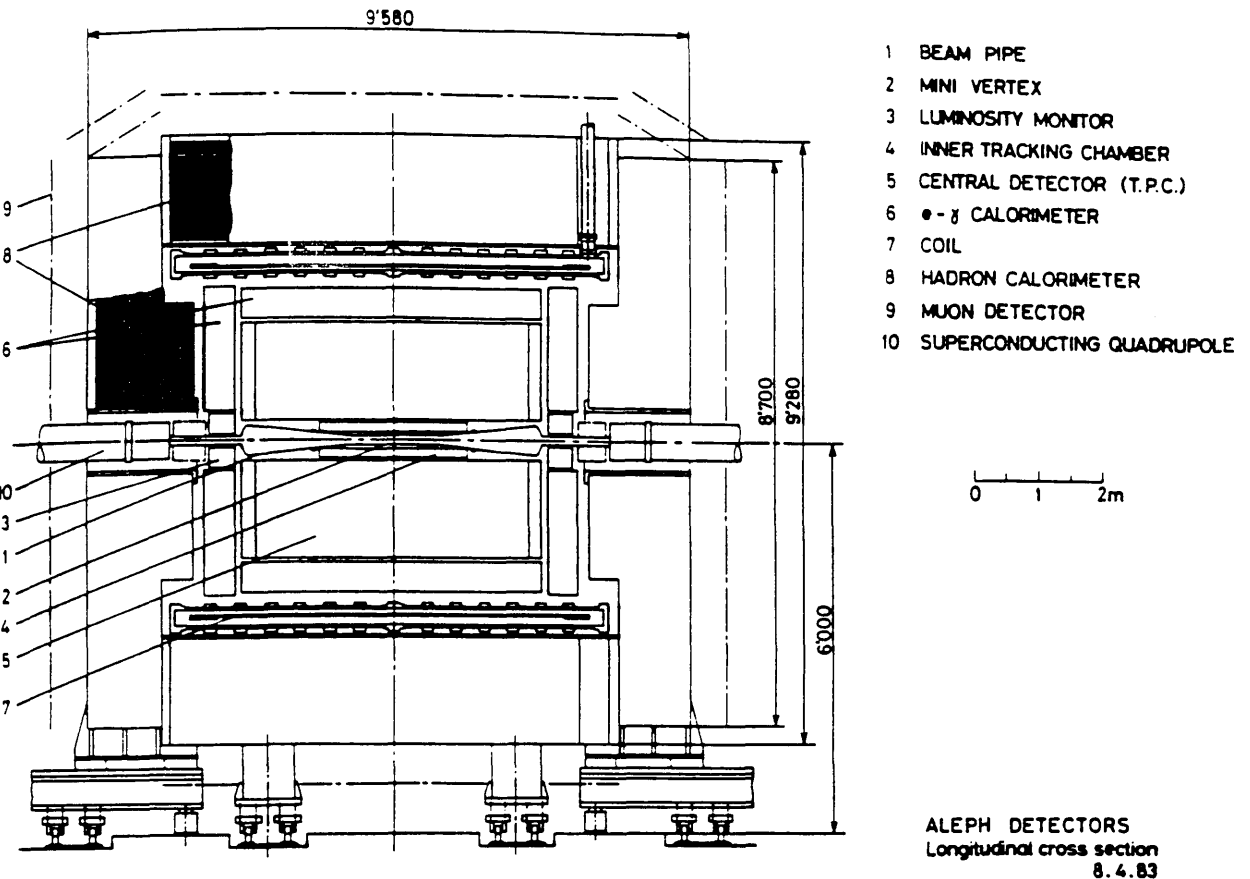


Fig.3.1

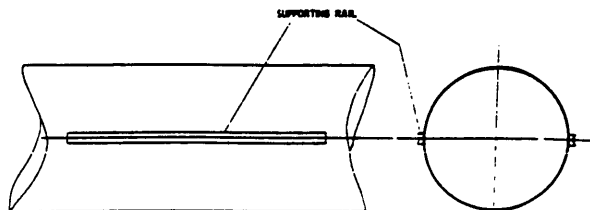
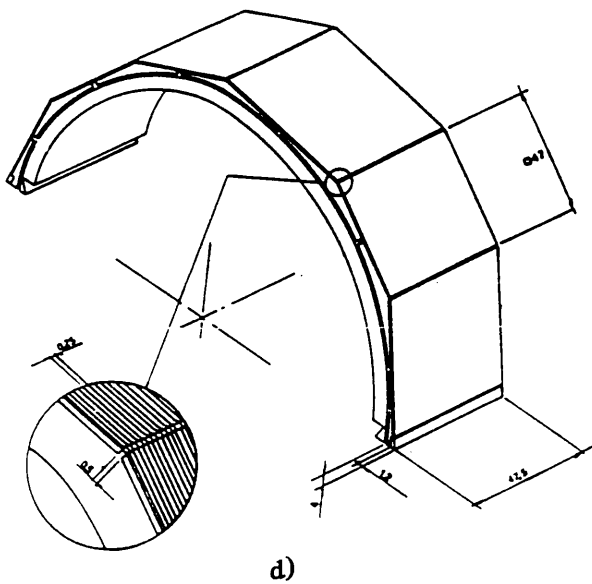
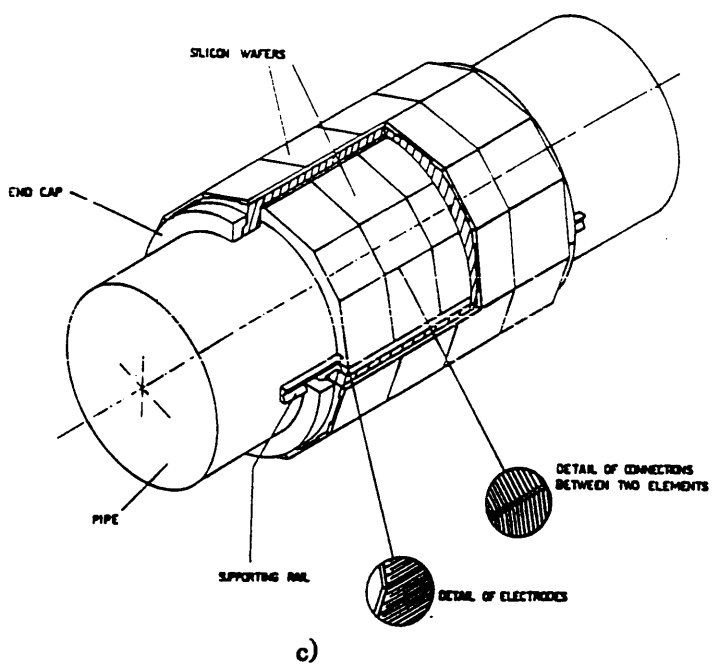
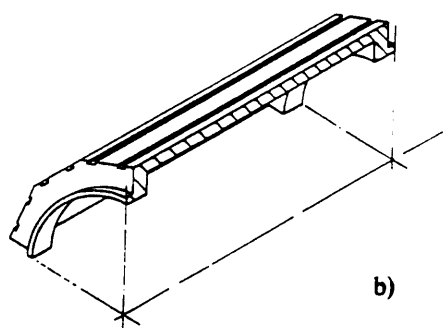
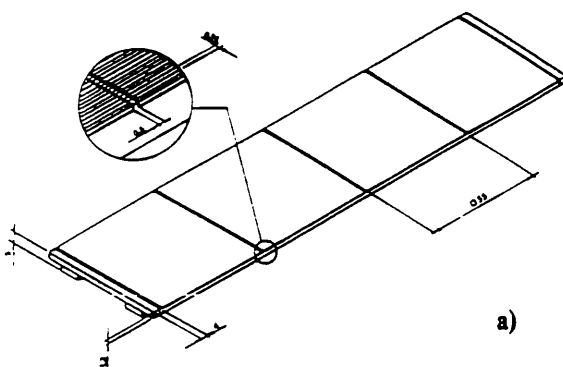


Fig.3.2

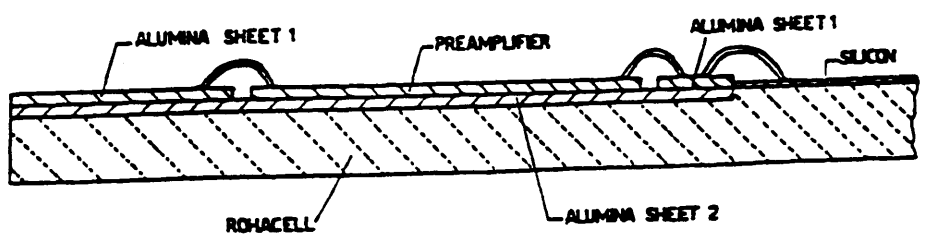
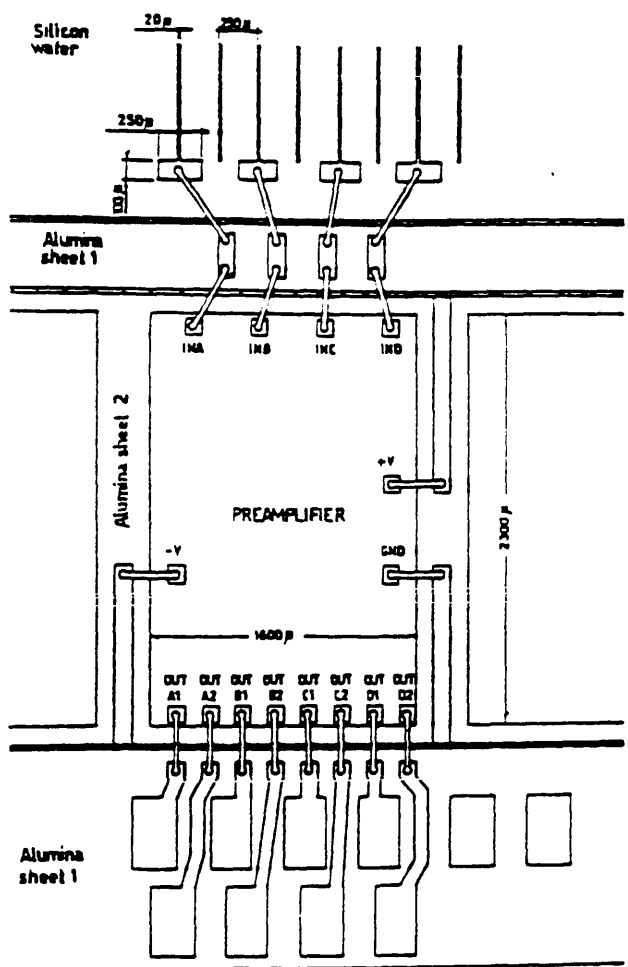


Fig.3.3

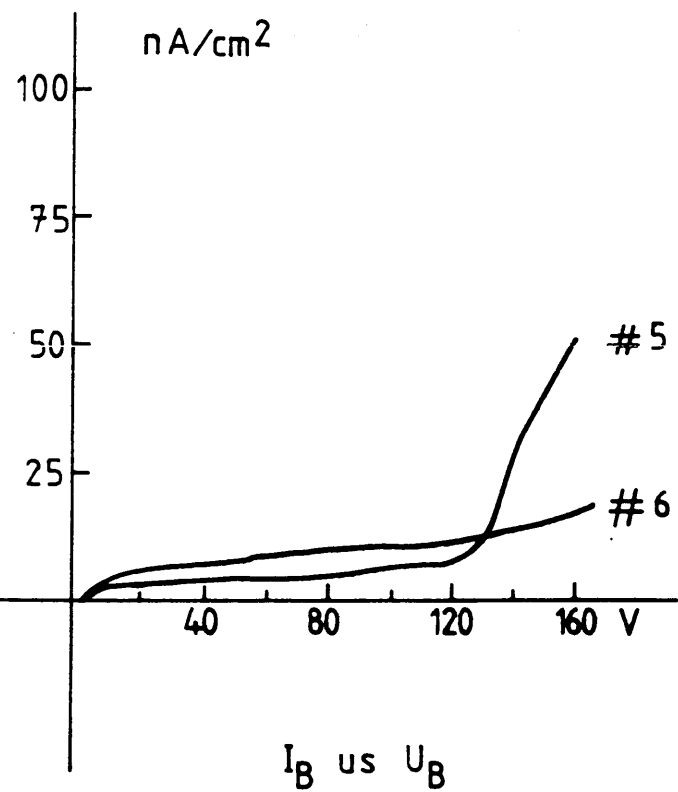


Fig.3.4(a)

CAPACITANCE / U_B

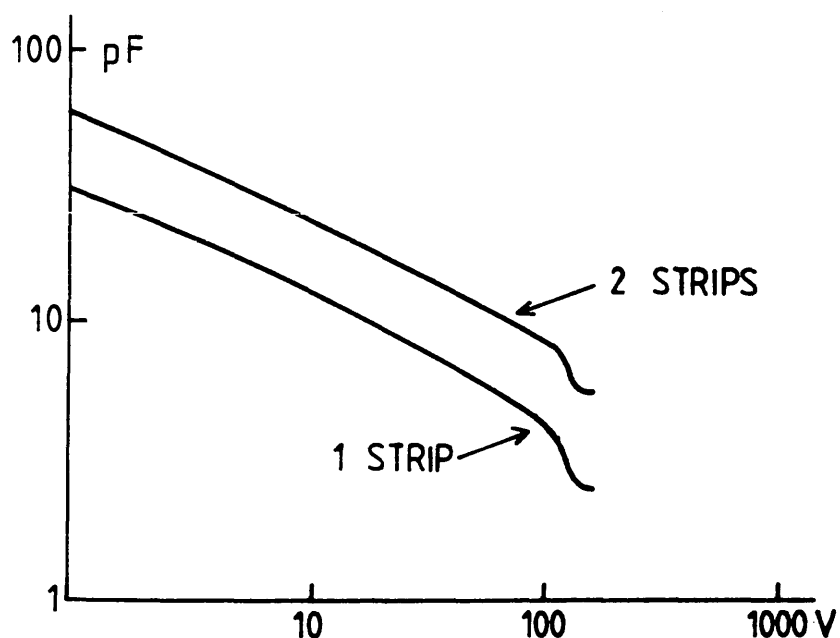
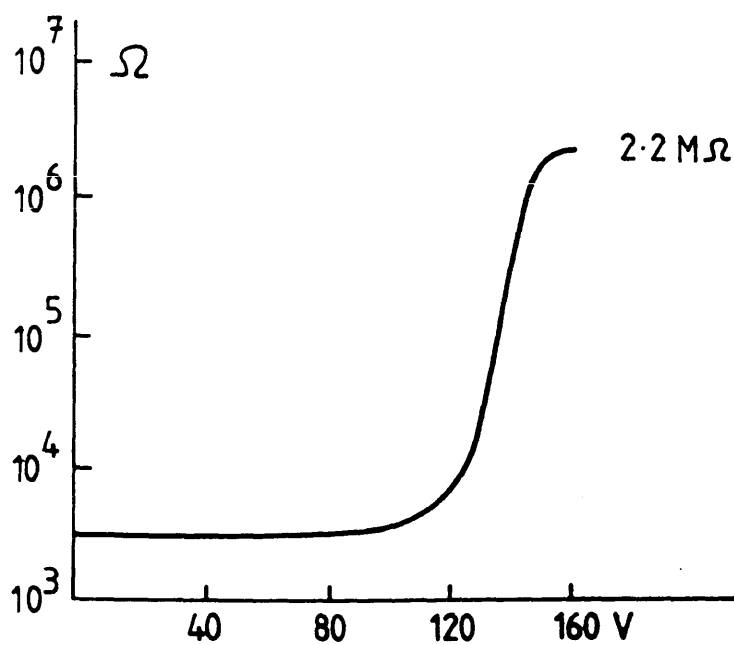


Fig.3.4 (b)

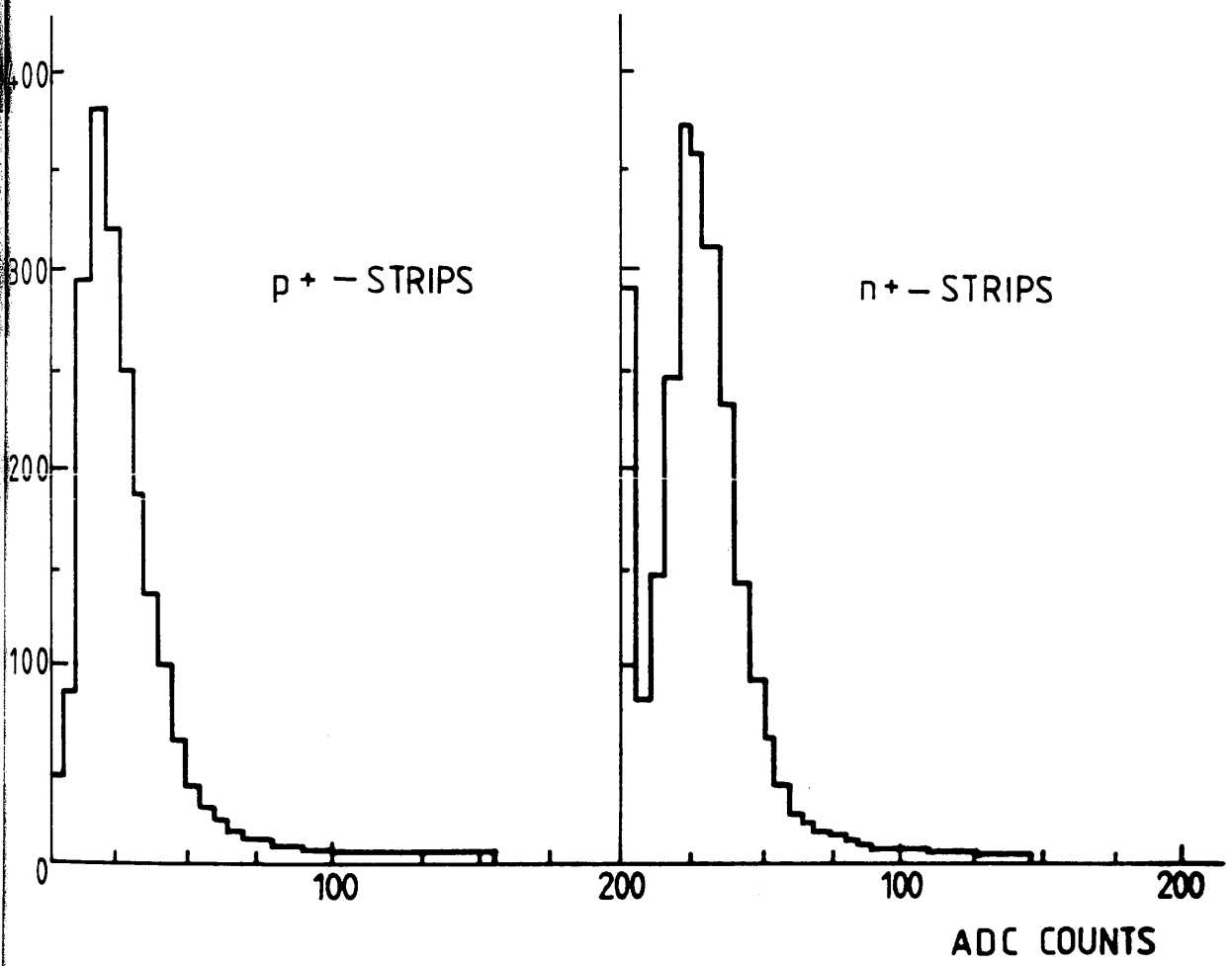
INTERSTRIP RESISTANCE / U_B



FULLY DEPLETED AT ~ 150 V

Fig.3.4(c)

TEST WITH β -SOURCE (Ru 106)



COLLECTED CHARGE

DETECTOR $10 \times 10 \mu\mu^2$

Fig.3.5

Detector Unit (face)

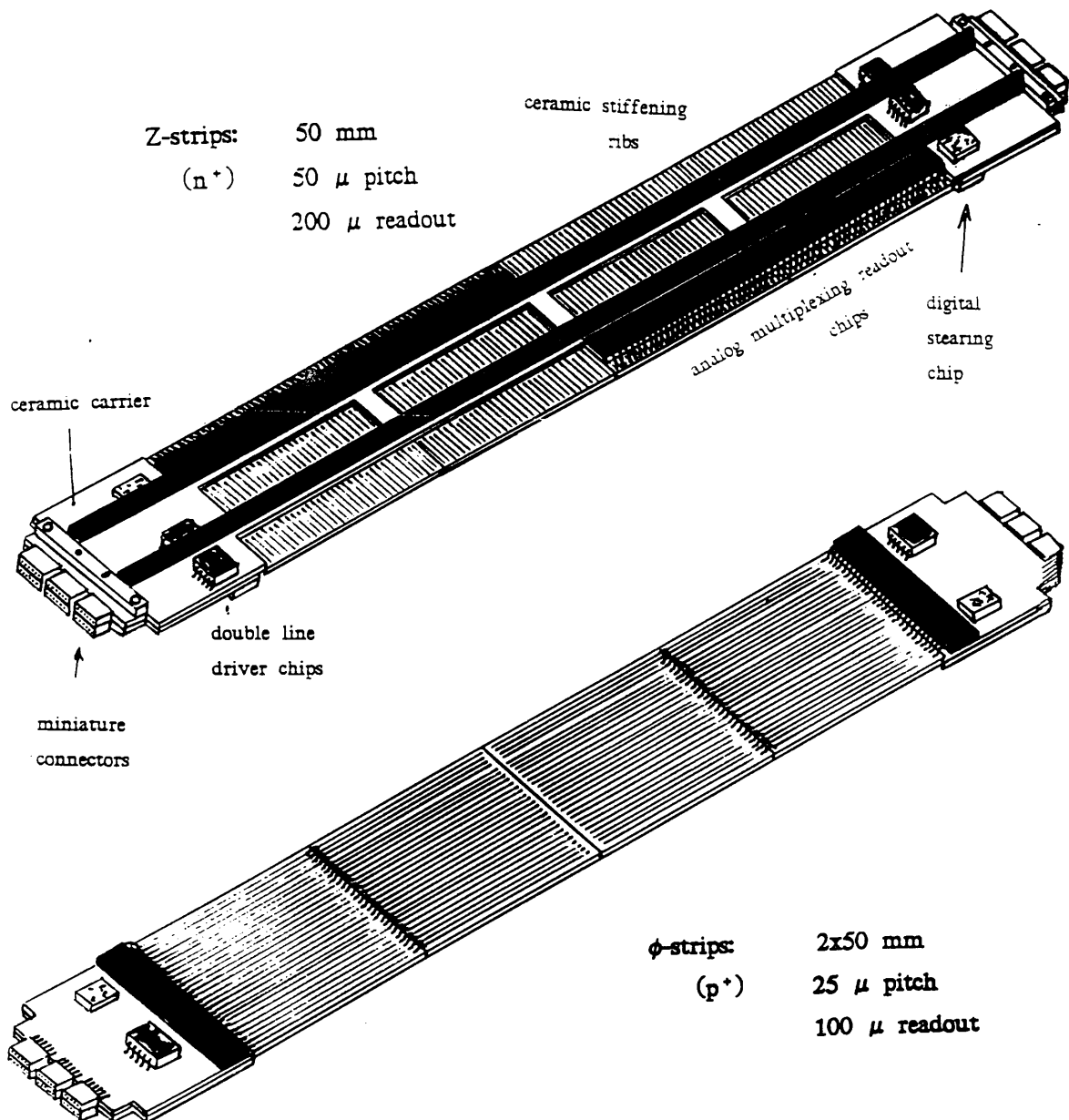


Fig.3.6

READ OUT ELECTRONICS

LOCAL: CHIP ON BOARD

REMOTE: FASTBUS & CAMAR

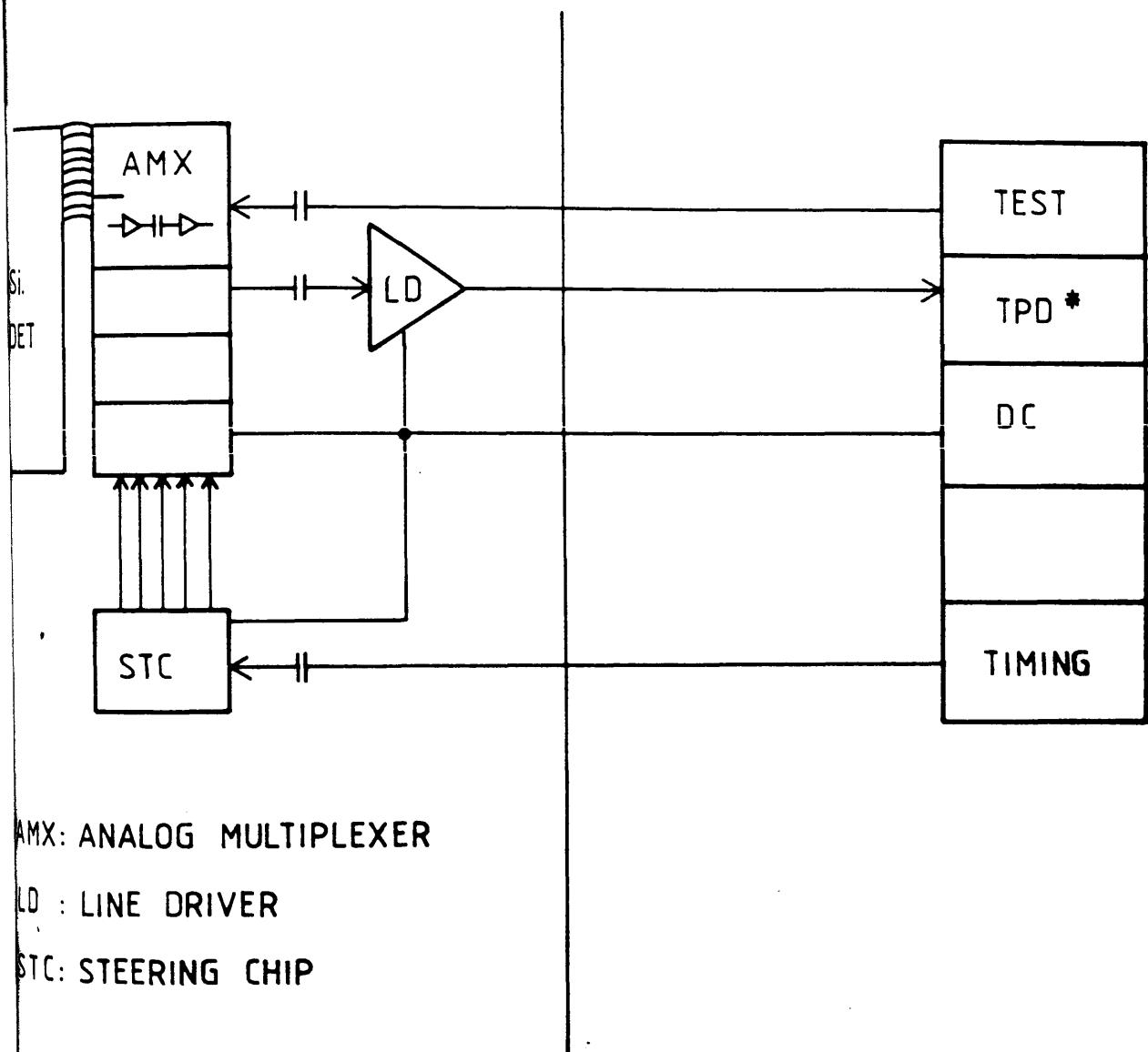


Fig.3.7

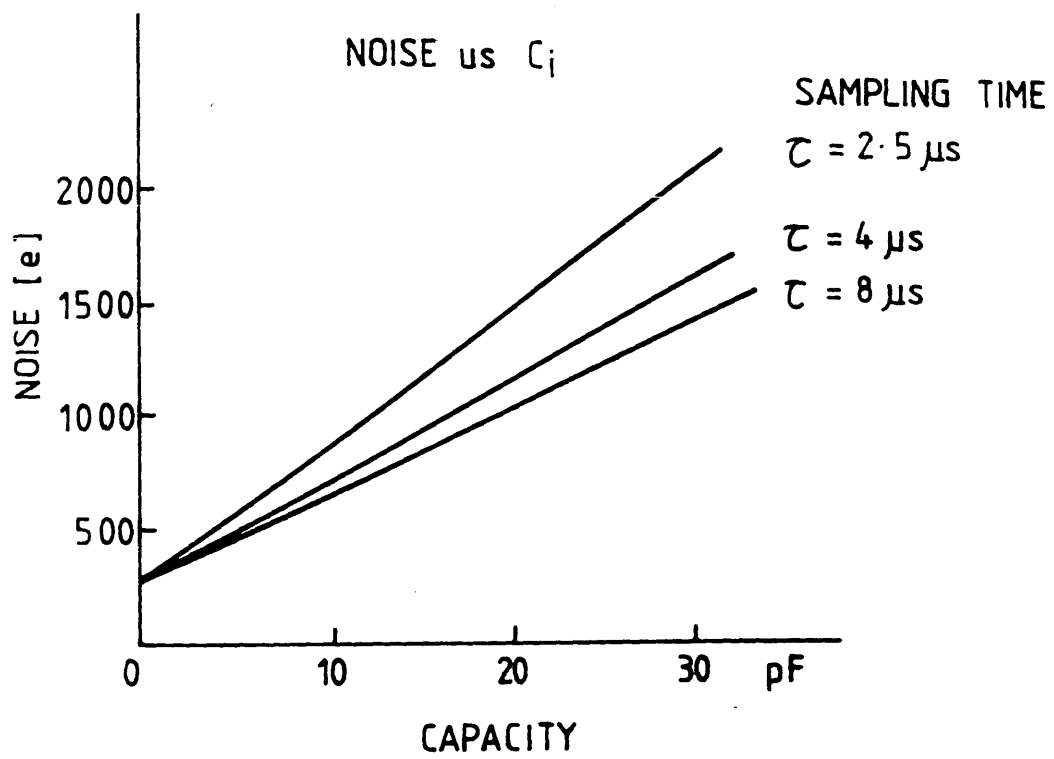


Fig.3.8

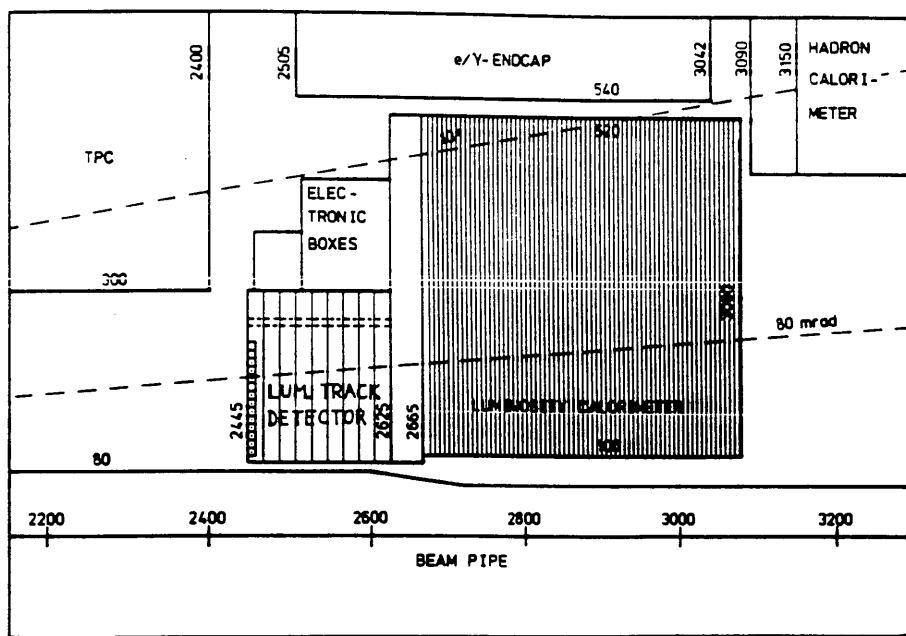
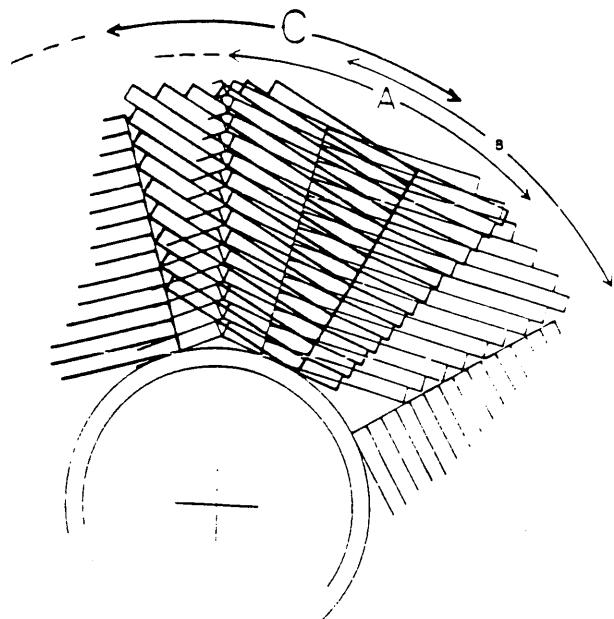
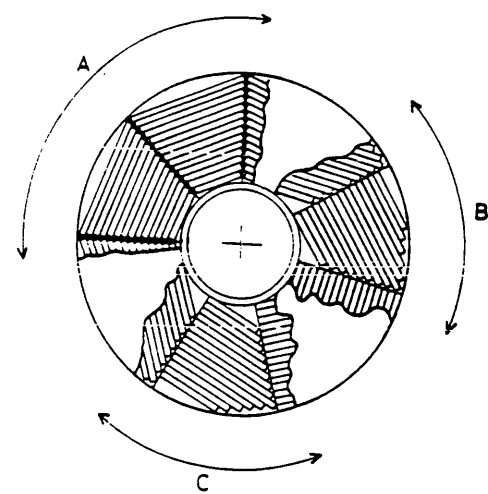


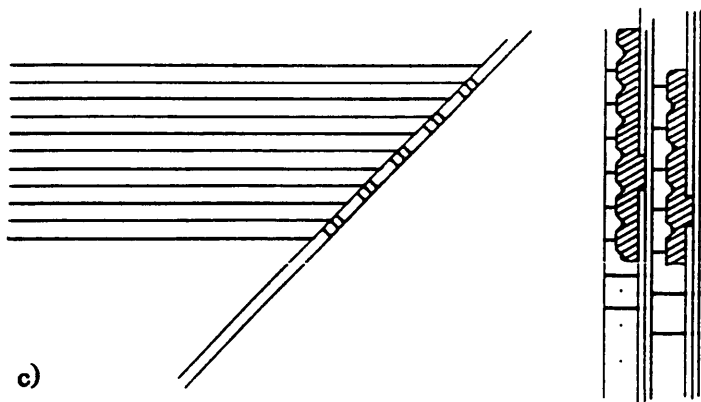
Fig.3.9



a)



b)



c)

Fig.3.10

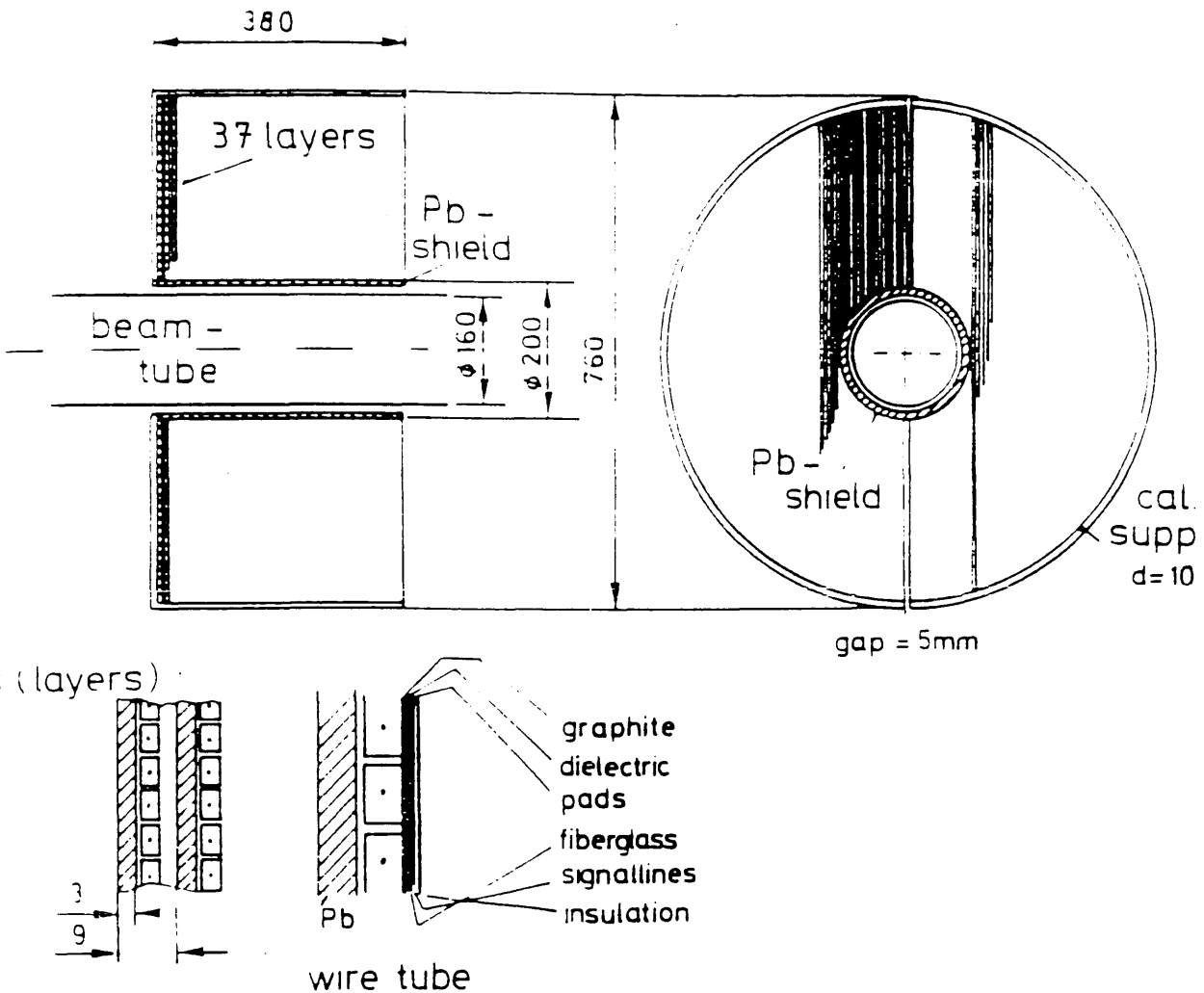


Fig.3.11

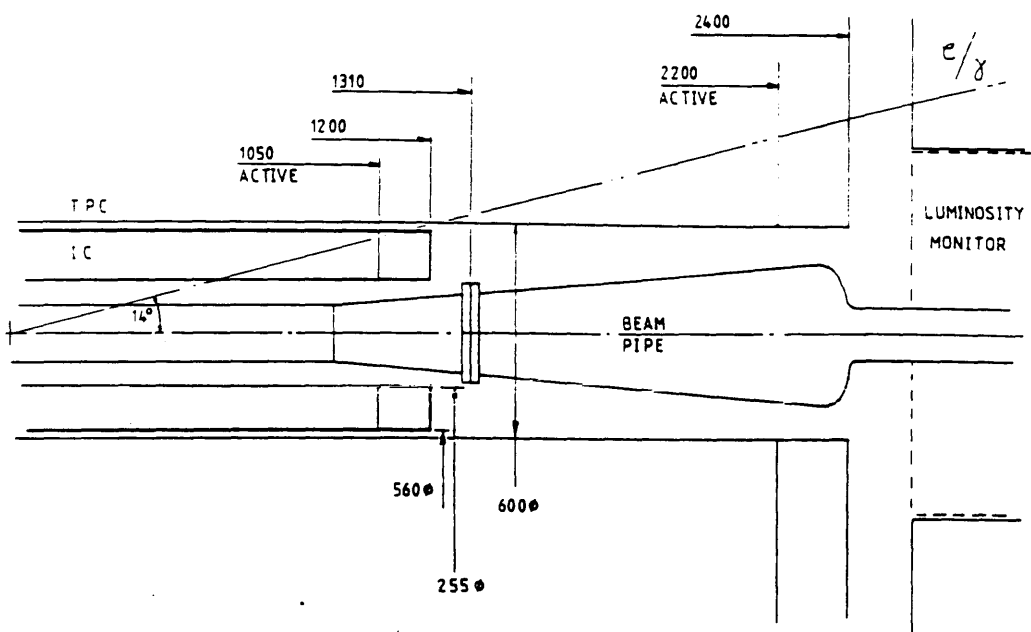


Fig.3.12

R- ϕ RESIDUAL, LAYER 1

R- ϕ RESIDUALS

$$\sigma = 120 \pm 2 \text{ } \mu\text{m}$$

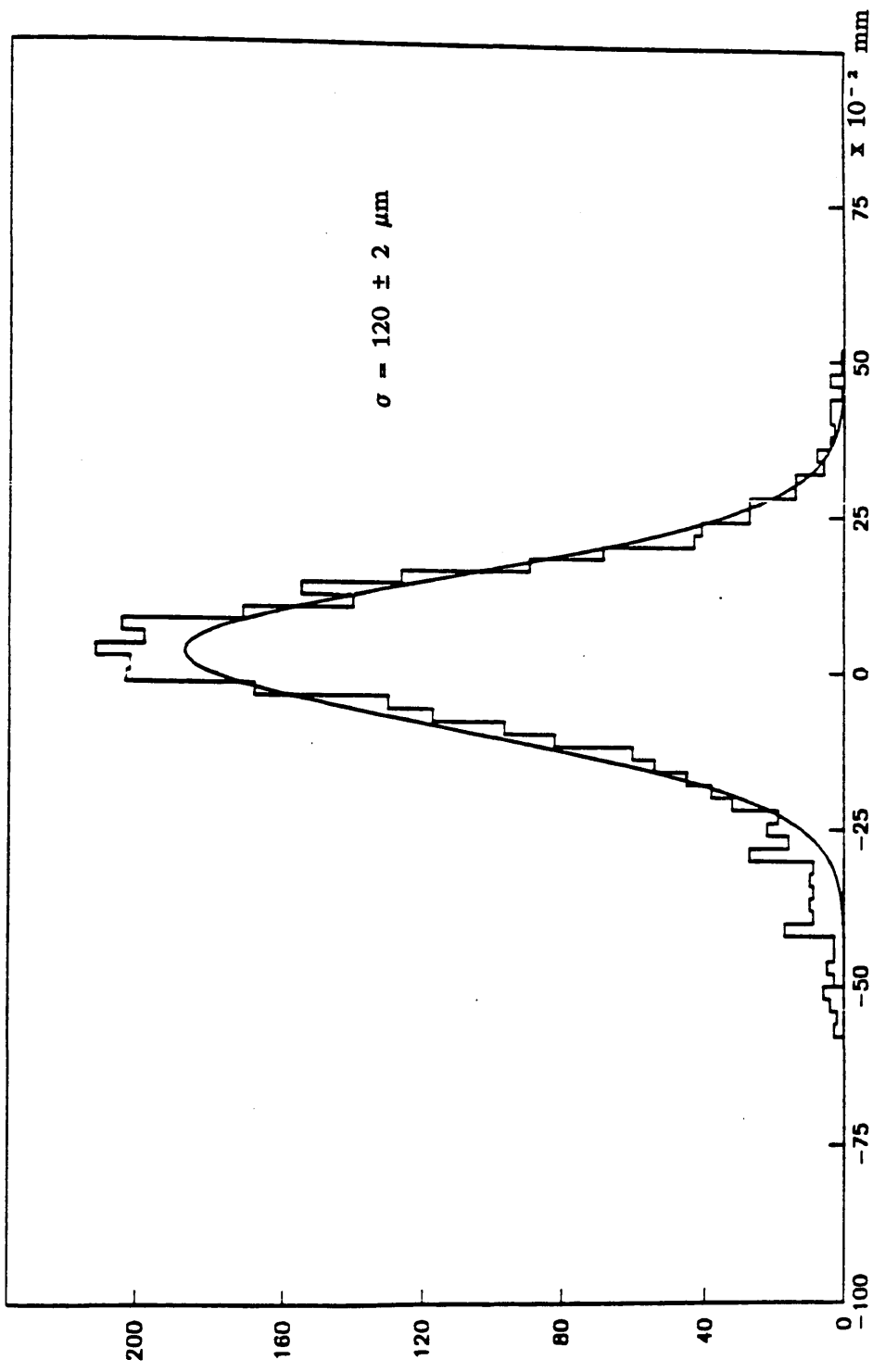


Fig.3.13 (a)

R- ϕ RESIDUALS

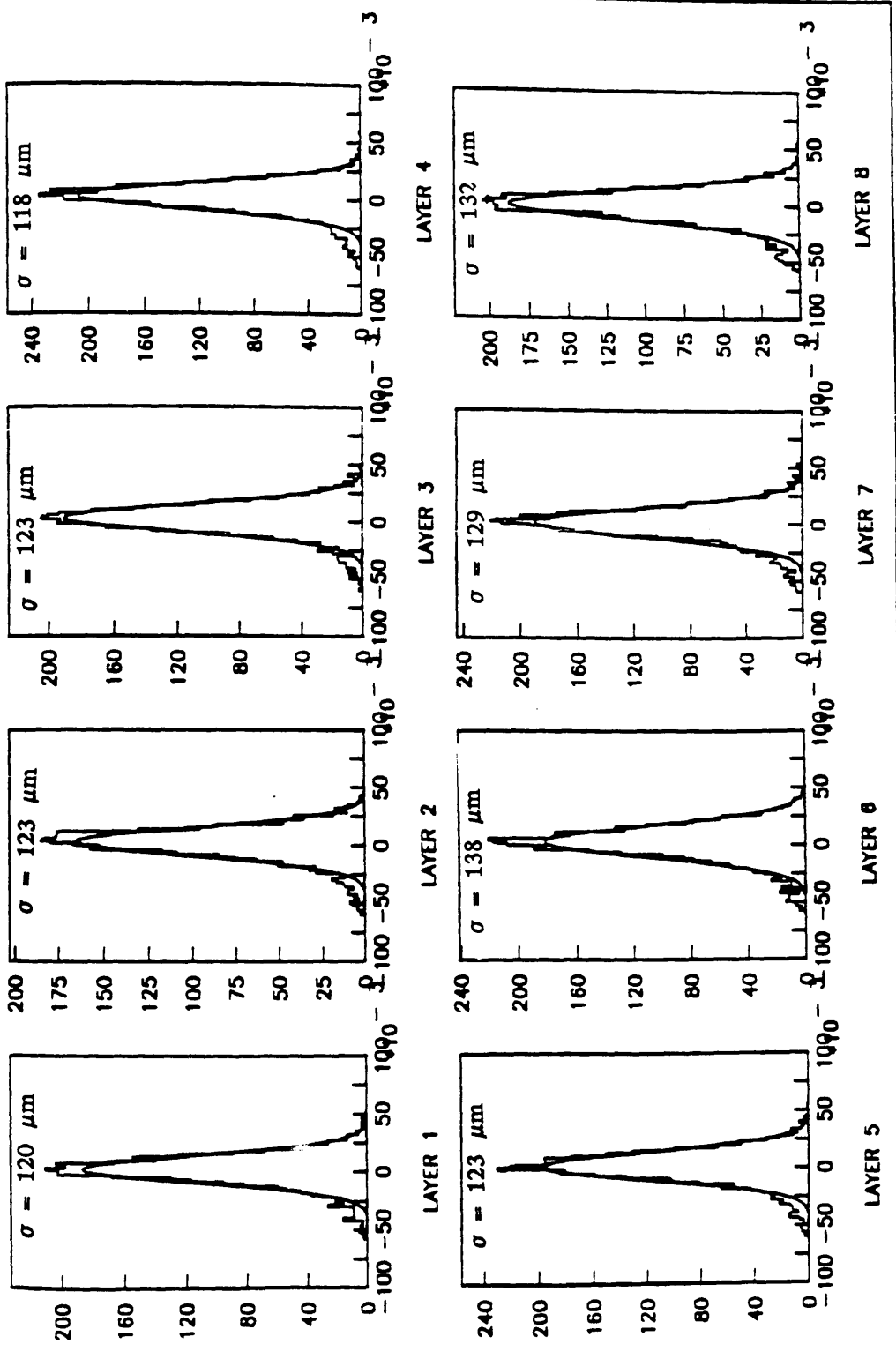


Fig.3.13 (b)

Orientation of wires

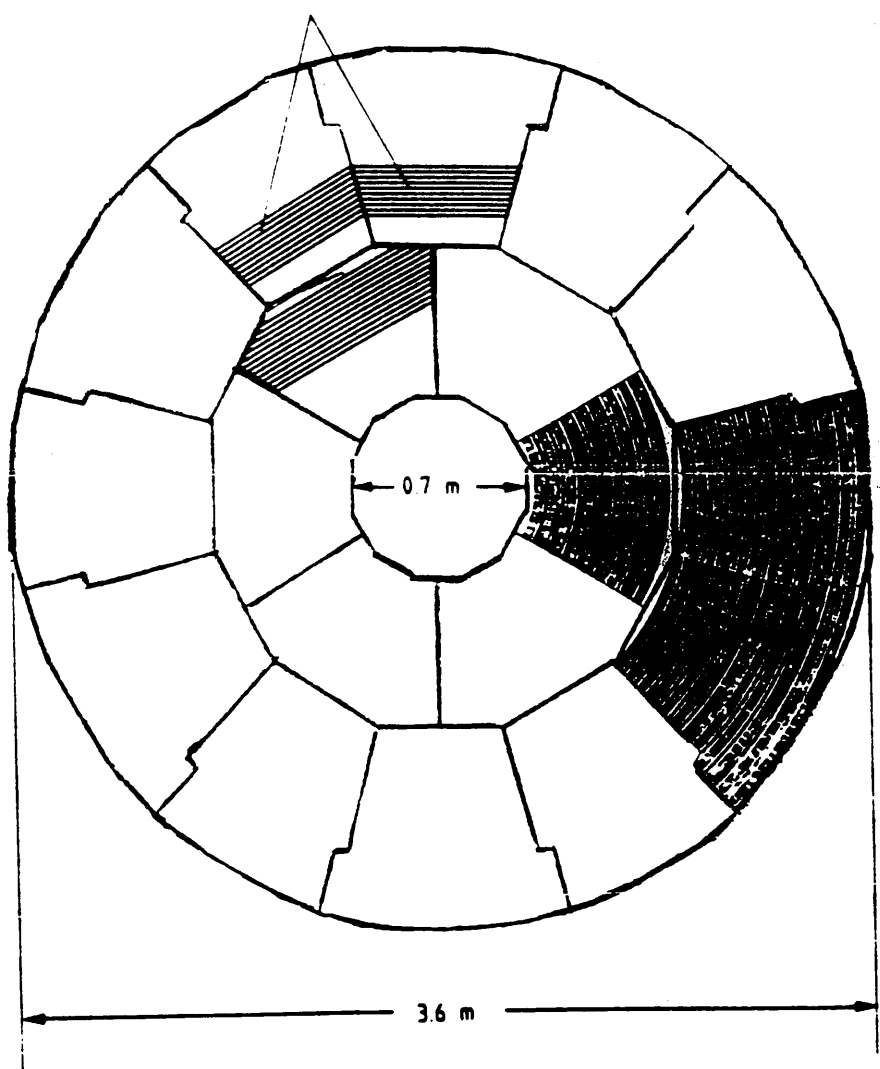


Fig.3.14

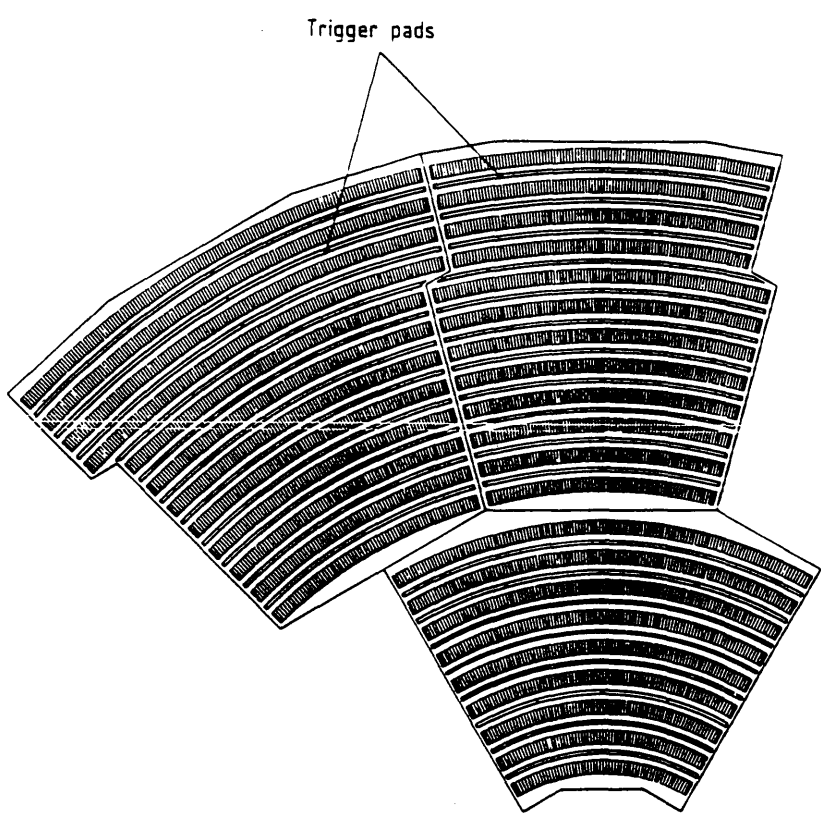


Fig.3.15

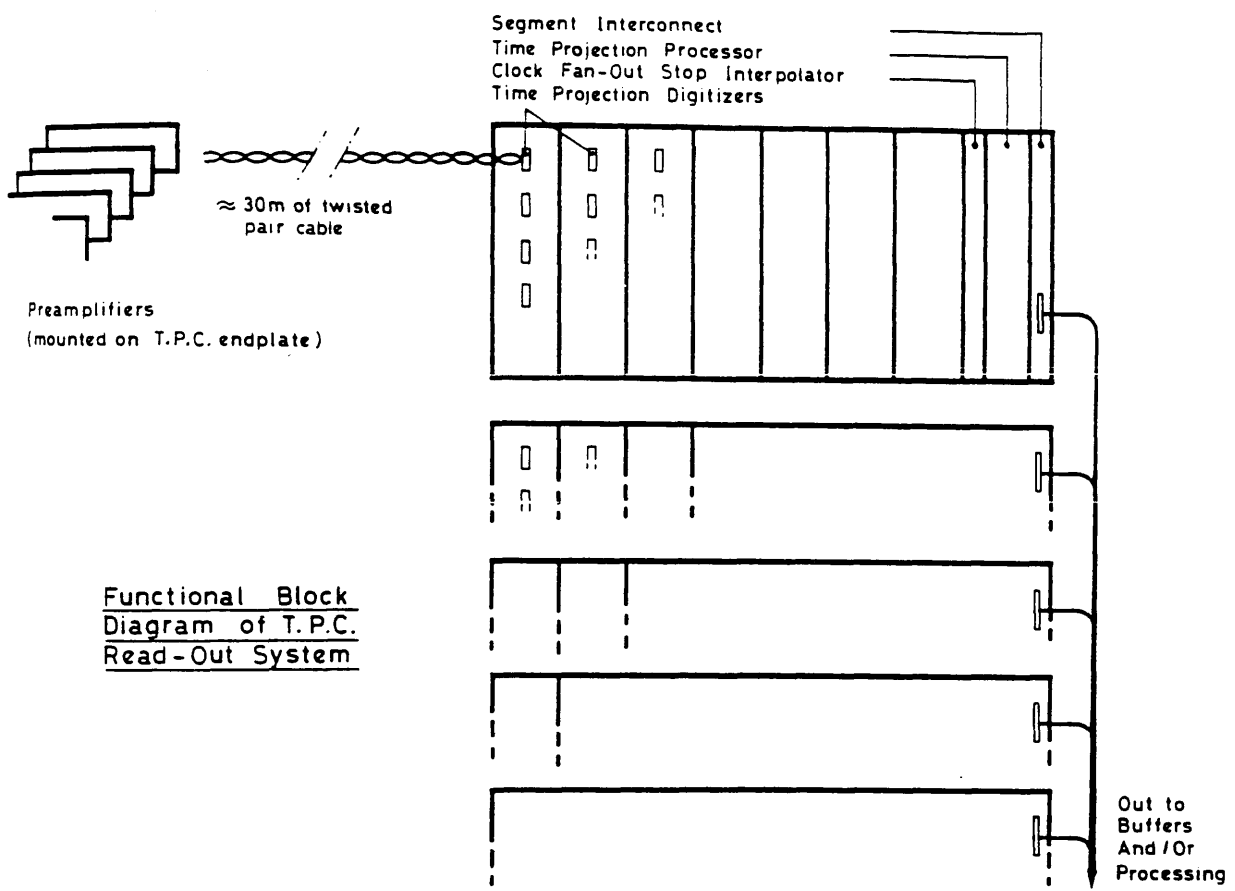


Fig.4.16

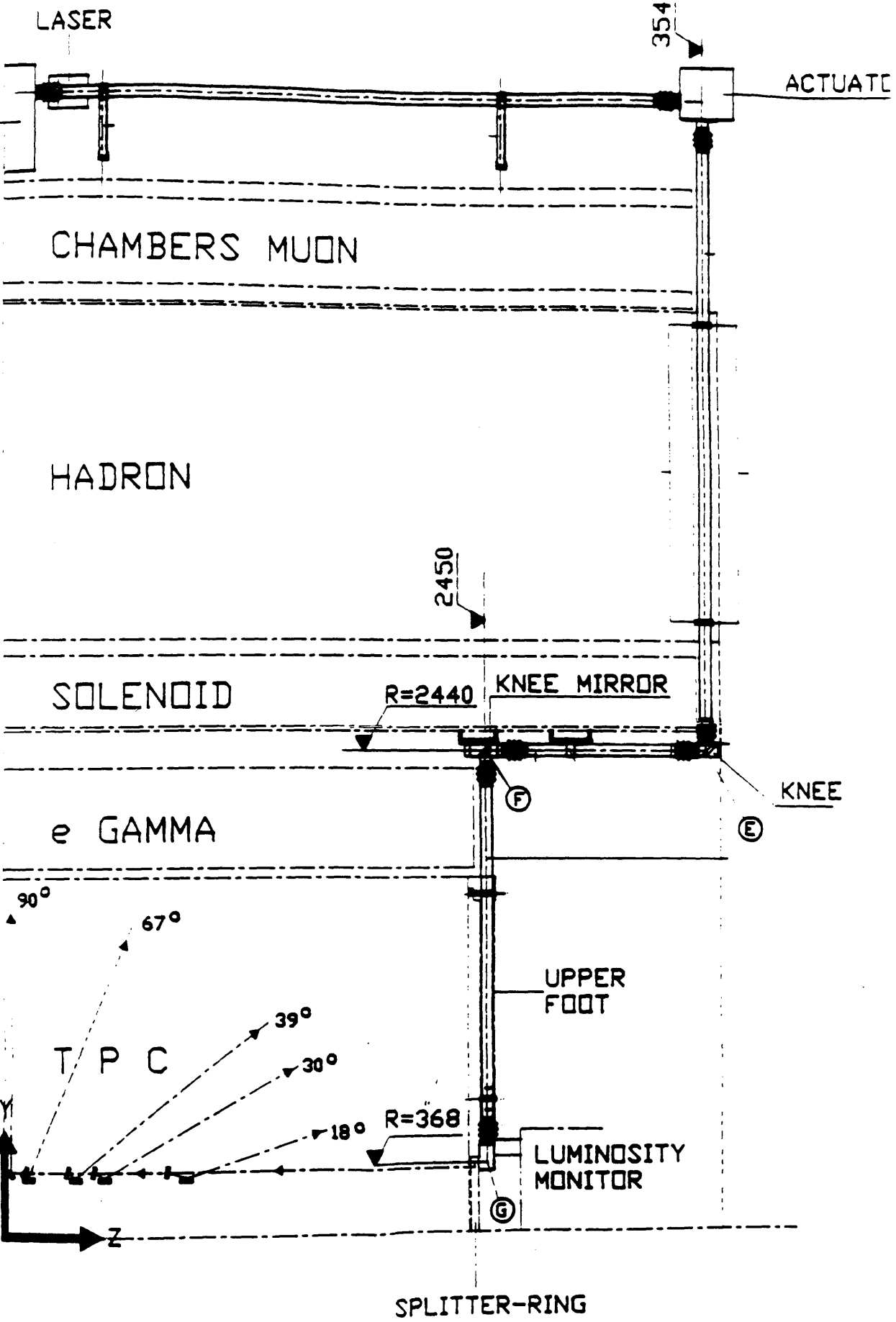
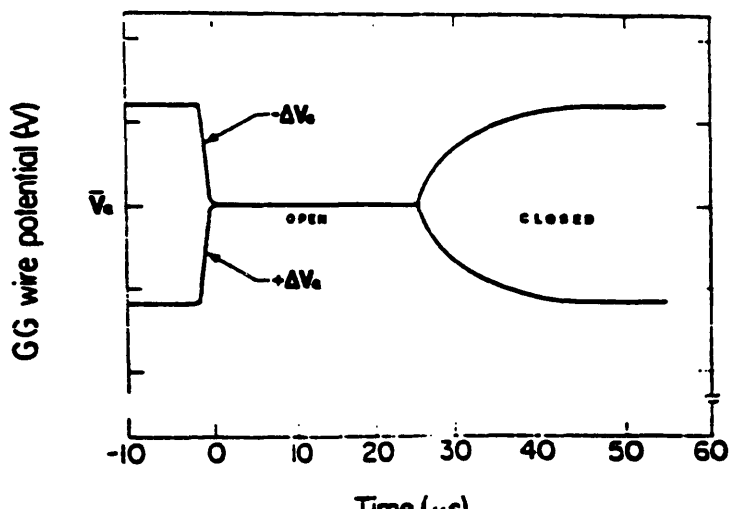
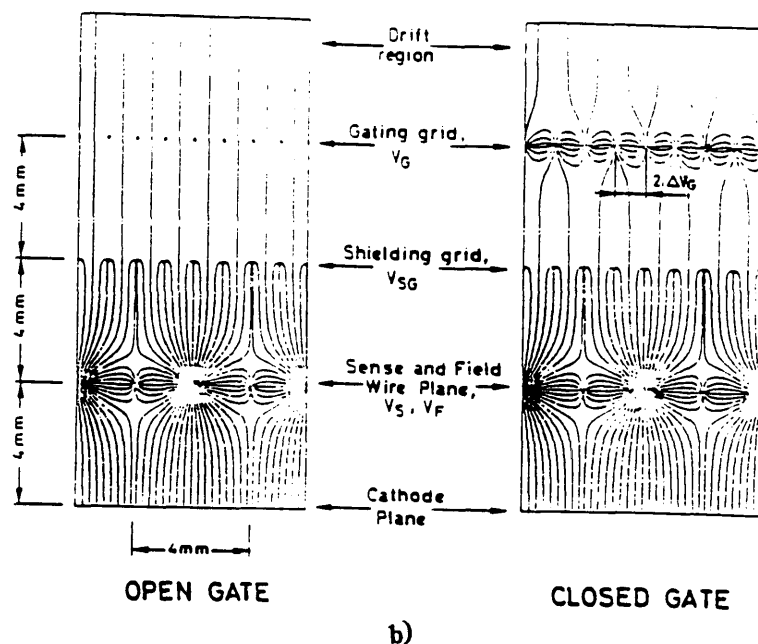


Fig.3.17

OPEN AND CLOSED GRID CONFIGURATIONS



a)

Fig.3.18

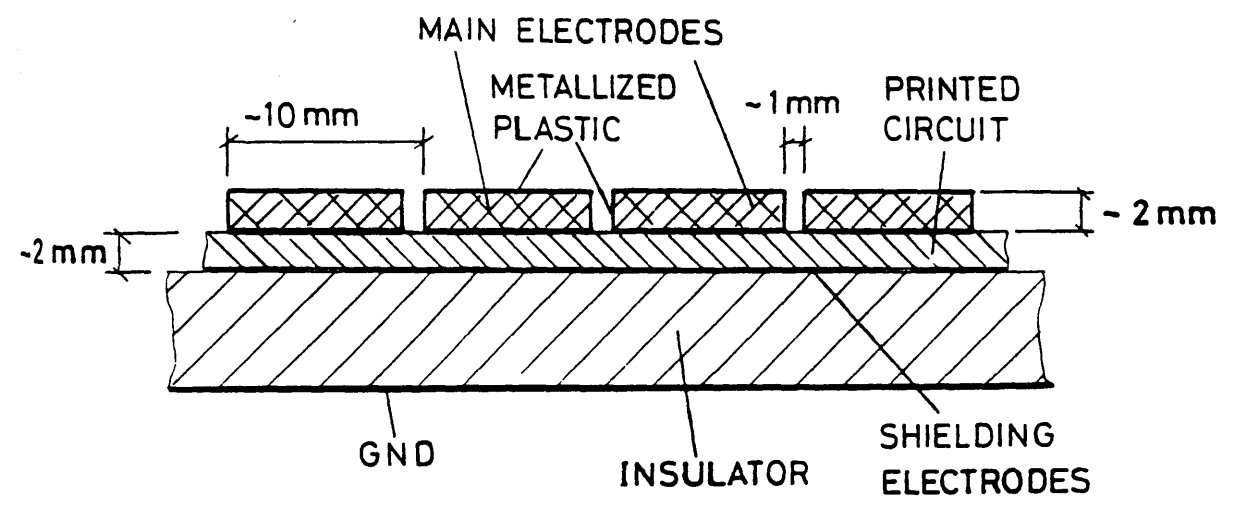
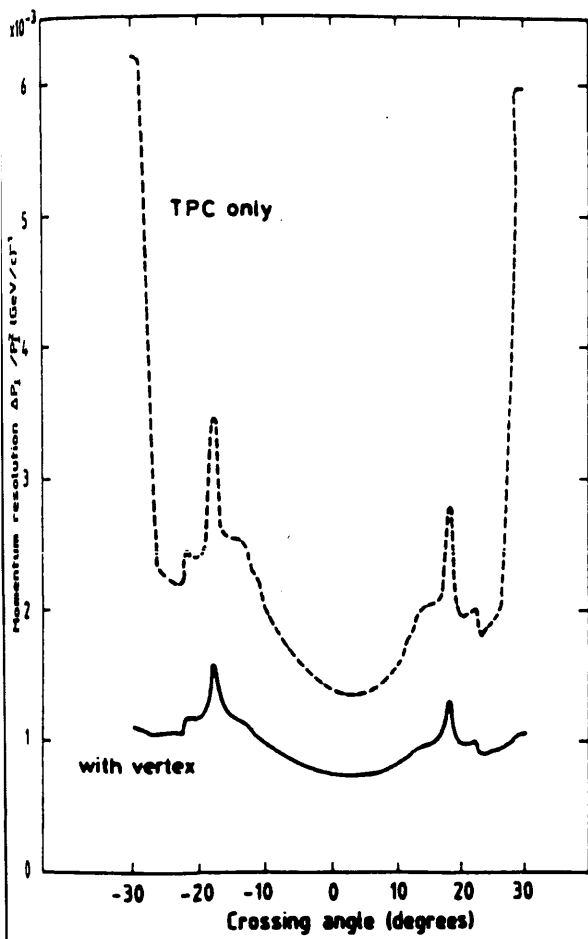
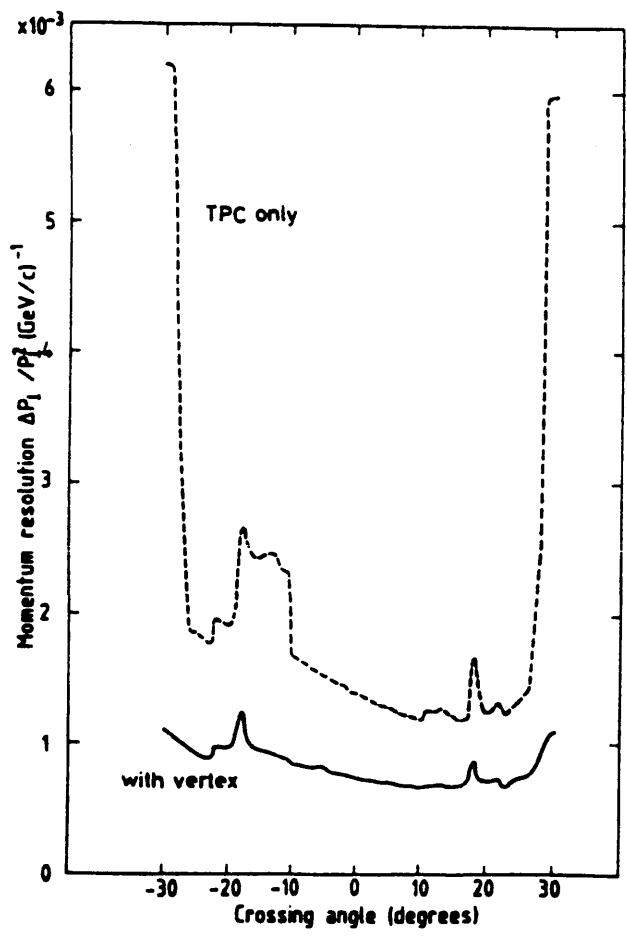


Fig.3.19



a)



b)

Fig.3.20

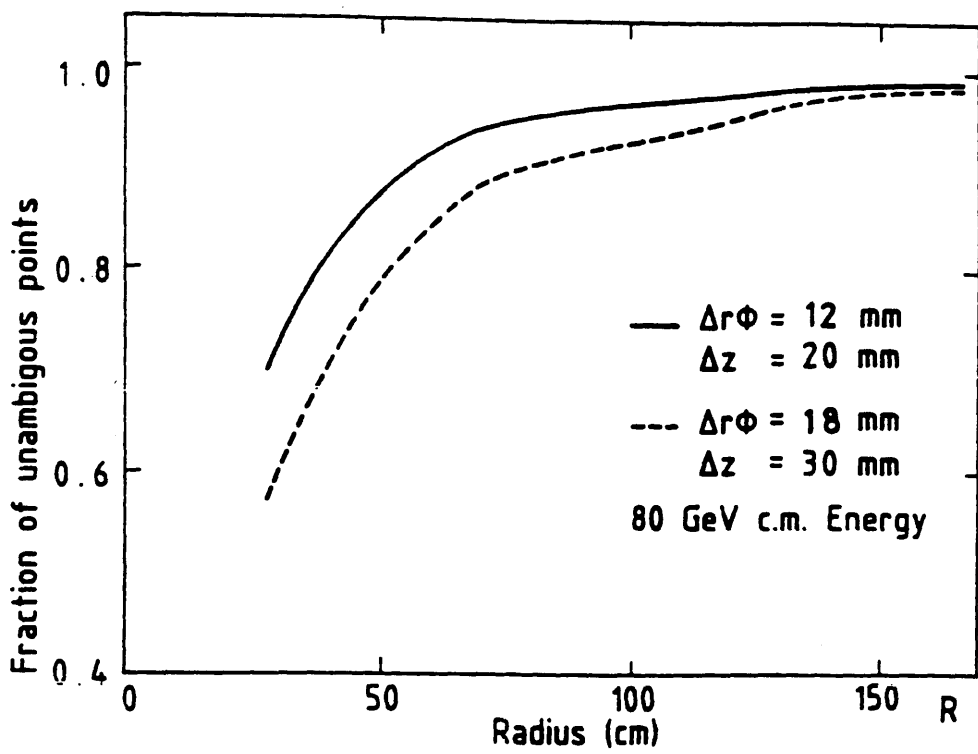


Fig.3.21

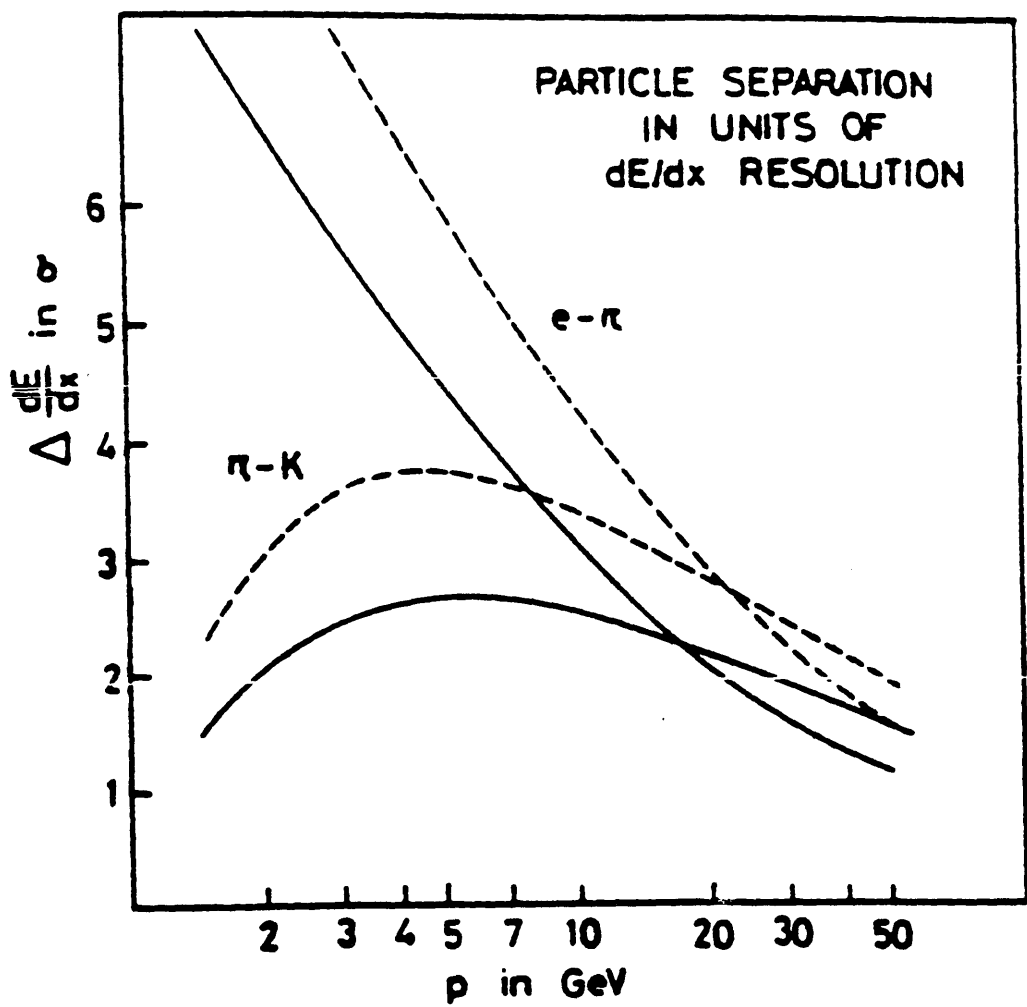
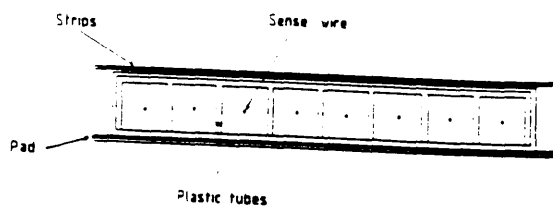
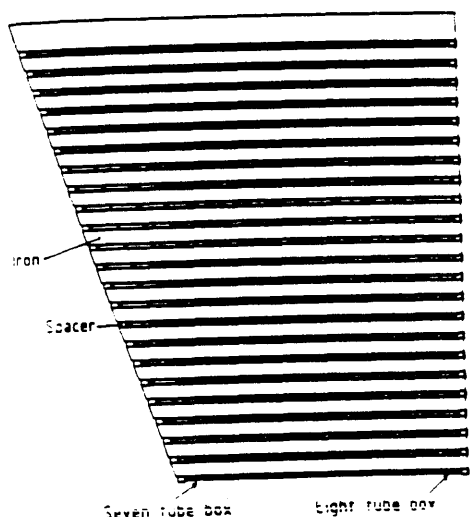


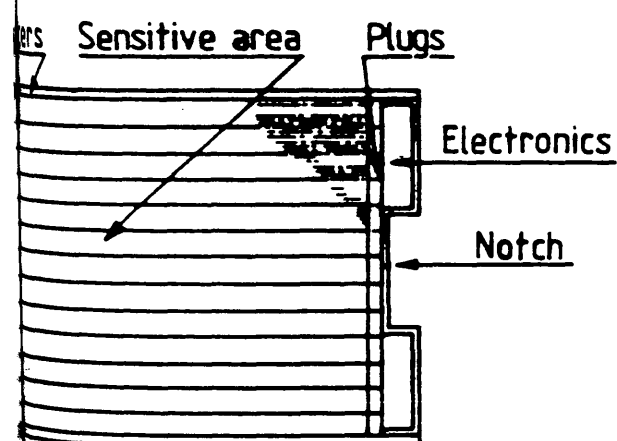
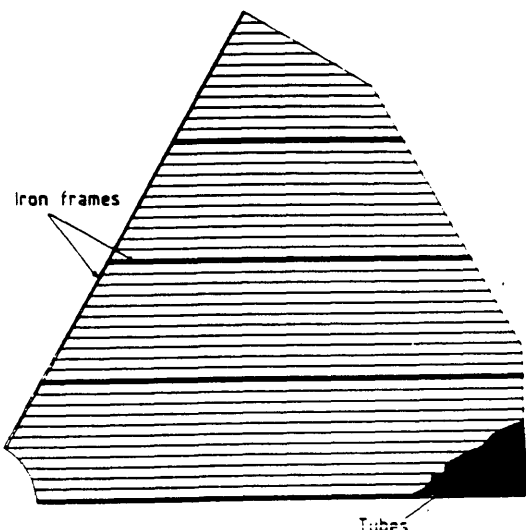
Fig.3.22



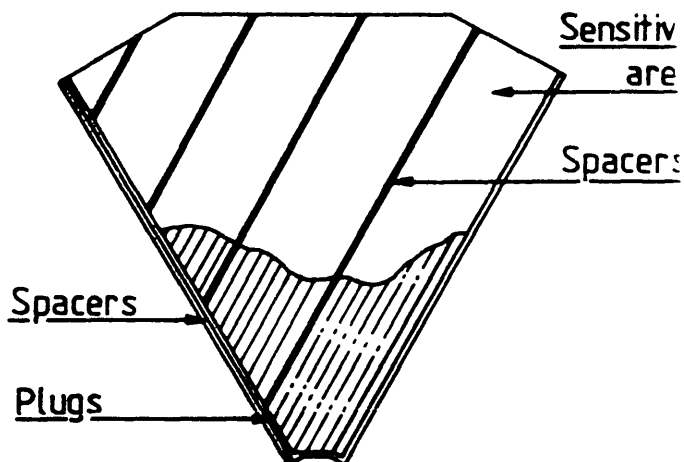
BARREL MODULE



END CAP SEXTANT



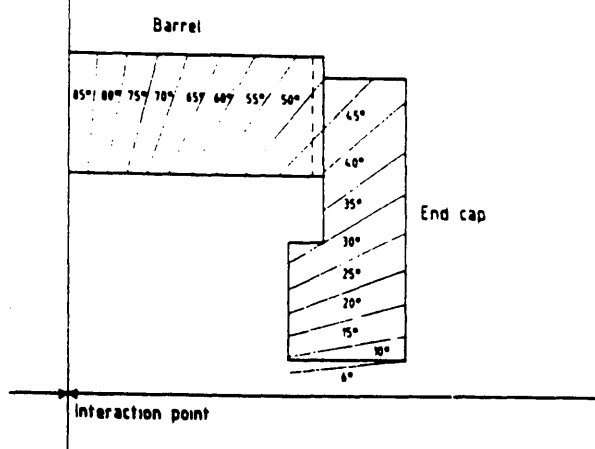
Dead areas in the barrel



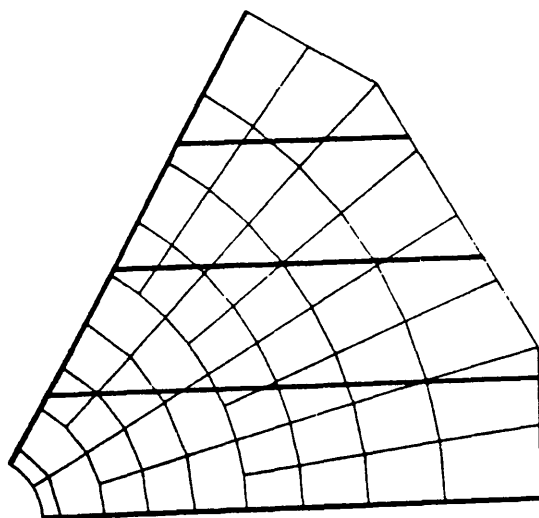
Dead areas in the end caps

Fig.3.23

TOWER θ-GEOMETRY



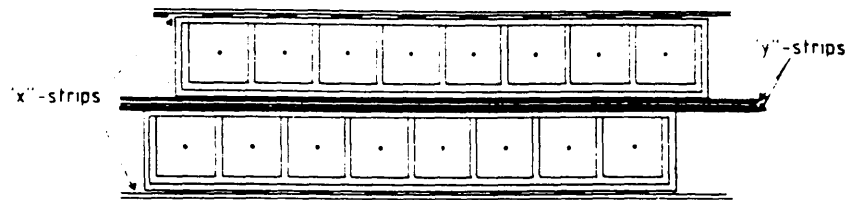
END CAP TOWER GEOMETRY



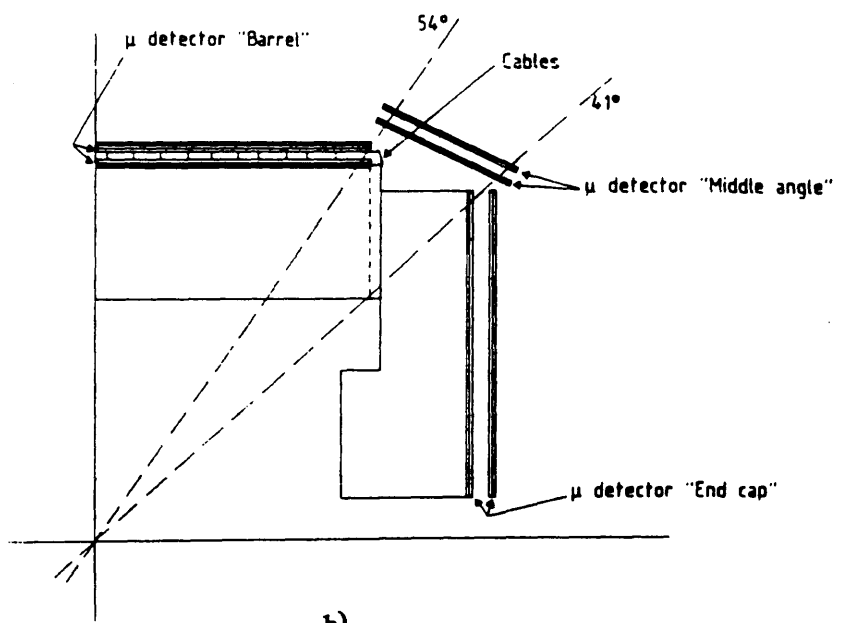
b)

Fig.3.24

MUON DOUBLE LAYER



a)



b)

Fig.3.25

Chapter 4 THE ALEPH ELECTROMAGNETIC CALORIMETER (ECAL)

In the construction of the calorimeter granularity is emphasized, because a good transverse granularity (approximately the size of the E.M. shower) is the best possible solution for pattern recognition. It simplifies the identification of electrons inside hadronic jets and facilitates the separation of photon energy from the background produced by interacting hadrons.

4.1 General Description of the Calorimeter

The ECAL is constructed in a way that allows a 4π solid angle coverage for events, and it is installed inside the hadron calorimeter. It is able to detect electromagnetic showers coming directly from the interaction point, with a minimum amount of intervening matter and with minimum extrapolation of electron tracks from the TPC. Under these conditions ECAL achieves the highest possible spatial resolution and electron identification capability. The calorimeter is of the lead/wire-chamber sandwich type, as shown in Fig.4.1. The wire chambers are made of aluminium extrusions, with read-out by segmented cathode pads. The chambers are filled with a mixture of 80% xenon, 20% carbon dioxide. Originally the choice of gas was 50% Argon, 50% Ethane, but it was found that this mixture did not give sufficient energy resolution in the presence of a magnetic field, when testing the prototype. A resolution of only $24\%/\sqrt{E}$ was obtained in a magnetic field of 1.37 T, compared to $18\%/\sqrt{E}$ in the absence of the magnetic field. Using the shower simulation programme EGS, the worsening resolution was shown to be due to the very low energy electrons in the shower spiralling many centimeters along the wires. Xenon reduces the path length of low energy electrons by increasing the multiple scattering. For the end-cap chambers the 50:50 Argon, Ethane mixture can still be used, but so as to have only one gas system for the whole ECAL, it is proposed to utilise the mixture of 80% xenon, 20% carbon dioxide throughout. The shower is developed in lead plates 2mm thick. The secondary electrons from the shower create ionisation in the gas. The ionisation is amplified in an avalanche around the $25\mu\text{m}$ gold-coated tungsten wire placed at the centre of the extruded aluminium profile. The extrusion is closed along one side with mylar coated with a high resistivity layer of graphite, permitting the transmission of induced signals. The resistivity of the graphite should be high enough for its presence to affect only negligibly the pulse shape on the pad during the integration time of the amplifiers (a few μs).

The detector is built of two parts, the barrel section which is of twelve modules, each 5m long and 30° in azimuth, and two end-caps each made of twelve 30° petals. The internal structure of the end-cap modules is identical to that of the barrel modules, but they have

different module geometry. Towers in the barrel continue in the end-cap, but the sector structure gives a crack pointing to the interaction point, making a 2% dead zone. These cracks are used to take the signals out, in order to minimize the dead zones, disentangle them from the read-out lines and reduce their number. Each module is made of 45 stack layers, the structure of which is shown in Fig.4.2.

The barrel is being built in France, while the end-caps, each consisting of 12 petals, are constructed in the U.K.. Glasgow University has the responsibility for building 8 of the petals for the above.

The modules with the 45 layers are segmented in depth into three stacks as follows:

Stack 1, consisting of 10 layers with 2 mm lead sampling.

Stack 2, consisting of 23 layers with 2 mm lead sampling.

Stack 3, consisting of 12 layers with 4 mm lead sampling.

Pads from consecutive layers are connected to form towers pointing at the interaction region. Pad signals are summed in three depth-layers corresponding to the first 4 X₀ (10 layers), the central 9 X₀ (23 layers), and the last 9 X₀ (12 layers). Lead sampling layers of 4 mm thickness are used to economise on the number of layers in the last stack. The lateral size of the tower as seen along its axis is typically 3 cm x 3 cm. In the barrel region, the segmentation in azimuthal angle $\Delta\phi$ is $360^\circ/(32 \times 12) = 0.94^\circ$, in polar angle $\Delta\theta$ is $0.93^\circ \sin\theta$. With this segmentation there are 4096 (32×12) towers in each module, making a total of 49512 towers in the barrel. The end-caps are similarly organized. The segmentation in the region overlapping with the barrel uses the same $\Delta\phi$ and $\Delta\theta$ division. The inner region of the end caps have larger $\Delta\phi$ segments in order to keep the tower size roughly constant at 3cmx3cm. The total number of end-caps towers is 24576, i.e. 1024 towers per module. The total of 22 radiation lengths of lead is used to ensure a good containment of the showers at the highest LEP energies, while the total petal depth is less than 0.90 interaction length, i.e. a hadron will typically pass through the module with little deposition of hadron shower energy in the electromagnetic calorimeter. About 90% of the electromagnetic energy is deposited in the first two stacks. The difference in longitudinal structure helps with electron-hadron separation and low energy photon measurement. The total number of towers per module is 1024. Fig.4.3 shows an isometric view of the pad towers within the petal, illustrating the projective geometry design. The projectivity of the towers allows a high degree of shower energy containment. If an electron or photon hits the centre of one pad, about 70% of the energy is contained in the corresponding tower. The distribution of the energy between neighbouring towers helps to determine more precisely the centre of gravity of the shower, which provides

higher spatial resolution. The tower capacitance varies from place to place around 2nF , due to the number of connected layers, the size of the pads and the length of the pad tracks. The cross-talk capacitance is only between pads in the same azimuthal row (tracks running over pads) and mostly between neighbours, (adjacent tracks). The ratio between nearest-neighbour cross-talk capacitance and the total capacitance is around 4%. The cross-talk signal is further reduced to less than 1% by electronic time integration.

4.2 Electronics

Conceptually the electronic system consists of three parts as shown in Fig.4.4:

- i) the integrator/multiplexer circuits which are mounted on the calorimeter modules, (front-end electronics)
- ii) the analog-to-digital conversion units
- iii) the read out into the ALEPH data-acquisition system.

In order to obtain the excellent granularity of the detector, we need a large number of electronics channels. This can be achieved by multiplexing the signals directly at the detector modules. Since the signals from the detector are high, low-cost commercial integrating amplifiers and CMOS switches are used as the first stages of the detector for each tower. The above signals are coupled into groups of 32 and read out in turn into a summing amplifier which provides two analogue outputs, a high gain and a low gain output where the high gain is 8 times the low gain. The summing amplifier builds immediately a sum signal for the 32 channels to be delivered for triggering. Such a device makes the system insensitive to the variations in the detector capacitances and heavily reduces the contribution of the cross-talk signals, making relatively long input lines possible. The collecting time is rather long, a few microseconds. Further 8-way multiplexing at the ADC cards provides two 12 bit binary numbers which correspond to the high and low gain signals and which are fed into a computer for processing. This method also reduces the amount of pick-up noise introduced in the twisted pair transmission lines. The electronics circuits for the calorimeter are shown in Fig.4.5(a). The total number of towers in the ECAL is 72000, 48000 for the barrel and 24000 for the end-caps. The total number of channels then will be 216000. 6750 preamplifiers are required because each tower has three readouts and due to the dual gain of the summing amplifiers (low and high), this gives a total of 1688 ADC channels. The analogue multiplexing works by collecting electric charge from each detector element and transferring it to a storage capacitor (one for each element). This charge is then converted to a voltage which is transferred to the control of switches A, B, C, and D as shown in the Fig.4.5(b). The

operation of the multiplexing integrating circuits can be understood by the following simplified description. One can consider three modes of operation, (see Fig.4.5(b)):

- i) a reset mode with all switches closed
- ii) a data storage mode with the A switches closed and B, C, D open; at the same time the summed output is transmitted to the trigger electronics
- iii) a readout mode; switches A are opened and the 32 B switches are closed in sequence, the C switch being used to reset the summing amplifier after each measurement.

The electronic chain is calibrated by injecting test charges into the summing amplifier. This tests the summing amplifier, the driver, the line receiver, the voltage multiplexer, and the ADC.

When no charge is present on the detector pads a finite reading is still produced by the circuit. This is known as the pedestal for a particular channel. The pedestal value varies with temperature, power supply voltage and the charge injected on other channels. Two causes of pedestals are given below.

- 1) The switches are implemented using commercial CMOS technology. When these are opened charge is injected into the circuit on both sides of the switch.
- 2) Coupling can also occur into the analogue parts of the circuit from the control logic which operates the switches and is present on the same cards.

Keeping the temperature and power supply voltage constant and minimizing the cross-talk effect will allow the pedestal to be subtracted after the information has been digitised by alternately taking pedestal readings and digitised values.

To implement the analogue front-end electronics both hybrid and monolithic circuits were studied. The hybrids consist of discrete integrated circuits mounted on circuit boards together with a few other components whereas for the monolithics all the components are integrated together on a single package. Each hybrid contains 8 integrating amplifiers and the switching logic for the A and B switches whereas for the monolithics 16 integrating amplifiers are contained on a single package. These are mounted on each daughter card together with two summing amplifiers and the necessary C and D switches to give a total of 64 channels on each card. The latter are then mounted in a temperature regulated box containing 24 daughter cards which sits on the apparatus and forms the "front-end" part of the electronics.

The monolithic design was preferred because it is cheaper, more reliable, and offers improved

performance. However, delays in production of the final version of the monolithic were considered likely to cause significant hold-ups in installation of the electronics at LEP, and the hybrid circuit was finally selected.

4.3 ECAL Petal Construction

The petal construction starts by preparing the stack layers, shown in Fig.4.1, which are composed of two main parts :

- 1) Wire Planes
- 2) Lead Pad Board Layers

4.3.1 Wire Plane

The 5 cm wide aluminium extrusions are glued together side by side, using a transfer adhesive, onto a 0.5 mm thick aluminium backing sheet. The extrusions are welded to the aluminium sheet to provide good electrical contact. The proportional tubes formed along the plane are 3.8 mm high, 3.2 mm deep and 4.7 mm wide. Gold-plated tungsten anode wires of 25 microns in diameter are woven down the centre of tubes by a special machine designed for the purpose. Special care has to be taken at the termination of the wires to avoid high voltage problems. The design of the wire termination adopted in the end-cap petals is illustrated in Fig.4.6. The points to note are:

There are no sharp edges at the end of the extrusion, the corners are radiused and deburred using a rotating abrasive brush. There is a 2 mm gap between the end of the extrusion and the termination boards. This increases tracking path lengths and allows any foreign bodies which may collect here to be removed by cleaning. The tracking path from the wire anchor point to the aluminium is further increased by building a step into the anchor board. Wires are mechanically supported at intervals of 35 to 40 cm along their length, to maintain the required gain uniformity of (1- 2) % over the plane, by an acytal wire 0.9 mm diameter placed across slots cut in the extrusions. Injection moulded noryl pieces are then inserted into the slots to a depth where the top of the noryl piece is flush with the top of the ribs. Every adjacent pair of the (210) wires per plane is protected by 0.125 amp fuses to avoid a wire break by excessively high current. This arrangement also allows the isolation of broken wires within the complete module. In barrel modules every wire is protected by such a fuse. A fuse can be blown by applying a low voltage, high current negative pulse to the high voltage input. This pulse will bypass the anti-surge resistors (R4 and R5) in Fig.4.7, via the diodes ZD1, D2 and D1 and blow the fuse. The planes will withstand 2 kV on the anode wires without sparking or leakage. After assembly, the wire plane is subjected to two tests:

a) Flare Test

With a high voltage on the anode wires in air, a "Polaroid" photograph is taken of the corona discharge from the plane. The aim of this test is to locate broken wires, blown fuses, wires out of alignment, and the planarity of the plane. Fig.4.8(a) demonstrates some faults which can be seen clearly from the photograph taken of the wire plane by the Polaroid camera. A blown fuse can be clearly seen. Another photograph of a "good" wire plane is shown in Fig.4.8(b).

b) Tent Test

After the flare test, the planes are put into a gas "tent" and subjected to a high voltage some 200V higher than the normal operating voltage in a gas mixture of 90% Argon, 10% carbon dioxide, to look for localised sparking due to dirt in the planes as well as for wrongly fixed wires.

4.3.2 Lead Pad Board Layer

The cathode pads are made on conventional (but fairly large) printed circuit boards (PCB's). Five such boards are needed to cover the area of one layer of a petal. The specific θ, ϕ geometry of the end-cap pads makes the technique used in the barrel modules unsuitable here.

The segmented cathode printed circuit board is isolated from the wires by a graphite-coated mylar layer, and from the 2 mm or 4 mm thick lead converter by a 0.125 mm thick aluminised mylar layer. This sandwich, together with a wire plane forms a stack layer. The coupling capacity through the mylar is approximately 2pF for an area 3.2cmx3.2cm, which corresponds roughly to the distribution of the induced charge. While the leakage resistance should be much larger than a few $M\Omega$ per square, on the other hand the resistivity of the graphite should be low enough so that the D.C. current created in the chambers by background particles does not appreciably change the operating voltage. A resistivity between 100 $M\Omega$ and 10 $M\Omega$ per square is enough to ensure a voltage drop well below 1 Volt. A mixing of solvents containing 'aquadag' is sprayed onto mylar to achieve the required value of resistivity. This produces a resistivity, when dried, of between 2 and 2.8 $M\Omega$ per square. There are 20 different types of PCB's. Pads within the PCB's are arranged into 50 rows, in which the inner 8 rows have 8 pads, the next 16 rows have 16 pads, the next 16 rows have 24 pads, and the outer 10 rows have 32 pads. Fig.4.9 shows the arrangement of the pads within the PCB's .

Before stacking the layers in the petal, they are tested half a dozen at a time in a

"tank test". The group is enclosed in a closed tank filled with a gas mixture of 80% argon, 20% carbon dioxide, and the rate of sparking measured for normal operating high voltage and for voltages up to 200V above nominal. If the rate of sparking is within certain acceptance criteria, the planes are ready for stacking. Otherwise they are returned to the flare and tent tests again.

4.3.3 Stacking the Layers

The first 12 layers, i.e. the third stack, are stacked first. At 1800V in air, the current should not exceed 3 micro amp, and it should be zero below 1600 V. A pressure of 3 Bar is then applied to the layers for a week. Stack 2 is stacked using the same procedures in two steps of 12 and 11 layers, and finally the last 10 layers, i.e. stack 1, are added. After any addition of a group of layers, the petal is closed up and checked for sparking.

"Side-wiring" of the connections between pads to form towers follows stacking. On completion of this stage, a check is made for disconnected pads, broken wires, pads shorted together, and any other short circuits. This is achieved by measuring the capacitance and resistance of each tower. Following the connection of all anode signals and grounds, the petal is enclosed in its container. The container is designed with the requirements that it must support and constrain the internal components, (wire planes and the lead PCB layers), so that over a period of many years there will be no excessive movement or slipping which could result in deterioration of performance. It was concluded that holding the layers by pressure and friction alone was inadequate for the end-cap modules, all of which are held vertically. The lead and aluminium sheets are now supported directly on the box. The final design is a 6 mm thick aluminium alloy box which is strong enough to take the internal loads and to withstand the evacuation of the vessel. Individual layers are assembled against thin shims which rest in the corner of the box. Tests have been made on the lead to be used (4% antimony content), to check for an adequate safety margin against creep and buckling under the load.

A pressure of approximately 0.3 bar is applied by means of a bag between the 15 mm aluminium cover plate and the stack. The bag is filled with uncured epoxy resin to the desired pressure; the resin is then allowed to cure. The cover plate acts as a spring which accommodates the eventual small creep of the stack.

After closing the container it is evacuated and filled with a mixture of 80% argon, 20% carbon dioxide. Another check is then made similar to that carried out after finishing the side wiring of the petal. In addition, the gas leakage from the container is measured and should be below 10^{-4} mbar l/sec.

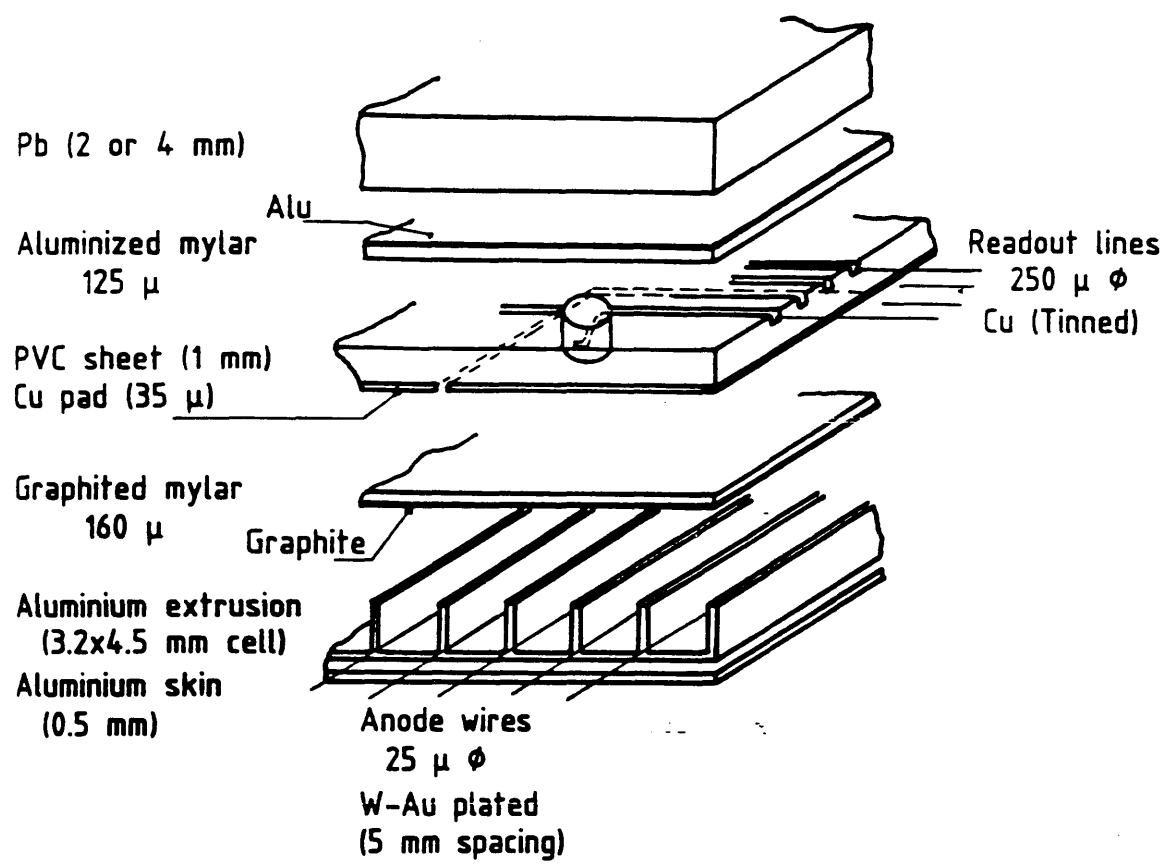


Fig.4.1

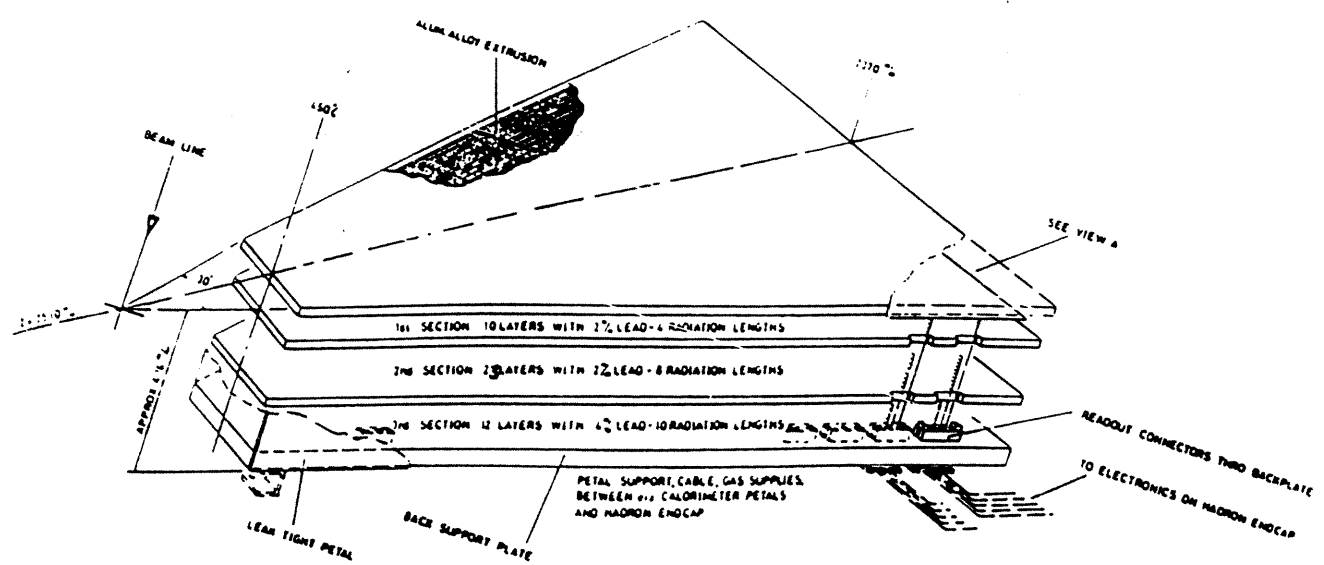


Fig.4.2

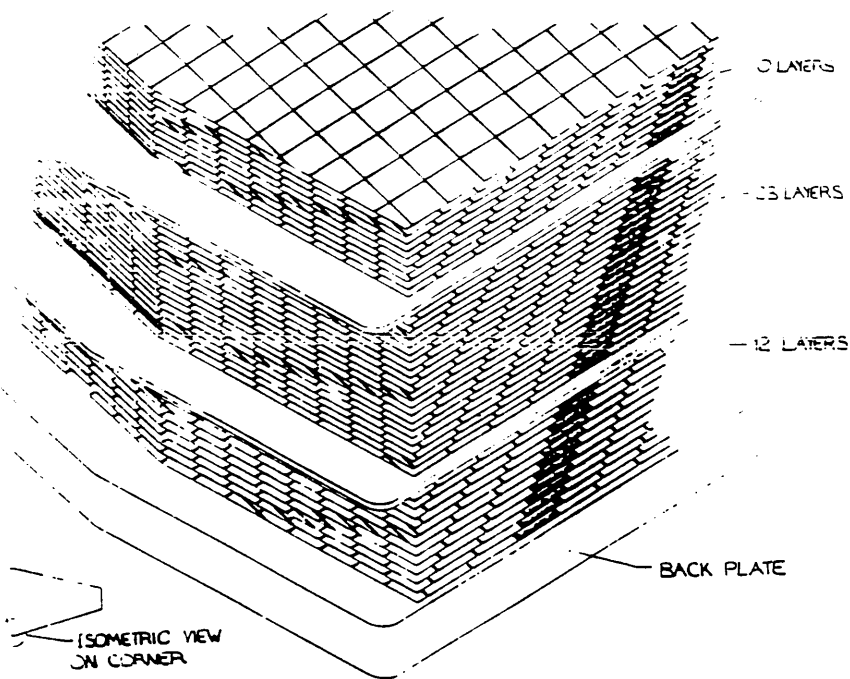


Fig.4.3

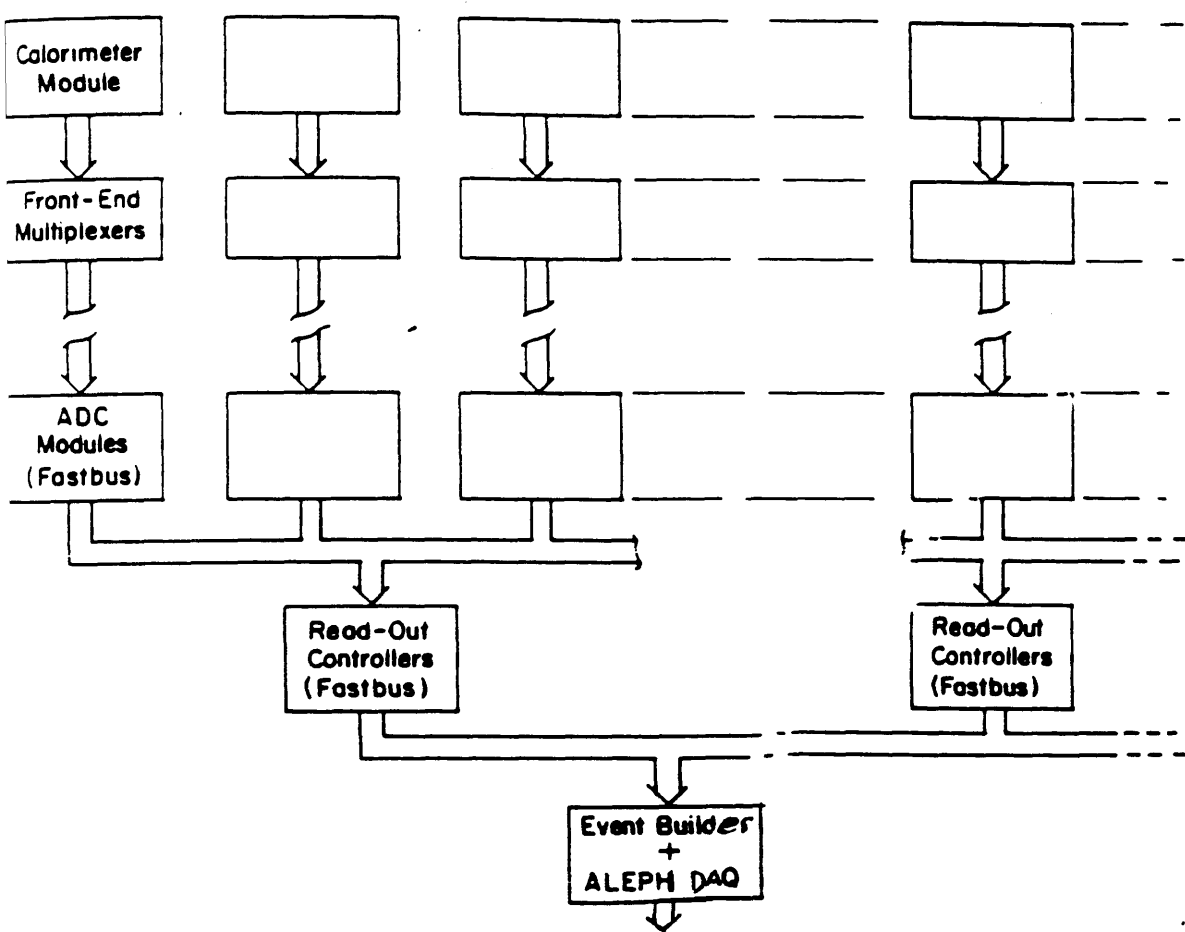


Fig.4.4

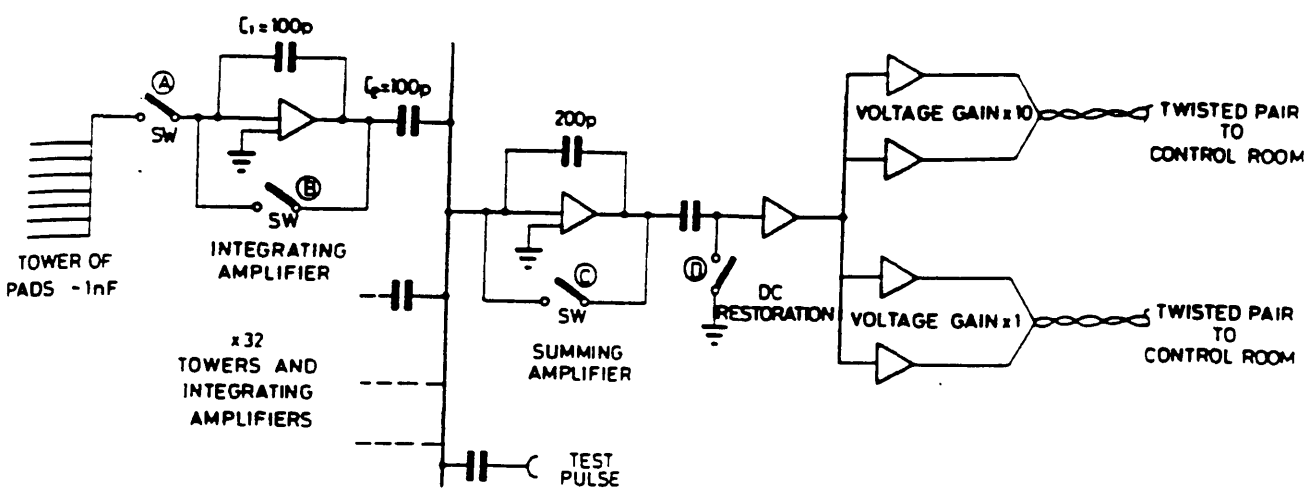
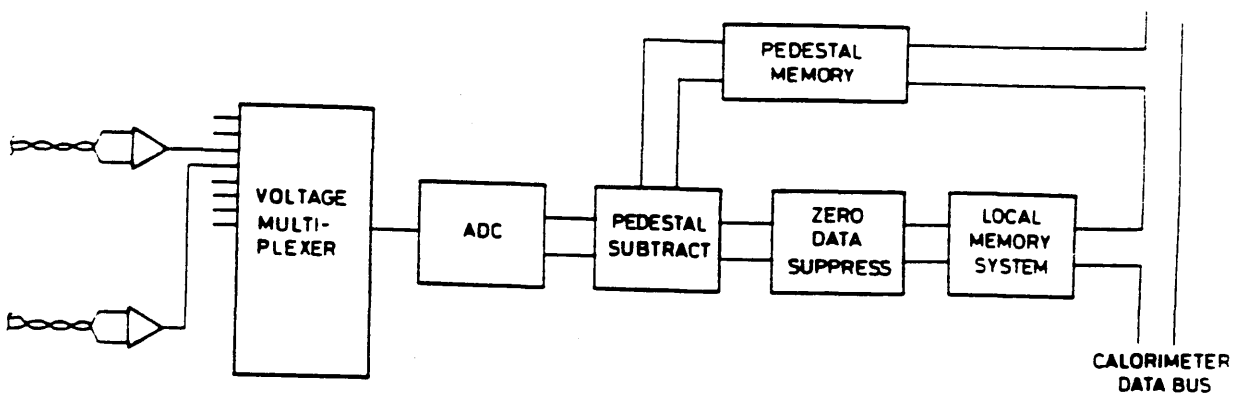


Fig.4.5 a)

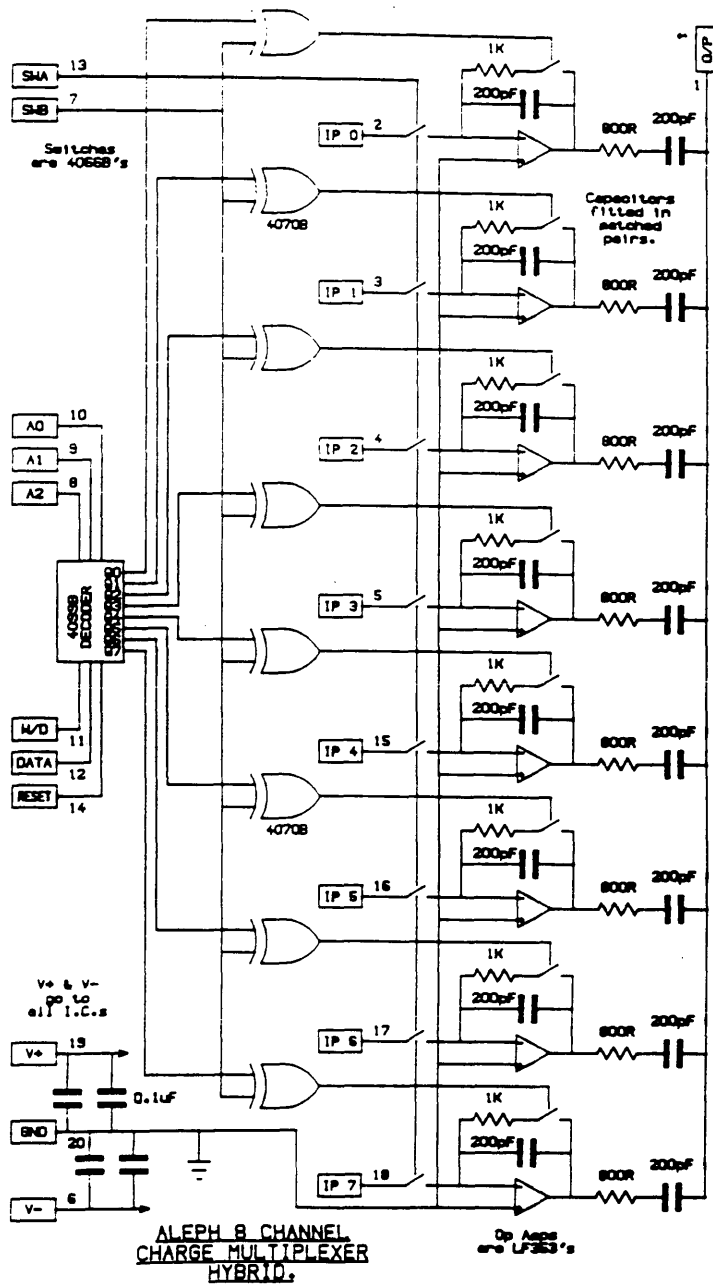


Fig.4.5 b)

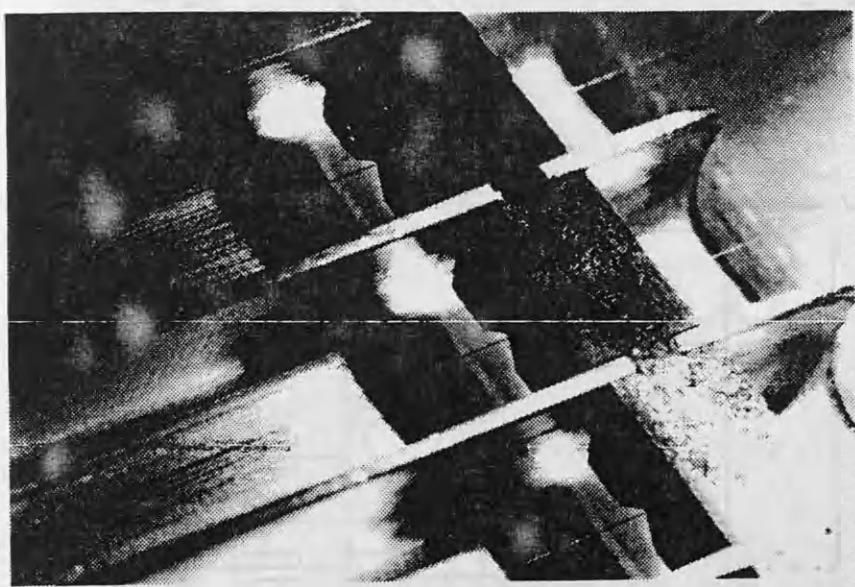


Fig.4.6

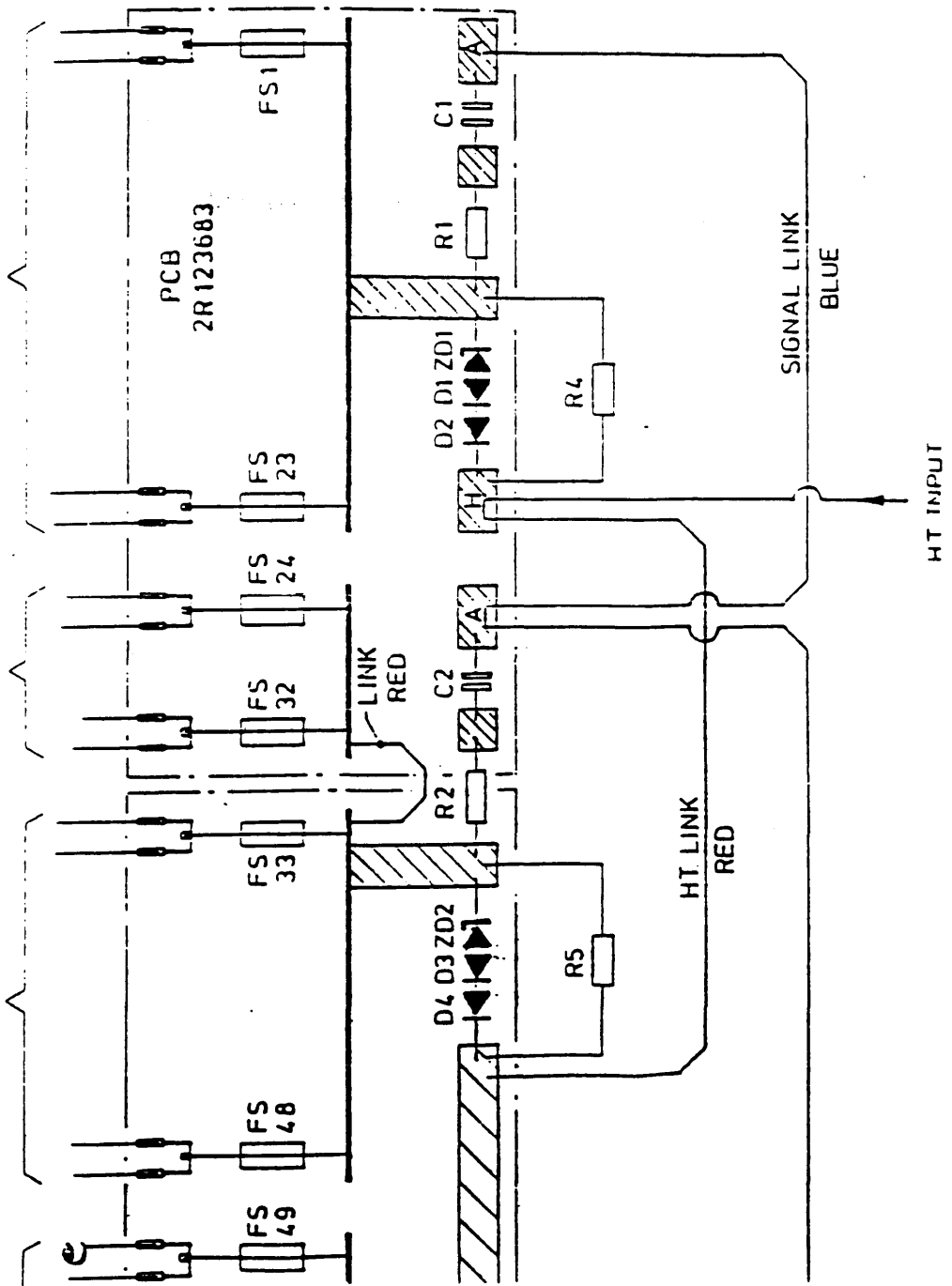
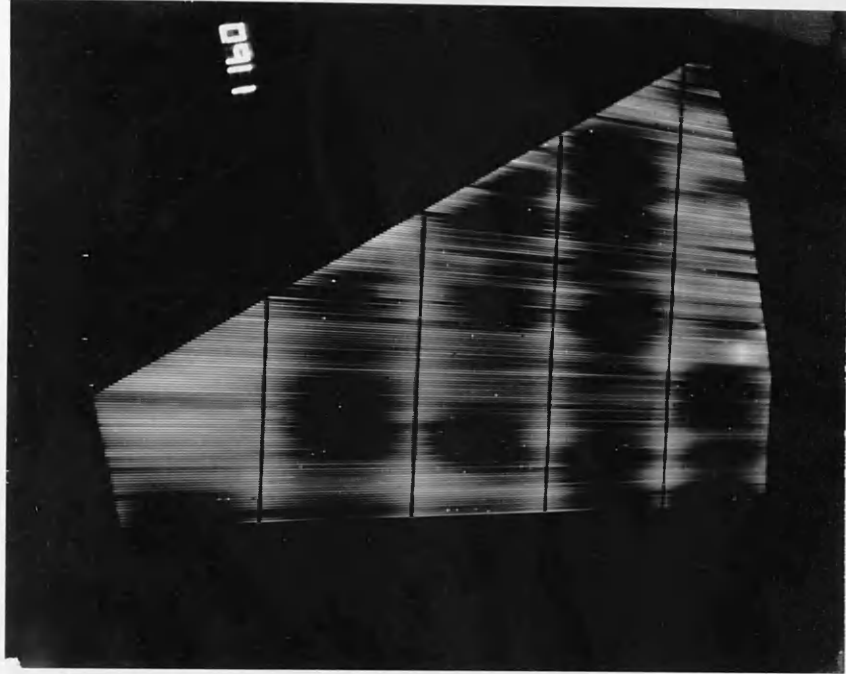
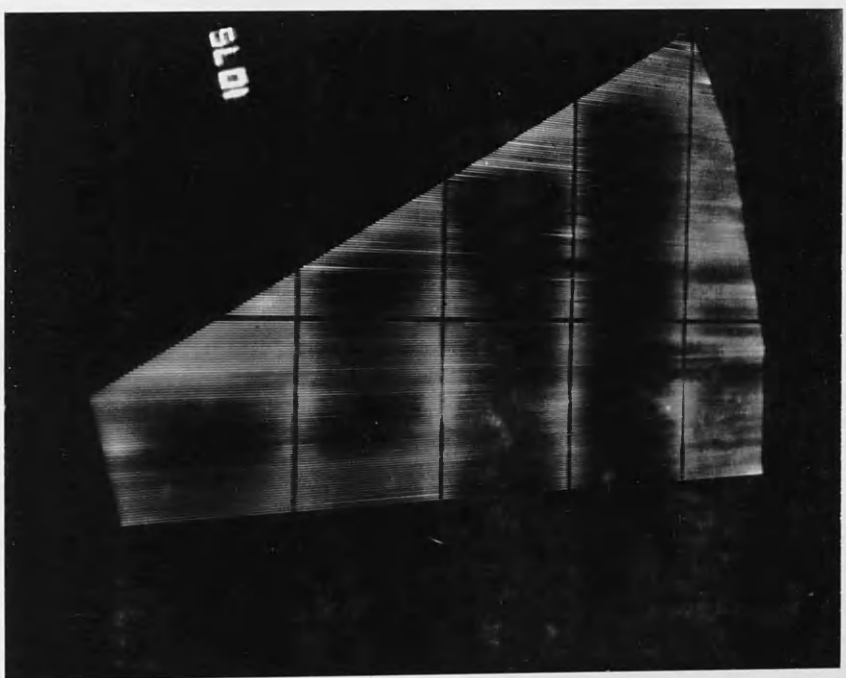


Fig.4.7



b)



a)

Fig.4.8

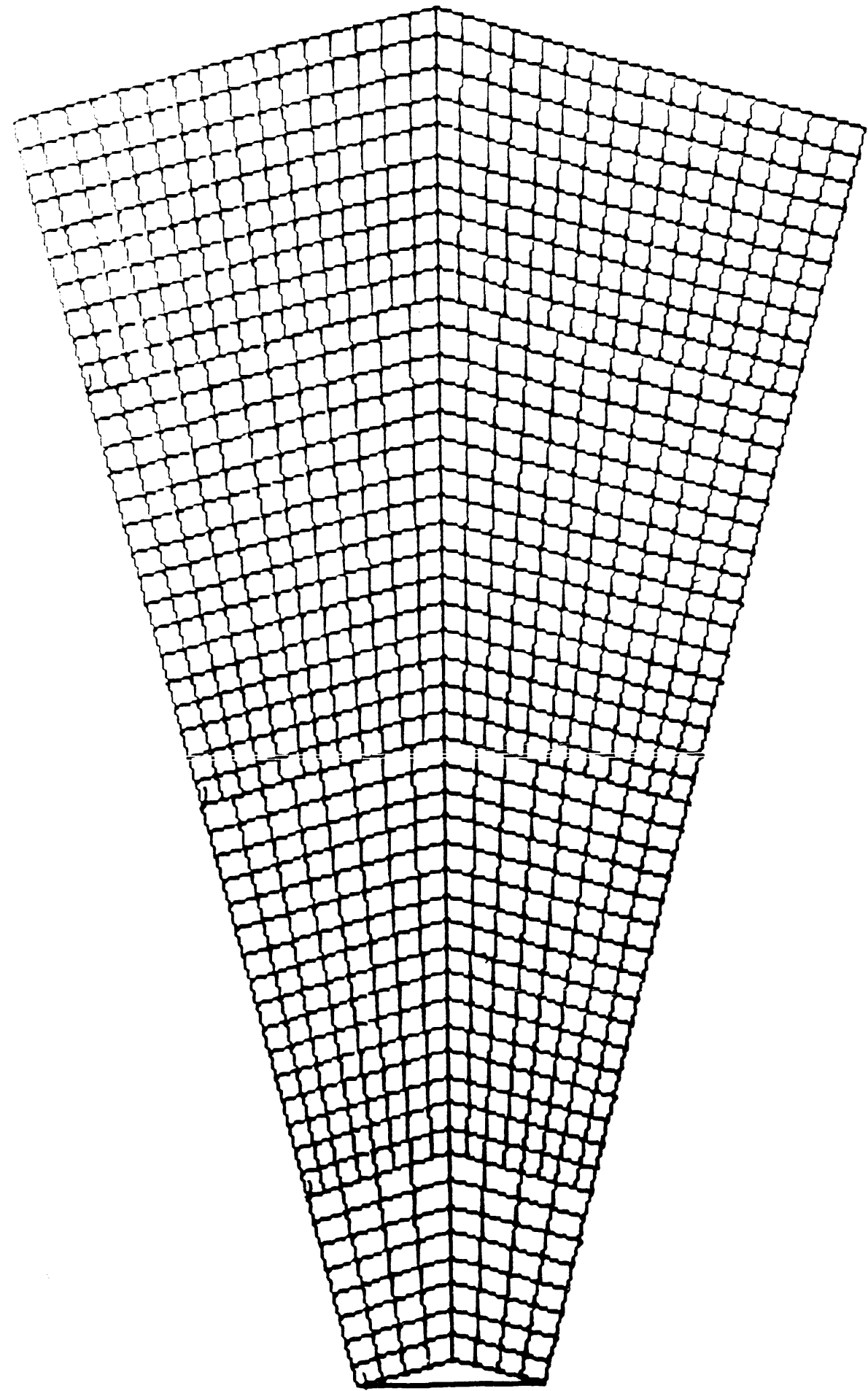


Fig.4.9

Chapter 5 TESTS OF COMPLETE ECAL MODULES

In this chapter the detector uniformity is studied and results of tests on some factors which contribute to the uniformity i.e. mechanical tolerance, electronics stability, high voltage, pressure, and temperature are given. Also included are details of tests on the complete modules which include anode wire pulsing, cosmic ray tests, and the test beam running. Some experimental results from the above tests are presented.

5.1 Effect of mechanical tolerances on uniformity

The main contributions to petal non-uniformity are due to wire diameter, gap size, and wire position tolerances.

Wire radius r : The dependence is $S = k.r^4$. Over the length needed for one plane, the typical variations are 0.1% in radius; variations from plane to plane are less important. In addition the high energy showers are measured over about 100 wires and this reduces the fluctuations to a negligible level.

Wire position: The effect of a lateral displacement has been calculated to be less than 1% signal variation for $\pm 200 \mu\text{m}$ displacement. The flatness of the layers was measured using a stack consisting of 40 layers of lead, cathodes, and aluminium extrusions and it was found to be good to $50 \mu\text{m}$ between wire supports (every 45 cm). The wire supports themselves are accurate to $30 \mu\text{m}$. Averaged over many layers, the non-uniformity from this source should be less than 1%.

Extrusion size: The signal is fairly insensitive to the lateral size of the cell (less than 1%/100 μm , whilst the extrusion precision is $\pm 30 \mu\text{m}$). The variation with the cell height is 1%/100 μm . A pressure of 100 g/cm^2 on the dry stack ensures uniform contact between the cathode and the extrusions. The gap height is therefore defined by the tolerance of the extruded aluminium profile. Typical variations were measured with a "gap-gauge" inserted inside the dry stack; they were found to be $\pm 30 \mu\text{m}$. Shower simulation shows that by averaging over different cells and layers, a point-to-point shower response uniformity of $\pm 0.8\%$ over a module can be established. In addition to construction effects, the uniformity of the modules is highly affected by the stability in time of different variables such as temperature, (which should be uniform to within 0.5 C degree), voltage, pressure, gas composition plus electronics stability. Variations due to voltage, pressure, or temperature are monitored continuously with time. The gain dependence on the previous variables was found to be $V^{16.2}$ (for 50:50 Argon/Ethane), $V^{16.8}$ (for 80:20 Xenon/CO₂), $p^{-6.5}$, and $T^{6.5}$ respectively. There is no difficulty in keeping the voltage constant to the required accuracy (less than 1V). For a closed constant volume, the collected charge is then globally insensitive

to temperature and pressure, but the differentials in temperature reflect on pressure, $\Delta P/P = \Delta T/T$. The stability of a calorimeter running closed for weeks has been measured to be better than 1%. The differentials in pressure due to heavy gases, (especially xenon), can be corrected. The gas composition effect has been checked. The contamination of the gas composition by air, oxygen, and water must be controlled at the level of few tenths of a mbar partial pressure. The calorimeter can be pumped down to check for leaks and outgassing, then filled with a slowly circulating gas mixture. This should keep the mixture homogeneous and stable.

Due to the absorption of Xe and CO₂ on the graphite in the ECAL modules the influence of the gas composition on the gain was studied with different concentrations of Xe and CO₂. A signal variation of 1-2 % was found when comparing compositions of 75:25 and 85:15 with the normal composition of 80:20.

In addition it was proved that the sensitivity of the gain to variations in temperature, pressure, and high voltage could be described by

$$\Delta T = 1^\circ \rightarrow \Delta G/G = 1.5\%$$

$$\Delta P \approx 1\% \rightarrow \Delta G/G = 1\%$$

$$\Delta V = 1 \text{ V} \rightarrow \Delta G/G \approx 1\% \text{ at } 1330 \text{ V}$$

All together this gives $\Delta G/G \approx 2\%$.

The results show 7% gain variations for 1% composition variations but fortunately it was seen that the rate of absorption of Xe and CO₂ seems to be at the same level, so that the gas composition will not vary so as to generate gain variations.

The wire chamber gas amplification is measured using small test chambers (platinis), incorporated in the petal structure. The stability of the electronics is checked and corrected for by pulsing only the summing amplifiers. The ratio of the capacitors in the chips is tightly controlled.

The importance of the uniformity in the pad response is clear, e.g. in searching for the Z° particles through toponium decay into Higgs + gamma. This reaction has a clean signature characterized by a monochromatic photon, the Higgs mass being determined by the missing-mass technique. If the mass of the Higgs is less than the mass of toponium and that of toponium less than the mass of Z°, the toponium decay into Higgs plus photon is allowed. In order to detect the monochromatic photons, the fluctuations in pad signals between different parts of the detector should not be more than about 1%, because the intrinsic resolution of the calorimeter is $0.18/\sqrt{E}$ GeV, or about 2.85% around 40 GeV. The uniformity of some modules was checked in a test beam. Some early (test beam) results on the relation between the ECAL signal and high voltage and pressure are shown in Figs.5.1 and 5.2.

5.2 Calibration Procedure

To establish the 1% uniformity needed in the ECAL, a fine calibration should be done to the ECAL modules. The final calibration procedures must be established after comprehensive tests on the complete modules in addition to the calibration of the electronic readout system. In the following paragraph the tests on the complete modules and electronic calibration are discussed.

5.2.1 Calibration of the electronics

The electronics chain is calibrated by injecting a test charge on the summing amplifiers. This tests the summing amplifier, the driver, the voltage multiplexer, and the ADC. Using samples of hybrid multiplexer front-end electronics, it was found that the 32 channels of the multiplexer have identical calibration to within 1%. The calibration constant obtained will be used directly in the data-acquisition modules to correct data for gain variations.

5.2.2 Tests of Complete Modules

The following tests have to be done to the complete modules in order to achieve the desired uniformity needed for the calorimeter which include :

- 1) Wire pulsing
- 2) Cosmic ray testing
- 3) Tests in a particle beam

1) Wire Pulsing

The petal pulsing is done via the anode readout lines. The pulsing is controlled by the MUX45 and uses a NIM FANOUT unit. By injecting a known amount of charge onto the anode wires, the response of both pads and wires may be checked. Missing pads and disconnected wires can easily be detected, and the necessary corrections applied. It has also been found possible to measure the effect of the wire supports underneath the pads. Fig.5.3 shows results from wire pulsing of the first petal constructed and pulsed in Glasgow. A missing wire is quite obvious, as are missing pads, from the pad response. When corresponding pads are missing from consecutive layers within a stack, it implies a missing tower. In Fig.5.4, a pulse height distribution over the whole petal surface area is illustrated.

The wire pulsing data show large fluctuations in the pad response, even after normalisation to

the pad area. Fig.5.5 illustrates these fluctuations in the normalised signals from pad (25-12), (i.e. row 25, column 12), from each of the 45 layers of petals 4 and 6.

An attempt was made to correlate the fluctuations to the pad area and to the length of read-out track from the pad to the edge of the PC board. In order to achieve this, a "mini-" wire pulsing system was arranged with a single layer of the calorimeter. A block diagram of the electronics is shown in Fig.5.6. The system allows the possibility of pulsing wires individually, in groups or all together. An additional option allowed the pulsing of the wires with the fuses removed, to allow the study of the contribution of the fuses to the signals from the pads near the broad end of the petal, in particular. Their contribution was thought to be significant because they lie underneath the unshielded part of the tracks from the broad-end pads.

From the diagram of the PC board layout in Fig.5.7 one can recognize three different regions. The pads in region 1 have a very short unshielded track length of about 2mm; pads from region 2 have 17mm of track length lying over the soldered ends of the anode wires at the left hand side, and region 3 (broad end) pads have 46mm of unshielded track length in addition to the existence of the fuses mentioned above.

The mean value of the signal per unit pad area for region 1 was found to be 0.702 ± 0.068 , while for region 2 it was 0.742 ± 0.067 and for region 3 was 0.893 ± 0.107 .

In order to try to understand the regional differences, the following procedures were adopted to study different aspects of the contributions to the output signal from the pads:

- To ensure that the wire plane module was as flat as possible for the tests, lead blocks were used to simulate the effect of the hydraulic compression used in completed petals. (It was clear that the pad signals associated with wire pulsing varied with the pressure applied, up to some limit).

- The linearity of the analysis system was investigated using the variation of measured signal with input voltage, using a fixed, known capacitance and with capacitance, using a fixed input voltage. The performance is shown in Figs.5.8 and 5.9. The range of capacitances chosen in Fig.5.9 is comparable with the pad-wire capacitance variation from the narrow to the broad end of the petal layers. The wire-pad capacitance was typically a few picofarads, as determined by comparison with standard values, and consistent with the value calculated theoretically, treating the aluminium extrusion as an approximation to a cylinder, as shown in

Fig.5.10.

The capacitance per unit length is then given by

$$C = 4\pi\epsilon/\ln(r/W)$$

where ϵ is the permittivity of the gas, r is the radius of the cylindrical tube and W the anode wire radius. For the 25 micron diameter anode wire of the planes used here, the capacitance per meter is $14 \text{ pF} \pm 2\text{pF}$. The contribution to the capacitance from the read-out pad is one quarter of this value, so for a total wire length under the pad of 25 cm, the capacitance will be of the order of 1 pF.

The stability of the measuring system was checked by comparing the pulse from the pulse generator and the pulse from a particular pad, and was found to be better than 1% over the duration of the measurements.

- To eliminate the contribution of the read-out track length to the signal, for both the shielded and unshielded parts, signals were taken from the second pad column, since this set of pads has very small track length and the pad signal variation is therefore due almost entirely to the pad area. It was found that the mean value of the signal, normalised to the pad area, was 0.665 ± 0.045 for this set of pads. The measured signal was also found to be proportional to the wire length under the pad for this set of pads.

- The contribution of the fuses to the pad signals from the broad end pads was established by measuring the signals with and without the fuses in place. The mean value of the signal was reduced to 0.816 ± 0.114 , without fuses, compared to the mean of 0.893 ± 0.107 for region 3 with the fuses in position.

The results quoted above show that the differences in the mean signal per unit area measured for regions 1, 2, and 3 may be explained as due to the effect of varying track lengths, particularly the unshielded portions, and to the effect of anode fuses located to the unshielded tracks.

2) Cosmic Ray Test

Since it was impossible to test all completed petal modules in a test beam, testing with cosmic rays is the only realistic source of further information about the uniformity of response of pads and wires.

A description of the experimental set up for the ALEPH cosmic ray petal testing and wire pulsing rig at RAL is given below, (cf. Fig.5.11).

The petal is mounted on a large iron frame. A group of scintillators and wire chambers, fixed before and behind the petal, are used as triggers in defining the track of the incoming muons from the cosmic ray muon flux. The trigger is constructed using signals from nine plastic scintillators, two small 25cmx25cm scintillators situated above the petal on the gallery, and eight large scintillators on the floor below the petal. The scintillators are arranged to define a beam of particles which mimics the situation in the completed detector at LEP.

There are two varieties of MWP chambers in the system

- large (ex NA4) chambers
- small 30cmx30cm chambers (from NA1)

These six small chambers the "top chambers" serve to define the incoming track. The ten NA4 chambers in the system are located three above the petal and seven below.

The petal is provided with high voltage in such a way that each of the 45 layers can be individually monitored. Petal readout is by FASTBUS ADC modules. The anode readout is controlled by the MUX45 FASTBUS module in its own special crate. The ADC's are controlled by the FASTBUS SEQUENCER. The sequencer holds several readout configuration programs, selectable by the user. In this system the FASTBUS ADC's and sequencer communicate with a CAMAC crate for readout and programming.

The cosmic-ray muon direction and position are measured by the wire proportional chambers, and cosmic-rays which are directed along a tower axis (within ± 0.1 rad) are selected. A week of data taking is sufficient for calibrating to $\pm 0.5\%$ about 100 different regions in a module (i.e. groups of 32 towers). The calibration procedure has now been checked in a test beam. Cosmic-ray tests are sufficient, since non-linearity effects as a function of energy are small (4 % at 40 GeV), and are expected to be constant for small modules.

For the purpose of the uniformity studies of the petals using the cosmic ray tests the stack was subdivided into thirty regions as shown in Fig.5.12. The main results of the uniformity scan for the existing petals are summarized below

Petal	stack 1 energy	% deviations from mean			Ratios		
		stack 1	2	3	1	(2/1)	(3/1)
1	70.6	1.4	2.1	1.5		1 : 2.12	: 1.16
3	85.4	2.1	1.8	1.0		1 : 2.21	: 1.15
4	66.0	1.5	1.8	0.9		1 : 2.30	: 1.20
5	65.2	1.6	1.8	1.3		1 : 2.17	: 1.15
7	85.0	1.5	1.4	1.4		1 : 2.20	: 1.15
9	78.6	1.3	1.7	1.3		1 : 2.24	: 1.18
10	61.0	1.8	1.7	1.5		1 : 2.20	: 1.10
11	60.7	1.2	1.7	1.4		1 : 2.60	: 1.37
12	71.4	1.7	1.6	1.7		1 : 2.21	: 1.17

The above results are for regions 1 to 11 and 16 to 20 inclusive, thus avoiding possible leakage out of the back of the petal for stack 3 and also avoiding regions with poor statistics. Note that petal 11 had several planes off for much of the data, hence the poor ratio results.

3) Tests in a Particle Beam

Exposing the modules to beams of pions, muons, positrons, and electrons with different energies has provided the relative response to hadrons, muons, and electromagnetic showers.

The aim of the beam test was to achieve the final calibration of the module before installation of the detector. The tests also allowed various aspects of the module behaviour to be studied, such as pad response, gas gain dependence on HV and temperature, stability of electronics and the effects of gas leakage on the gas mixture. The stability of the electronics was studied through the variations of the pedestals, the mean values of different channels showing wide variations when they should be the same. The variations in pad pedestals were more clear than in the wire pedestals. Variations of the pedestals for a typical tower and for a typical wire plane are shown in Fig.5.13.

The modules were tested in the X7b beam in the West area at CERN, with beams of (5 to 30) GeV π 's, (5 to 55) GeV μ 's, (2.5 to 70) GeV e^+ and e^- . The layout of the X7b experimental area is shown in Fig.5.14. The tests were done with different HV and with mixtures of 80:20 argon:CO₂ and 80:20 Xenon:CO₂. The response of the calorimeter to pions is shown in Fig.5.15, which represents the energy deposition in the ECAL for a 10 GeV π^- . The linearity of the calorimeter is shown in Fig.5.16. Fig.5.17 shows the energy resolution for the petal from the 1987 test beam run at CERN with electrons. The pion resolution and the

e/h ratio for the calorimeter are shown in Figs. 5.18 and 5.19.

In the analysis of test beam data obtained using muons of 55GeV during the summer of 1987, the study concentrated on results obtained with an 80:20 argon CO₂ mixture and an HV of 1330 V.

Unlike electron beams, the muon beam is very spread out at the petal so that only about 50% have a position determination from the Saclay chamber and only 10% pass through the momentum spectrometer. Hence no requirement is made in this analysis of hits in the Saclay or beam spectrometer chambers. The petal was divided into regions identical to those used for the cosmic ray analysis.

To obtain the muon signal the following steps were taken:

- the maximum energy tower was found in each stack;
- the maximum towers in the stacks were required to line up roughly;
- the energy in the nearest neighbour towers to the maximum was summed;
- the energy in other towers was then summed.

The signal was taken to be the energy in the maximum tower + that in the nearest neighbours less a background normalised from the energy in the other towers. Typically about 15% of the energy is in the nearest neighbours, while the background subtraction contributes less than 1%. The position of the maximum signal pad in stack 2 decided into which zone an event was applied . The means of the pads and wire signals in each zone is given in Table 1 and 2, these are simply the histogram means (range 0.0 - 2.0 GeV). The means for the petal as a whole are also presented along with the corresponding values for the two sides independently.

Two fits were applied to the energy distributions, a gaussian fit to the peak and a Landau distribution in which the mean of the function was used. Neither gave any better results than the histogram means, the mean results are given in Table 3. As an alternative method of presenting the data, the histograms means of the energy distributions are plotted as functions of sec(θ) and ϕ in Figs. 5.20,21,22,23.

The longitudinal energy deposition profile is shown in Fig.5.24 and for comparison that for row 3 col. 7. The reason for this shape of plot is as yet unknown.

The means of the signals in the stacks have been calculated from the various runs covering

the area of the petal. The numbers are histogram means and so not absolutely correct. The statistical errors are of the order of 1%. The means are tabulated in Tables 1 and 2 along with the corresponding region used for the cosmic ray analysis. It should be noted that each point of the test beam scan covers a larger area than these regions so there is some overlap. Hence these numbers should be treated with some caution in comparison with the cosmic ray data.

	Region	Mean	Statistical Error (%)	Total Area (cm ²)
1	Region 1	1.00	1.0	1.00
2	Region 2	1.00	1.0	1.00
3	Region 3	1.00	1.0	1.00
4	Region 4	1.00	1.0	1.00
5	Region 5	1.00	1.0	1.00
6	Region 6	1.00	1.0	1.00
7	Region 7	1.00	1.0	1.00
8	Region 8	1.00	1.0	1.00
9	Region 9	1.00	1.0	1.00
10	Region 10	1.00	1.0	1.00
11	Region 11	1.00	1.0	1.00
12	Region 12	1.00	1.0	1.00
13	Region 13	1.00	1.0	1.00
14	Region 14	1.00	1.0	1.00
15	Region 15	1.00	1.0	1.00
16	Region 16	1.00	1.0	1.00
17	Region 17	1.00	1.0	1.00
18	Region 18	1.00	1.0	1.00
19	Region 19	1.00	1.0	1.00
20	Region 20	1.00	1.0	1.00
21	Region 21	1.00	1.0	1.00
22	Region 22	1.00	1.0	1.00
23	Region 23	1.00	1.0	1.00
24	Region 24	1.00	1.0	1.00
25	Region 25	1.00	1.0	1.00
26	Region 26	1.00	1.0	1.00
27	Region 27	1.00	1.0	1.00
28	Region 28	1.00	1.0	1.00
29	Region 29	1.00	1.0	1.00
30	Region 30	1.00	1.0	1.00
31	Region 31	1.00	1.0	1.00
32	Region 32	1.00	1.0	1.00
33	Region 33	1.00	1.0	1.00
34	Region 34	1.00	1.0	1.00
35	Region 35	1.00	1.0	1.00
36	Region 36	1.00	1.0	1.00
37	Region 37	1.00	1.0	1.00
38	Region 38	1.00	1.0	1.00
39	Region 39	1.00	1.0	1.00
40	Region 40	1.00	1.0	1.00
41	Region 41	1.00	1.0	1.00
42	Region 42	1.00	1.0	1.00
43	Region 43	1.00	1.0	1.00
44	Region 44	1.00	1.0	1.00
45	Region 45	1.00	1.0	1.00
46	Region 46	1.00	1.0	1.00
47	Region 47	1.00	1.0	1.00
48	Region 48	1.00	1.0	1.00
49	Region 49	1.00	1.0	1.00
50	Region 50	1.00	1.0	1.00
51	Region 51	1.00	1.0	1.00
52	Region 52	1.00	1.0	1.00
53	Region 53	1.00	1.0	1.00
54	Region 54	1.00	1.0	1.00
55	Region 55	1.00	1.0	1.00
56	Region 56	1.00	1.0	1.00
57	Region 57	1.00	1.0	1.00
58	Region 58	1.00	1.0	1.00
59	Region 59	1.00	1.0	1.00
60	Region 60	1.00	1.0	1.00
61	Region 61	1.00	1.0	1.00
62	Region 62	1.00	1.0	1.00
63	Region 63	1.00	1.0	1.00
64	Region 64	1.00	1.0	1.00
65	Region 65	1.00	1.0	1.00
66	Region 66	1.00	1.0	1.00
67	Region 67	1.00	1.0	1.00
68	Region 68	1.00	1.0	1.00
69	Region 69	1.00	1.0	1.00
70	Region 70	1.00	1.0	1.00
71	Region 71	1.00	1.0	1.00
72	Region 72	1.00	1.0	1.00
73	Region 73	1.00	1.0	1.00
74	Region 74	1.00	1.0	1.00
75	Region 75	1.00	1.0	1.00
76	Region 76	1.00	1.0	1.00
77	Region 77	1.00	1.0	1.00
78	Region 78	1.00	1.0	1.00
79	Region 79	1.00	1.0	1.00
80	Region 80	1.00	1.0	1.00
81	Region 81	1.00	1.0	1.00
82	Region 82	1.00	1.0	1.00
83	Region 83	1.00	1.0	1.00
84	Region 84	1.00	1.0	1.00
85	Region 85	1.00	1.0	1.00
86	Region 86	1.00	1.0	1.00
87	Region 87	1.00	1.0	1.00
88	Region 88	1.00	1.0	1.00
89	Region 89	1.00	1.0	1.00
90	Region 90	1.00	1.0	1.00
91	Region 91	1.00	1.0	1.00
92	Region 92	1.00	1.0	1.00
93	Region 93	1.00	1.0	1.00
94	Region 94	1.00	1.0	1.00
95	Region 95	1.00	1.0	1.00
96	Region 96	1.00	1.0	1.00
97	Region 97	1.00	1.0	1.00
98	Region 98	1.00	1.0	1.00
99	Region 99	1.00	1.0	1.00
100	Region 100	1.00	1.0	1.00

Table 5.1

PADS

Zone	stack 1	stack 2	stack 3
1	0.279±0.002	0.677±0.003	0.711±0.004
2	0.285±0.002	0.691±0.003	0.705±0.004
3	0.286±0.002	0.689±0.004	0.712±0.005
4	0.291±0.002	0.684±0.004	0.700±0.005
5	0.292±0.002	0.691±0.003	0.706±0.005
6	0.289±0.002	0.678±0.003	0.724±0.005
7	0.290±0.002	0.696±0.003	0.718±0.004
8	0.285±0.003	0.702±0.004	0.715±0.006
9	0.284±0.002	0.676±0.003	0.718±0.004
10	0.287±0.001	0.687±0.002	0.726±0.003
11	0.290±0.002	0.687±0.004	0.717±0.006
12	0.288±0.004	0.673±0.007	0.685±0.011
13	0.283±0.003	0.656±0.006	0.656±0.009
14	-	-	-
15	-	-	-
16	0.261±0.002	0.685±0.004	0.713±0.005
17	0.268±0.002	0.710±0.003	0.724±0.005
18	0.267±0.003	0.708±0.005	0.711±0.006
19	0.265±0.002	0.698±0.003	0.735±0.005
20	0.272±0.002	0.709±0.004	0.740±0.005
21	0.276±0.003	0.704±0.005	0.724±0.006
22	0.276±0.002	0.710±0.004	0.734±0.005
23	0.272±0.003	0.717±0.006	0.714±0.008
24	0.299±0.003	0.701±0.005	0.715±0.008
25	0.294±0.002	0.720±0.004	0.741±0.005
26	0.277±0.003	0.732±0.005	0.732±0.006
27	0.289±0.004	0.711±0.006	0.561±0.010
28	0.271±0.004	0.711±0.006	0.561±0.009
29	-	-	-
30	-	-	-
Means	0.281±0.011	0.698±0.015	0.721±0.011
Ratio of mean signals	10.000	24.823	13.284
Left side Means	0.287±0.004	0.687±0.008	0.714±0.008
Right side Means	0.275±0.012	0.709±0.014	0.727±0.010

Table 5.2

WIRES

Zone	stack 1	stack 2	stack 3
1	0.221±0.001	0.547±0.002	0.581±0.003
2	0.232±0.002	0.578±0.003	0.585±0.004
3	0.237±0.002	0.575±0.003	0.580±0.005
4	0.231±0.002	0.560±0.003	0.579±0.004
5	0.232±0.002	0.559±0.003	0.586±0.004
6	0.240±0.002	0.583±0.003	0.612±0.004
7	0.237±0.001	0.579±0.002	0.596±0.003
8	0.224±0.001	0.572±0.003	0.595±0.005
9	0.224±0.001	0.572±0.003	0.589±0.003
10	0.227±0.001	0.570±0.002	0.592±0.002
11	0.233±0.002	0.562±0.003	0.583±0.005
12	0.230±0.004	0.544±0.006	0.540±0.009
13	0.230±0.003	0.553±0.005	0.537±0.007
14	-	-	-
15	-	-	-
16	0.205±0.001	0.552±0.003	0.578±0.004
17	0.217±0.002	0.589±0.003	0.607±0.004
18	0.219±0.002	0.589±0.004	0.618±0.006
19	0.213±0.001	0.587±0.003	0.614±0.004
20	0.212±0.002	0.577±0.003	0.595±0.004
21	0.233±0.002	0.590±0.004	0.592±0.005
22	0.223±0.002	0.584±0.003	0.589±0.004
23	0.219±0.003	0.581±0.005	0.579±0.006
24	0.226±0.002	0.547±0.004	0.566±0.006
25	0.216±0.002	0.550±0.003	0.566±0.004
26	0.208±0.002	0.563±0.004	0.567±0.005
27	0.223±0.003	0.547±0.005	0.432±0.008
28	0.209±0.002	0.547±0.004	0.437±0.007
29	-	-	-
30	-	-	-
Means	0.225±0.010	0.572±0.014	0.589±0.015
Ratio of mean signals	10.000	25.447	13.580
Left side Means	0.232±0.006	0.570±0.011	0.589±0.010
Right side Means	0.217±0.008	0.574±0.017	0.588±0.019

Table 5.3

GAUSSIAN FIT TO PEAK

PADS

	stack 1	stack 2	stack 3
Means	0.231 ± 0.012	0.623 ± 0.020	0.596 ± 0.015
Ratio of mean signal	10.000	27.006	13.394
Left side Means			
	0.236 ± 0.006	0.607 ± 0.009	0.587 ± 0.007
Right side Means			
	0.225 ± 0.015	0.639 ± 0.013	0.605 ± 0.015

WIRES

Means	0.180 ± 0.011	0.503 ± 0.016	0.474 ± 0.013
Ratio of mean signals	10.000	27.921	13.639
Left side means			
	0.189 ± 0.007	0.498 ± 0.013	0.473 ± 0.012
Right side Means			
	0.172 ± 0.007	0.508 ± 0.018	0.475 ± 0.016

LANDAU FIT

PADS

Means	0.286 ± 0.012	0.770 ± 0.019	0.741 ± 0.017
Ratio of mean signals	10.000	26.922	13.424
Left side Means			
	0.293 ± 0.003	0.759 ± 0.014	0.731 ± 0.016
Right side Means			
	0.279 ± 0.013	0.781 ± 0.016	0.751 ± 0.017

WIRES

Means	0.227 ± 0.012	0.626 ± 0.016	0.600 ± 0.017
Ratio of mean signals	10.000	27.557	13.693
Left side Means			
	0.236 ± 0.006	0.623 ± 0.014	0.599 ± 0.017
Right side Means			
	0.219 ± 0.009	0.630 ± 0.017	0.602 ± 0.017

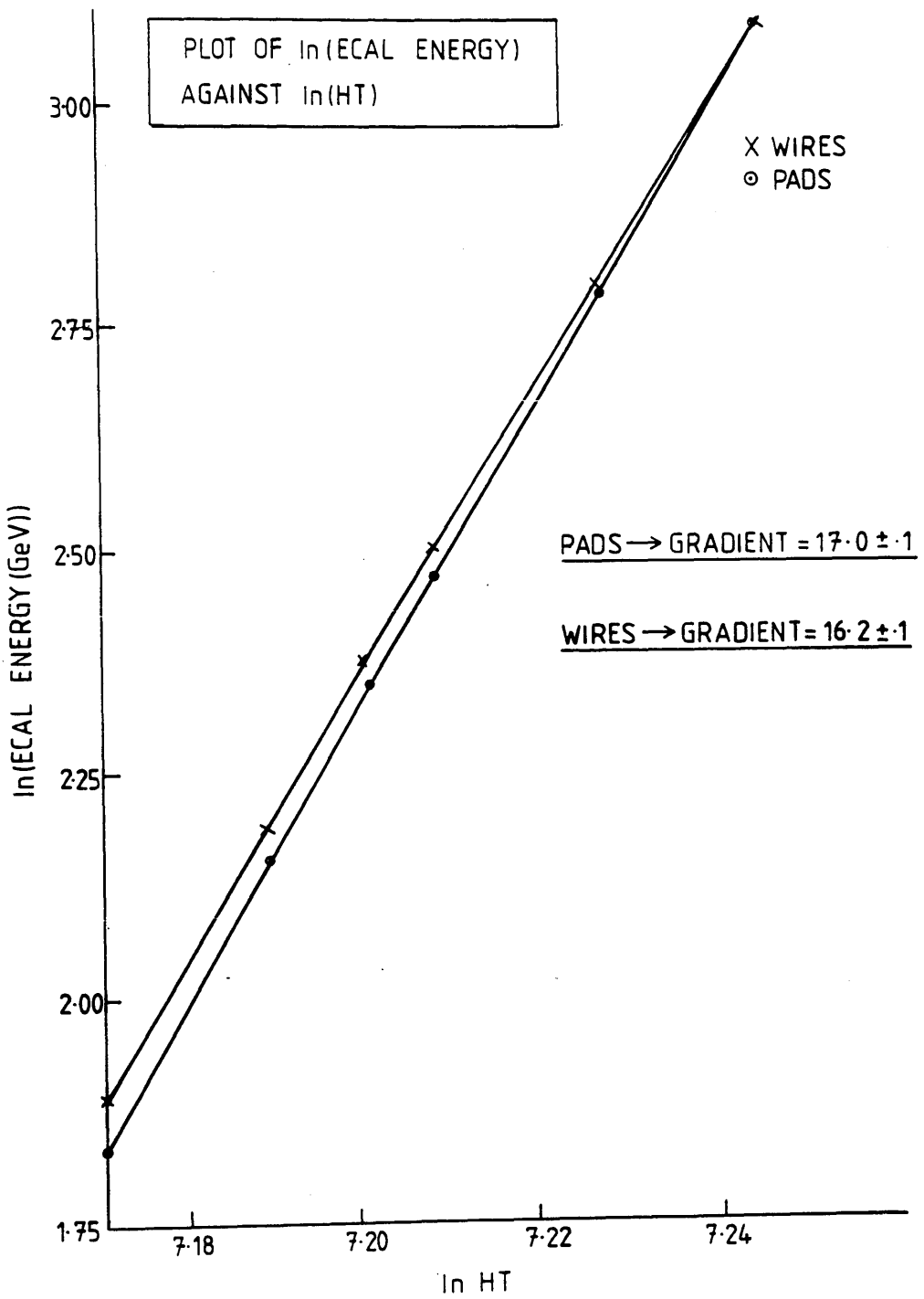


Fig.5.1

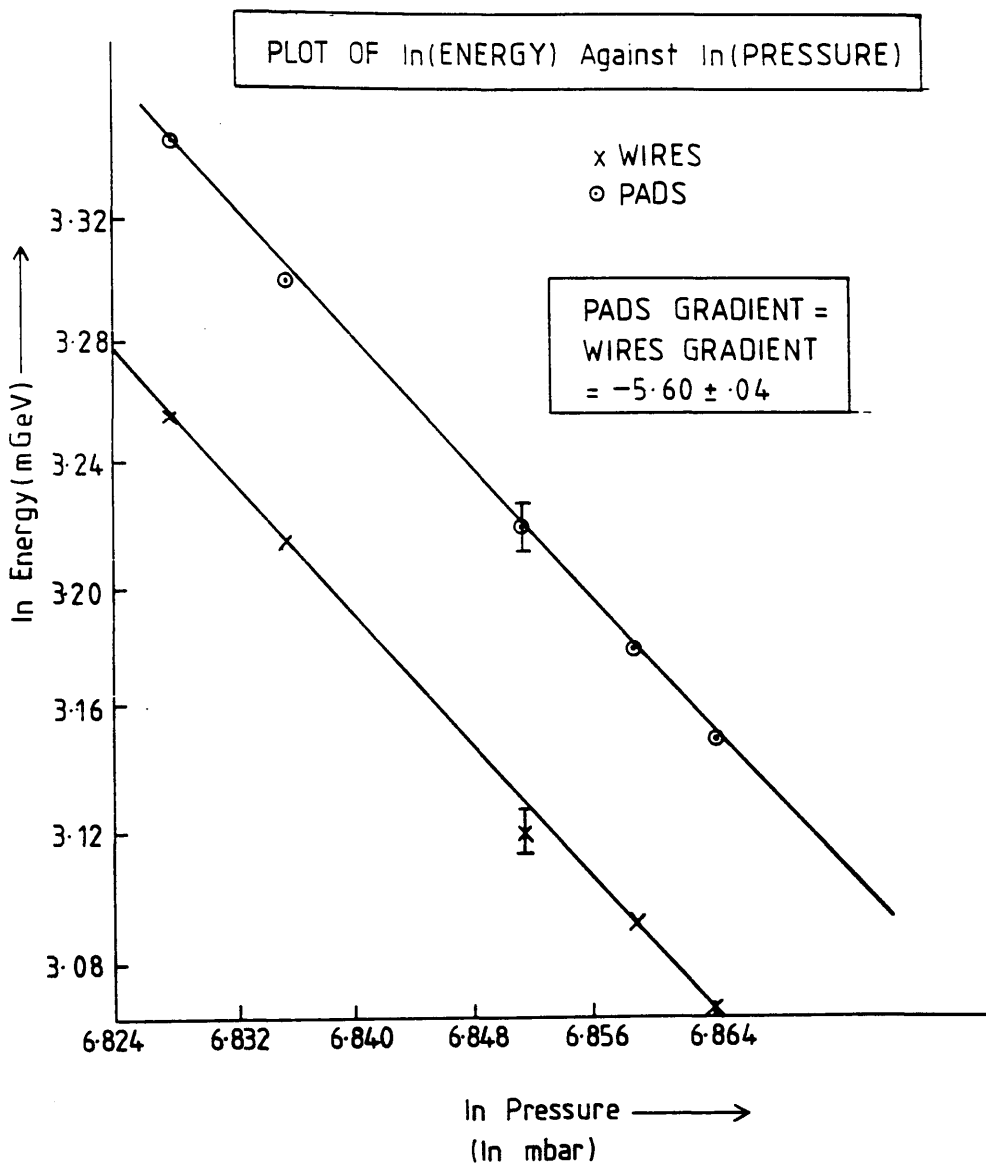


Fig.5.2

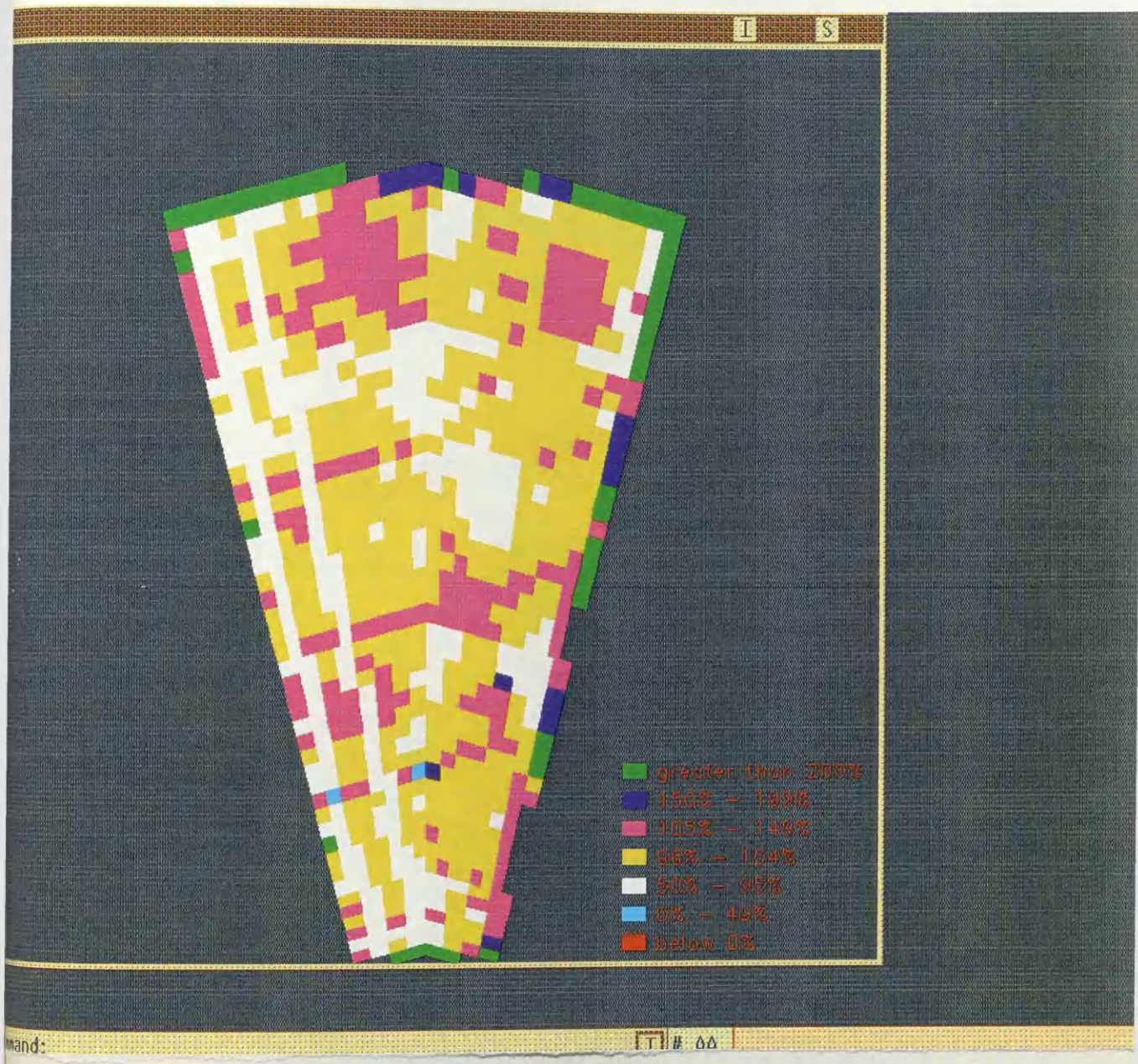


Fig.5.3

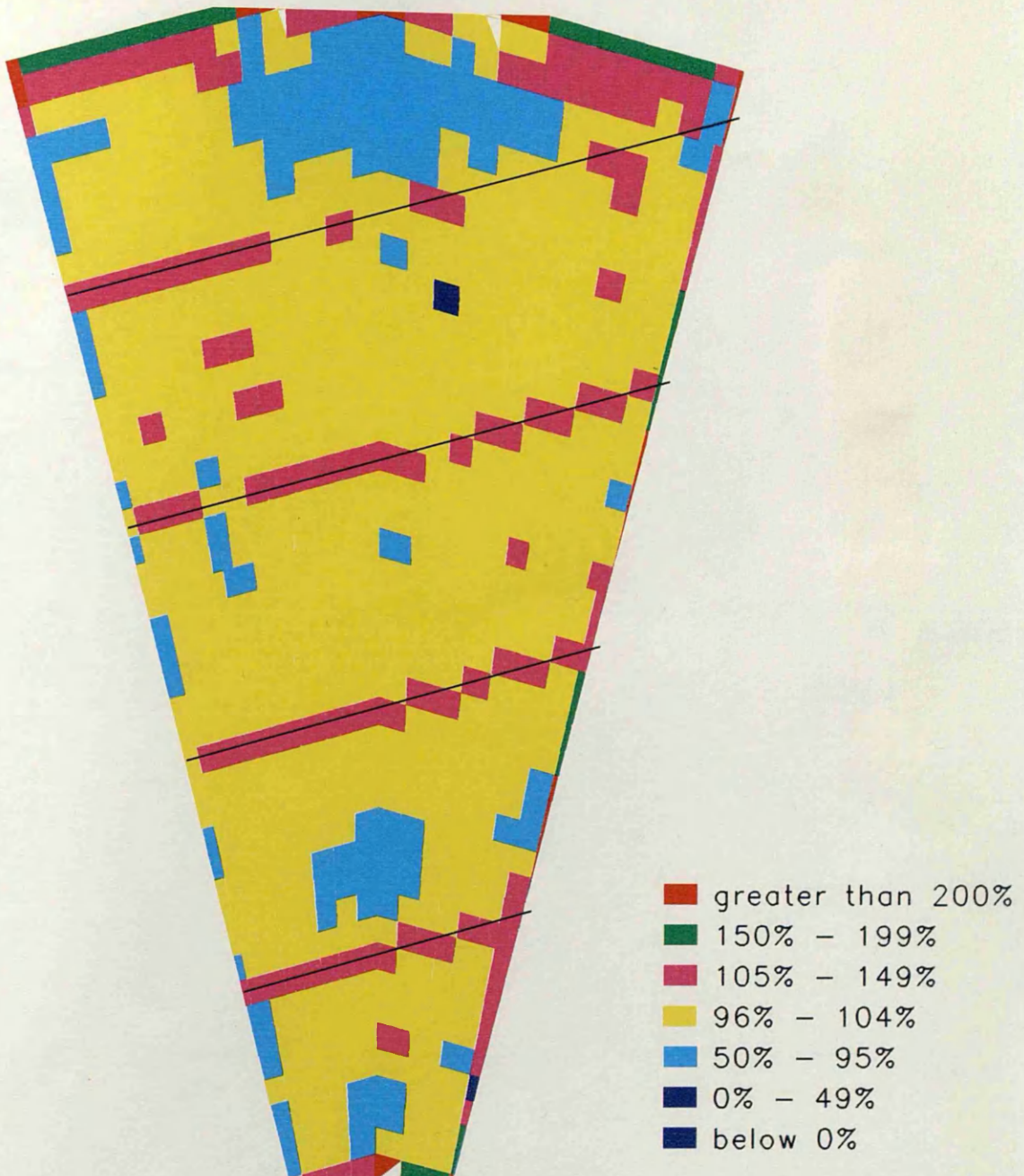


Fig.5.4

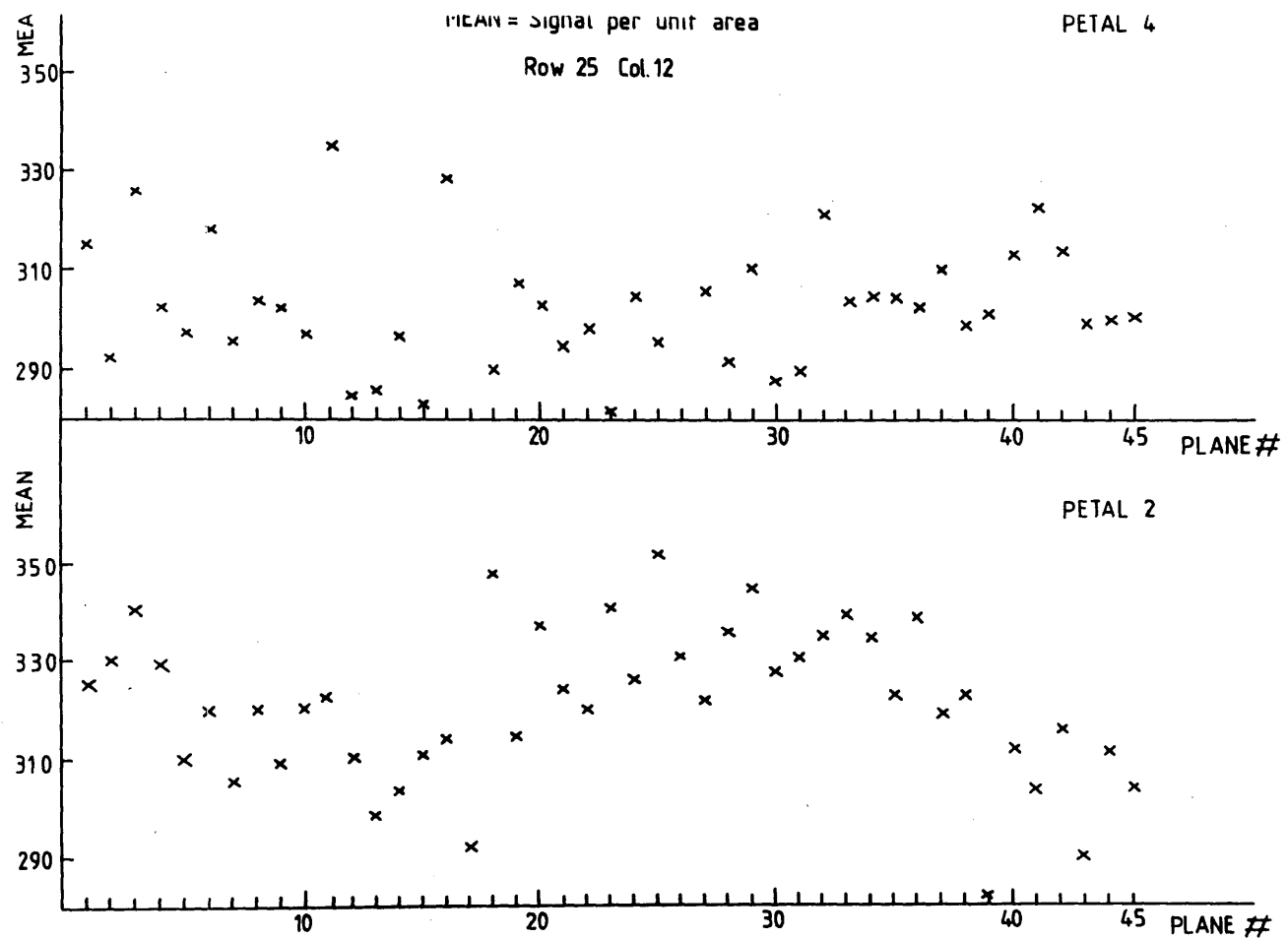


Fig.5.5

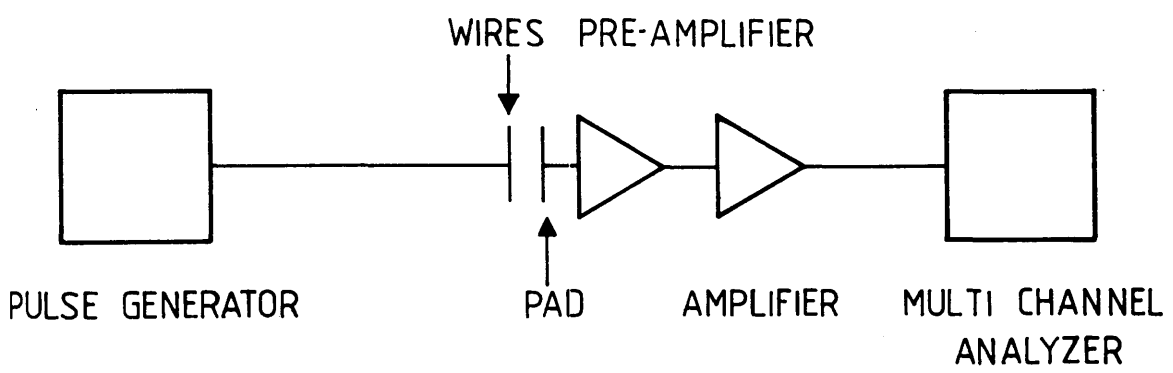


Fig.5.6

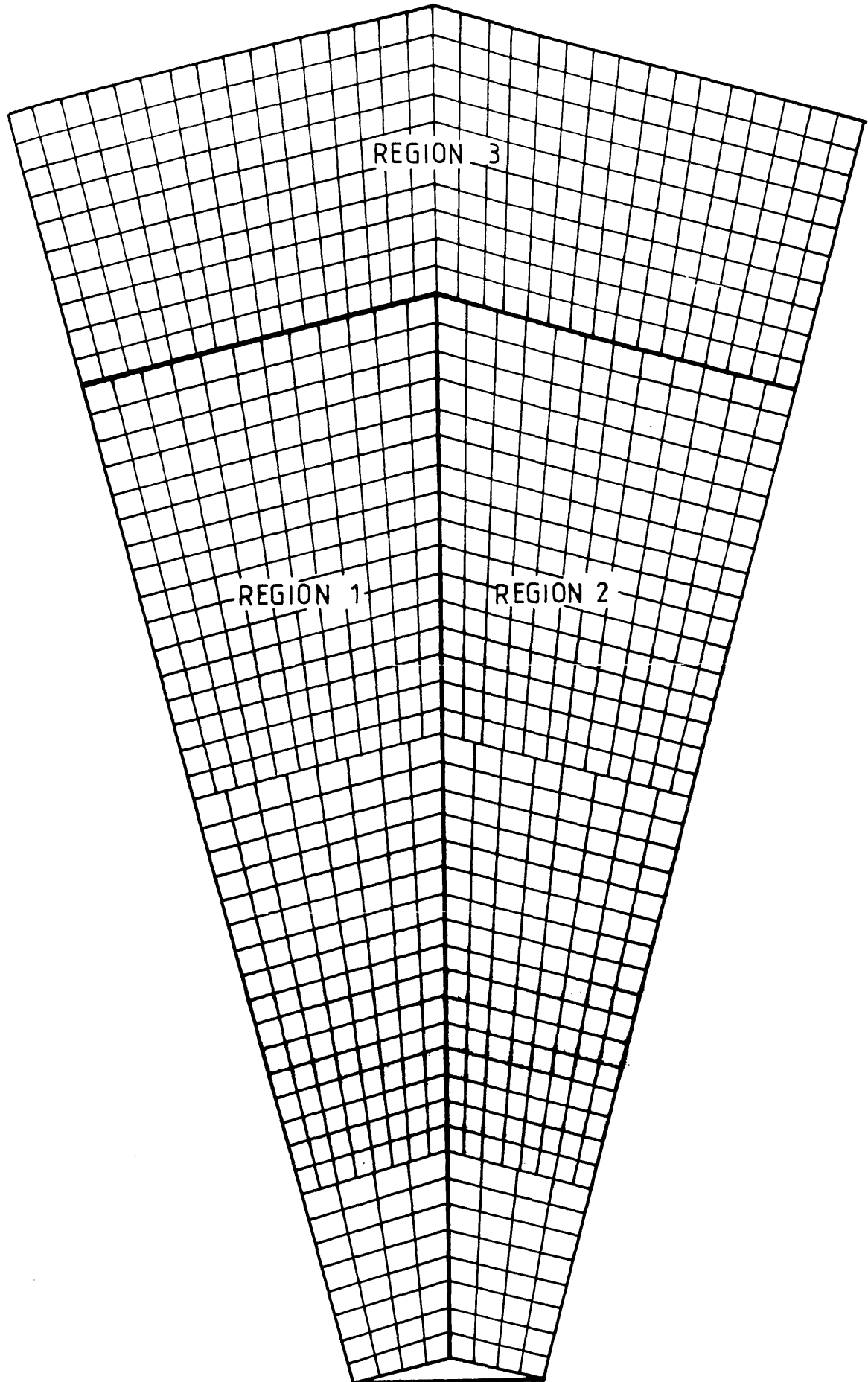


Fig.5.7

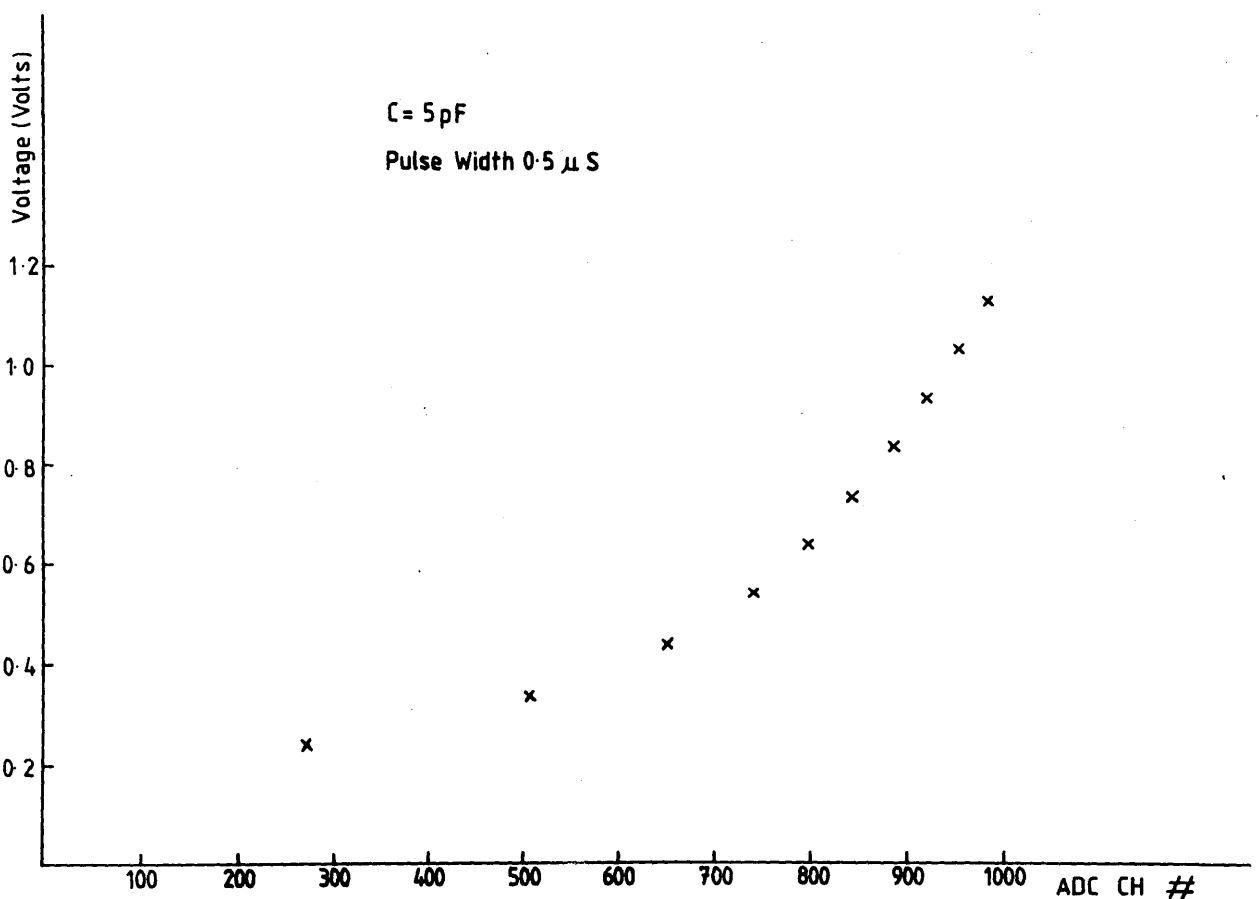


Fig.5.8

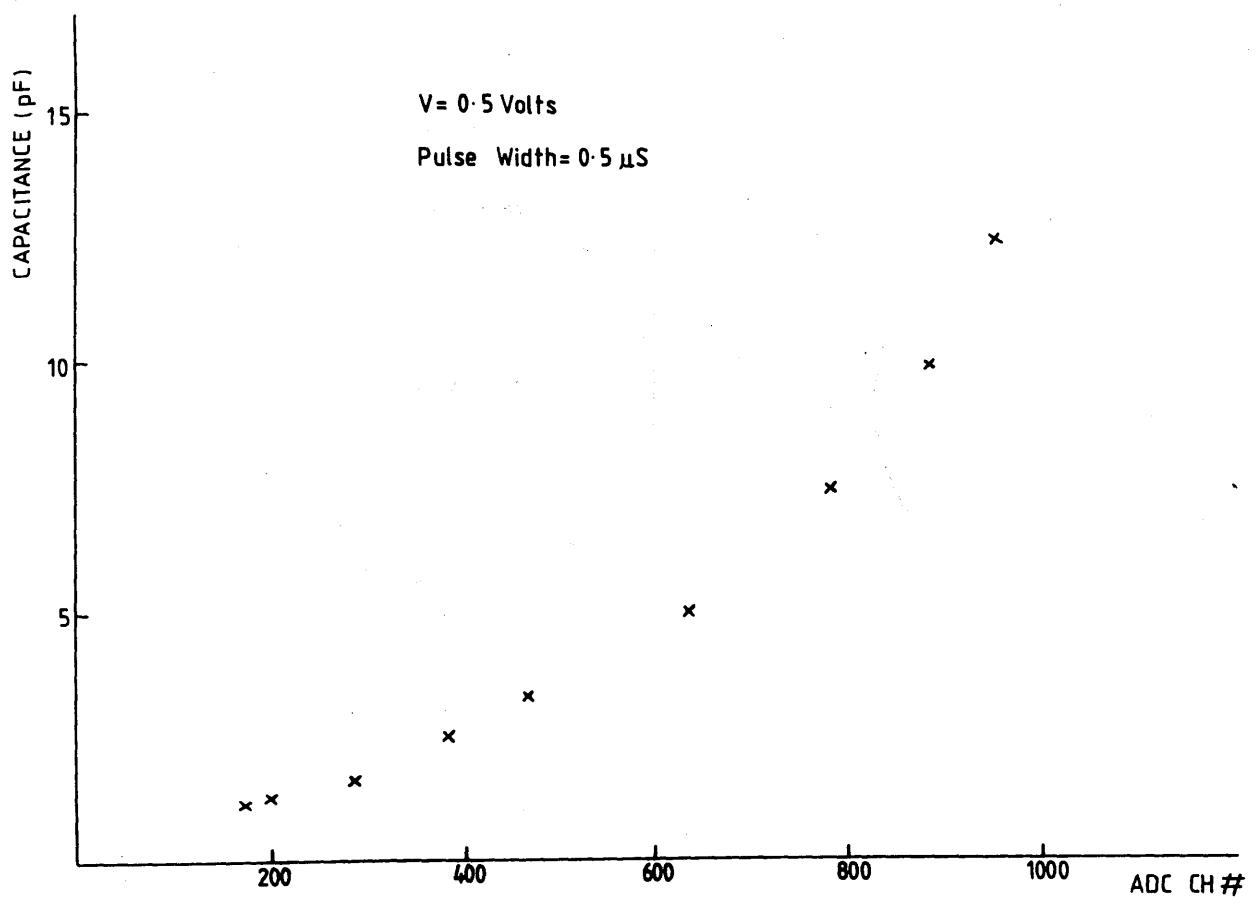


Fig.5.9

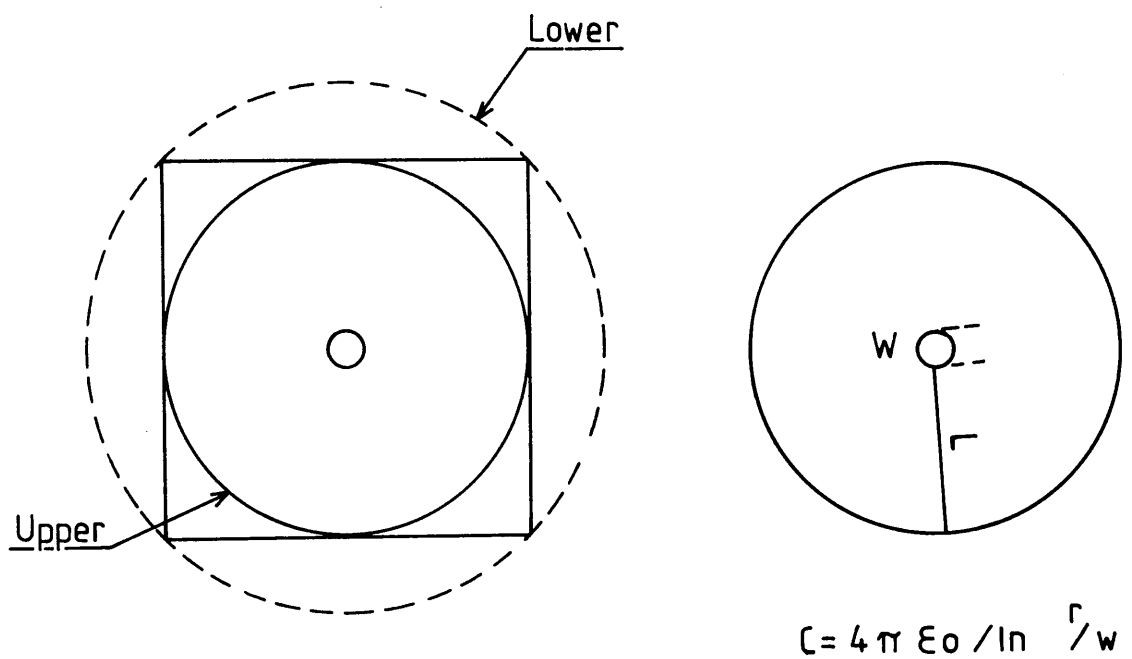


Fig.5.10

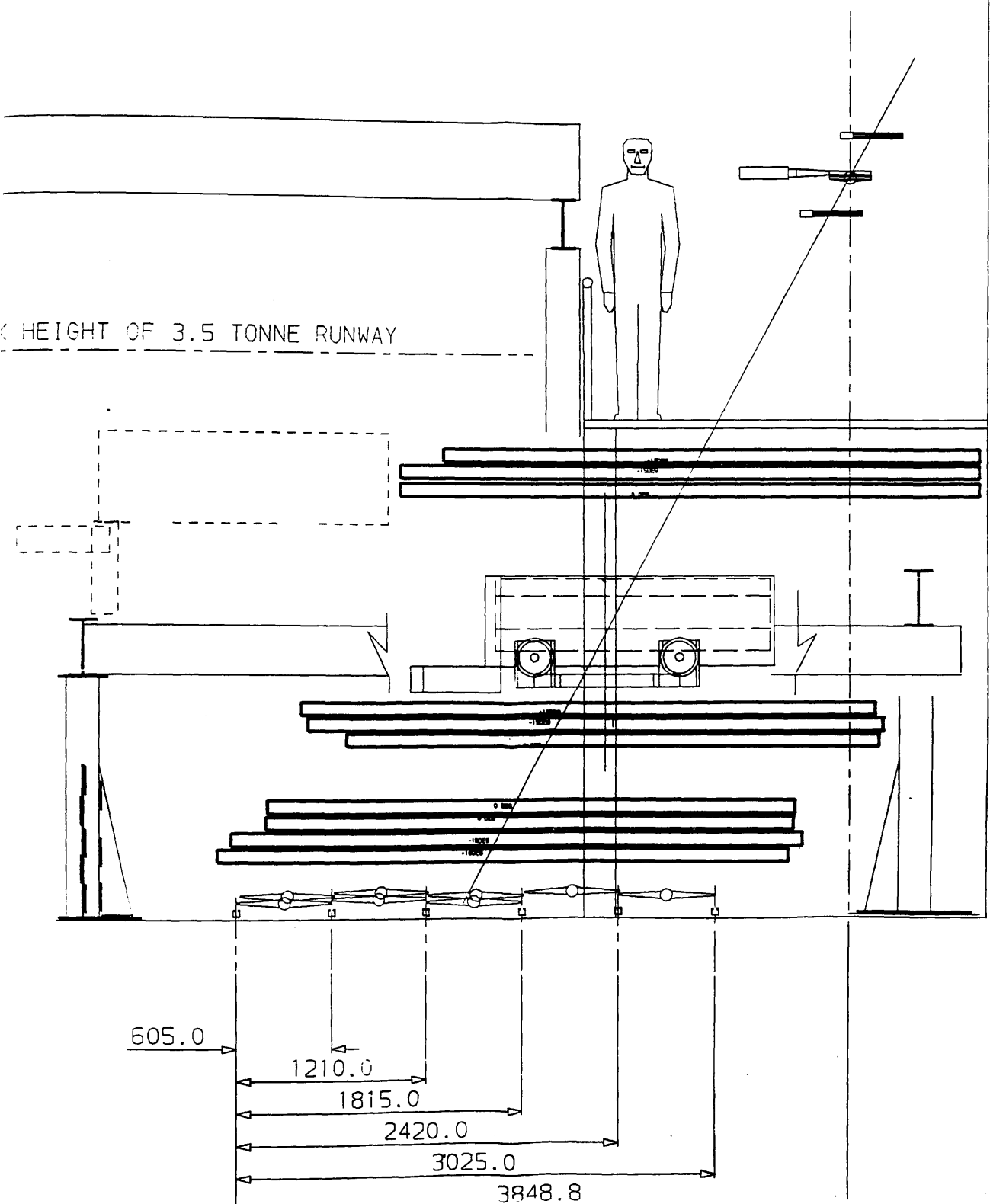


Fig.5.11

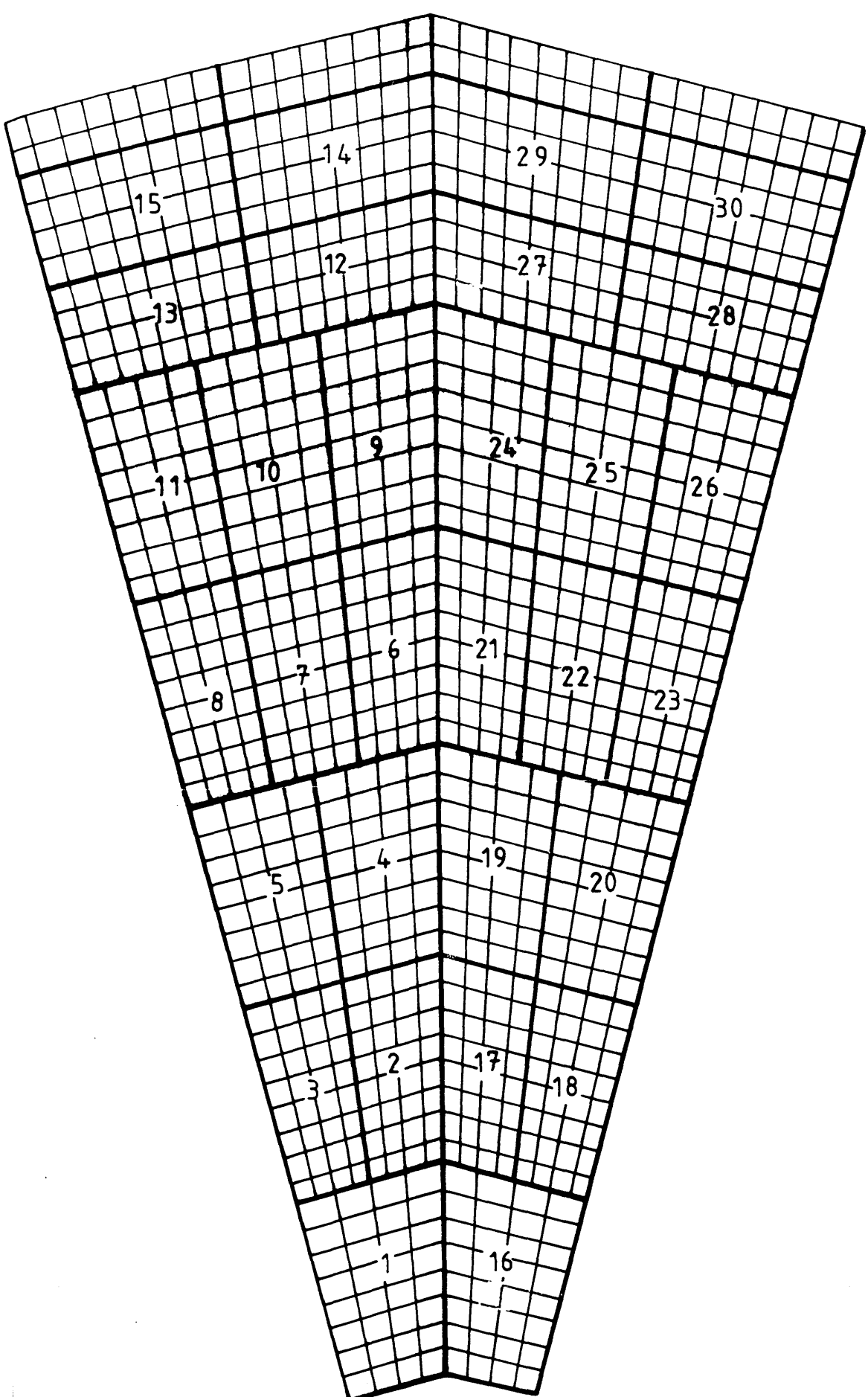
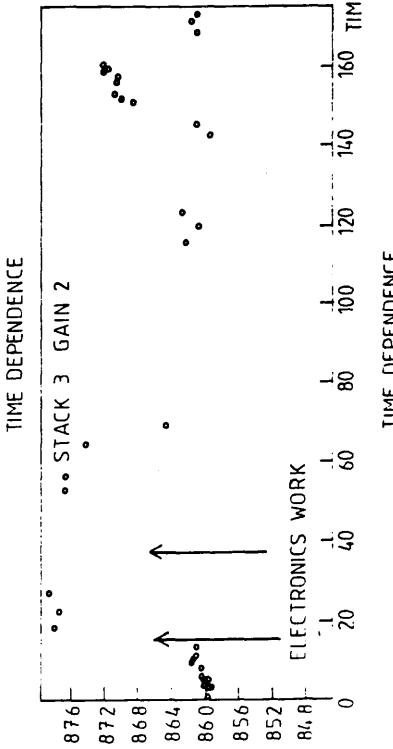
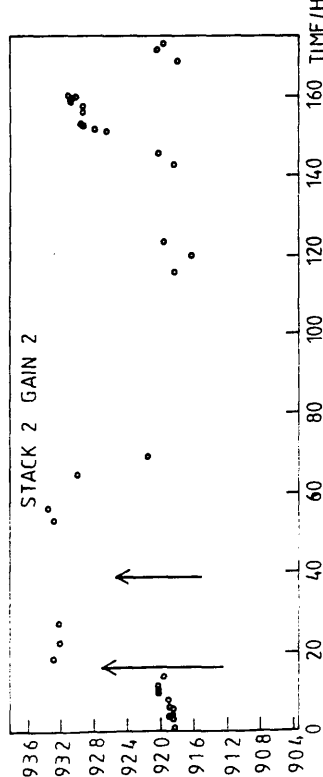
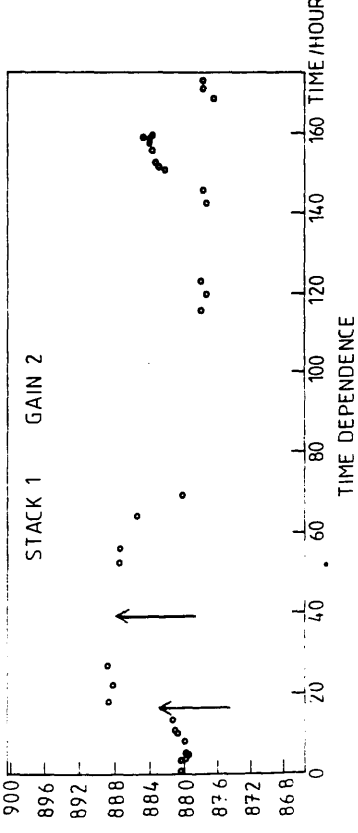


Fig.5.12

VARIATION OF ACTUAL PEDESTAL WITH
TIME FOR A TYPICAL TOWER



VARIATION OF ACTUAL PEDESTAL WITH
TIME FOR A TYPICAL WIRE PLANE

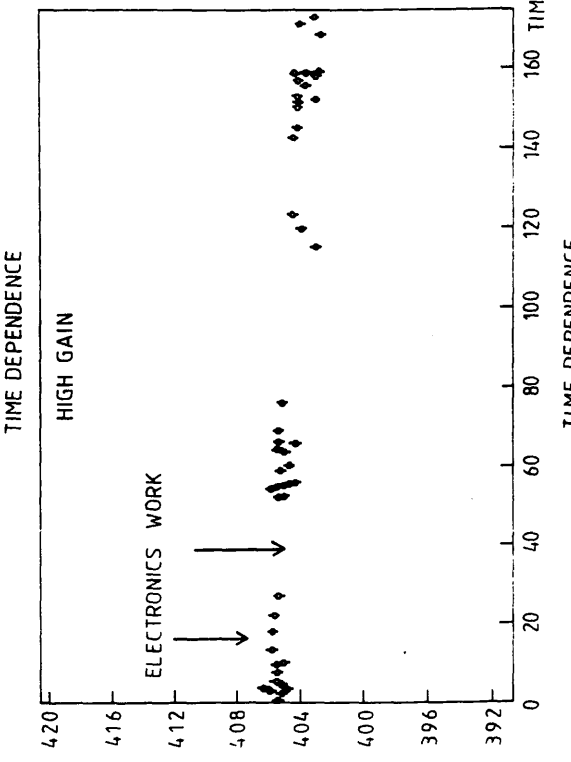
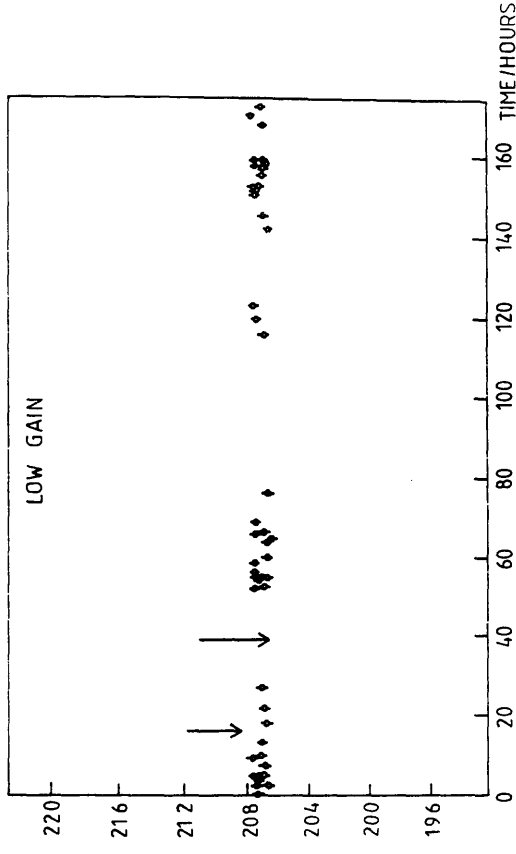


Fig.5.13

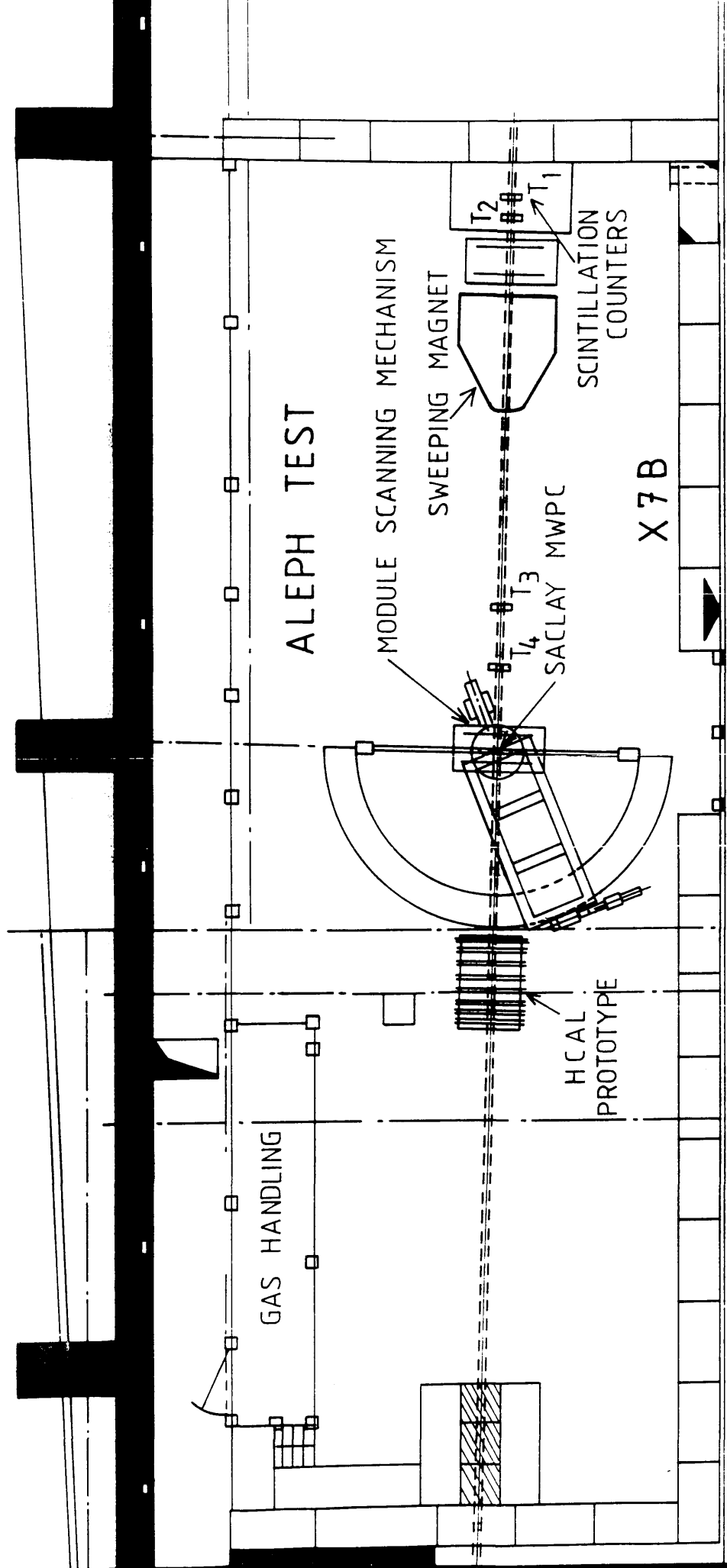


Fig.5.14

ENERGY DEPOSITED IN ECAL π 10GeV PETAL

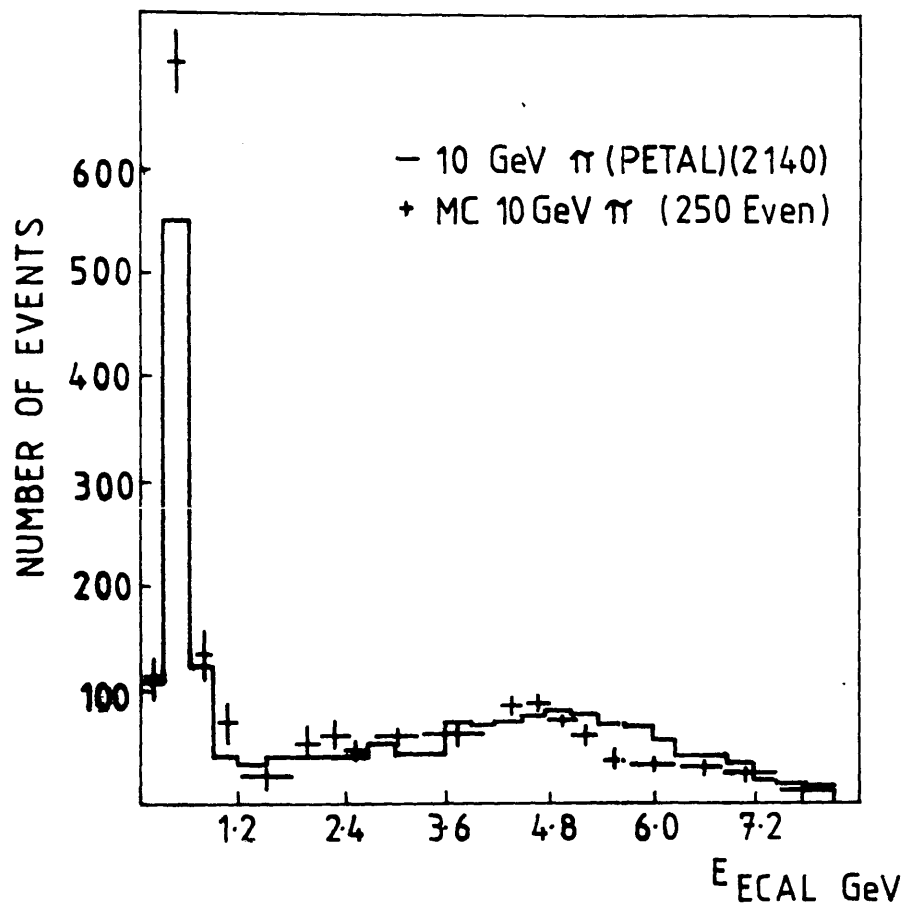


Fig.5.15.

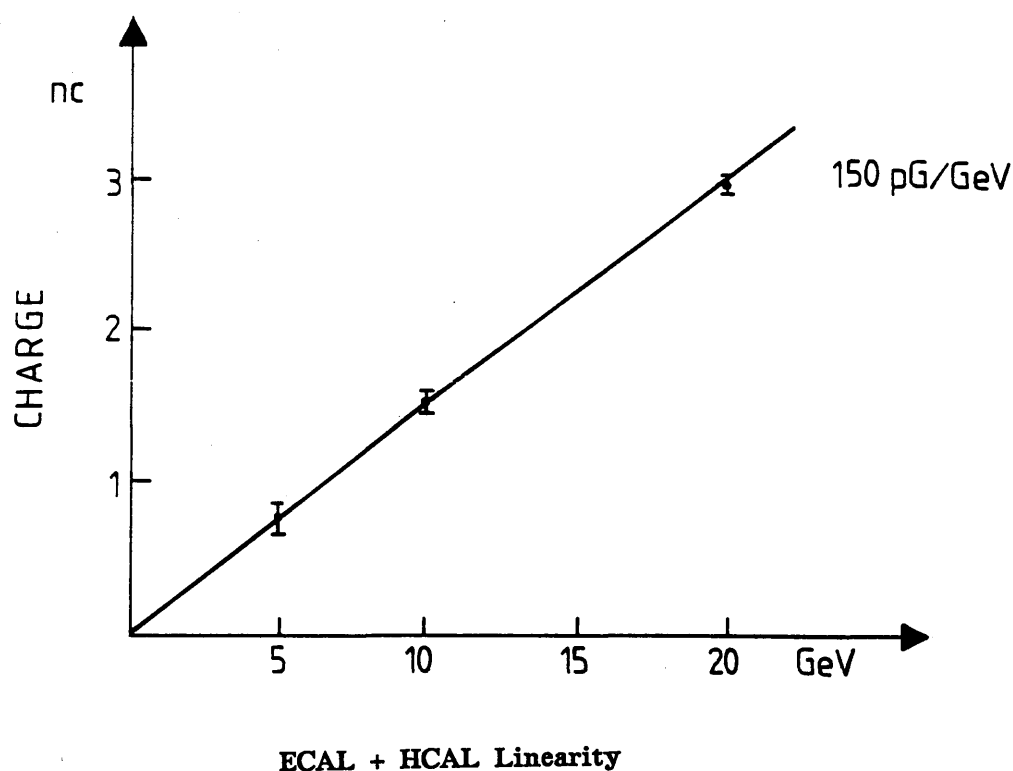


Fig.5.16

ENERGY RESOLUTION-ELECTRONS

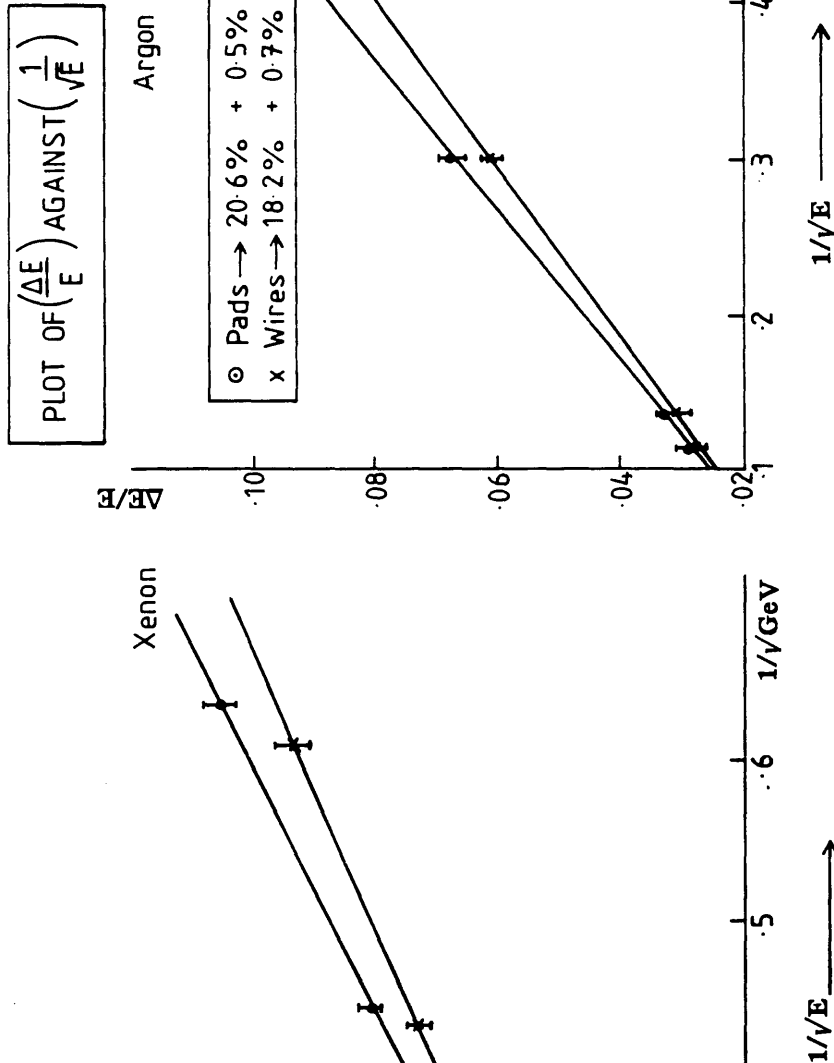
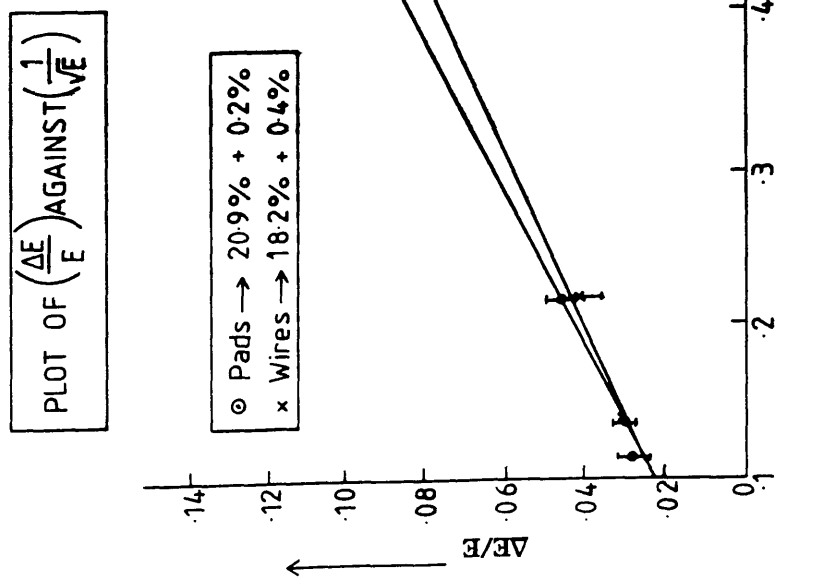


Fig.5.17

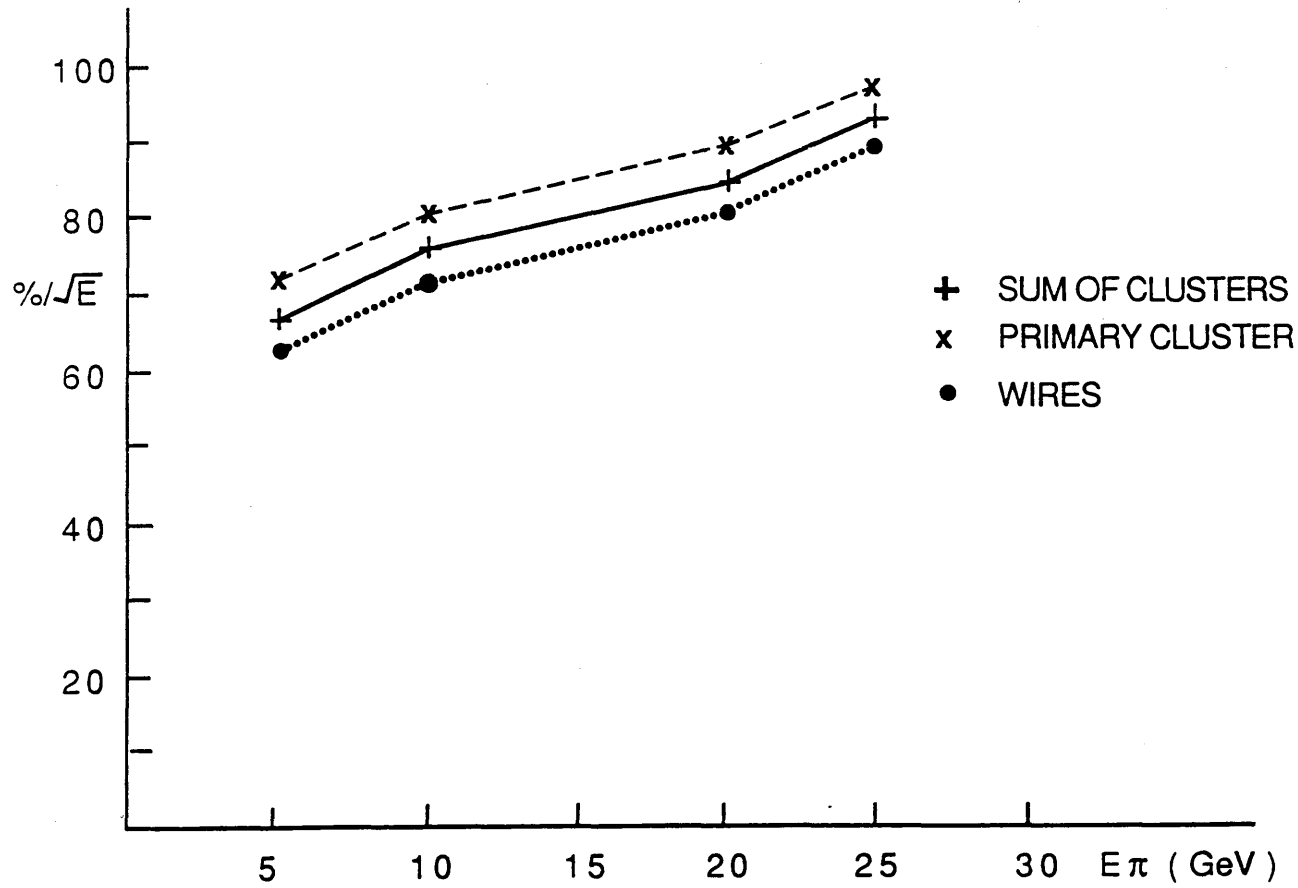


Fig.5.18

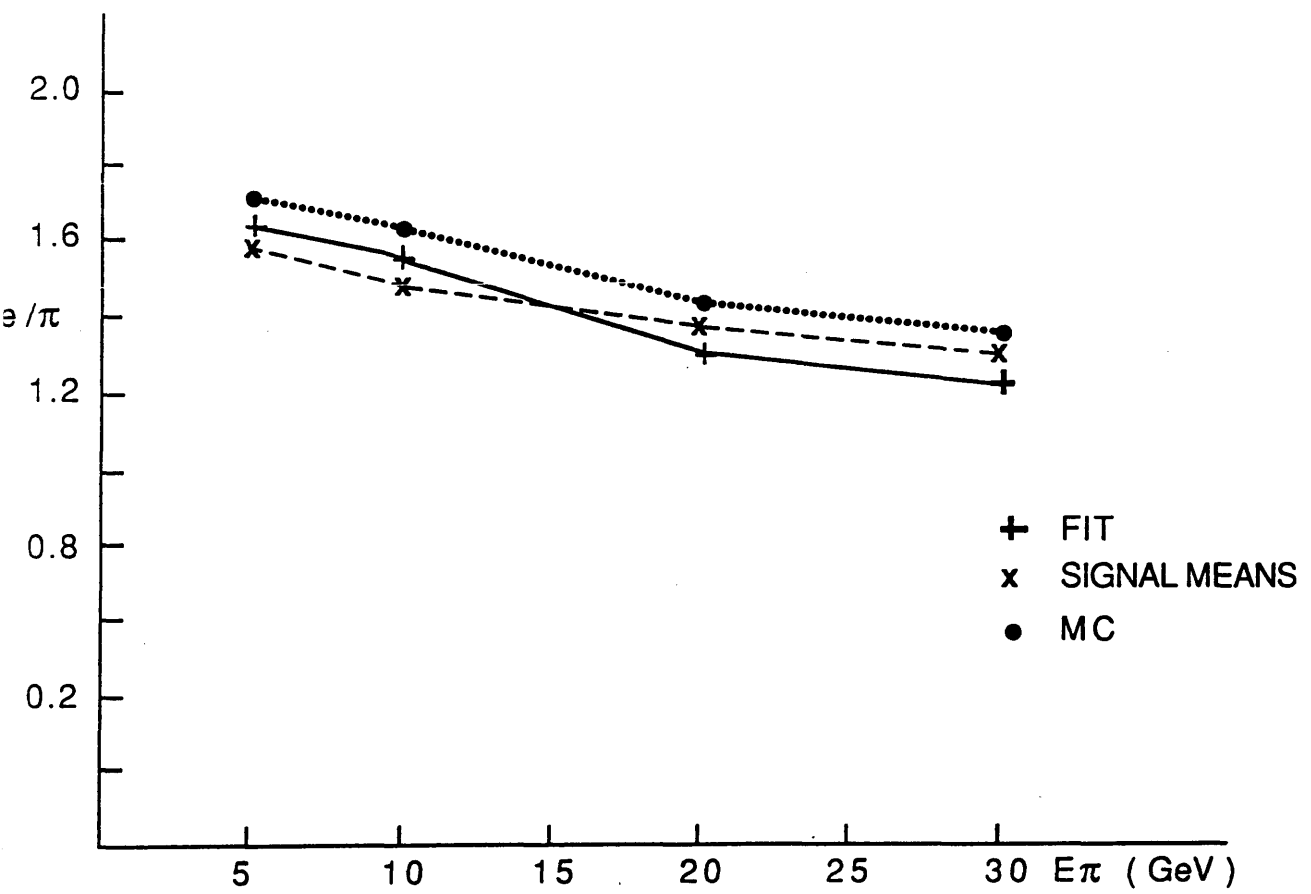


Fig.5.19

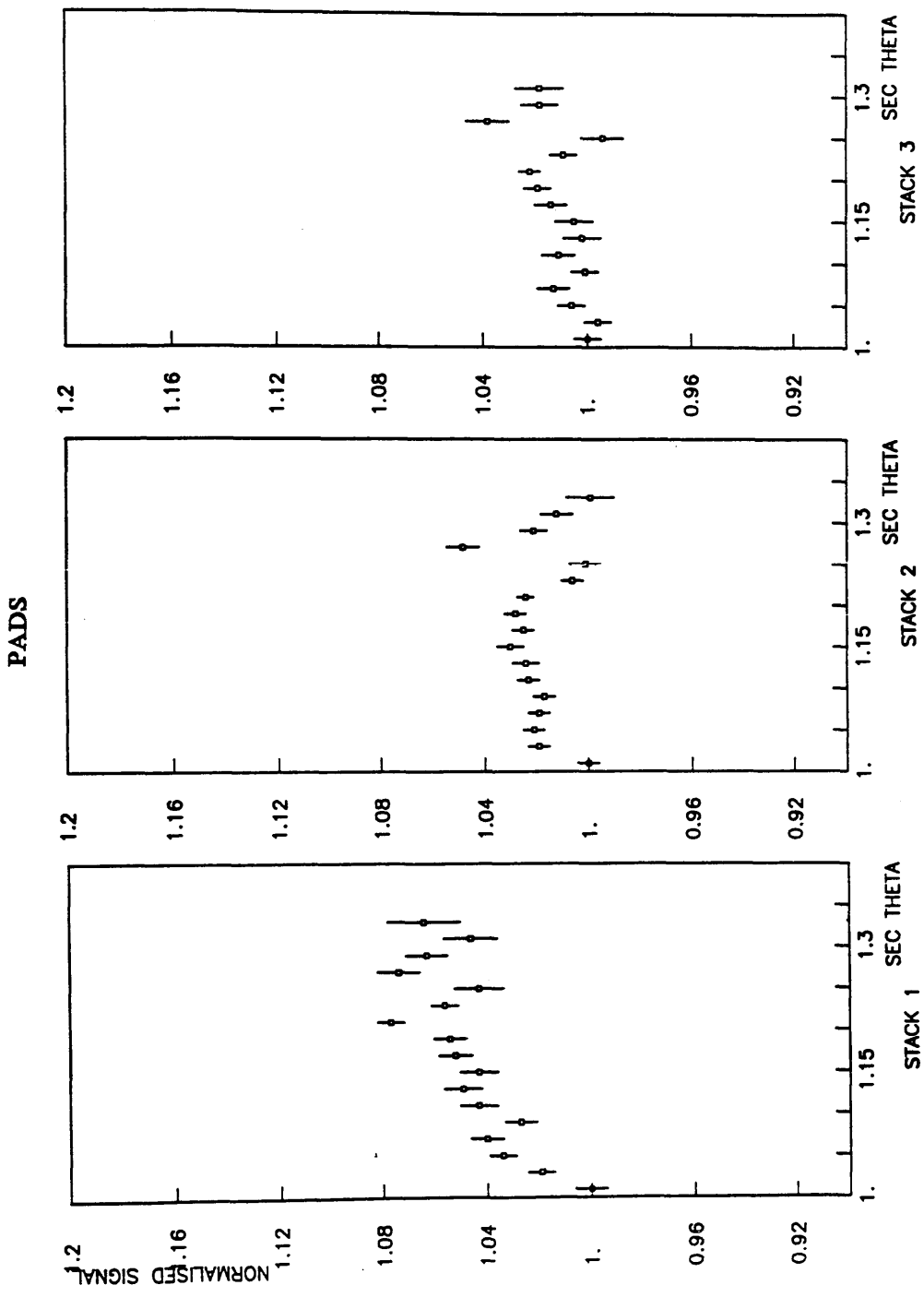


Fig.5.20

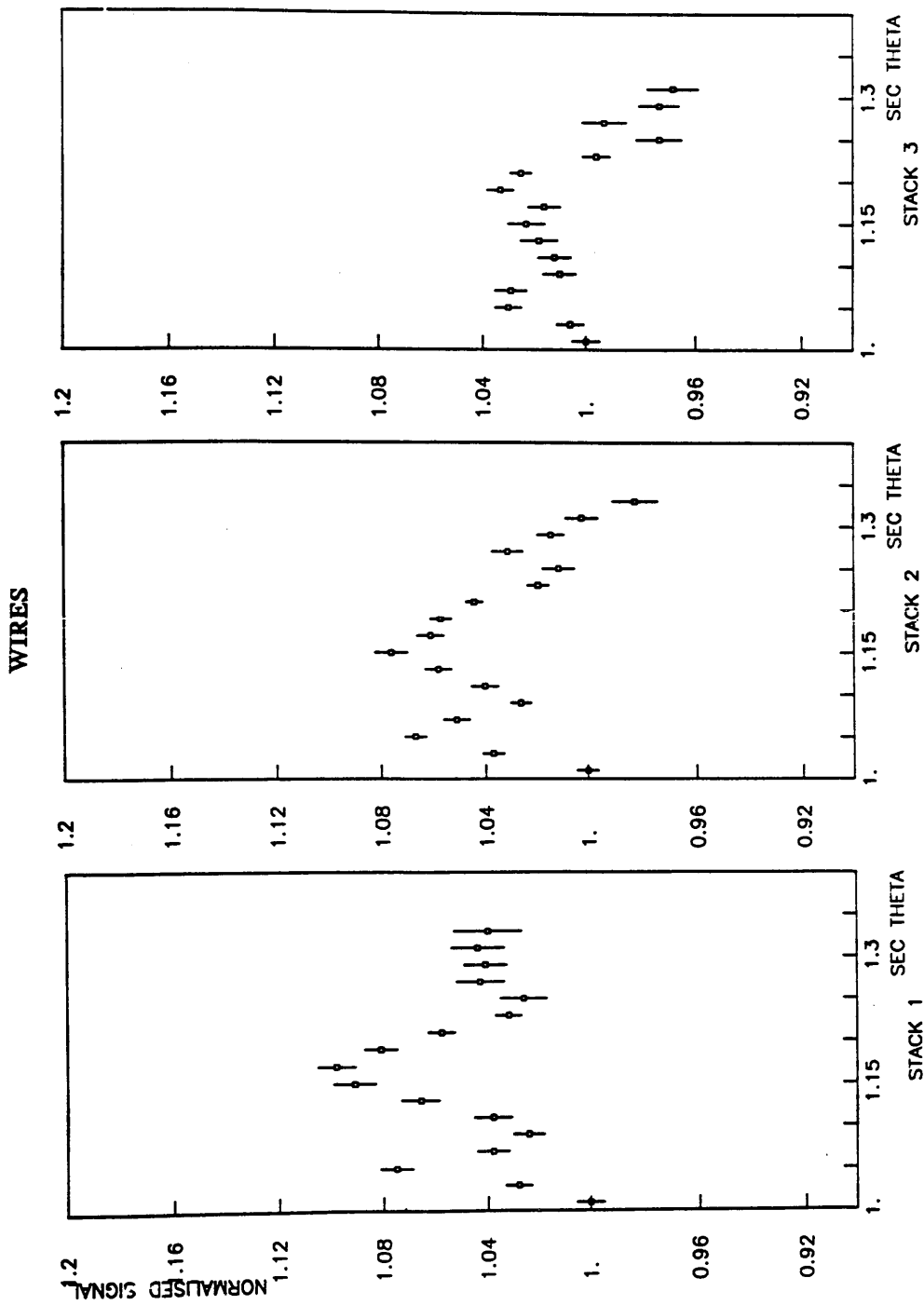


Fig.5.21

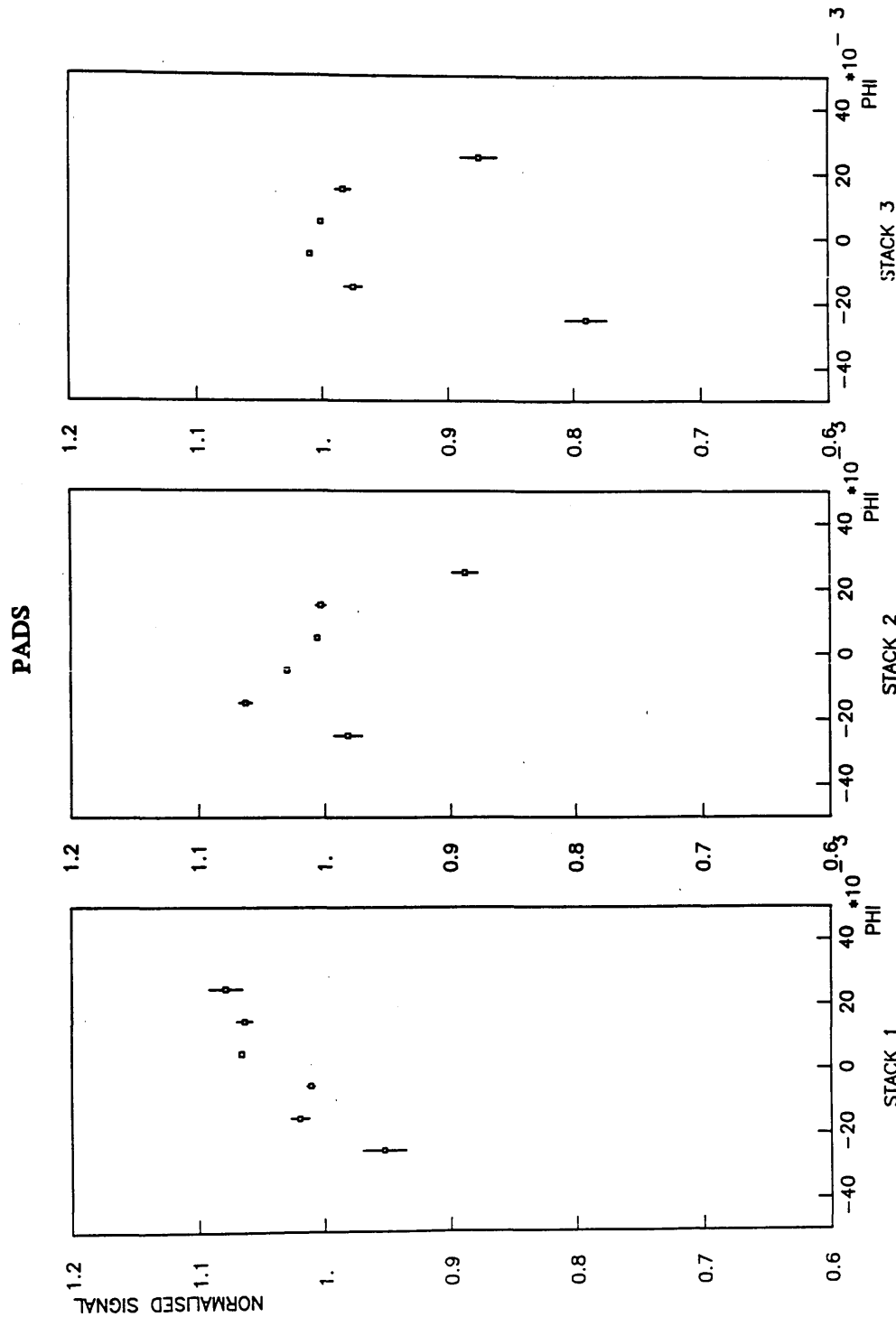


Fig.5.22

WIRES

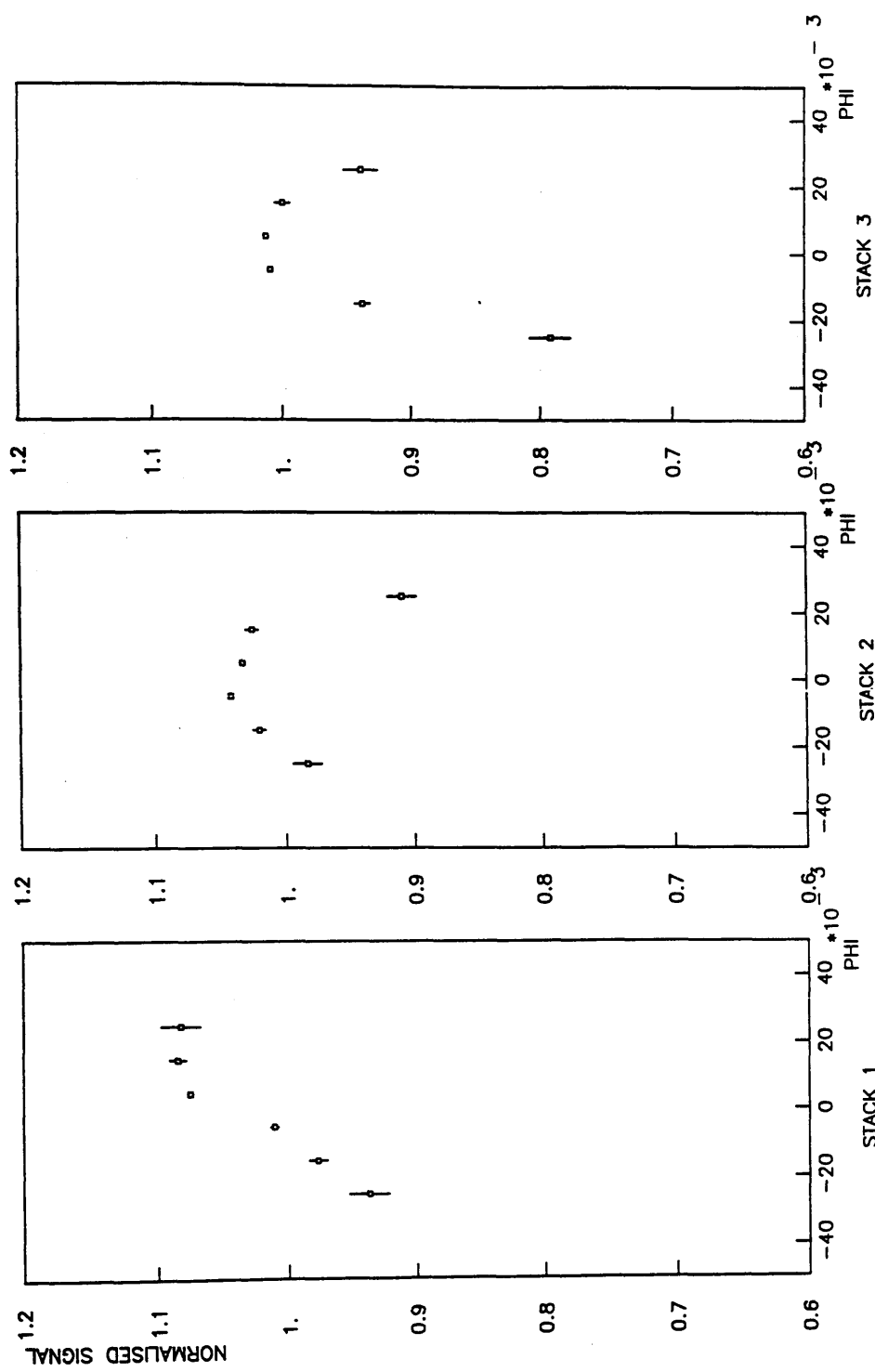


Fig.5.23

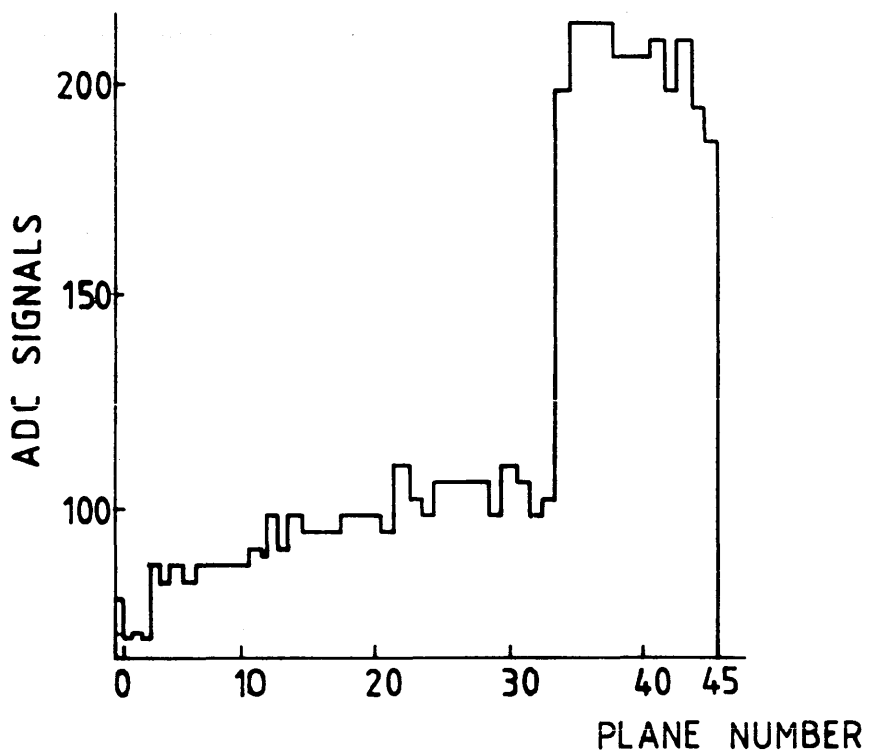


Fig.5.24

Chapter 6 Summary and Conclusions

The ALEPH detector described in Chapter 1 is made up of many components built by various groups from different universities and research centres all over Europe, and beyond. The detector is now in its final construction stage and all its components are undergoing comprehensive tests in preparation for data taking when the LEP accelerator turns on in July next year.

In the earliest, and perhaps most fundamental, measurements of the mass and the width of the Z^0 , the determination of energy plays an important role. As discussed in Chapter 1, it is concluded that a $(\Delta E/E) \approx 3 \times 10^{-4}$ is achievable. From the results of section 1.6.2 a luminosity determination to an accuracy of 2% can be reached with LCAL and SATR. Tests on the superconducting coil also show the capability of the apparatus to supply the highly uniform magnetic field needed for the detector. The results presented in chapter 3 from tests of the ALEPH components prove the ability of the ALEPH subsystems to achieve their design objectives.

So far as the ECAL is concerned, the most important characteristic to be fully understood and well established through the construction stage is the uniformity of the module response within a 1% limit or so. Different tests have been done on the modules throughout the construction stages, in the assembly of the modules and on the completed modules. All the evidence from results of wire pulsing, cosmic ray tests and test beam running are compatible with attaining the uniformity limit mentioned above. The effects of mechanical tolerances on the uniformity have been studied and the results presented in section 4.3 prove the adequacy of the tolerance levels required. In section 5.1 results from the slow control system show that the gas gain can be satisfactorily monitored to allow pressure and temperature and composition changes to be corrected. In section 5.2 wire pulsing is proved to be an important tool for the discovery of faults during the construction stage, due to e.g., missing pads, missing towers, broken wires etc.. In the final calibration of modules, appropriate corrections will be applied according to the faults discovered in the wire pulsing. The electronics used in the ECAL proved satisfactory through all tests done, as illustrated by results shown in section 5.2.2.

Fig.6.1 shows a uniformity map for petal 9, and shows the capability of wire pulsing in the simple determination of module uniformity at an early stage.

A uniformity of better than 2% has been achieved from the cosmic ray test. A similar result was obtained from uniformity studies using electron test beam data.

The ECAL resolution has been studied from data taken in test beams, and results from early analysis lie between (18-20)%/ \sqrt{E} for electron beams. In addition modules show good linearity, as mentioned in section 5.2.2.

A value between 1.2 and 1.65 for e/h is obtained from the comparison of test beam data from electrons with those from pions of energy between 5 GeV and 30 GeV.

The study of the detailed properties of the calorimeter will continue during the final preparation and installation of the detector in pit 4 ready for data in 1989.

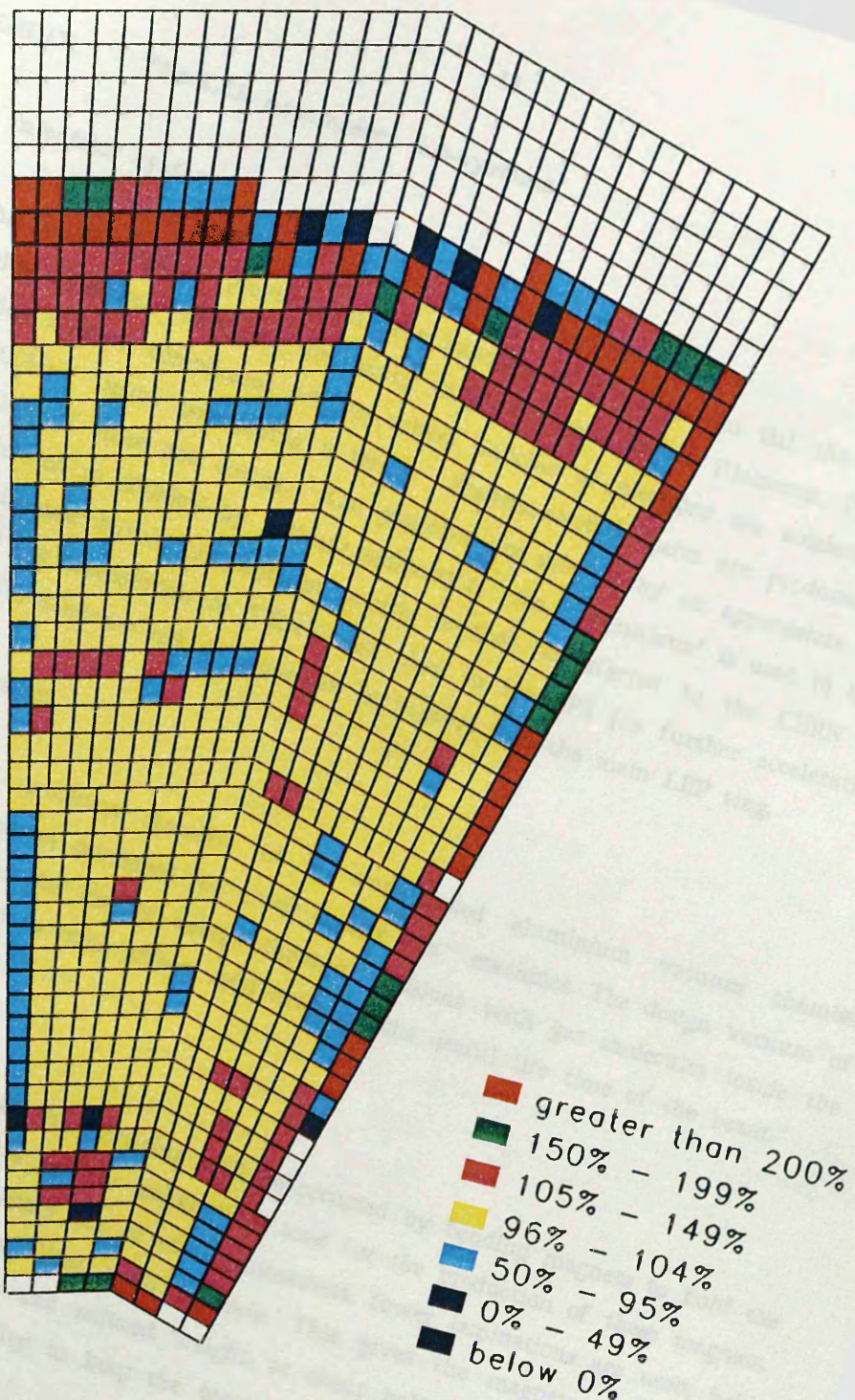


Fig.6.1

APPENDIX 1 - The LEP Accelerator sub-systems

1. The injection system

This is designed to provide sufficient bunches of e^+ and e^- to fill the ring within about twelve minutes. Electrons are easily obtained from heated filaments. Positrons are obtained with a more complicated scheme, where bunches of electrons are accelerated to an energy of 200MeV before bombarding a target. Positron-electron pairs are produced through interchangeability of mass and energy. The positrons are selected by an appropriate magnetic field and accelerated to 600MeV by a linear accelerator. An 'accumulator' is used to build up a sufficiently intense bunch of positrons, which is then transferred to the CERN proton synchrotron (PS) for acceleration to 3.5GeV and then to the SPS for further acceleration to 22GeV. At 22 GeV, electrons and positrons can be injected into the main LEP ring.

2. The vacuum system

Electrons and positrons circulate in a water-cooled aluminium vacuum chamber constructed using techniques developed for lower energy e^+e^- machines. The design vacuum of 3×10^{-6} Torr will reduce the loss of energy through collisions with gas molecules inside the chambers to the level where other effects will determine the useful life time of the beam.

3. The magnets

About 22 kilometres of the LEP ring will be occupied by bending magnets to hold the particles on their circular orbits. A new technique is used for the production of these magnets. Instead of building cores completely out of steel laminations, fewer laminations are used, held apart by spacers and the gaps filled with concrete. This gives the magnets the required quality, great mechanical rigidity and reduced weight, at about half the cost of conventional magnets, in addition to their ability to keep the beams in their orbits with a low magnetic field even at the highest energies.

4. The acceleration system

The energy loss in LEP operation due to synchrotron radiation is relatively small compared to other e^+e^- colliders because of the large radius of the LEP orbit. Nevertheless, the most crucial components of the project are the radiofrequency accelerating cavities (RFC) and their power supplies. It is these cavities which supply the energy to accelerate the

electrons and positrons, and to replace the energy lost by synchrotron radiation. The radiated power from a charged particle is given by:

$$P_r = 2/3 \{c r_0 c^2 \gamma^4 / \rho^2\}$$

where r_0 = the classical radius of the particle and P_r depends mainly upon the radius of the particle. The ratio between the radiated energy from an electron and a proton having the same energy and the same bending radius is about 10^{13} . The radiated energy per turn per particle is given by

$$\begin{aligned} \Delta E &= P_r 2\pi\rho/c \\ &= (4\pi/3)r_0 m_0 c^2 \gamma^4 / \rho \\ &= C \gamma^4 / \rho \end{aligned}$$

C is independent of particle type.

For electrons

$$\Delta E(\text{keV}) = 88.5 E^4 (\text{GeV}) / \rho \text{ (m)}$$

which means that for LEP, at 55 GeV and $\rho = 3100\text{m}$ we get $\Delta E = 260\text{MeV/turn}$, rising to 1.3 GeV/turn at 85 GeV. The total radiated power from the beam of N particles is given by:

$$Nf\Delta E = nfC\gamma^4 / \rho = (I/e) C\gamma^4 / \rho$$

where f is the revolution frequency.

For LEP at 55 GeV, with a beam current of 3 mA, the total radiated power in the two beams is 1.6 MW and it approaches 10 MW at 85 GeV. This power has to be supplied by the rf. system, but the more important thing is to dispose of the radiated energy without causing any damage to machine components or experiments. In addition to the radiated power, the associated ohmic loss in the rf. structure has to be supplied. This is given by

$$P_c = (k/e)^2 C^2 \gamma^8 / \rho^2 Z_s L_c$$

where k = a factor representing the over voltage, Z_s = shunt impedance per unit length of the accelerating structure, and L_c = the length of this structure.

This loss depends strongly on the beam energy. The total estimated ohmic loss in the rf. structure of LEP is about 12 MW at 55 GeV, and starts to become prohibitive if one would like to approach 100GeV. This kind of loss gives the main incentive for the development of superconducting rf. structures. If this development proves successful, the radiation limit in LEP may be lifted to (120/130)GeV per beam. The construction of much higher energy circular accelerators seems doubtful because of the above losses and this has led to an interest in developing linear colliders, the first of which is now being commissioned at SLAC.

Acceptance and Emittance

The x, z coordinates of the beams are given by

$$x, z = K_{x, z} \sqrt{\frac{\chi_{\beta_{x, z}}}{p_0}} \cos \left(\int \frac{ds}{\chi_{\beta_{x, z}}} + \phi_{x, z} \right)$$

where P_0 is the particle momentum and $P_0 = eB_0R_0$, R_0 is the radius of the accelerator, B_0 a constant magnetic field, K and ϕ are integration constants

$$\chi_{\beta_x} = \frac{R_0}{\sqrt{1-n}}, \quad \chi_{\beta_z} = \frac{R_0}{\sqrt{n}},$$

where $\chi_{\beta} = \lambda_{\beta}/2\pi$.

R_0 and n are kept constant during the acceleration. This gives

$$x, z = \frac{K_{x, z}}{\sqrt{p_0}} \cos \left(\frac{s}{\chi_{\beta_{x, z}}} + \phi_{x, z} \right)$$

if we introduce $\xi = x, z$, and $\chi_{\beta} = \chi_{\beta_{x, z}}$ we obtain

$$\xi = K (\chi_{\beta}/p_0)^{1/2} \cos \left(\int ds/\chi_{\beta} + \phi \right).$$

For the slope of the particle orbit we get correspondingly

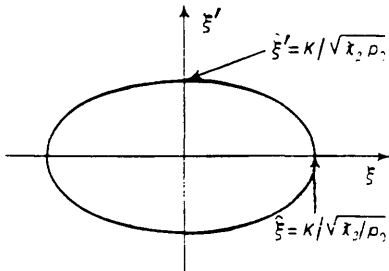
$$\frac{d\xi}{ds} = \xi' = K (\chi_{\beta} p_0)^{-1/2} \sin \left(\int ds/\chi_{\beta} + \phi \right)$$

and combining the two gives

$$\xi^2 + \chi_{\beta}^2 \xi'^2 = K^2 \chi_{\beta}^2 / p_0$$

This means that, in the (ξ, ξ') -plane the particles trace an elliptical orbit as shown in Fig.1.B1.

Fig.1.B1



The area of this ellipse is $\pi K^2 p_0^{-1}$ and the "shape" (ratio of diameters) is $\lambda\beta$. In a given machine there is a maximum possible amplitude a (e.g. given by the vacuum chamber or other restrictions). The area of the corresponding ellipse is called the acceptance, and is a property of the particular accelerator:

$$A = \pi a^2 / \lambda\beta$$

The particles in a beam oscillate with different amplitudes and phases. The particle with the largest amplitude ξ we assume follows the ellipse drawn in Fig.1.B1 above. All other particles follow orbits of the same shape but located inside. In such a case the area inside the drawn "maximum" ellipse is a measure of the size of the beam, and this area is called the emittance of the beam

$$E = \pi \xi^2 / \lambda\beta$$

which is an important beam property. $E \propto p_0^{-1}$ which means that the emittance diminishes with increasing momentum, i.e. the beam shrinks away from the vacuum chamber.

Instead of ξ' , one could have chosen as variable the corresponding transverse momentum

$$p_t = P_0 d\xi / ds.$$

In this case one would have obtained an invariant emittance very often written in normalized form as

$$E_n = \beta\gamma E = \text{invariant}$$

Correspondingly for the acceptance

$$A_n = \beta\gamma A \propto p_0$$

A practical consequence of the expressions for acceptance and emittance is the choice of high energy for injection into the accelerator. The beam size has a Gaussian distribution of amplitudes. In practice one therefore uses standard deviations of amplitude distributions to describe the beam emittance.

APPENDIX 2 - Polarisation in LEP

The magnetic guide field together with the synchrotron radiation lead to a polarization of the beam with the positron (electron) spin parallel (anti-parallel) to the magnetic guide field (). The polarization increases with time with a time constant which depends on the energy.

$$P(t) = P_0(1-e)^{-t/\tau} \quad \text{with}$$

$$P_0 = 8/3/15 \approx 0.92$$

$$\tau^{-} = (5\sqrt{3}/8) c \{ r^2 e \gamma^5 / a \rho^2 R \}$$

where $\gamma = E/m_e$, $a = 1/137$, R = average radius of the ring, and ρ = bending radius in the magnet.

The build up time for DORIS and SPEAR is given by

$$T = 165/E^5 \text{ h (E in GeV).}$$

so that $T = 5\text{h}$ for $E = 2 \text{ GeV}$ and $T = 15 \text{ minutes}$ for $E = 4 \text{ GeV}$. At LEP the natural polarization time at 50 GeV is 3.5h . This can be reduced to just over 1 h by the use of eight asymmetric wigglers, in which short, strong magnets alternate with long, weak magnets. With the right choice of polarity the polarization is strongly enhanced in the right direction and only weakly reduced by the magnets of the opposite sign. The wigglers required for radiation damping at injection have been designed to have a useful degree of asymmetry for this purpose. The build up time as a function of energy is given in Fig.1.B2, while Fig.1.B3 shows a degree of polarization at LEP in the presence of the linear spin resonance. Since the lifetime of the beam, (i.e. the time over which the luminosity drops by a factor of e), is of the order $3\text{-}5$ hours, studies with polarized beams at DORIS and SPEAR become practical for $E \geq 3 \text{ GeV}$. The polarization is destroyed when the ring operates near a machine resonance, so that one can obtain polarized beams only for certain sets of machine parameters.

The polarized beam could be an important tool in asymmetry measurements around the Z° pole, even in the context of conventional gauge theories. Results from PETRA have shown that beams can be maintained polarized up to a luminosity approaching the maximum achievable, in line with earlier theoretical predictions. Polarized beams provide the means for making precise absolute measurements of beam energy in storage rings, using an artificially induced spin resonance. Since the value of the gyromagnetic anomaly is known very accurately, the measurement of spin precession frequency determines the beam energy. This method has been extensively used at Novosibirsk, and has been successfully applied in PETRA and in DORIS. For LEP 1 when measuring m_Z a transverse polarization is enough, and a polarimeter is needed to reach a level of $\pm 20 \text{ MeV}$ in δm_Z . Polarized beams provide an extra degree of freedom for understanding the nature of fundamental interactions at high energies. If a measured longitudinal polarization of the e^- beam is available, the advantages

will be great for precision tests of the electroweak theory at the Z^0 . The sensitivity of AFB to $\sin^2 \theta_W$ is greatly increased, and one can also measure the left-right asymmetry A_{LR} with great precision. Moreover, A_{LR} is very sensitive to $\sin^2 \theta_W$. The same accuracy as that in the case of no polarization can be obtained in only 40 days of running with measured longitudinal polarisation.

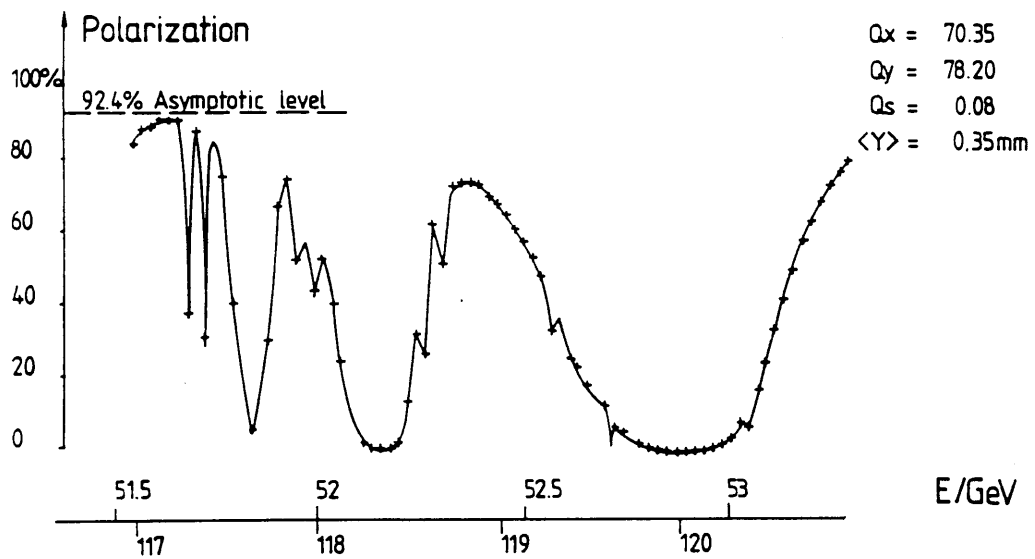


Fig.1.B2

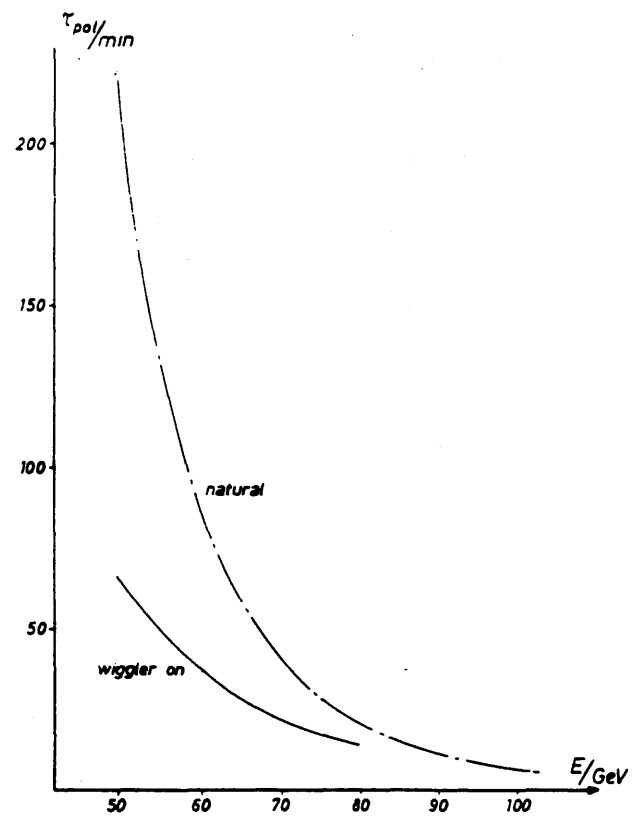


Fig.1.B3

REFERENCES

1. Electron Positron Collisions, F.M. Renard, (Editions Frontieres,1984).
2. Electron-Positron Interactions, B. H. Wiik and G. Wolf, (Springer-Verlag, 1979).
3. Proceedings of the International School of Physics "Enrico Fermi", Elementary Particles, Edited by N. Cabibbo, (North-Holland, 1986)
4. Collider Physics, V.Barger and R.J.N. Philips, (Addison-Wesley, 1987).
5. Very high energy electron positron colliding beams for the study of weak interactions, Nucl. Instr. and Methods 47(1976) 136.
6. Radiative corrections to the Z^0 resonance, J.P. Alexander et al. SLAC-PUB-4376, UM-HE-87-18, LBL-23819, August 1987.
7. 1986 CERN School of Physics, CERN 87-02, 30 March 1987.
8. Precision studies of the electroweak theory at the Z^0 , G. Altarelli et al., Physics at LEP Vol. 1, CERN 86-02
9. Toponium physics at LEP, Physics at LEP Vol. 1, CERN 86-02 W. Buchmuller et al.
10. D. Bernard, ALEPH 88-29, 21/03/88
11. J. D. Hansen, ALEPH 88-30, 31/03/88
12. E. Neugebauer, ALEPH 88-32, 5/4/88
13. D. Cowen et al., ALEPH 86-137, 20/11/87
14. A. Farilla et al., ALEPH 86-54, 24/4/1986
15. R. Johnson et al., ALEPH 87-85, 9/10/87
16. A. Voigtlander et al., ALEPH 88-79, 7/7/88

17. G. Catanesi et al., ALEPH NOTE 147, 20/11/85
18. J. Q. Zhang, ALEPH HADCAL 85-5, 1/10/85
19. M. De Palma, ALEPH-HADCAL, 85-3, May 1985
20. A. Jahn, ALEPH 87-89, 20/10/87
21. Calorimetry in high energy physics, C. W. Fabjan, CERN -EP/85-54
22. Fluctuations in Calorimetry Measurements, U. Amaldi, CERN-EP/80-212
23. Detectors For Particle Radiation, K. Kleinknecht, (Cambridge University Press, 1987).
24. Calorimetry In Particle Physics, G. Barbiellini, CERN, Geneva,
25. L3 Collaboration, Nucl. Instr. and Methods A254(1987) 535-541
26. E. Lorenz, Nucl. Instr. and Methods 225(1984) 500-504
27. Massayuki Murashita et al., Nucl. Instr. and Methods A243(1986) 67-76.
28. B. Cox et al., Nucl. Instr. and Methods 219(1984) 487-490 and 491-494.
29. Measurements of longitudinal and lateral developments of electromagnetic cascades in lead, copper and aluminium , G. Bathow et al., Nuclear Physics B20 (1970) 592-602
30. Radiation Detection and Measurements, G.F. Knoll, (Wiley, 1980)
31. Introduction to Experimental Particle Physics, R. Fernow, (Cambridge University press 1986).
32. Energy loss of particles in dense matter calorimetry, Richard Wigmans NIKHEF-H/87-12.
33. On the theoretical understanding and calculation of sampling calorimeters, H.Bruckmann et al., DESY 87-064.

34. Experimental Techniques in High Energy Physics, (Frontiers in physics, ed. T. Ferbel, Addison-Wesley, 1987)
35. G. Barbiellini, CERN-EP/88-57, Geneva, Switzerland
36. Calorimeters: Gaseous read out compared to alternatives, C.W. Fabjan CERN-EP/86-45.
37. B. Bleichart et al., Nucl. Instr. and Methods A254(1987) 529-534.
38. C. W. Fabjan et al., Nucl. Instr. and Methods 141(1977) 61-80.
39. Masami Chiba et al., Nucl. Instr. and Methods 190(1981) 15-18.
40. Tadayoshi Doke et al., Nucl. Inst and Methods A237(1985) 475-485.
41. M. Edwards, The ALEPH Electromagnetic Calorimeter, RAL-86-007
42. The ALEPH pictorial electromagnetic calorimeter, Nucl. Instr. and Methods, 225(1984) 481-492.
43. J. Engler, Nucl. Instr. and Methods, 217(1983) 9-18.
44. P. Campana, Nucl. Instr. and Methods, 225(1984) 505-508.
45. L. Valyi et al., Nucl. Instr. and Methods, 171(1980) 251-257
46. ALEPH Technical Report 1983, CERN/LEPC/83-2, LEPC/P1, 15/5/1983
47. ALEPH Status Report 1984, CERN/LEPC/84-15, LEPC/M50, 10/9/1984
48. H. Dietl, ALEPH plenary meeting at CERN, 17-18 sept. 1987
49. M. Cattaneo, ALEPH plenary meeting at CERN, 17-18 sept. 1987
50. E. Neugebauer, ALEPH plenary meeting at CERN, 17-18 sept. 1987

51. H. Meinhard, ALEPH plenary meeting at Barcelona 20-21 May 1988
52. W.-D. Schlatter, ALEPH in numbers, December 10, 1987
53. A. K. McKemey, ALEPH plenary meeting at CERN, 17-18 sept. 1987
54. T.R. Edgecock, ALEPH ECAL meeting at RHBNC, 6-8 January 1988
55. M. Green et al., ALEPH 88-87, EMCAL 88-4, 26/7/1988

